Ph.D. Dissertation

Geophysical investigations of the subduction zone in Peru and the 2017 Pohang earthquake in South Korea

페루 섭입대와 2017년 포항지진의 지구물리학적 연구

by

임호빈

August 2020

School of Earth and Environmental Sciences
College of Natural Sciences
Seoul National University

Geophysical investigations of the subduction zone in Peru and the 2017 Pohang earthquake in South Korea

페루 섭입대와 2017년 포항지진의
지구물리학적 연구

지도교수 김 영 희

이 논문을 이학박사 학위논문으로 제출함
2020 년 8 월

서울대학교 대학원
지구환경과학부
임 호 빈

임호빈의 이학박사 학위논문을 인준함
2020 년 8 월

위 원 장 정 해 명 (인)

부위원장 김 영 희 (인)

위 원 강 태 섭 (인)

위 원 이 준 기 (인)

위 원 김 성 룡 (인)

Abstract

This thesis provides a better understanding to the subduction zone in southern Peru and the 2017 Pohang earthquake in South Korea. The southern Peru is a transitional zone from the normal-dipping to the flat slab regions. I defined the geometry of the Nazca slab using the intra-slab earthquakes and converted teleseismic phases (previous published studies). The P and S waves obtained by the double-difference tomography indicate different hydration states of the slab and mantle wedge or layer. The Pohang earthquake occurred near the enhanced geothermal power plant on 15 November 2017. One of the main goal was to suggest a physical understanding to explain the occurrence of the earthquake in a framework of the linear poroelasticity. I suggested that the timing of the earthquake is attributed to slow fluid diffusion.

I improved the availability of the permanent seismic data deployed in South Korea. The most of the broadband seismometers in South Korea (30 of 52 in 2016) are a type of borehole. While the borehole seismometers produce low human-induced noise, they might have a drawback of an uncertain orientation. I developed a new method obtaining the orientation without having to assume for an isotropic medium (i.e., anisotropic medium). This method normalizes the effect of seismic sources and determines the orientation of a seismometer. I applied the method to the Korean data in 2005–2016. Also, we anticipated that this method can be applied to more noisy environment (e.g., ocean bottom).

The ongoing research is about the Clark fault in southern California using a dense geophone array. The 129 geophones were deployed across the distance of about 2.5 km, slightly oblique to the fault. One of 42 teleseismic earthquakes was usable to compute P-wave receiver functions for imaging the fault. The width of the fault zone is inferred

as about 460 m from the delayed P-wave arrivals (up to 0.6 s) and a bifurcation of a reflection branch. Deconvolution of the vertical-component signal recorded from one station distant ($\sim$1.2 km) from the fault was effective to identify phases that are reverberated in or refracted by the narrow fault zone.

Keywords: Subduction zone, 2017 Pohang earthquake, Poroelasticity, Anisotropy, Orientation, Clark fault

Student Number: 2014-21308

Contents

List of Tables

List of Figures

Chapter 1

Introduction

The structure of Earth's interior cannot be studied directly. Because different types of seismic waves behave differently when they encounter material in different states at depths, seismic stations can detect and record strengths of the different types of waves and the directions from which they came. In my Ph.D. training, I analyzed both regional and teleseismic waveforms by means of teleseismic receiver function (RF) and seismic tomography to image the subsurface structures beneath tectonically interesting regions. Seismic images are then used to understand structural velocity heterogeneities and infer the origin of such velocity anomalies. During the course of study, two major earthquakes on 11 September 2016 and 15 November 2017 occurred in Korea, and I had a chance to understand those source properties.

Chapter 2 introduces a framework based on RFs to determine the horizontal orientation of the seismometer. The proposed method enables to produce robust estimates on the orientation even in the medium with seismic anisotropy and dipping layers beneath the sensor. The isotropic-medium assumption can make the orientation deviated from the true sensor orientation by over 10° (Schulte-Pelkum et al., 2001; Wang

et al., 2016). Radial receiver function (R-RF) and tangential receiver function (T-RF) are calculated by deconvolving the radial and tangential components of teleseismic waves, respectively, from the vertical component. Through harmonic decomposition of stacked R-RF and T-RF in backazimuth gathers, the sensor orientation angle is determined by minimizing a constant harmonic term of the T-RF at and near 0 s. Both P and PP phases are used to enhance the backazimuthal coverage. This method is applied to 52 broadband stations in South Korea and two ocean bottom seismometers (OBSs) involving relatively lower signal-to-noise ratio (SNR). Also, our new algorithm can scan and detect the change of sensor orientation in time.

Chapter 3 show seismic images based on the double-difference constraints from local earthquakes (Zhang and Thurber, 2003), and we discuss velocity heterogeneities within subducting slab and mantle wedge structure. Our study region in southern Peru includes a transition in slab geometry from flat to normal, a decrease in magmatic activity, subductions of a ridge (the Nazca ridge) and a fracture zone (the Nazca fracture zone). Regional earthquakes are detected and located to provide a first-order the flat-to-normal geometry of the Nazca slab. P and S wave velocities and their ratio (Vp/Vs) are calculated using the double-difference tomography (Zhang and Thurber, 2003). Along-arc velocity variation indicates that the subduction of the Nazca ridge affects the serpentinization in the forearc region, retardation of the metamorphism of the slab to a denser mineral (e.g. eclogite), and high temperature in the mantle wedge above the normal-dip slab.

Chapter 4 shows the poroelastic response on the Mw 5.5 earthquake in Pohang, South Korea, on 15 November 2017. The high-pressure hydraulic stimulation has begun in Pohang Enhanced Geothermal System (EGS) site since January 2016, and the space-time variation of seismicity before this event is well correlated with fluid injection record (Grigoli et al., 2018; Kim et al., 2018). This chapter explains the poroelastic change in stress with the fluid injection and compares relocated seismicity

and the spatio-temporal evolution of Coulomb stress to decipher conditions for causing the fault failure.

Chapter 5 shows teleseismic constraints on the fault-zone system in Clark fault, southern California. Dense geophone array is deployed at a linear line nearly perpendicular to the fault strike. We attempt to compute high-frequency receiver functions to probe seismic structure within the crust and more importantly the fault damaged zone at shallow depths. Preliminary results show that the fault-zone velocity structure is complicated and responsible for generating reverberated phases. To investigate the fault-zone structure, more sophisticated methods for deconvolution, removing the near-surface structure effect, and/or stacking are required, which we leave for future study.

Following Ben-Menahem (1995), topics in the seismology can be grouped into nine, as Table 1.1. For a concise summary, each chapter is linked to one in Table 1.1. In Chapter 2, the new method solving the orientation problem in the anisotropic medium is developed (8 in Table 1.1). Chapter 3, imaging P and S wave structures in the Peruvian subduction zone, is linked to 6. One of main objective of the chapter 4 is to reveal the physical mechanism of the occurrence of the Pohang earthquake (5 in Table 1.1). The aim of the chapter 5 is to image near-surface fault structure and it is related to 6 in Table 1.1.

Table 1.1: Nine groups of topics in seismology (modified from Ben-Menahem, 1995).

1.	Inventing and improving seismometer
2.	Theory of seismic fields in the Earth
3.	Surface waves
4.	Free oscillations of the Earth
5.	Seismic sources (earthquakes)
6.	Earth's internal structure
7.	Anelasticity
8.	Anisotropy
9.	Phenomenology

Chapter 2

Measurement of seismometer orientation using the tangential *P*-wave receiver function based on harmonic decomposition

This chapter is published in

Lim, H., Kim, Y., Song, T. R. A., & Shen, X. (2018). Measurement of seismometer orientation using the tangential P-wave receiver function based on harmonic decomposition. *Geophysical Journal International*, **212**(3), 1747–1765.

Abstract

Accurate determination of the seismometer orientation is a prerequisite for seismic studies including, but not limited to seismic anisotropy. While borehole seismometers on land produce seismic waveform data somewhat free of human-induced noise, they might have a drawback of an uncertain orientation. This study calculates a harmonic decomposition of teleseismic receiver functions from the P and PP phases and determines the orientation of a seismometer by minimizing a constant term in a harmonic expansion of tangential receiver functions in back azimuth near and at 0 s. This method normalizes the effect of seismic sources and determines the orientation of a seismometer without having to assume for an isotropic medium. Compared to the method of minimizing the amplitudes of a mean of the tangential receiver functions near and at 0 s, the method yields more accurate orientations in cases where the back-azimuthal coverage of earthquake sources (even in the case of ocean bottom seismometers) is uneven and incomplete. We apply this method to data from the Korean seismic network (52 broadband velocity seismometers, 30 of which are borehole sensors) to estimate the sensor orientation in the period of 2005–2016. We also track temporal changes in the sensor orientation through the change in the polarity and the amplitude of the tangential receiver function. Six borehole stations are confirmed to experience a significant orientation change (10°–180°) over the period of 10 years. We demonstrate the usefulness of our method by estimating the orientation of ocean bottom sensors (OBSs), which are known to have high noise level during the relatively short deployment period.

2.1 Introduction

Three components of a seismometer are used in most seismic studies for constraining earthquake sources and structural complexities on Earth. The orientation of horizontal components is critical for various seismic methods such as teleseismic receiver functions, studies of anisotropy, body- and surface-wave polarization and surface wave dispersion. Among these methods, the studies of seismic anisotropy in particular require accurate orientation of the horizontal components for meaningful interpretation, not only on the state of deformation in the crust and mantle in various tectonic settings but their deformation history in the past (e.g., Long and Silver, 2009; Long and Becker, 2010).

The orientation of a seismometer can be misaligned during its installation and maintenance. Errors in the orientation of the horizontal components were previously estimated based on the polarization of body wave (Yoshizawa et al., 1999; Schulte-Pelkum et al., 2001) and surface wave (Laske, 1995; Laske and Masters, 1996; Larson, 2000; Larson and Ekström, 2002; Stachnik et al., 2012; Zha et al., 2013). In some cases, the sensor orientation is misaligned by more than 10° even in quality stations in Global Seismographic Network (GSN) (e.g., Larson and Ekström, 2002). However, these methods typically assume that the medium beneath the station is isotropic and that any effect from structure and anisotropy beneath the station on body-wave and surface-wave polarization and arrival angle can be minimized by averaging over a large number of measurements from different back azimuth. Since the back-azimuth path coverage is typically incomplete, the estimated orientation can deviate from the true sensor orientation by over 10° (Schulte-Pelkum et al., 2001; Wang et al., 2016).

In this study, we design a new algorithm to scan and detect the change of sensor orientation by utilizing teleseismic receiver functions, which, by construction, remove the effect of source complexities and source-side structure response and isolate

structure response beneath the receiver (e.g., Vinnik, 1977; Langston, 1979). Radial receiver function (R-RF) and tangential receiver function (T-RF) are calculated by deconvolving the radial and tangential components of teleseismic waves, respectively, from the vertical component. Through harmonic decomposition of stacked R-RF and T-RF in back-azimuth gathers (e.g., Park and Levin, 2016), we determine the sensor orientation angle by minimizing a constant harmonic term of the T-RF at and near 0 s. To demonstrate the utility of our proposed method, we measure the sensor orientation of surface and borehole broadband seismometers installed at 52 sites in South Korea and compare them against previous estimates (Fig. 2.1). We also apply this method to relatively lower signal-to-noise ratio (SNR) data from two ocean bottom seismometers (OBS) in Cascadia Initiative (Toomey et al., 2014) to discuss the usefulness of our method when the azimuthal data gap is relatively large during the temporary seismic deployment.

2.2 Method

2.2.1 Harmonic decomposition of the receiver function

Typically, the amplitude of the R-RFs is back-azimuth independent when the subsurface structure is flat-layered isotropic media. However, azimuthally-varying arrivals are often observed on both R- and T-RFs, indicating a breakdown of P–SV to SH decoupling in the presence of dipping layer and/or anisotropy. The azimuthal (i.e., horizontal symmetry axis) anisotropy leads to a characteristic 180°-periodic back-azimuthal pattern in RFs (Levin and Park, 1998), whereas a dipping interface or dipping symmetry axis introduces a 360°-periodic back-azimuthal pattern (Cassidy, 1992). Previous studies (e.g., Girardin and Farra, 1998; Farra and Vinnik, 2000; Bianchi et al., 2010; Vinnik et al., 2012; Schulte-Pelkum and Mahan, 2014; Audet, 2015; Park and Levin, 2016) applied the harmonic decomposition method to extract

the periodicity of T-RFs in back azimuth and constrained the velocity structure and the presence of anisotropy at depths. In this study, we utilize the harmonic decomposition method to the direct teleseismic P and PP phases in the context of R-RF and T-RF to estimate the orientation of the horizontal components.

2.2.2 Estimation of sensor orientation

Park and Levin (2016) showed theoretically that the R-RF can be decomposed into constant and sinusoidal harmonic terms, and the T-RF only to the sinusoidal harmonic terms when either an anisotropic layer or a dipping isotropic layer is present beneath the receiver. In this study, the unmodelled sensor misorientation is introduced as a constant harmonic term in the T-RFs. Following the approach of Park and Levin (2016) and their equation (44), we theoretically lay out how to determine the sensor orientation in this section.

The R- and T-RFs can be fitted by regression with five harmonic terms:

$$\begin{aligned} RF_R &= H_{R1} + H_{R2}\cos\theta + H_{R3}\sin\theta + H_{R4}\cos 2\theta + H_{R5}\sin 2\theta, \\ RF_T &= H_{T1} + H_{T2}\cos\theta + H_{T3}\sin\theta + H_{T4}\cos 2\theta + H_{T5}\sin 2\theta \end{aligned} \tag{2.1}$$

where the θ is back azimuth. The first terms on the right-hand side of the equations for RF_R and RF_T are called a constant harmonic term and the others are called harmonic sinusoidal terms. Given N data in back azimuth, the regression is applied to solve the following set of two linear equations:

$$\begin{aligned} \mathbf{G}\mathbf{m}_R &= \mathbf{d}_R, \\ \mathbf{G}\mathbf{m}_T &= \mathbf{d}_T \end{aligned} \tag{2.2}$$

where $\mathbf{d}_R$ and $\mathbf{d}_T$ are data matrices, with dimension of $N \times M$. Here, M indicates the data length of the RFs. The $\mathbf{G}$ is a matrix with the size of N-by-5 and the kth row of $\mathbf{G}$ is [1 cosθ_k sinθ_k cos2θ_k sin2θ_k], where θ_k is the back azimuth corresponding to the kth row of $\mathbf{d}_R$ and $\mathbf{d}_T$. In our analysis, N is no more than 72 because both R- and T-RFs are stacked over a 5° interval in back azimuth to improve the SNR. The harmonic terms of the R- and T-RFs are

$$\begin{aligned} \mathbf{m}_R^T &= \begin{bmatrix} H_{R1} & H_{R2} & H_{R3} & H_{R4} & H_{R5} \end{bmatrix}, \\ \mathbf{m}_T^T &= \begin{bmatrix} H_{T1} & H_{T2} & H_{T3} & H_{T4} & H_{T5} \end{bmatrix} \end{aligned} \tag{2.3}$$

where the superscript T denotes a transpose operation. The harmonic terms of the equation (3) can be solved by the standard least squares:

$$\begin{aligned} \mathbf{m}_R &= \left(\mathbf{G}^T\mathbf{G}\right)^{-1}\mathbf{G}^T\mathbf{d}_R, \\ \mathbf{m}_T &= \left(\mathbf{G}^T\mathbf{G}\right)^{-1}\mathbf{G}^T\mathbf{d}_T \end{aligned} \tag{2.4}$$

By introducing an arbitrary angle φ in clockwise direction from the north, we can now represent $\mathbf{d}_R^{'}$ and $\mathbf{d}_T^{'}$ as the data matrix of the misoriented sensor using the rotation matrix,

$$\begin{bmatrix} \mathbf{d}_R^{'} \\ \mathbf{d}_T^{'} \end{bmatrix} = \begin{bmatrix} \cos\varphi\mathbf{I}_N & \sin\varphi\mathbf{I}_N \\ -\sin\varphi\mathbf{I}_N & \cos\varphi\mathbf{I}_N \end{bmatrix} \begin{bmatrix} \mathbf{d}_R \\ \mathbf{d}_T \end{bmatrix} \tag{2.5}$$

where $\mathbf{0}$ and $\mathbf{I}$ are zero and identity matrices, respectively, and their subscripts indicate the dimension. Then, the resultant harmonic terms due to the misalignment, $\mathbf{m}_R^{'}$ and $\mathbf{m}_T^{'}$, can be expressed as

$$\begin{bmatrix} \mathbf{m}_R^{'} \\ \mathbf{m}_T^{'} \end{bmatrix} = \begin{bmatrix} \left(\mathbf{G}^T\mathbf{G}\right)^{-1}\mathbf{G}^T & \mathbf{0}_{5\times N} \\ \mathbf{0}_{5\times N} & \left(\mathbf{G}^T\mathbf{G}\right)^{-1}\mathbf{G}^T \end{bmatrix} \begin{bmatrix} \mathbf{d}_R^{'} \\ \mathbf{d}_T^{'} \end{bmatrix} \tag{2.6}$$

Combining the equations (2.5) and (2.6), we have

$$\begin{bmatrix} \mathbf{m}_R^{'} \\ \mathbf{m}_T^{'} \end{bmatrix} = \begin{bmatrix} \left(\mathbf{G}^T\mathbf{G}\right)^{-1}\mathbf{G}^T & \mathbf{0}_{5\times N} \\ \mathbf{0}_{5\times N} & \left(\mathbf{G}^T\mathbf{G}\right)^{-1}\mathbf{G}^T \end{bmatrix} \begin{bmatrix} \cos\varphi\mathbf{I}_N & \sin\varphi\mathbf{I}_N \\ -\sin\varphi\mathbf{I}_N & \cos\varphi\mathbf{I}_N \end{bmatrix} \begin{bmatrix} \mathbf{d}_R \\ \mathbf{d}_T \end{bmatrix} \tag{2.7}$$

By placing the rotation matrix in front, we can further decrease the dimension from $2N$-by-$2N$ to 10-by-10, and equation (2.7) can be written as

$$\begin{bmatrix} \mathbf{m}_R^{'} \\ \mathbf{m}_T^{'} \end{bmatrix} = \begin{bmatrix} \cos\varphi\mathbf{I}_5 & \sin\varphi\mathbf{I}_5 \\ -\sin\varphi\mathbf{I}_5 & \cos\varphi\mathbf{I}_5 \end{bmatrix} \begin{bmatrix} \left(\mathbf{G}^T\mathbf{G}\right)^{-1}\mathbf{G}^T & \mathbf{0}_{5\times N} \\ \mathbf{0}_{5\times N} & \left(\mathbf{G}^T\mathbf{G}\right)^{-1}\mathbf{G}^T \end{bmatrix} \begin{bmatrix} \mathbf{d}_R \\ \mathbf{d}_T \end{bmatrix}. \text{ That is,} \tag{2.8}$$

$$\begin{bmatrix} \mathbf{m}_R^{'} \\ \mathbf{m}_T^{'} \end{bmatrix} = \begin{bmatrix} \cos\varphi\mathbf{I}_5 & \sin\varphi\mathbf{I}_5 \\ -\sin\varphi\mathbf{I}_5 & \cos\varphi\mathbf{I}_5 \end{bmatrix} \begin{bmatrix} \mathbf{m}_R \\ \mathbf{m}_T \end{bmatrix} \tag{2.9}$$

where $\mathbf{m}_R$ and $\mathbf{m}_T$ are the harmonic terms of RFs from the misoriented sensor, and $\mathbf{m}_R^{'}$ and $\mathbf{m}_T^{'}$ are the terms from the orientation correction. The equations (2.5) and (2.6) mean that the regression and rotation are commutative. We note that solving equation (2.6) is computationally more cost-effective than solving equation (2.5). Using equation (2.3), equation (2.6) can be written as

$$\begin{aligned} H_{Ri}^{'} &= \mathbf{m}_R^{'}(i,:) = \cos\varphi\mathbf{m}_R(i,:) + \sin\varphi\mathbf{m}_T(i,:) = \cos\varphi\mathbf{m}_R H_{Ri} + \sin\varphi\mathbf{m}_T H_{Ti}, \\ H_{Ti}^{'} &= \mathbf{m}_R^{'}(i,:) = -\sin\varphi\mathbf{m}_R(i,:) + \cos\varphi\mathbf{m}_T(i,:) = -\sin\varphi\mathbf{m}_R H_{Ri} + \cos\varphi\mathbf{m}_T H_{Ti} \end{aligned} \tag{2.10}$$

where the integer i is from 1 to 5. We then define a misfit function $f\ (\varphi)$, which is based on the root-mean-square in a window bounded by integers M_1 and M_2 ($1 \leq M_1 < M_2 \leq M$), as

$$\begin{aligned} f(\varphi) &= \sqrt{\frac{1}{M_2 - M_1} \sum_{j=M_1}^{M_2} \left[H'_{Ti=1}(j)\right]^2} \\ &= \sqrt{\frac{1}{M_2 - M_1} \sum_{j=M_1}^{M_2} \left[-\sin\varphi \mathbf{m}_R(1,j) + \cos\varphi \mathbf{m}_T(1,j)\right]^2} \end{aligned} \tag{2.11}$$

where φ ranges from 0° to 180°. One can determine the orientation φ_{min} by minimizing the $f(\varphi)$ through a grid-search scheme (with an increment of 0.01° in this study). The error of φ_{min} can be estimated by bootstrapping 90 percent random selection from a row of the data matrices $\mathbf{d}_R$ and $\mathbf{d}_T$ in equation (2.2) without repetition. Since we stack the R- and T-RFs over a 5° interval in back azimuth, the size of randomly selected data matrices in bootstrapping is no more than 64-by-M. Ambiguity between the φ_{min} and φ_{min}+180° can be resolved by choosing an orientation that yields a positive polarity of a constant harmonic term in the R-RF.

2.3 Synthetic test

In order to examine the robustness of our proposed method, we first compute synthetic RFs (Levin and Park, 1997; Frederiksen and Bostock, 2000) and show results from a series of synthetic tests based on several velocity models and ranges of back azimuth data coverage. Here we select the data window of −1.0 s and 1.0 s in the T-RFs in the misfit calculation. We compare these results with those from the method of minimizing the amplitudes of a mean of the T-RFs within the data window. Also, we

consider more realistic event distribution (from Korean seismic network and ocean bottom seismic network) to test the effect of slowness variation on the harmonic terms of the RFs. The event distribution from the Korean network ensures nearly complete back-azimuth coverage, whereas that from the ocean bottom seismic network does not. Lastly, we examine how the level of noise and range of back-azimuthal data coverage interplay in the estimation of the orientation angle. In sections 2.3.1, 2.3.2, and 2.3.3, we discuss synthetic tests performed free of noise, whereas section 2.3.4 illustrates synthetic test performed with the addition of noise.

2.3.1 Synthetic test for six representative models with full back-azimuth data coverage

We perform synthetic tests from a few velocity models, which produce some noticeable peaks in the T-RFs near 0 s as a function of back azimuth. In this test, we assume full back-azimuthal coverage of earthquakes and slowness range from 0.04 to 0.08 s/km. Fig. 2.3 shows six representative layered velocity models and corresponding synthetic T-RFs in back azimuth within the data window. Anisotropy strength, its fast axis direction, and a thickness of the anisotropic layer are chosen arbitrarily in this test. We first examine the effect of a different thickness (0.5 km or 3 km) of the topmost anisotropic layer with (1) a horizontal fast axis over an isotropic half space (Figs 2.3a and d) or with (2) a tilted (45°) fast axis over an isotropic half space (Figs 2.3g and j). Fig. 2.3(m) displays a model with two isotropic layers divided by an interface with a 10° dip, whereas Fig. 2.3(p) includes an additional anisotropic dipping layer on top of the isotropic medium. Also, we test the effect of a sensor misorientation of 1° using the six models.

Four-lobed patterns with back azimuth are distinctively shown in Figs 2.3(b) and (e), and two-lobed patterns in Figs 2.3(h), (k), (n) and (q). In particular, the T-RFs from the models with the thin topmost anisotropic layer (Figs 2.3a, d, g and j)

show distinctive polarity reversal in the vicinity of 0 s, caused by both the coupling between the P, SV and SH at the interface between the thin anisotropic and isotropic layers (Levin and Park, 1998). Synthetic T-RFs from the model with an anisotropic topmost layer near 0 s, as expected, display waveform shape similar to the derivative of a Gaussian pulse (Figs 2.3b, e, h and k; Levin and Park, 1998). Even if the sensor is misoriented by only 1°, the mean of the T-RFs from the six models is no longer zero (Figs 2.3c, f, i, l, o and r). Maximum amplitudes of the T-RFs within the data window in Figs 2.3(b), (e), (h), (k), (n) and (q) are 0.4%, 2.9%, 0.6%, 5.9%, 3.1% and 3.1% (with respect to vertical P), respectively. If the sensor is misoriented by 1°, maximum amplitudes of the T-RFs in Figs 2.3(c), (f), (i), (l), (o) and (r) become 1.7%, 3.6%, 2.0%, 6.3%, 4.3% and 4.3% (with respect to vertical P), respectively. For comparison, robust signals from the transition zone seismic discontinuities are typically observed at 2–5% with respect to vertical P. This indicates that the sensitivity of T-RFs to the sensor orientation is probably on the order of 1° in this instance.

2.3.2 Synthetic test with non-uniform back-azimuth data coverage

We next test a case where the back-azimuthal distribution of earthquakes is not uniform and incomplete. In this case, we set up a model with a 3 km-thick topmost anisotropic layer (Fig. 2.3j), which produces the two-lobed pattern of T-RFs against back azimuth (Fig. 2.3k). Fig. 2.4 shows R- and T-RFs, their means, and their five harmonic terms in the case of complete and poor back-azimuthal coverage. In the case of complete back-azimuthal data coverage, we observe that the constant harmonic term in the T-RFs (H_{T1}) is identical to a mean value of the T-RFs and they are both zero (Fig. 2.4a). In the case of incomplete back-azimuthal distribution, the mean of the T-RFs is no longer zero near 0 s within the data window and can be biased in the direction where earthquakes are concentrated (Fig. 2.4b). We note that T-RFs with a single large data gap in back azimuth yields the largest peak in the mean of T-RFs

than those with several small data gaps (e.g., Fig. 2.4b). However, H_{T1} remains zero regardless of incomplete back-azimuthal distribution. See Fig. 2.A.1 for the case from the model (Fig. 2.3d), which shows the four-lobed pattern of T-RFs in back azimuth.

2.3.3 Synthetic test with the back-azimuth coverage based on real earthquake distribution

Using more realistic distribution of the earthquakes, we examine the effect of the variation in the slowness on the harmonic terms of the R- and T-RFs under the noise-free condition (Fig. 2.5). First, we consider the event distribution from the Korean seismic network, which well exceeds 90% coverage of back azimuth during the period of ∼10 years (Fig. 2.2). We compute synthetic R- and T-RFs, which are based on the back azimuth and slowness of the available 2,430 earthquakes recorded from the station JJB (with the longest operation period) in South Korea from both P and PP waves. Then, these RFs are stacked with a bin of 5° in back azimuth. Fig. 2.5(a) shows that the amplitudes of the H_{T1} are nearly zero. Alternatively, we consider the earthquake distribution for both P and PP arrivals from the OBS J61C from the Cascadia Initiative (Toomey et al., 2014), and calculate the harmonics of the RFs. We note that the back-azimuth coverage for the OBS during 9 months is far less complete than that for Korean seismic network (Fig. 2.A.2). We still observe that the amplitudes of the H_{T1} are nearly zero from the OBS data (Fig. 2.5b). Fig. 2.6 shows the misfit functions $f(\varphi)$ of the synthetic RFs using the model (Fig. 2.3j) and the earthquake distributions (e.g., Fig. 2.2 for the station JJB and Fig. 2.A.2 for the OBS J61C). Two minima of the $f(\varphi)$ based on the synthetics occur at 0° even with the realistic variations in both back azimuth and slowness (Fig. 2.6). The ambiguity between the minima can be resolved by selecting the φ that makes the H_{R1} positive.

2.3.4 Case for various noise levels on synthetic data

In this section, we further explore how various levels of noise and back-azimuthal data coverage affect the orientation estimates. We generate synthetic seismograms using the model shown in Fig. 2.3(j) (Fig. 2.7a), considering various levels of random noise (0–200%) and data gap in back azimuth (0°–300°). The 50% level of noise means that the root-mean-square of the noise is close to a half of the amplitude of the vertical component. The same level of uncorrelated noise is added to all three components. A line in Fig. 2.7(b) roughly indicates the angle estimate deviated from the true orientation as the noise level and back azimuth coverage range vary. Two green boxes in Fig. 2.7(b) roughly indicate the ranges of both noise level and back azimuth of earthquakes from the Korean seismic network and the Cascadia Initiative. The upper limit of the noise level is a reciprocal of an average of the SNR in the vertical component.

This synthetic test for the orientation estimate as a function of the noise level and the back-azimuthal coverage provides useful information on determining a sensor operational period (Fig. 2.7b). As the operational period extends, the back azimuth data gap (horizontal axis of the plot) decreases and so is the uncertainty of the estimate, and vice versa (Fig. 2.7b). While the noise level is site-specific and can be decreased with filtering and applying SNR criterion, a high SNR condition can cause the poor back-azimuthal coverage.

2.3.5 Correlation between radial and tangential harmonic terms

Park and Levin (2016) analytically showed that H_{R2} and H_{R4} correlate negatively with H_{T3} and H_{T5}, respectively, and H_{R3} and H_{T5} correlate positively with H_{T2} and H_{R4}, respectively. The polarities of the correlations from our data are opposite to what Park and Levin (2016) presented because we define our tangential component

opposite to what they used in the left-handed coordinate system in defining radial, tangential, and vertical direction. The correlations between the radial and tangential harmonic terms are observed except for the H_{R3}, H_{T2}, H_{R5} and H_{T4}, which have nearly zero amplitudes (Fig. 2.4). The correlation between H_{R2} and H_{T3} is observed even in the case with the variations in slowness and back azimuth (Fig. 2.5). To quantify a degree of the observed correlation, we estimate a confidence range for non-randomness in the correlation between the harmonics in a time window of −2.0–2.0 s (Bendat, 2010). A degree of freedom is set as the length of the time window (4.0 s) times a corner frequency (2.5 Hz and 1.5 Hz for South Korea and the Cascadia Initiative, respectively).

2.4 Data analysis

2.4.1 Data acquisition and processing of Korean network data

For the RF calculation, we collect teleseismic earthquakes of a magnitude greater than 5.5 recorded at 52 stations (which includes 30 borehole sensors) in South Korea (Fig. 2.1) from 2005 to 2016 (Fig. 2.2a). We analyze teleseismic P and PP arrivals to help mitigate uneven distribution of earthquake sources and provide a more filled back-azimuthal coverage (Fig. 2.2a). For the P-wave RFs, the epicentral distance range of 30°–100° is chosen to avoid complex triplicated mantle P waves (less than 30°) and complication from the core-mantle boundary (distances greater than 100°).

Similarly, for the PP-wave RFs, the epicentral distance range is chosen at 100°–180°. By including the PP-wave RFs, the back-azimuthal gaps of P-RFs in the East Pacific Rise and the Mexico-Peru-Chile subduction zone (Fig. 2.2a) can be filled. The total number of earthquakes for P and PP phases is 3,051 and 1,651, respectively. All waveforms (neglecting the SNR) are cut to 30 s before and 180 s after P and PP arrival times before the RF calculation. The R- and T-RFs are calculated in the frequency

domain with the water level of 10^{-2} (Langston, 1979). In order to remove the high frequency noise, a Gaussian pulse with a half-width (1σ) of 2.5 Hz is convoluted with the RFs. We observe that the half-width from 1.0 to 4.0 Hz yields stable orientation estimates (Fig. 2.A.3). After the RF calculation, we stack both R- and T-RFs over a 5° interval in back azimuth.

2.4.2 Data acquisition and processing of OBS data

We select earthquakes recorded from two broadband OBSs (J61C and J39C) in the Cascadia Initiative. The OBSs J61C and J39C are deployed in deep water at 2673 m and 2656 m water depth and involve relatively lower noise level compared to those in shallow water (Lodewyk and Sumy, 2014). From these two OBSs, the earthquakes with the magnitude greater than 5.5 are collected from September 2013 to June 2014. The ranges of the epicentral distance for the P and PP phases for the RF calculation are the same as those for the Korean seismic network. The numbers of earthquakes for the P and PP phases are 276 and 95, respectively (Fig. 2.A.2). All waveforms are cut to 50 s before and 250 s after P and PP arrival times before deconvolution.

Prior to the deconvolution procedure, we apply a bandpass filter between 0.1 and 1.5 Hz, the same frequency band used by Audet (2016) for the Cascadia Initiative data and Akuhara and Mochizuki (2015) for OBSs offshore Japan. The lower cutoff frequency of 0.1 Hz is effective to remove an influence of infragravity wave. The water level in the deconvolution is set at 10^{-2}. We stack both R- and T-RFs over a 5° interval in back azimuth.

2.5 Results

2.5.1 Orientation estimates for Korean seismic network

The orientations of all 52 stations in South Korea are presented in Table 2.1. The orientation for each station is estimated for a specific period (denoted as validation period), which is defined by a start and an end of the period when the polarity and/or the amplitude of the T-RFs in the data window shifts significantly. Alternatively, the validation period is manually set when the sensor replacement/maintenance record is available (Table 2.B.1). Table 2.1 includes a total of 65 measurements of orientation for different validation periods from two methods, which are (1) the minimization of H_{T1} in the data window and (2) the minimization of the amplitudes of a mean of the T-RFs. In Table 2.1 and Table 2.B.2, we include results from the method (2) for comparison. In addition, Table 2.B.2 shows orientation estimates based on non-stacking approach. The difference between the orientation estimates from the two methods is illustrated in Fig. 2.A.4, and it increases as the back-azimuthal coverage decreases. However, all values are confined within and less than 1°, except for three stations that show large differences (2.3° of SEHB, 7.6° of INCN^{00} and 4.6° of KOHB; not shown in Fig. 2.A.4). We note that differences in orientations between two cases (with and without stacking) are overall small for Korean network data except for the stations INCN^{00}, KOHB and NPR (Table 2.B.2).

Uncertainty estimates (1σ) of the orientation from the method (1) are shown in Table 2.1. The 57 out of 65 measurements have an uncertainty of less than 1° (Table 2.1). Table 2.1 also includes previous estimates for some stations (Ekström and Busby, 2008; Shin et al., 2009; Lee and Rhie, 2015; Lee and Sheen, 2015) for comparisons. We note that estimates from station SMKB (for a validation period of 2014/04–2014/06) involve relatively large uncertainty value (Table 2.1) due to poor back-azimuthal coverage (44%). Lee and Sheen, 2015 previously reported changes in

the orientation for that station, which have not been reported by the seismic network operator.

We confirm that significant temporal variations of the polarity and amplitude of the T-RFs likely had stemmed during sensor replacement/maintenance (e.g., Table 2.B.1). Of the 52 stations examined, we present results from three stations (HSB, MGB, and SEHB) that show substantial changes in both polarity and amplitude of the T-RFs. First, we illustrate such changes by showing T-RFs stacked over an interval of two months without overlap (Figs 2.A.5a, c and e for stations HSB, MGB and SEHB, respectively). Second, we show the maximum and minimum amplitudes of the stacked T-RFs in the data window (Figs 2.A.5b, d and f for stations HSB, MGB, and SEHB, respectively; Fig. 2.A.6 for the other stations). Our results show that six borehole stations experience sudden orientation change ranging from 12° (at station MGB) to 178° (at station SMKB) over the period of 10 years (Table 2.1).

Fig. 2.8 shows the misfit function $f(\varphi)$ of stations HSB, MGB and SEHB at different periods. The data from station HSB shows that $f(\varphi)$ for the period of 2005/01–2007/01 is minimized at 144.7° with a plus sign for the mean of H_{R1} (Fig. 2.8a). The orientation for the period of 2008/01–2015/01 is estimated as 228.5° (48.5°+180°) because $f(\varphi)$ is minimized at 48.5° with a minus sign for the mean of H_{R1} (Fig. 2.8b). The orientation estimates for station MGB are 134.7°, 10.8° and 359.2° (179.2°+180°) for three different periods (Figs 2.8c, d, and e). The estimates for station SEHB are 264.5° (84.5°+180°) and 77.2° in two different periods (Figs 2.8f and g).

We show temporal changes of $f(\varphi)$ and φ_{min} for stations HSB, MGB and SEHB with a moving window of one year (Fig. 2.9, background color and solid black lines, respectively). The orientation angles for the stations and their validation periods (Table 2.1) are also marked as references (Fig. 2.9; white ticked lines). We find periods that involve a sudden change in φ_{min}, which are 2007–2008 for HSB (Fig. 2.9a) and 2009/10–2010/4, 2010/6–2010/12 and 2012/10–2013/2 for MGB (Fig. 2.9b). These

correspond to the time when the orientation had changed, which is consistent with a record of the sensor replacement/maintenance (Table 2.B.1). Besides the record, we also identify other periods when either maximum or minimum amplitude of the T-RFs is statically changed (Figs 2.A.5b, d and f for stations HSB, MGB, and SEHB, respectively). We report that the period of 2011–2012 for station SEHB involves a significant change in φ_{min} (Fig. 2.9c), which is considered to be the orientation change but not noted by the seismic network operator. In addition, we observe that both $f(\varphi)$ and φ_{min} slightly deviate from the reference during the periods of 2005/08–2006/12, 2008/10–2009/08 and 2013/06–2014/10 for HSB (Fig. 2.9a) and during the periods of 2007/02–2007/06 and 2011/10–2012/10 for MGB (Fig. 2.9b). Such periods moderately coincide with the temporal fluctuation of back-azimuthal coverage of earthquakes (Figs 2.A.5a and b).

We next show how the harmonic terms of R- and T-RFs, and also means both R- and T-RFs, for the three stations change with the orientation correction based on the method (1) (Fig. 2.10). The amplitudes of H_{T1} for the different periods are minimized and essentially nearly zero after the orientation correction (Fig. 2.10). We now observe strong coherence in waveform between the harmonic terms for different validation periods, and between the means after the correction. This correlation is expected unless there is any temporal change in structure and significant change in the distribution of the earthquakes. We observe that H_{R2} and H_{R4} correlate negatively with H_{T3} and H_{T5}, respectively, and H_{R3} and H_{T5} correlate positively with H_{T2} and H_{R4}, respectively (Figs 2.10, 2.A.7, 2.A.8, and 2.A.9). We note that the amplitudes of H_{R4}, H_{R5}, H_{T4}, and H_{T5} are small. Thus, we do not see a clear correlation in waveform between the different harmonics (see Figs 2.A.7, 2.A.8, and 2.A.9).

Lastly, we show T-RFs and H_{T1} for the selected station HSB with and without the orientation correction (Fig. 2.11). The similar two-lobed patterns of the T-RFs with back azimuth are revealed by the correction (Figs 2.11c and d). See Figs 2.A.10

for the stations MGB and SEHB, respectively.

2.5.2 Orientation estimates for OBS network

Our estimates based on the harmonic decomposition are compared against previous estimates based on the minimization of stacked T-RFs at 0.0–5.0 s (Janiszewski and Abers, 2015) and surface wave arrival angles (Lodewyk and Sumy, 2014) (Table 2.2). Our estimates are similar to the estimates by Lodewyk and Sumy, 2014 and the estimates by Janiszewski and Abers, 2015. We note that slight deviation between the estimates might stem from the different data selection criteria and processing.

We observe very small positive amplitudes of H_{R1} near 0 s even after the orientation corrections (Fig. 2.12). Such small amplitude of H_{R1} makes the range of $f(\varphi)$ very narrow (Fig. 2.A.11). From the data from J61C, the orientation is estimated as 190.2° (10.2°+180°) (Fig. 2.A.11a). The orientation estimate for J39C is 89.0° (Fig. 2.A.11b).

The correlations between H_{R2} and H_{T3} and between H_{R3} and H_{T2} of the J61C are observed strong, whereas those between H_{R4} and H_{T5} and between H_{R5} and H_{T4} are weak (Fig. 2.12a). The correlations between the harmonic terms for J39C are not all visibly clear because of small amplitudes at and near 0 s (Fig. 2.12b). Fig. 2.13 shows the T-RFs before and after the orientation correction for the two OBSs.

2.6 Discussion

Most indirect seismic methods in determining the orientation inevitably involve inaccuracy due to uncertain medium seismic properties beneath the receiver. The medium is assumed to be isotropic and homogeneous in the horizontal direction (e.g., Ekström and Busby, 2008; Shin et al., 2009; Zha et al., 2013; Lee and Sheen, 2015; Lee and Rhie, 2015; Wang et al., 2016). If the anisotropy of the medium were strong, the

particle motion of the P wave is no longer parallel to its propagation direction. The same applies to the Rayleigh wave. Furthermore, the minimum-time path between the source and receiver might not coincide with the shortest-distance path if the medium is laterally heterogeneous. Although our estimates based on the teleseismic RFs can also be influenced by the uncertainty in the nature of the medium, the degree of its dependency can be much less than that of the studies based on the particle motions. Our method works well in the presence of anisotropy and/or dipping structures beneath the receiver (e.g., Fig. 2.3). Nevertheless, to make a single measurement of orientation with an uncertainty less than 1°, we require a relatively large dataset with nearly full back-azimuthal coverage of teleseismic earthquakes (e.g., Fig. 2.2).

2.6.1 Orientation estimates of the Korean seismic network

Most of the orientations for stations in South Korea are measured with over 85 percent of back-azimuthal coverage (Table 2.1). Using both P and PP phases, the 70, 80, and 90% of the back-azimuthal coverage are guaranteed by over 8, 10 and 21 months of station operational periods (Figs 2.2b and 2.14) or 250, 350, and 750 earthquakes, respectively (Fig. 2.A.12a). Even in the case of relatively poor back-azimuthal coverage at station MGB (73%), our value (359.2°±0.7°; Table 2.1) still agrees reasonably well with the previous estimate (Lee and Sheen, 2015; a difference of 3.2°). It is difficult to statistically compare our estimate with the previous estimate because different types of data (e.g., teleseismic body-wave phase versus regional body-wave phase versus) and different data processing (e.g., passband) are involved in determining the orientation. The measurement for station SEHB includes the smallest back-azimuthal coverage (59%), and our estimate for this station is 3.5°±1.7°.

For Korean network data (the case with the nearly full back-azimuthal coverage), the back-azimuthal coverage at 20 months reaches to about 90% (Fig. 2.15a; 750 earthquakes, Fig. 2.A.12a), and the orientation (φ_{min}) converges to a steady value

after 20 months (Fig. 2.15c). The orientation angle at 20 months slightly deviates from the best estimate by 0.3°, which is smaller than the uncertainty. We note that just over three months the measured orientation deviates from the best angle only by 6° with about 60% back-azimuthal coverage.

The harmonics H_{R2} and H_{T3} and the H_{R3} and H_{T2} correlate negatively and positively, respectively (Fig. 2.15b). The observed correlation between the harmonic terms are quantified in terms of a confidence range for randomness in the correlation (Bendat, 2010) (Fig. 2.15b, pink color). While the correlation value between the H_{R2} and H_{T3} reaches to -1 just after one month, the correlation between the H_{R3} and H_{T2} slowly converges to 0.6 (Fig. 2.15b). The observed slow convergence and relatively low correlation (still within the confidence range of 95%) for the H_{R3} and H_{T2} are primarily due to small amplitudes of the H_{R3} and H_{T2}. Similarly, the correlation between the H_{R4} and H_{T5} and H_{R5} and H_{T4} are scattered within the confidence range during the whole period of ten years. Assuming back-azimuthal coverage of earthquakes is good, strong correlation (beyond the confidence range of 95%) between the orthogonal harmonic terms may further supports the reliability of our orientation estimates (Figs 2.10 and 2.15). The orientation angle is deviated by about 5° from the final estimate during the period of 2005–mid-2006, although a degree of correlations between H_{R3} and H_{T2} and between H_{R5} and H_{T4} in 2005–mid-2006 is observed high (Fig. 2.15b).

We observe that the harmonic terms from most stations (except for the stations in oceanic islands) in South Korea share similar patterns in waveforms within the data window near 0 s (Fig. 2.10), and we suspect that this is in part due to the structure. For instance, a negative pulse just before 0 s and a positive pulse just after 0 s are shown in the H_{R2} (conversely in the H_{T3}) of the stations (Fig. 2.10). The common features of the harmonic terms might indicate an approximately southward dipping of the fast axis in the anisotropic top layer beneath South Korea, as illustrated in

Figs 2.3(g) and (j). A separate analysis of P coda phases is required for a precise investigation on the crustal seismic structure of Korea.

2.6.2 Applicability of the method on OBS data

One clear difference in the harmonic terms of the RFs between the land-based stations and OBSs is the amplitude of the H_{R1} within the data window near and at 0 s. Observed small amplitudes of the H_{R1} ($\sim$0.1%) in the OBS data can be a source of a problem in the orientation correction for the OBS (Fig. 2.12). Small amplitudes of the R-RFs typically arise from a nearly vertical incidence of the teleseismic P phase due to the presence of the sedimentary layer with low P-wave velocity (Kawakatsu and Abe, 2016). The pseudo vertical incidence of P can yield a very shallow range of the $f(\varphi)$, which makes it difficult to determine φ_{min} in the presence of noise since the orientation estimate depends on the amplitude of the H_{R1} near 0 s.

Despite the high background noise embedded in the OBS data (Webb, 1998; Lin et al., 2010), the RFs at OBS station J61C show clear correlation between H_{R2} and H_{T3} and between H_{R3} and H_{T2} (Fig. 2.12a), as expected in an anisotropic or dipping media (Park and Levin, 2016). Our estimates generally agree with previous estimates based on slightly different data processing scheme (Janiszewski and Abers, 2015) and different seismic phase (Lodewyk and Sumy, 2014). Because of shorter operation period for the OBSs ($\sim$9 months), the back-azimuthal coverage reaches to about 80% in 9 months (Fig. 2.15d; 380 earthquakes in Fig. 2.A.12b) and the orientation estimate (φ_{min}) just begins to converge (Fig. 2.15f).

If the noise level is assumed at 80% in the OBS data, about 70% of back-azimuthal coverage is required to obtain the orientation estimate with 5° uncertainty (Fig. 2.7b). For example, this can be achieved approximately within 4–7 months of the deployment in Pacific, Atlantic, Indian Oceans, and North America and 9–14 months in southeastern Asia, South America and Africa (Fig. 2.14).

2.7 Conclusions

We calculate teleseismic receiver functions from the P and PP phases using the harmonic decomposition method and determine the orientation of a seismometer by minimizing a constant term in a harmonic expansion of T-RFs in back azimuth near and at 0 s. This approach is applied to data from 52 stations in South Korea and two OBSs from the Cascadia Initiative project. Our method works well in the presence of anisotropy and/or dipping structures beneath the receiver. Also, the method yields a much more robust estimate than those obtained by minimizing the average amplitude of the T-RFs near 0 s. In particular, the method effectively determines the orientation in the case of deficient back-azimuthal coverage of earthquakes (i.e., from the OBSs). The station operational period of about one year guarantees ∼80 percent of the back-azimuthal coverage with the usage of both P and PP phases from earthquakes with a magnitude over 5.5 recorded in the seismic network in South Korea. Our analysis shows that the operational period of the station of 20 months (recording about 750 earthquakes) is required for a single measurement of orientation with an uncertainty less than 1°. We keep track of the history of the orientation of a total 52 broadband velocity seismometers for the period of 2005–2016 by detecting its period when the polarity and the amplitude of the T-RFs are largely changed. Of the 30 borehole stations in South Korea, six stations are confirmed to experience a significant orientation change (12° to ∼178°) during the 10-year period. Our method can be applied to any broadband data, regardless of sensor types and orientation, for seismic studies (i.e., receiver functions).

Table 2.1: Orientation correction estimates for the stations in South Korea.

STA	Orientation (°; from harmonic decomposition)	Error (°; 1σ)	%Back azimuth coverage	Orientation (°; from mean of T-RF)	Validation period From	Validation period To	Previously reported data (°)		
BAR	5.5	0.4	94	5.5	2007-12	2015-01			
BGD	359.5	0.6	100	359.6	2005-01	2015-01	359.8[a]	357.2[c]	
BOSB	31.5	0.6	87	31.3	2012-08	2015-01	33.6[b]		
BUS2	9.3	0.3	99	9.4	2005-01	2015-01			
CHC2	3.8	0.6	90	3.9	2012-08	2015-01			
CHJ2	10.5	0.4	99	10.6	2005-01	2015-01			
CHNB	19.4	0.6	100	19.3	2005-01	2015-01	13.5a	15.3[c]	
DACB	268.4	0.3	94	268.5	2010-08	2015-01	267.6[b]		
DAG2	3.5	0.3	93	3.5	2010-08	2015-01			
DGY2	9.6	0.4	94	9.5	2010-08	2015-01			
EMSB	338.2	0.6	93	338.2	2012-12	2015-01	337.0[b]		
EURB	104.4	0.9	86	105.1	2012-06	2014-08	106.0[b]		
GAHB	128.5	0.3	94	128.6	2008-10	2015-01	130.7[b]		
GKP1	5.4	0.5	97	5.4	2005-01	2015-01	4.2[a]	3.4[c]	
GOCB	234.5	0.5	89	234.3	2012-08	2015-01	235.0[b]		
GSU	146.2	0.6	99	146.5	2005-01	2015-01	142.6[a]	147.7[b]	140.8[c]
GWYB	120.5	0.7	90	120.0	2012-08	2015-01	123.3[b]		
HALB	355.4	1.1	92	355.1	2012-08	2015-01	221.3[b]		
HAMB	121.0	0.5	90	120.8	2012-08	2015-01	125.0[b]		
HAWB	246.7	0.6	89	247.1	2012-08	2015-01	246.2[b]		
HKU	8.2	0.5	96	8.3	2005-01	2015-01	9.1[a]	5.6[c]	
HSB	144.7	0.8	83	144.5	2005-01	2007-01			
HSB	228.5	0.4	96	228.6	2008-01	2015-01	224.3[a]	226.2[b]	221.6[c]
HWCB	3.3	0.3	93	3.4	2010-08	2015-01	2.4[b]		
HWSB	60.9	0.9	96	60.7	2008-01	2012-10	59.0[a]	66.9[b]	59.0[c]
HWSB	–	–	–	–	2014-01	2014-06[b]	155.6[b]		
IMWB	196.7	0.4	92	197.1	2012-08	2015-01	196.1[b]		
INCN^{00}	335.3	5.0	92	327.7	2009-10	2012-10	356[d]	359[d]	
INCN^{00}	4.6	1.1	90	4.0	2013-10	2016-01	358[d]		
INCN^{10}	359.2	0.6	94	359.2	2009-10	2012-10	355[d]	357[d]	359[d]
INCN^{10}	0.1	0.4	90	359.7	2013-10	2016-01	0[d]		
JEO2	2.7	0.4	89	3.0	2012-08	2015-01			
JJB	237.1	0.7	94	236.5	2007-10	2012-10	235.8[a]	237.6[c]	
JJB	233.8	1.2	82	233.3	2014-01	2016-01			
JJU	1.9	0.6	100	1.8	2005-01	2015-01			
JRB	194.7	0.3	99	194.7	2006-10	2015-01	193.7[a]	191.6[b]	192.5[c]
JSB	245.0	0.3	99	245.2	2006-10	2015-01	245.5[a]	245.3[b]	243.0[c]
KOHB	256.3	4.7	93	251.7	2009-08	2013-12	190.4[b]		
KOHB	–	–	–	–	2014-04	2014-06[b]	3.5[b]		
KSA	4.4	0.3	99	4.2	2005-01	2015-01	0.7[a]	1.2[c]	
MGB	134.7	0.5	96	134.8	2005-03	2009-08	134.2[a]	133.2[c]	
MGB	10.8	0.9	87	10.8	2010-11	2012-12			
MGB	359.2	0.7	73	359.2	2013-06[b]	2014-06[b]	356.0[b]		
NAWB	148.6	0.7	90	148.8	2012-08	2015-01	151.2[b]		
NPR	2.9	1.0	100	3.2	2005-01	2015-01	4.3[a]	4.2[c]	
OKCB	251.1	0.5	92	250.9	2012-08	2015-01	253.5[b]		
OKEB	35.2	1.1	96	34.8	2011-10	2015-01	18.2[b]		
SEHB	264.5	0.5	92	264.2	2008-11	2011-01			
SEHB	3.5	1.7	59	1.2	2011-02	2012-07			
SEHB	77.2	0.4	93	77.2	2012-08	2015-01	74.9[b]		
SEO	358.1	0.3	100	358.1	2005-01	2015-01			
SEO2	0.9	0.4	93	1.2	2010-08	2015-01			
SES2	7.3	0.6	89	7.2	2012-08	2015-01			
SHHB	326.3	0.4	92	326.2	2011-10	2015-01	325.6[b]		
SMKB	355.0	3.8	63	355.9	2013-09[b]	2014-03[b]	2.4[b]		
SMKB	172.6	0.9	44	172.3	2014-04[b]	2014-06[b]	165.4[b]		
SND	0.9	0.2	99	0.9	2005-01	2015-01	359.0[a]	358.4[c]	

(continued)

Table 2.1: (continued)

STA	Orientation (°; from harmonic decomposition)	Error (°; 1σ)	%Back azimuth coverage	Orientation (°; from mean of T-RF)	Validation period From	Validation period To	Previously reported data (°)		
SNU	3.8	0.6	92	3.8	2005-01	2007-09	5.5[a†]	5.2[c†]	
SNU	–	–	–	–	2007-11	2008-01			
SNU	3.5	0.3	96	3.9	2008-03	2015-01			
TJN	1.6	0.4	99	1.5	2005-01	2015-01	0.1[a]	355.0[c]	
ULJ2	358.0	0.3	94	358.1	2010-08	2015-01			
ULL	9.7	0.9	96	9.4	2005-01	2009-12			
ULLB	10.4	0.5	99	10.2	2006-10	2015-01	9.4[a]	20.0[b]	2.5[c]
YKB	194.9	0.3	97	194.9	2006-10	2015-01	191.0[a]	187.0[b]	195.7[c]
YNCB	309.0	0.7	90	309.1	2008-10	2010-08			
YNCB	21.0	0.5	94	20.8	2011-01	2015-01	28.4[b]		
YSB	13.6	0.4	94	13.8	2009-02	2015-01	13.8[b]		

The orientation angle ranges from 0° to 360° with clockwise direction, and our values indicate the angles that we need to correct from the misaligned north. We note that we apply this correction scheme to previous estimates (Ekström and Busby, 2008; Shin et al., 2009; Lee and Sheen, 2015; Lee and Rhie, 2015).

'00' and '10': location code given for the station INCN (`http://ds.iris.edu/mda/IU/INCN`) by the Data Management Center (DMC) of the Incorporated Research Institutions for Seismology (IRIS)

[a]Shin et al. (2009)

[b]Lee and Sheen (2015)

[c]Lee and Rhie (2015)

[d]Ekström and Busby (2008);
`http://www.ldeo.columbia.edu/~ekstrom/Projects/WQC/COMB_QC/POL_IU_S_ALL_EPO.html`

†Their periods of used data (2007/01–2008/09) contain the replacement dates of sensors: 2007-10-23 and 2008-02-18 (Table 2.B.1).

Table 2.2: Orientation correction estimates for the stations from Cascadia Initiative (Toomey et al., 2014).

STA	Orientation (°; from harmonic decomposition)	Error (°; 1σ)	%Back azimuth coverage	Orientation (°; from mean of T-RF)	Previously reported data (°; 1σ)	
J61C	190.2	6.6	79	185.9	200 ± 2^a	187 ± 9^b
J39C	89.0	4.1	79	97.1	105 ± 1^a	92 ± 9^b

The orientation angle ranges from 0° to 360° with clockwise direction, and our values indicate the angles that we need to correct from the misaligned north. We note that we apply this correction scheme to previous estimates (Janiszewski and Abers, 2015; Lodewyk and Sumy, 2014). For the uncertainty estimates, Janiszewski and Abers (2015) used the 95% confidence bounds from the F-test, with degrees of freedom determined from the net filter response of the signal. Our uncertainty estimates for J61C and J39 from the F-test are 3.3° and 2.5°, respectively. The difference in the two estimates for each station may arise from slightly different dataset and filtering.

[a]Janiszewski and Abers (2015)

[b]Lodewyk and Sumy (2014)

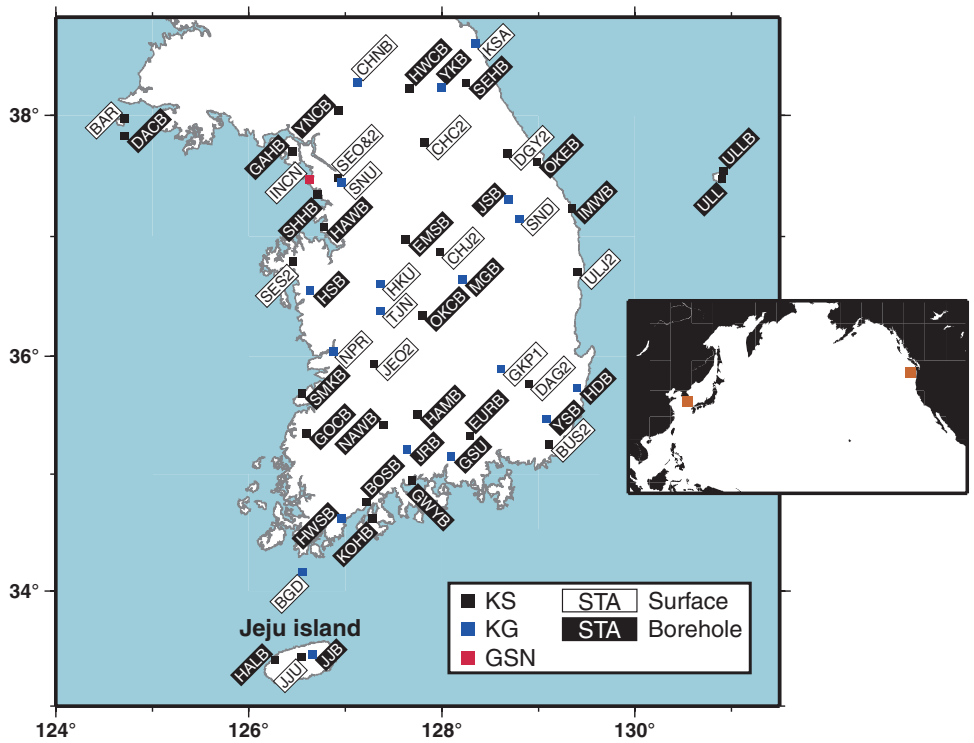

Figure 2.1: Map of seismic stations. The seismic networks are operated by Korea Meteorological Administration (KMA; denoted as KS) and Korea Institute of Geoscience and Mineral Resources (KIGAM; denoted as KG). GSN denotes Global Seismograph Network. A station code, SEO&2, denotes stations SEO and SEO2 that are located 0.7 km apart from each other. Of the total 53 station locations plotted, data from the station HDB is excluded in the analysis because of unstable sensor performance (Lee and Sheen, 2015). An inset shows the locations of Korean seismic network and ocean bottom sensor network of Cascadia Initiative (Toomey et al., 2014).

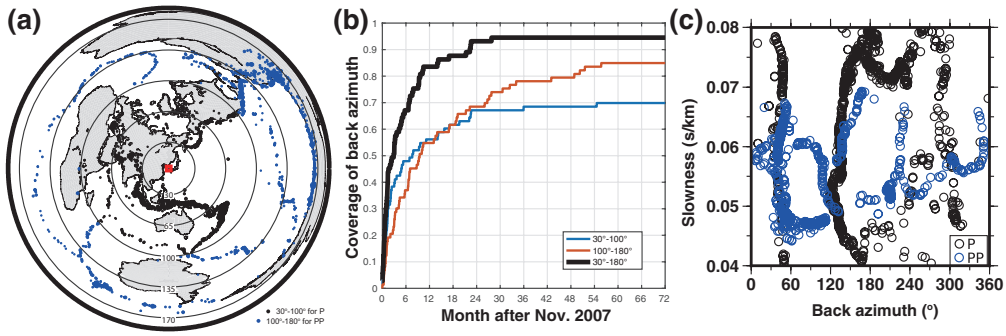

Figure 2.2: Distribution of teleseismic earthquakes in spatial and temporal scales, recorded from Korean seismic network. (a) The numbers of earthquakes for P and PP phases are 3,051 and 1,651, respectively, in 2005–2016. The location of the stations (Fig. 2.1) is indicated by a red rectangle. (b) Cumulative coverage in back-azimuth ray coverage for six years, discretized in 72 bins, after November 2007. By incorporating both P and PP phases, the back-azimuth coverage increases to 70, 80, 90 and 95 percent during the station operational period of about 8, 10, 21, and 30 months, respectively. (c) Distribution of the back-azimuth and slowness of the earthquakes in (b).

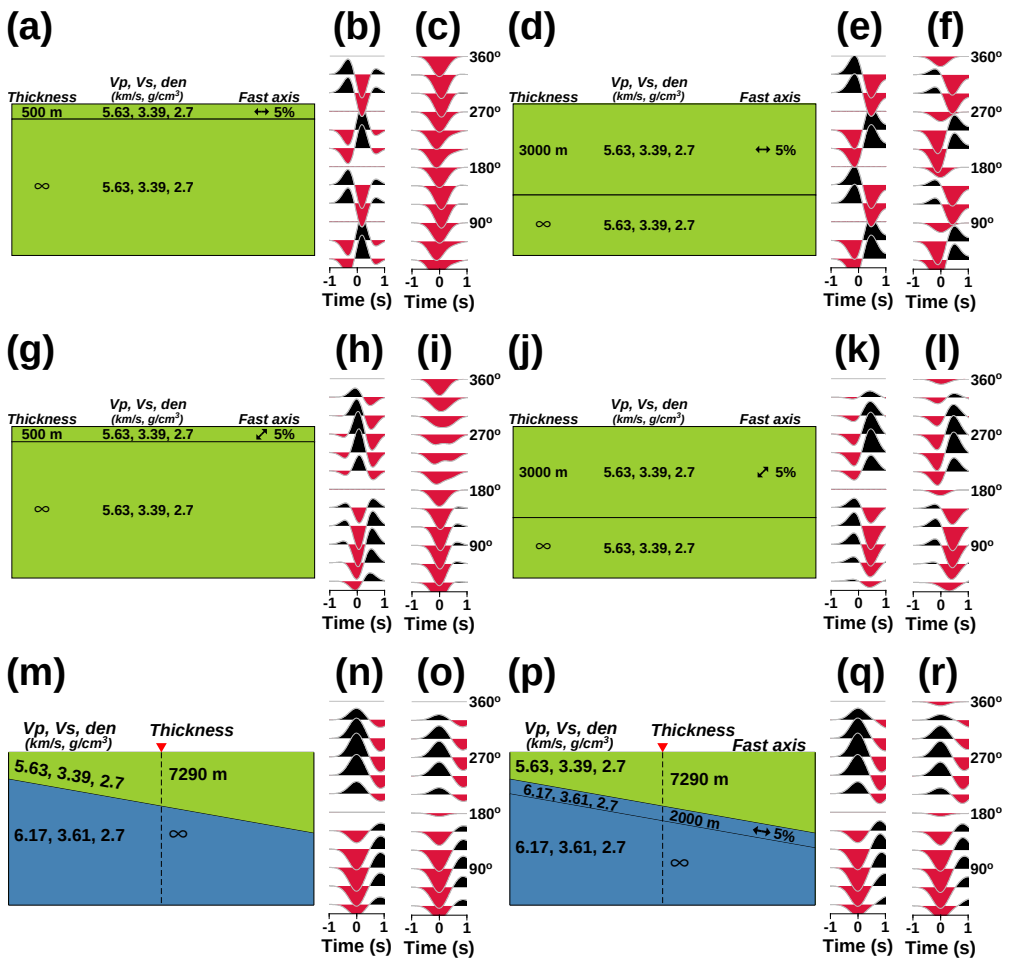

Figure 2.3: Six velocity structure models and corresponding synthetic T-RFs with back azimuth. The velocity model is shown in (a), (d), (g), (j), (m), and (p), and corresponding synthetic T-RFs in (b), (e), (h), (k), (n), and (q), assuming the sensor is properly oriented. The T-RFs from the sensor misoriented by 1° (clockwise rotation) are shown in (c), (f), (i), (l), (o), and (r). The thickness of a green layer (in panels m and p; above the location of a dashed line) and isotropic velocities of P- and S-waves of green and blue layers are taken from those of the upper and mid crusts in Kim et al. (2011). (continued)

Figure 2.3: (continued) The north is toward the right. The RFs from the models (a, d, g, and j) are calculated by the code *anirec* (Levin and Park, 1997) and the RFs from the models (m and p) by the code *raysum* (Frederiksen and Bostock, 2000). The angle of incidence is 25°. We note that the amplitudes of the synthetics are not scaled. The maximum amplitudes within −1–1 s are (b) 0.4%, (c) 1.7%, (e) 2.9%, (f) 3.6%, (h) 0.6%, (i) 2.0%, (k) 5.9%, (l) 6.3%, (n) 3.1%, (o) 4.3%, (q) 3.1%, and (r) 4.3%.

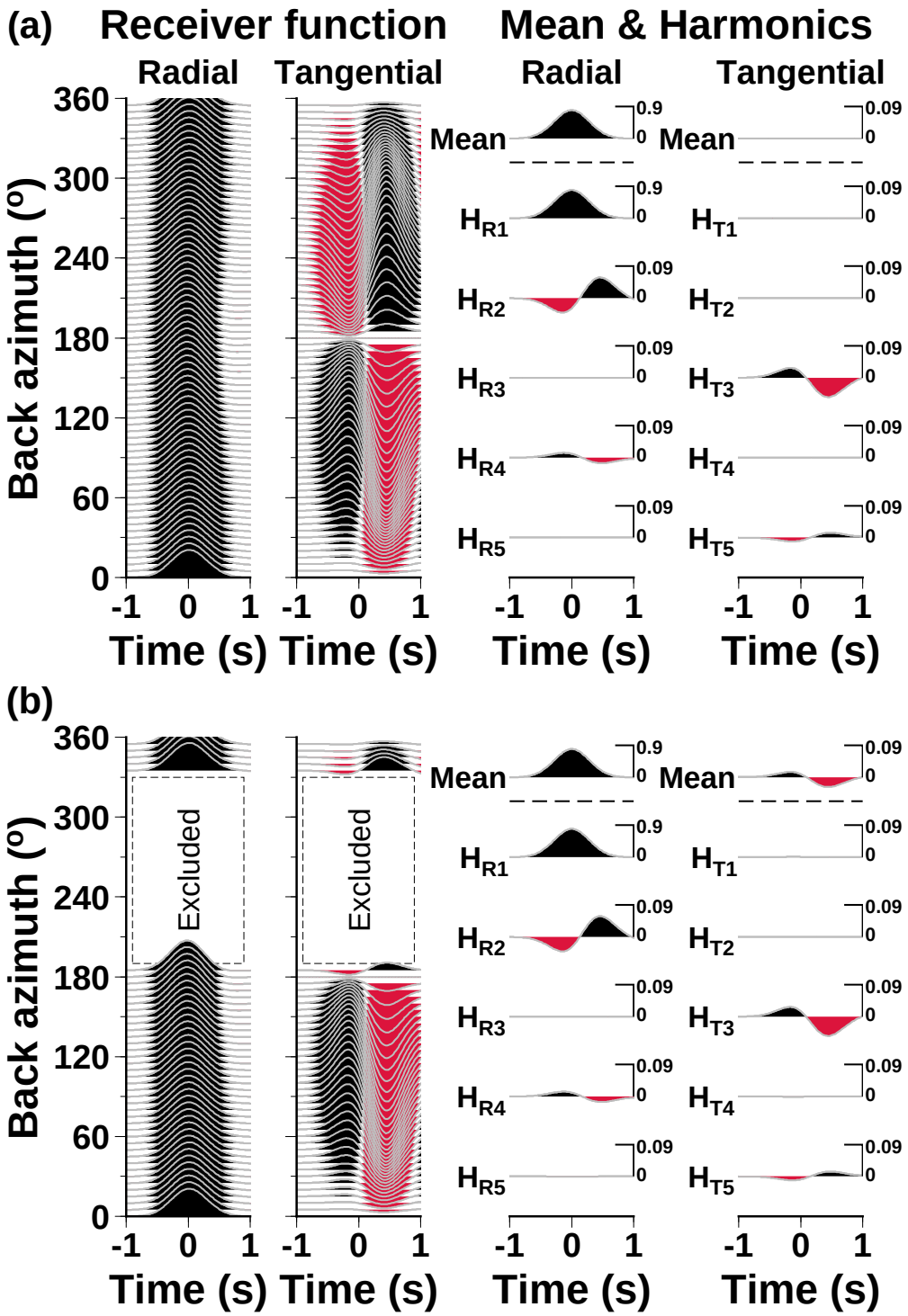

Figure 2.4: (Caption in next page)

Figure 2.4: Synthetic test results showing means and harmonic terms of both R- and T-RFs in the case of full (a) and poor (b) back-azimuthal coverage of earthquakes. We use the model with the 3 km-thick topmost anisotropic layer (Fig. 2.3j) to compute the R- and T-RFs (left panel), and their means and harmonics (right panel). The RF is sampled with an interval of 5° in back azimuth.

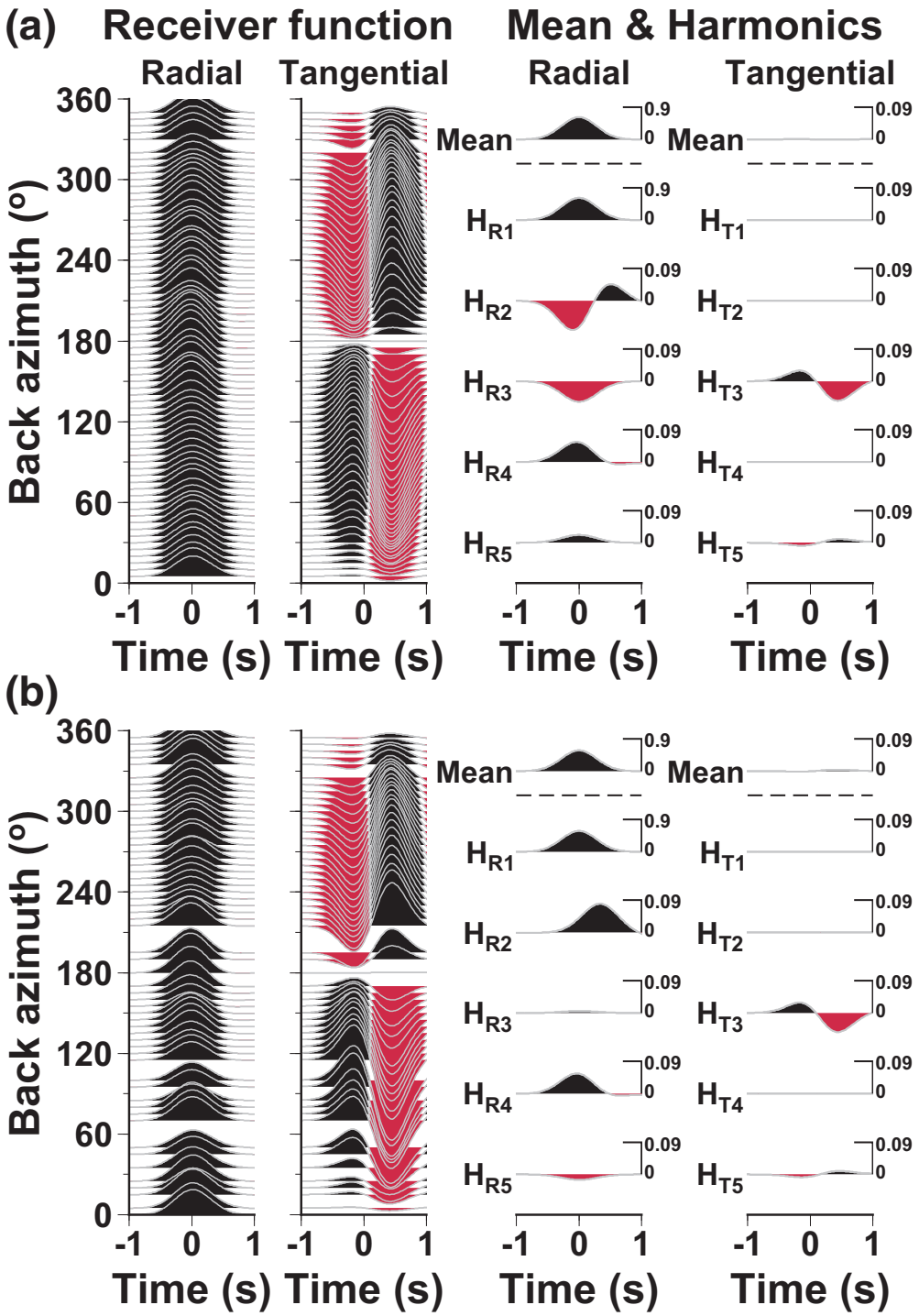

Figure 2.5: (Caption in next page)

Figure 2.5: Synthetic test results showing means and harmonic terms of both R- and T-RFs in the cases of realistic distributions of the earthquakes from (a) station JJB in South Korea (Fig. 2.2) and (b) OBS J61C (Cascadia Initiative). We use the model (Fig. 2.3j) to compute the R- and T-RFs (left panel), and their means and harmonics (right panel). The slowness is calculated with a 1D velocity model (**?**). The RFs are stacked by a bin of 5° in back azimuth.

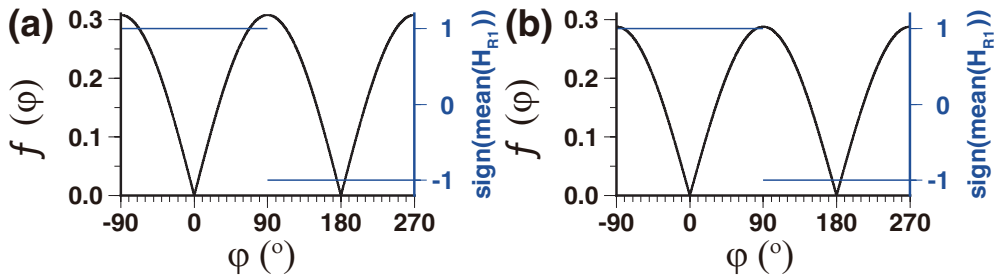

Figure 2.6: The function $f(\varphi)$ based on synthetic R- and T-RFs. The φ_{min} with a positive sign of the mean of the H_{R1} is 0.0°. The variations in the back azimuth and slowness are from (a) South Korea (station JJB) and (b) Cascadia Initiative (OBS J61C).

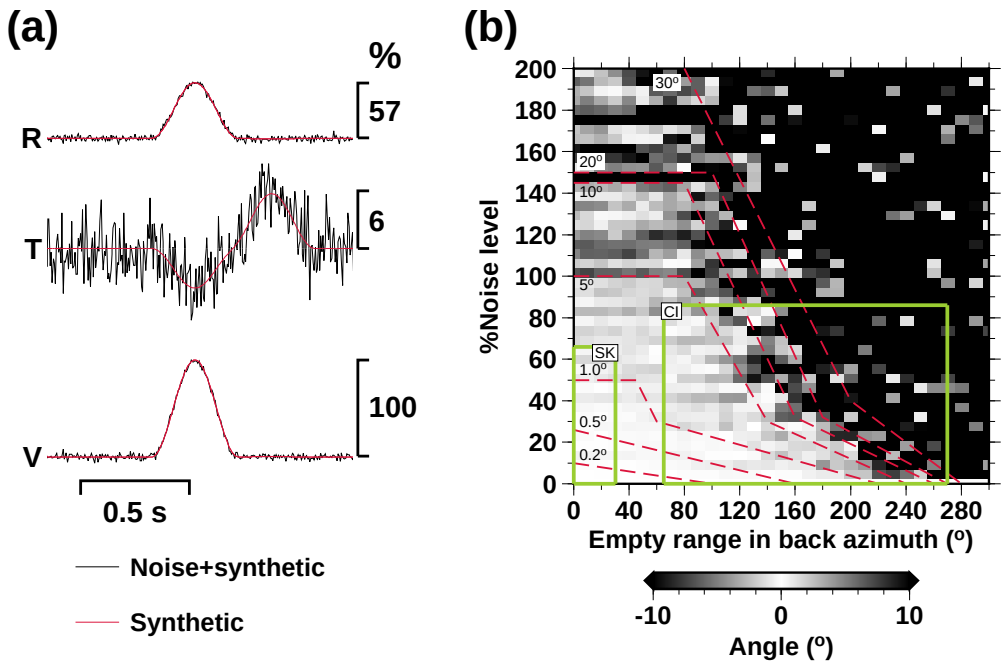

Figure 2.7: Synthetic test results showing how various noise levels and a degree of back-azimuthal coverage affect the orientation estimate. (a) An example of three-component synthetic seismograms with random noise of 2.3% at back azimuth of 110° where the tangential component is maximized, based on the model with the 3 km-thick topmost anisotropic layer (Fig. 2.3j). Amplitudes of the seismograms are scaled to the maximum amplitude of the vertical-component seismogram. (b) The angle estimate (deviated from the true orientation) by varying levels of noise and back azimuth coverage range. Red dashed lines roughly indicate the uncertainty range of 0.2°–30°. Empty range in back azimuth is centered on 270° following the set up in Fig. 2.4(b). Green boxes are approximate ranges in cases of South Korea (SK) and the Cascadia Initiative (CI).

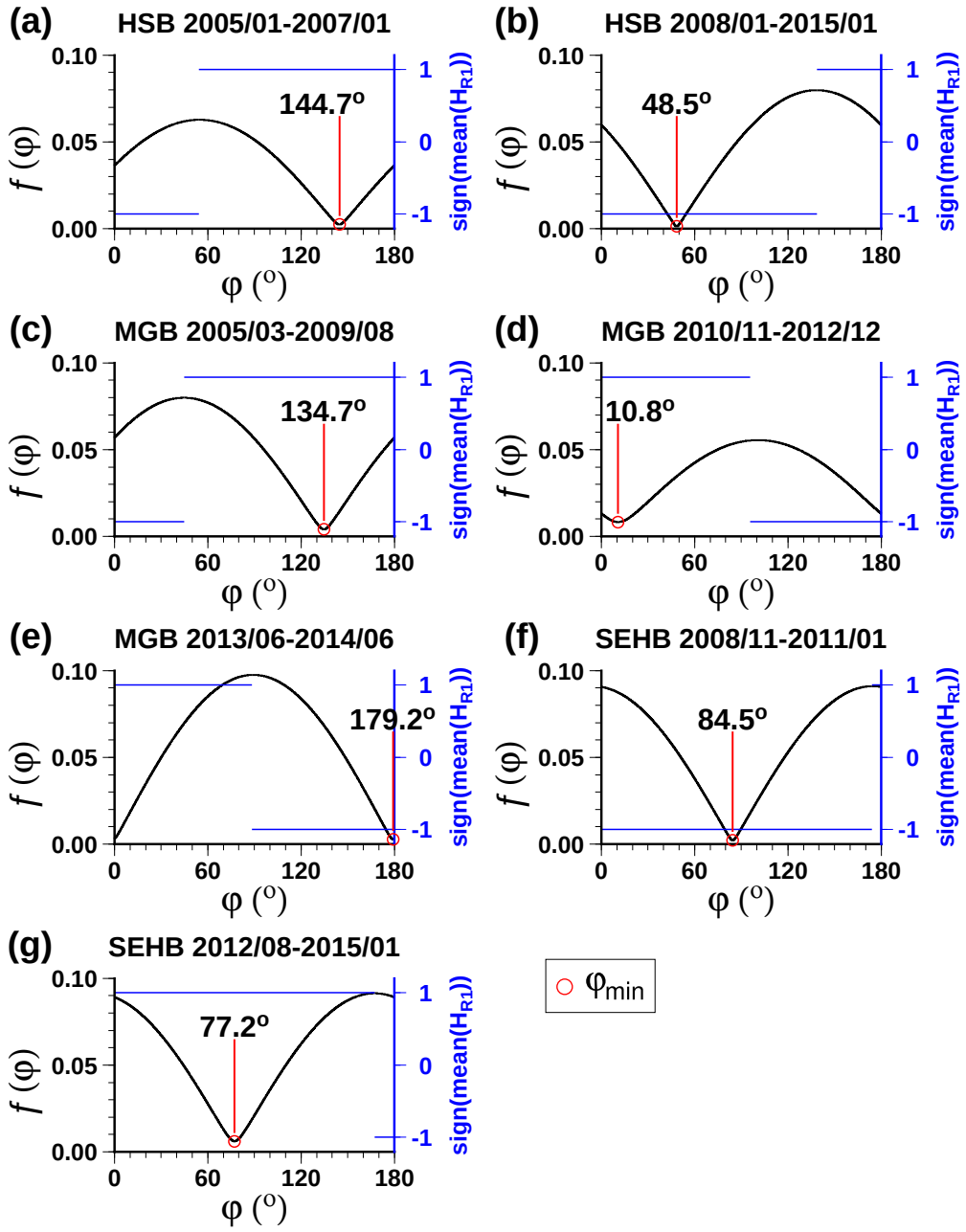

Figure 2.8: The function $f(\varphi)$ for stations HSB, MGB and SEHB plotted against φ for different periods. The φ_{min} for the different periods are 144.7° and 48.5° for HSB (a and b), 134.7°, 10.8° and 179.2° for MGB (c, d, and e), and 84.5° and 77.2° for SEHB (f and g).

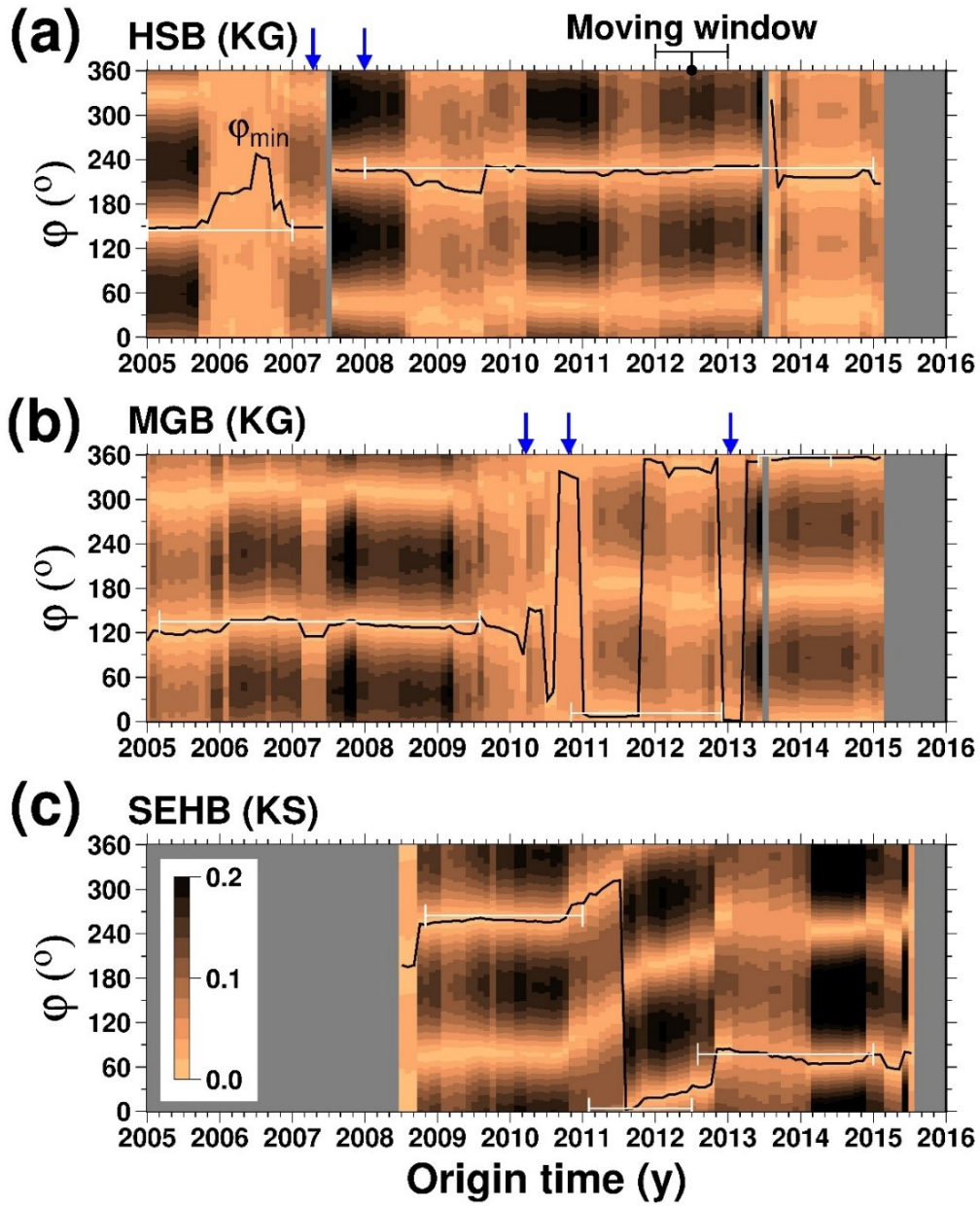

Figure 2.9: (Caption in next page)

Figure 2.9: The $f(\varphi)$ and φ_{min} as a function of time for stations HSB, MGB, and SEHB. The $f(\varphi)$ is calculated with an interval of two months and a moving window of 1 year. The $f(\varphi)$ and φ_{min} are represented by color and a solid black line, respectively. The validation periods for our orientation estimates (Table 2.1) are indicated by white ticked lines. Blue arrows indicate reported replacement date of sensors (Table 2.B.1). Gray background color means no data.

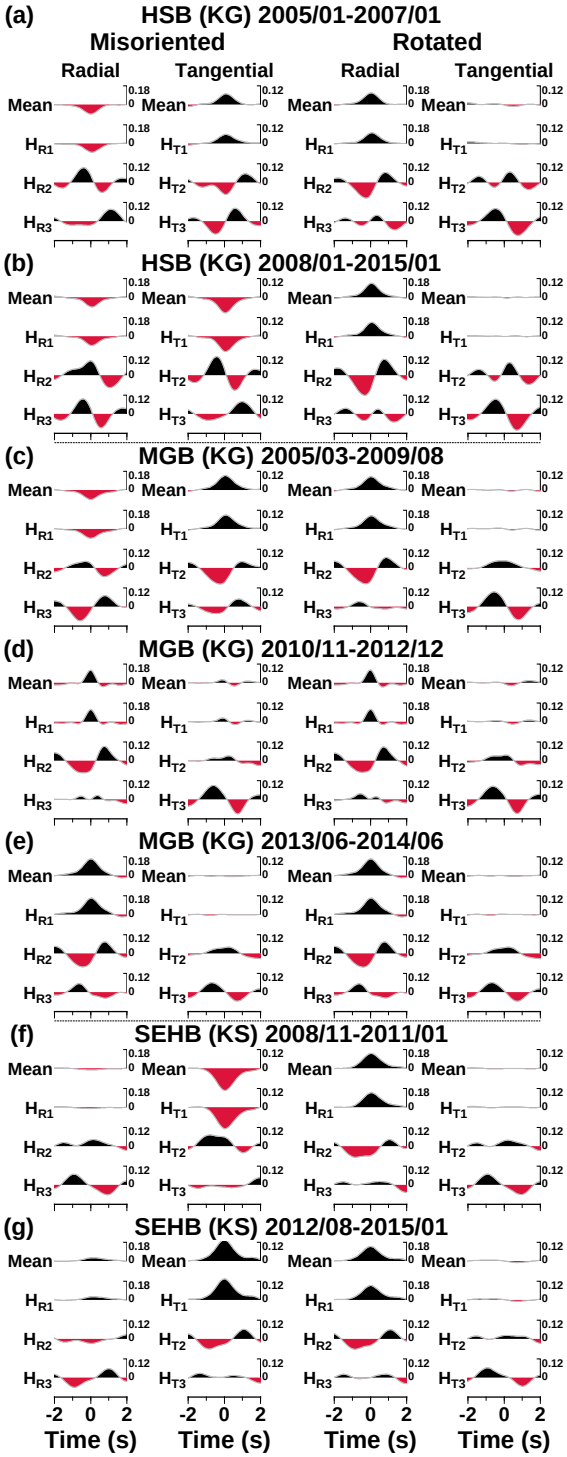

Figure 2.10: (Caption in next page)

Figure 2.10: Harmonic terms of R- and T-RFs, and their means for the stations HSB, MGB and SEHB prior to (left panel) and after the correction (right panel). Note that the amplitudes of the H_{T1} are minimized to nearly zero by the orientation correction. See Figs 2.A.7, 2.A.8, and 2.A.9 for H_{R4}, H_{R5}, H_{T4}, and H_{T5} for the stations.

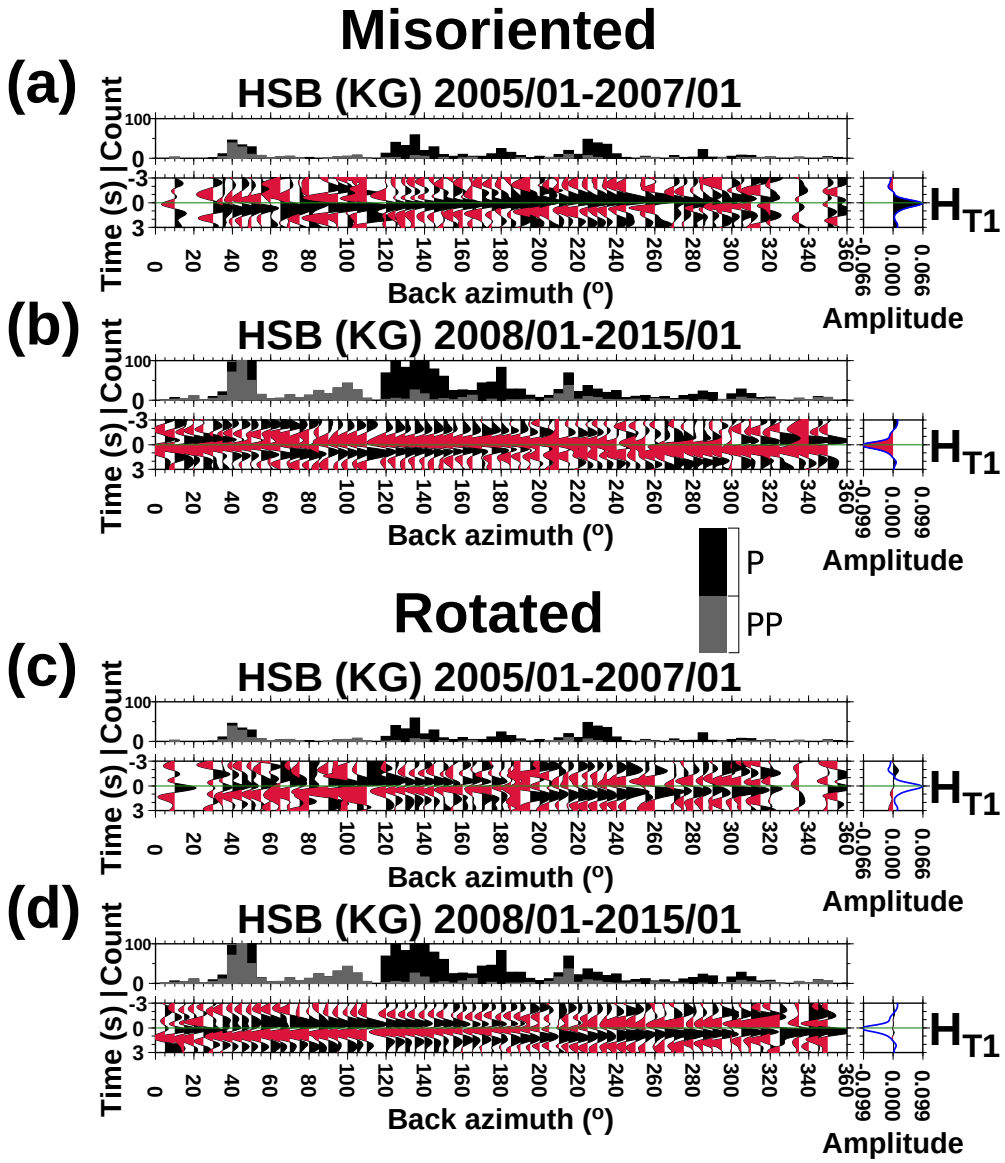

Figure 2.11: Stacked T-RFs plotted according to back azimuths for station HSB for each different validation period, prior to (a and b) and after the orientation correction (c and d). A solid green horizontal line marks a time of 0 s. The histogram in upper panel shows the number of earthquakes in each bin with a 5° window. The right panel shows a constant harmonic term of the T-RF (blue traces indicating not corrected waveforms). See Fig. 2.A.10 for stations MGB and SEHB.

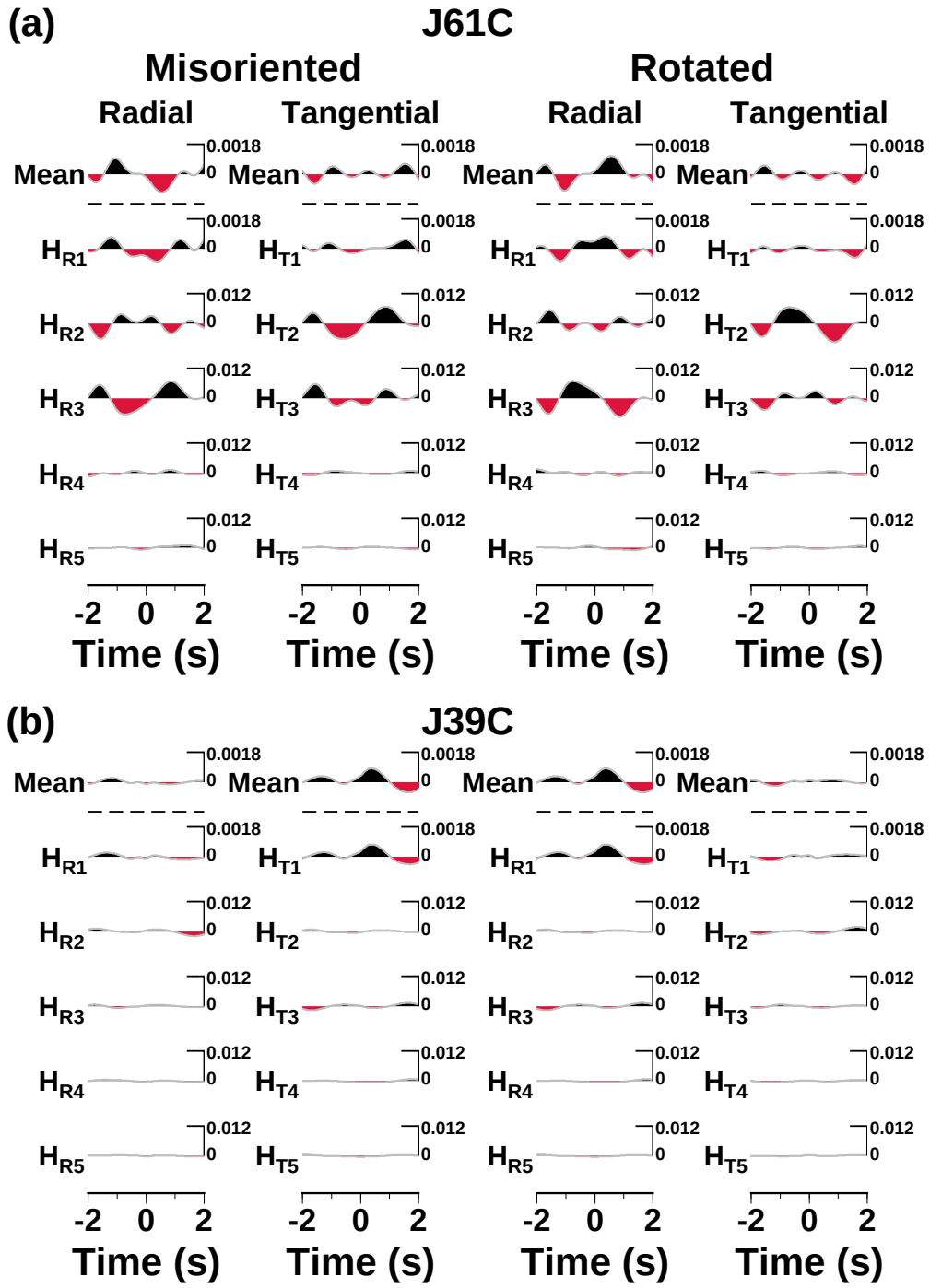

Figure 2.12: Harmonic terms of R- and T-RFs, and their means for the OBSs (a) J61C and (b) J39C prior to (first two columns) and after the correction (third and fourth columns).

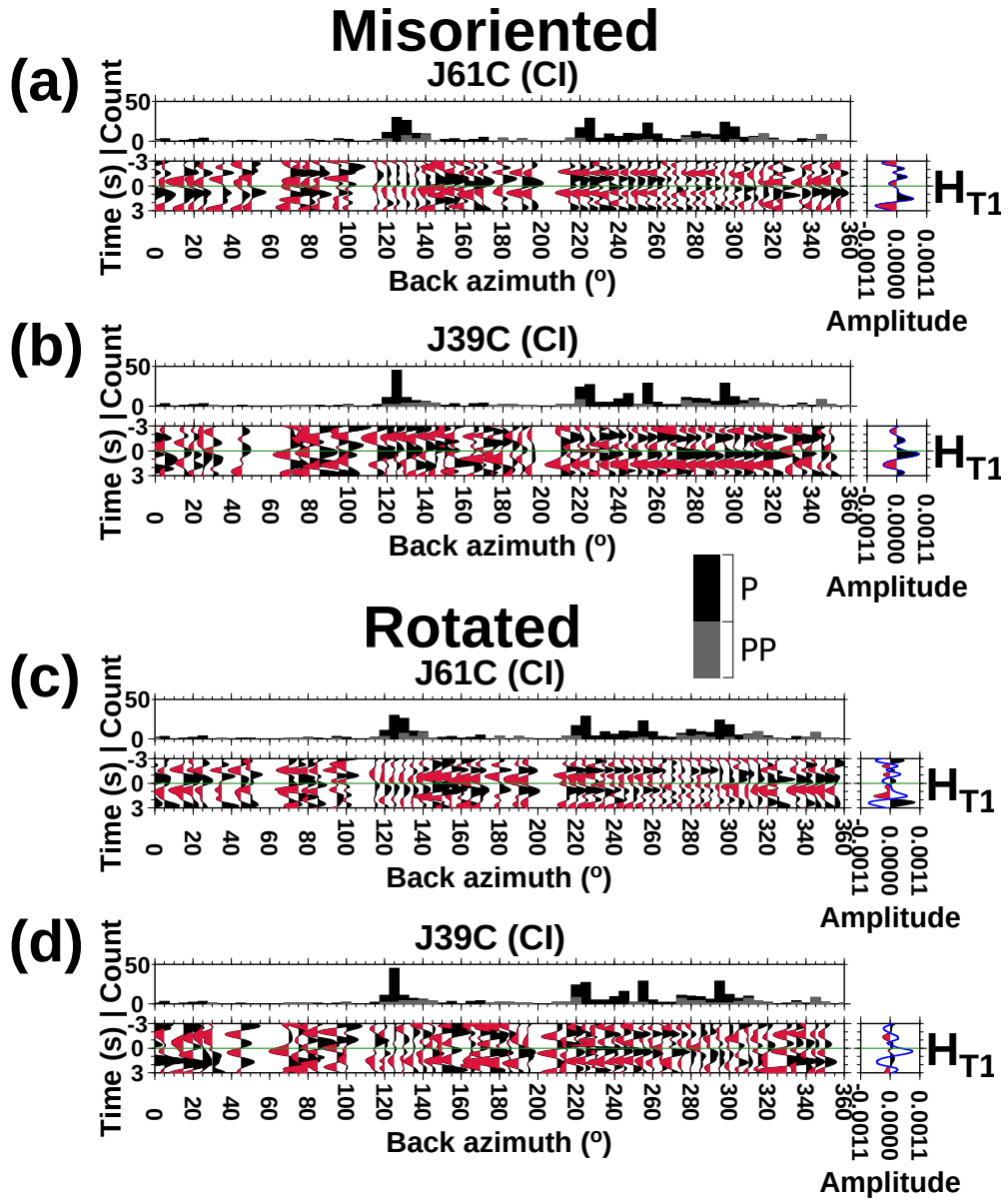

Figure 2.13: Stacked T-RFs plotted according to back azimuths for the OBSs J61C and J39C, prior to (a and b) and after the orientation correction (c and d). A solid green horizontal line marks a time of 0 s. The histogram in upper panel shows the number of earthquakes in each bin with a 5° window. The right panel shows a constant harmonic term of the T-RF (blue traces indicating not corrected waveforms).

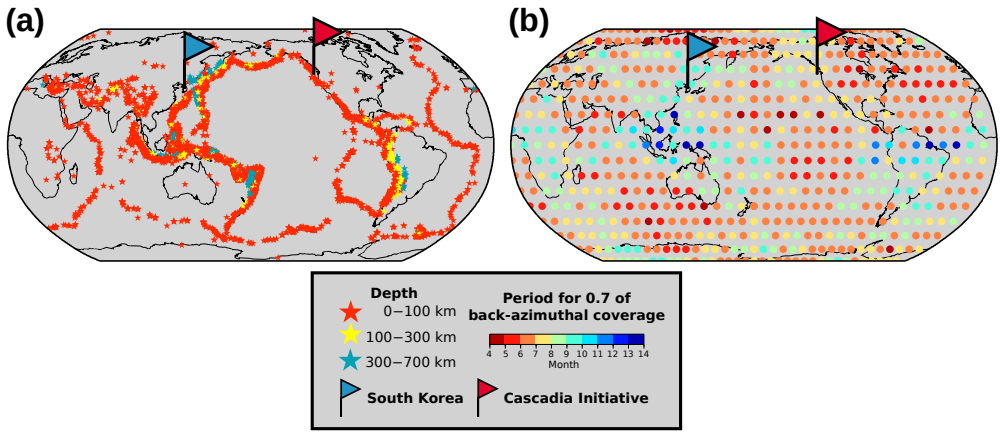

Figure 2.14: Global distribution of the earthquakes and the period for the 70% back-azimuthal coverage. (a) Distribution of the earthquakes in 14 months from November 2007 with magnitude larger than 5.5. (b) The variation of the period for the 70% of the back-azimuthal coverage using P and PP (distance ranging from 30° to 180°).

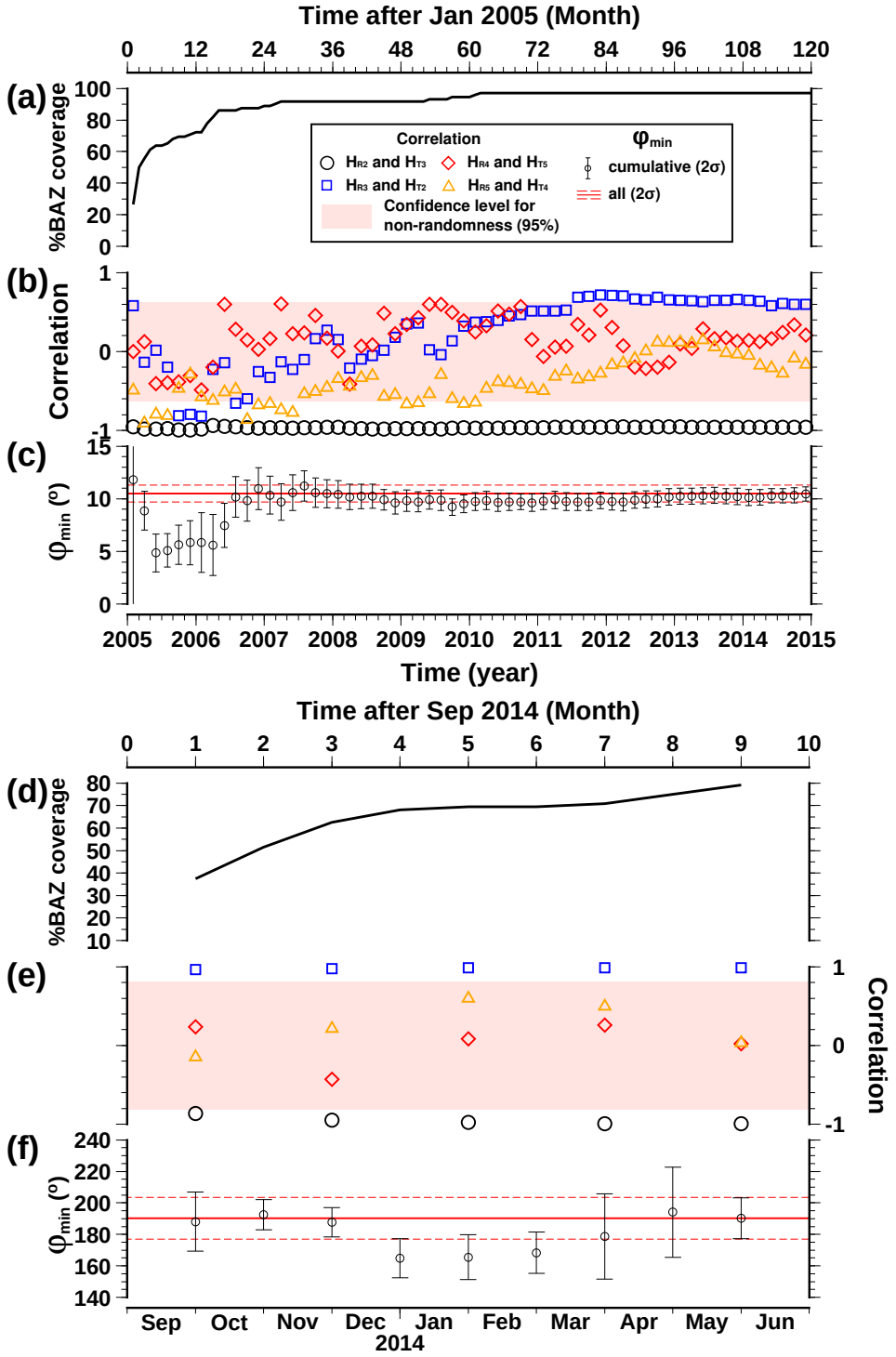

Figure 2.15: (Caption in next page)

Figure 2.15: Convergence of the orientation (φ_{min}) and corresponding back-azimuthal coverage, and correlation (in -2.0–2.0 s) between the harmonic terms with cumulative data (a, b, and c) for the station CHJ2 in South Korea and (d, e, and f) for the OBS J61C of the Cascadia Initiative. The confidence level for non-randomness (Bendat, 2010) is marked as pink color.

Appendices

2.A Supplementary materials (figure)

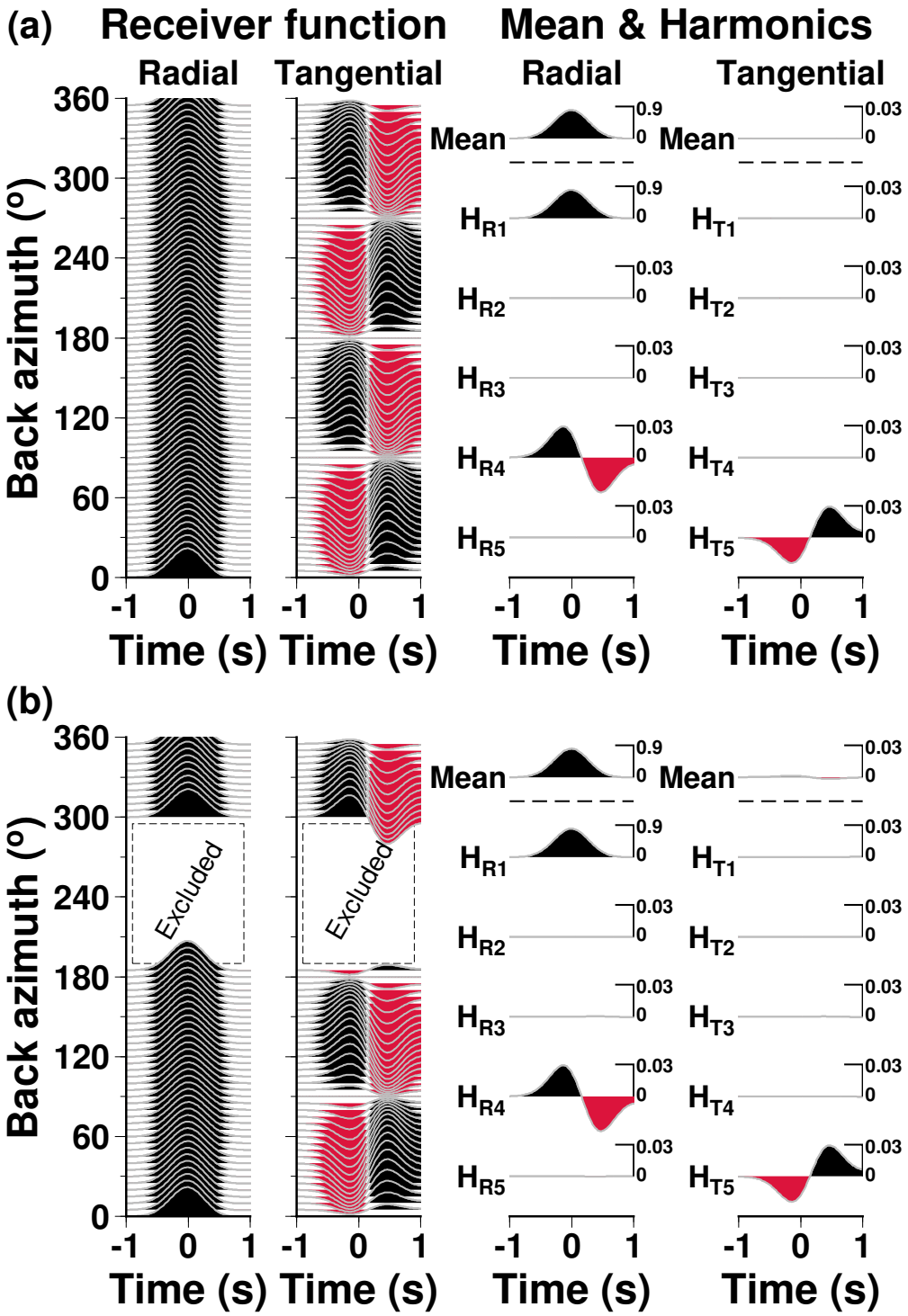

Figure 2.A.1: (Caption in next page)

Figure 2.A.1: Synthetic test results showing means and five harmonic terms of both R- and T-RFs in the case of full (a) and poor (b) back-azimuthal coverage of earthquakes. We use the model with the 3 km-thick topmost anisotropic layer (Fig. 2.3d) to compute the R- and T-RFs (left panel), and their means and harmonic terms (right panel). The RF is sampled with an interval of 5° in back azimuth.

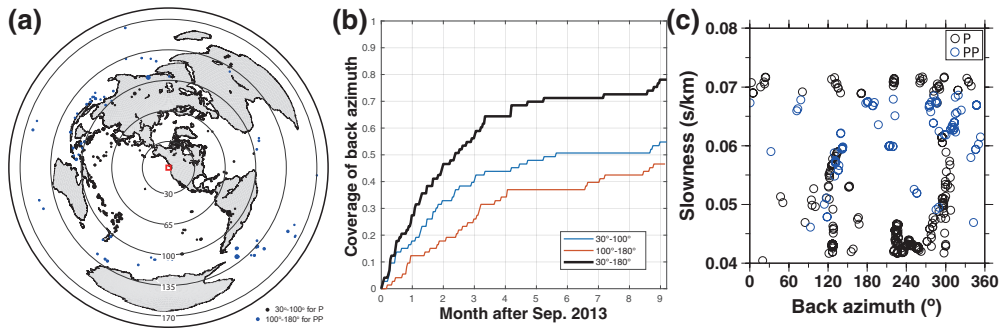

Figure 2.A.2: Distribution of teleseismic earthquakes in spatial and temporal scales, recorded from the OBS J61C (Cascadia Initiative; Toomey et al., 2014). (a) The numbers of earthquakes for P and PP phases are 276 and 95, respectively, in 2013–2014. The location of the station is indicated by a red rectangle. (b) Cumulative coverage in back-azimuth ray coverage for 9 months, discretized in 72 bins, after September 2013. (c) Distribution of the back azimuth and slowness of the earthquake in (b).

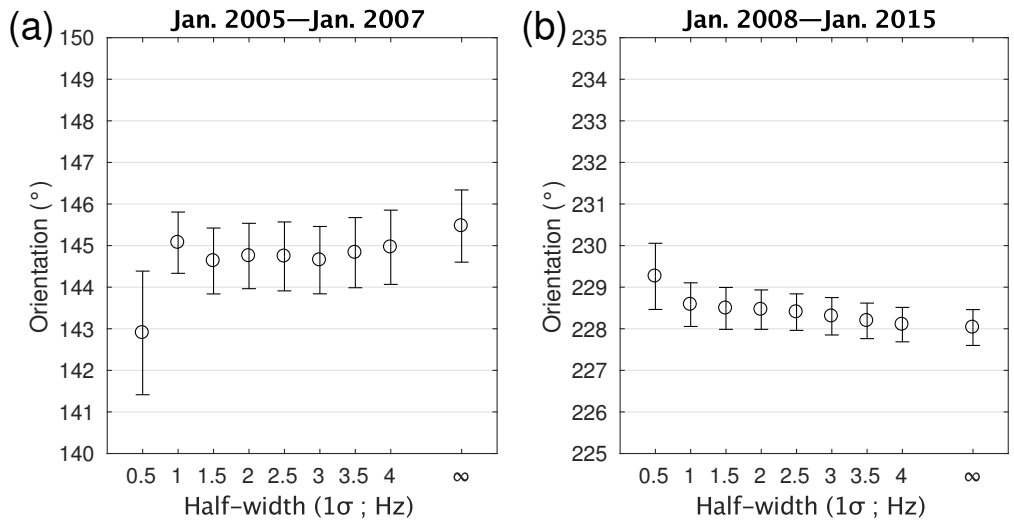

Figure 2.A.3: Orientation estimations using various half-widths in Gaussian lowpass filter for the station HSB. (a) Period of January 2005–January 2007 and (b) period of January 2008–January 2015. The infinity symbol means no filter.

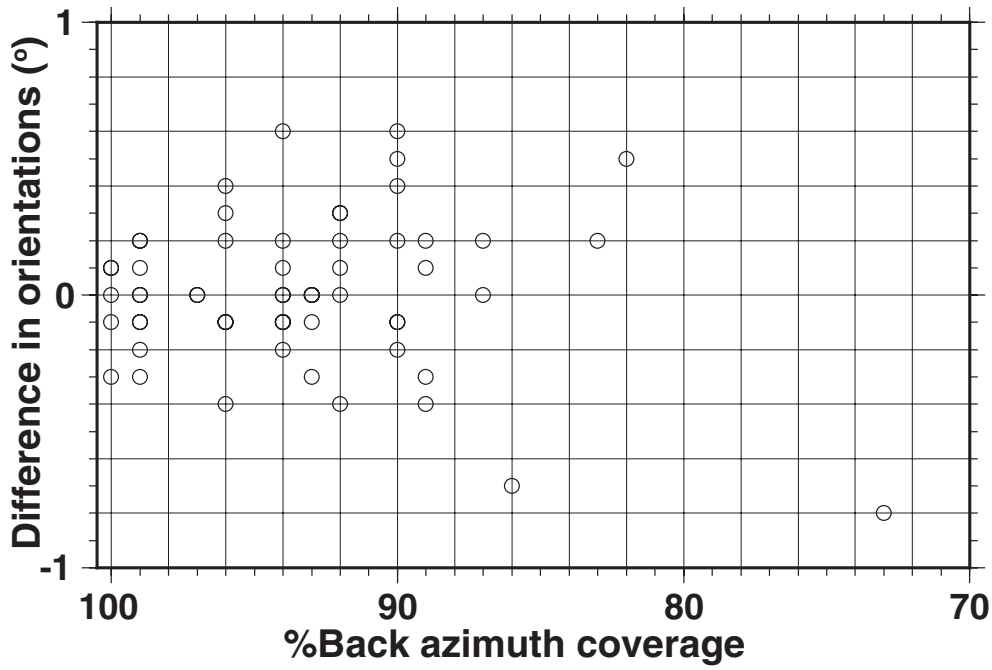

Figure 2.A.4: Difference between the orientation estimates from two methods, which are (1) the minimization of H_{T1} and (2) the minimization of the mean of T-RF near 0 s (Table 2.B.2). The stations SEHB, INCN^{00} and KOHB are excluded in this figure because of large differences (2.3°, 7.6°, and 4.6° respectively) in this figure.

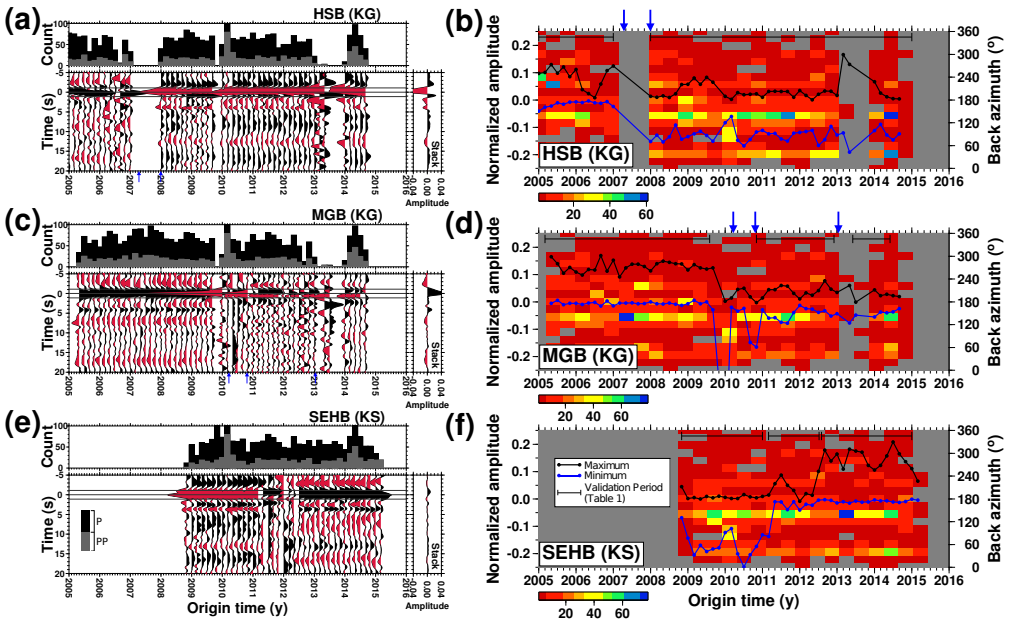

Figure 2.A.5: Stacked T-RFs and temporal change of their maximum and minimum amplitudes for stations HSB, MGB and SEHB. (a, c, and e) Stacked T-RFs (lower panel) and a histogram showing the number of earthquakes in each bin with a two-month window (upper panel) for stations HSB, MGB and SEHB. Blue arrows indicate reported replacement date of sensors (Table 2.B.1). (b, d, and f) Temporal change of the maximum and minimum amplitudes (black and blue lines, respectively) of the T-RFs within −1.2 to 1.2 s for stations HSB, MGB and SEHB. Colored background indicates the number of earthquakes in time and back azimuth. The fluctuation of either maximum or minimum amplitude can be partially explained by heterogeneous space-time occurrence of earthquakes. Gray background color means no data.

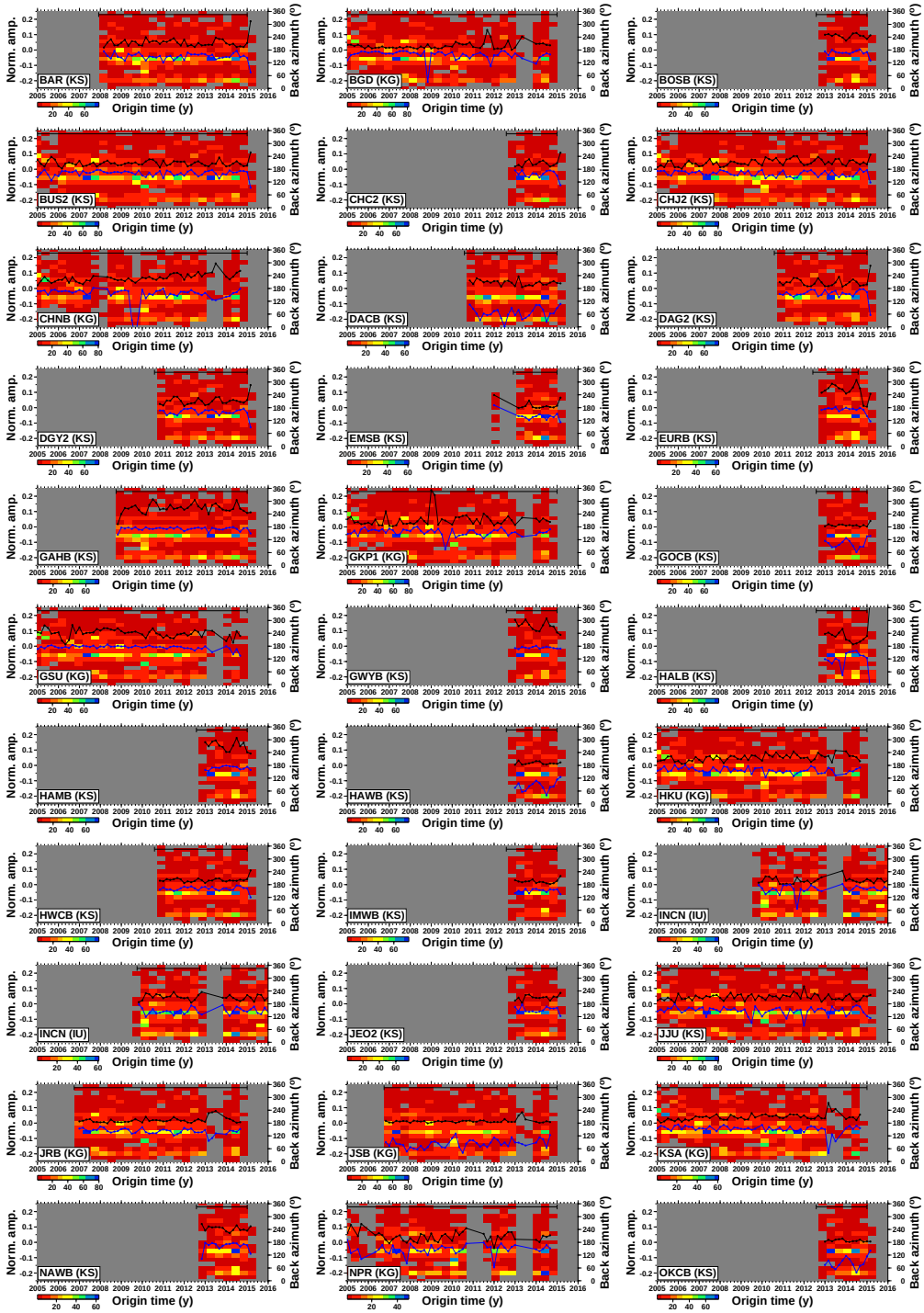

Figure 2.A.6: (Continued)

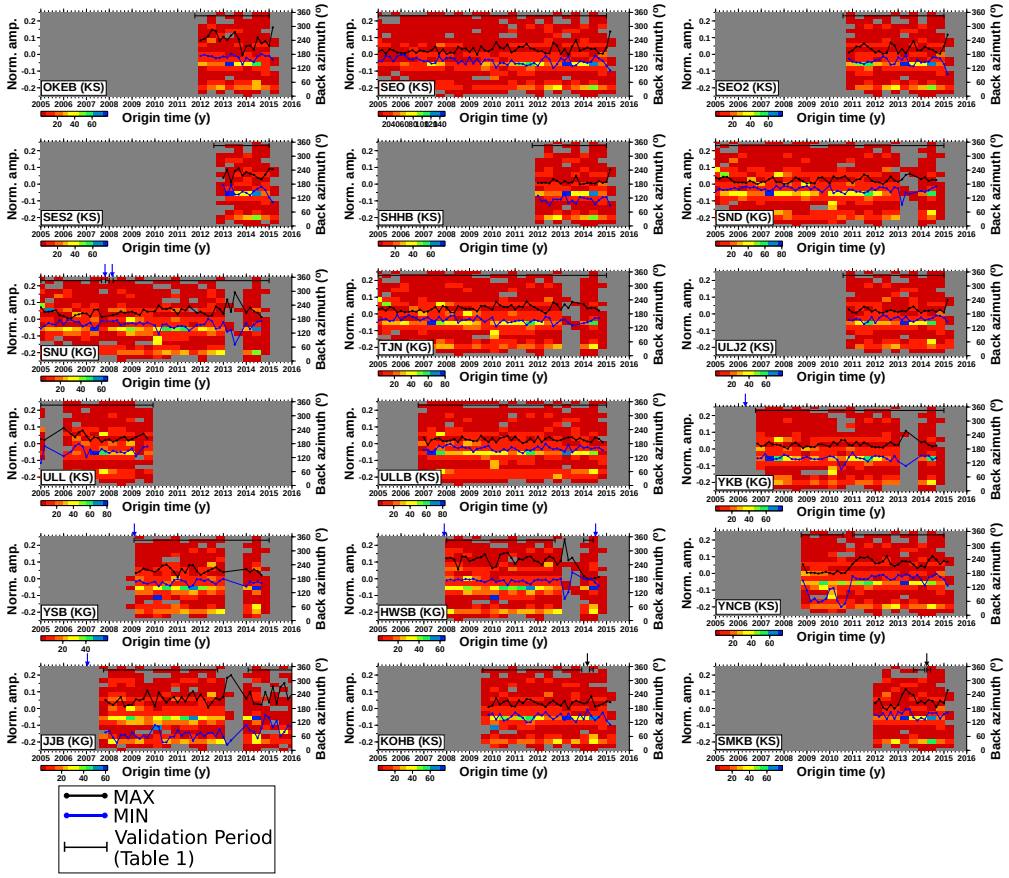

Figure 2.A.6: Temporal change of the maximum and minimum amplitudes (black and blue lines, respectively) of the T-RF within -1.2 to 1.2 s for 51 stations (including the station INCN '00' and '10'). See Figs 2.A.5b, 2.A.5d and 2.A.5f for stations HSB, MGB and SEHB. Colored background indicates the number of earthquakes in time and back azimuth. A blue arrow indicates reported replacement date of a sensor (Table 2.B.1). The fluctuation of either maximum or minimum amplitude can be partially explained by heterogeneous space-time occurrence of earthquakes. Gray background color means no data.

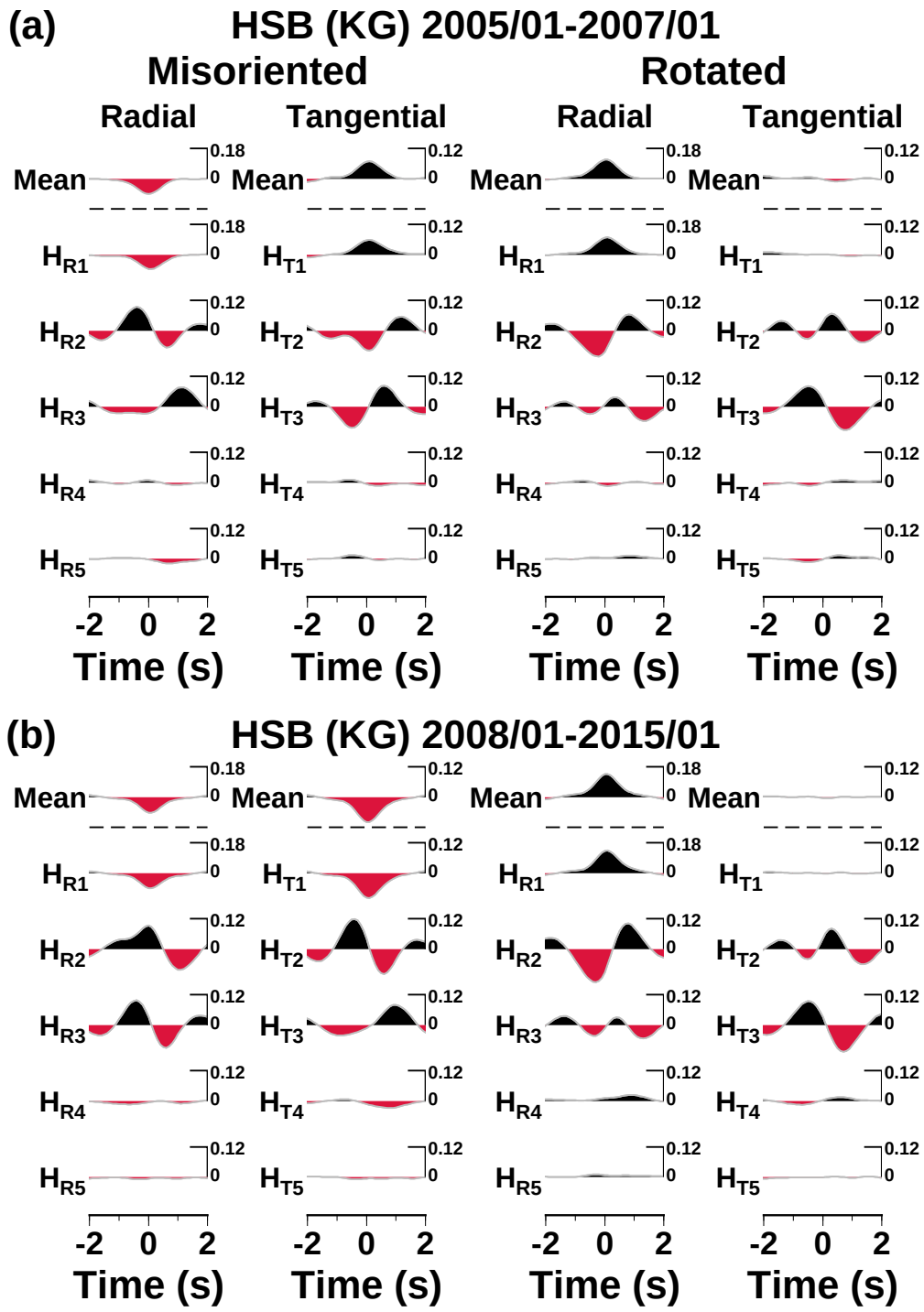

Figure 2.A.7: (Caption in next page)

Figure 2.A.7: Harmonic terms of R- and T-RFs, and their means for the station HSB during the two different validation periods. In each panel, first two columns show the results prior to the correction, and the third and fourth columns after the correction.

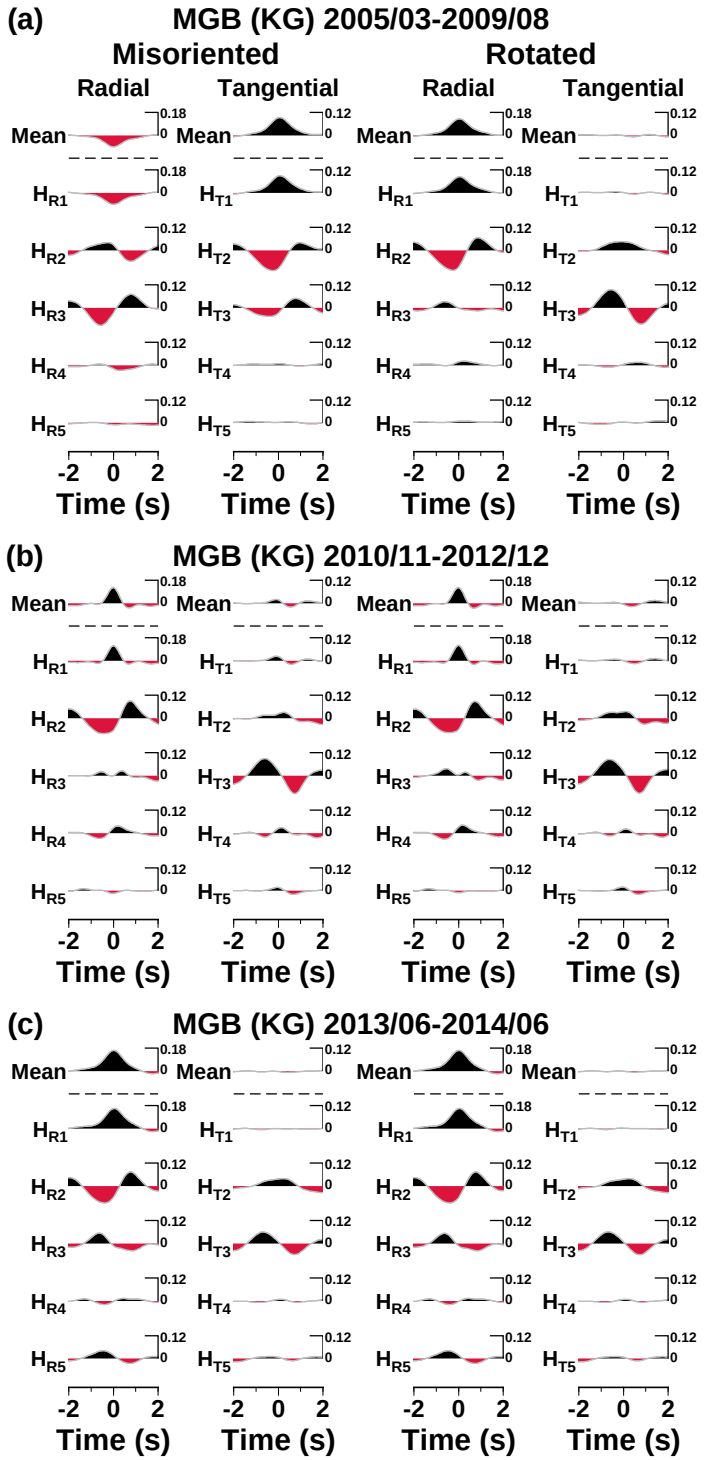

Figure 2.A.8: (Caption in next page)

Figure 2.A.8: Harmonic terms of R- and T-RFs, and their means for the station MGB during the three different validation periods. In each panel, first two columns show the results prior to the correction, and the third and fourth columns after the correction.

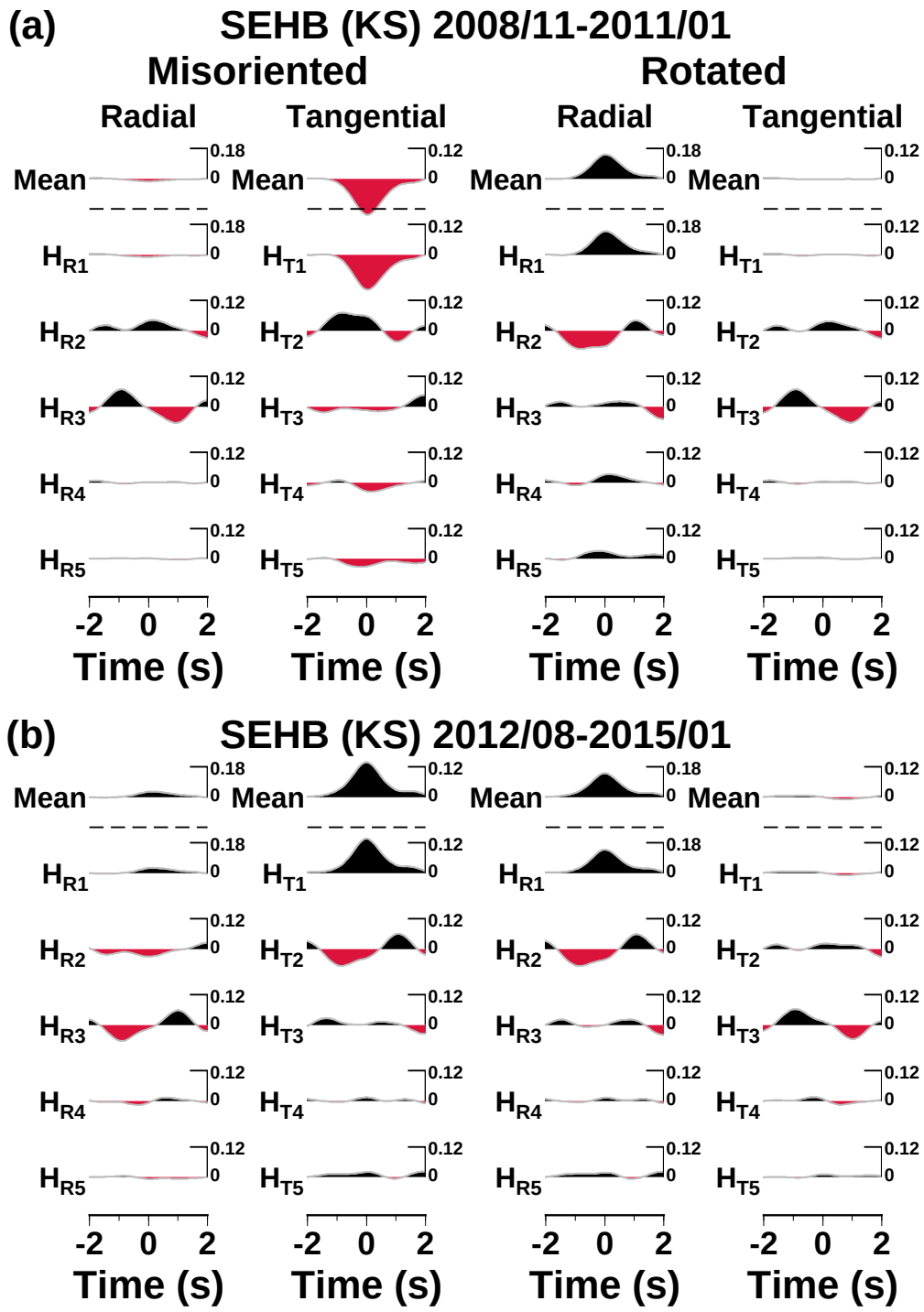

Figure 2.A.9: (Caption in next page)

Figure 2.A.9: Harmonic terms of R- and T-RFs, and their means for the station SEHB during the two different validation periods. In each panel, first two columns show the results prior to the correction, and the third and fourth columns after the correction.

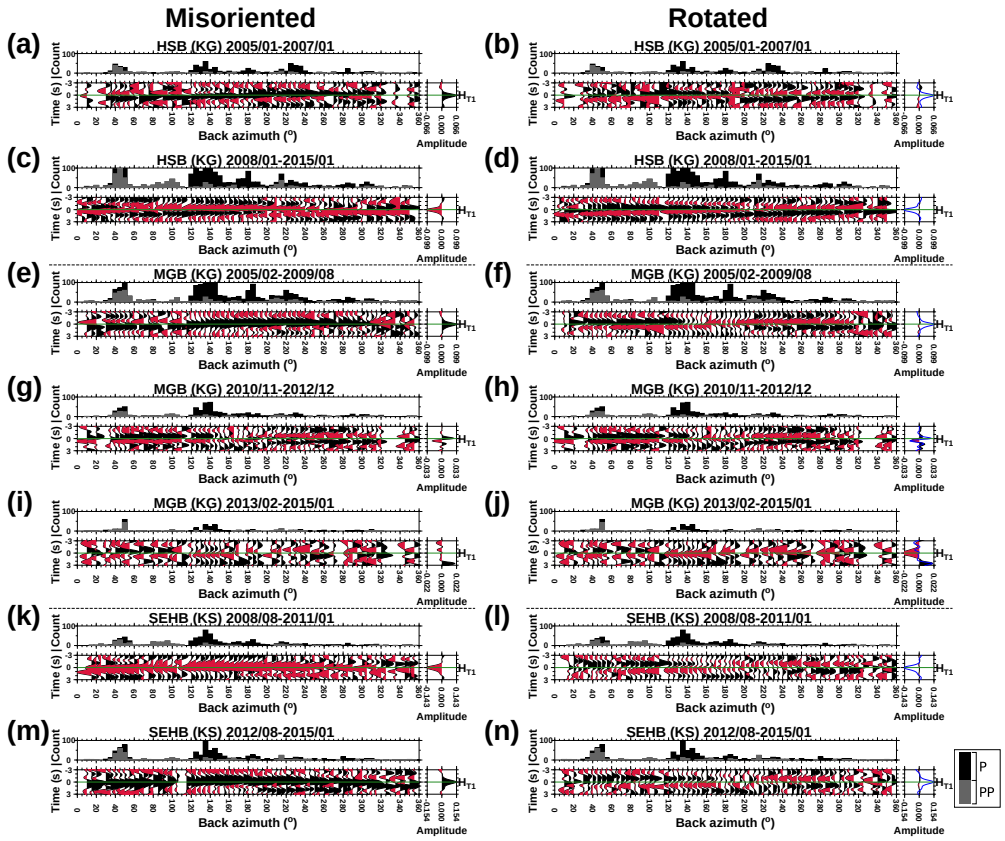

Figure 2.A.10: Stacked T-RFs plotted according to back azimuths for stations HSB, MGB and SEHB for each different validation period, prior to (a, c, e, g, i, k and m) and after the orientation correction (b, d, f, h, j, l and n). A solid green horizontal line marks a time of 0 s. The histogram in upper panel shows the number of earthquakes in each bin with a 5° window. The right panel shows a constant harmonic term of the T-RF (blue traces indicating not corrected waveforms).

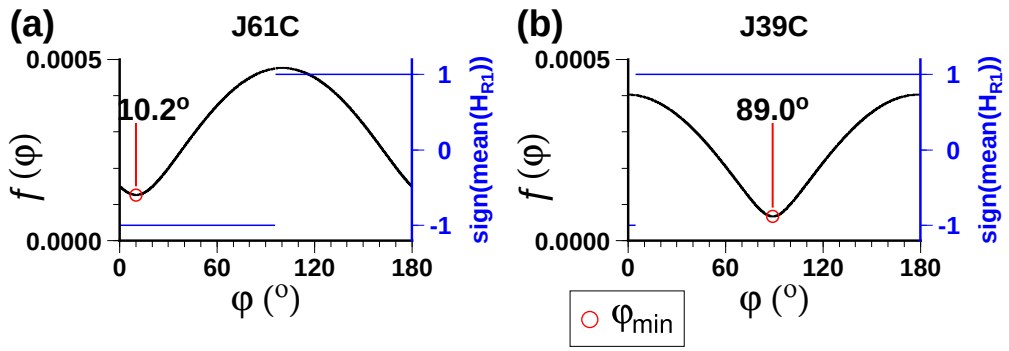

Figure 2.A.11: The function $f(\varphi)$ for OBSs (a) J61C and (b) J39C plotted against φ. Note that the range of the function $f(\varphi)$ is quite limited because of small amplitudes of the T-RFs at and near 0 s for the OBS data. Regardless of such small range in $f(\varphi)$, the φ_{min} can be determined as shown in the figure.

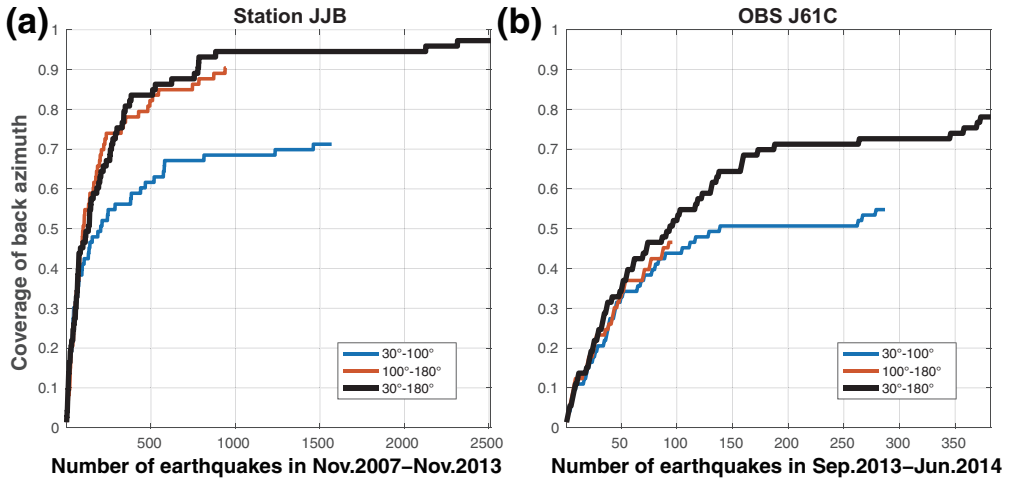

Figure 2.A.12: Back-azimuthal coverage plotted against the cumulative numbers of earthquakes for (a) the station JJB and (b) OBS J61C.

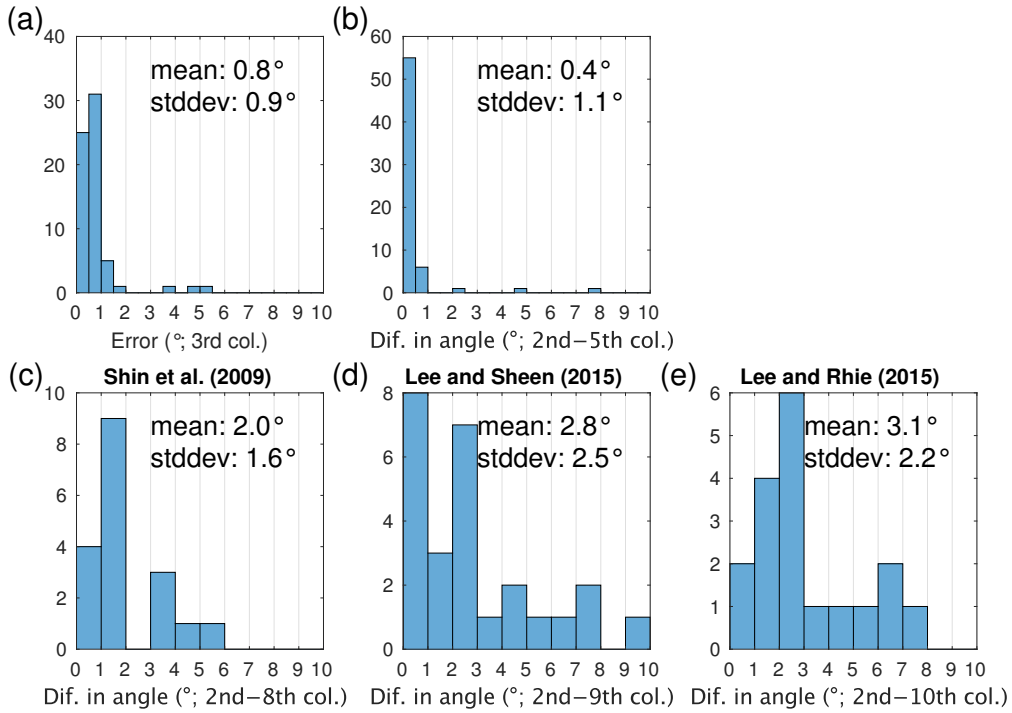

Figure 2.A.13: Histogram showing our uncertainties and differences in the orientation estimates shown in Table 2.1. (a) The error based on the bootstrapping method (the third column in Table 2.1). (b) Difference between the orientations determined by the minimization of H_{T1} (the second column) and the mean of T-RFs (the fifth column) (see also Fig. 2.A.4). Difference between ours (the second column) and previous estimates, (c) Shin et al. (2009) (the eighth column), (d) Lee and Sheen (2015) (the ninth column), (e) Lee and Rhie (2015) (the tenth column), respectively. The differences shown in (b), (c), (d), and (e) are root-mean-square values, and we exclude a few values which exceed 10°. Dif.—difference; col.—column; stddev—standard deviation.

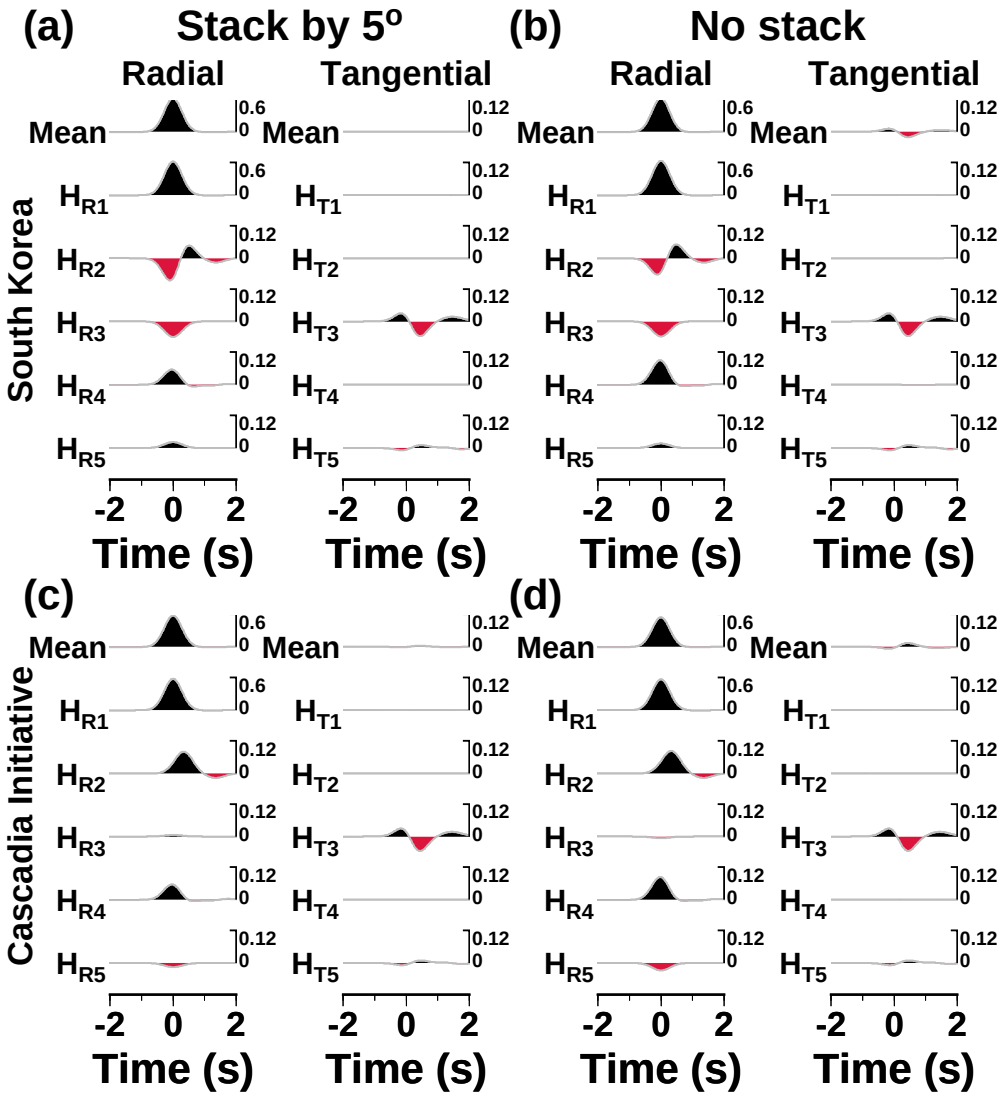

Figure 2.A.14: Synthetic test results showing means and harmonic terms of both R- and T-RFs in the cases of (a and b) for Korean seismic network and (c and d) the Cascadia Initiative when the RFs are stacked by 5° bin in back azimuth (a and c) and not stacked (b and d).

2.B Supplementary materials (table)

Table 2.B.1: Replacement date of velocity sensor of KG network in South Korea.

Station	Date		
	First	Second	Third
YKB	2006-04-21‡		
JJB	2007-01-16‡		
HSB	2007-04-13	2007-12-28	
SNU†	2007-10-23	2008-02-18	
HWSB	2007-11-22‡	2014-07-11	
YSB	2009-02-06‡	2016-07-20‡	
MGB	2010-03-19‡	2010-10-21	2013-01-14
HDB	2010-03-23‡	2012-11-14‡	
GSU	2016-04-20‡		
JSB	2016-08-09‡		

Based on the report provided by KIGAM on October 10, 2016
(`http://quake.kigam.re.kr/bbs/view.php?id=notice&no=24`)

†The sensor is deployed at surface; The others are deployed underground.

‡Date beyond the data acquisition period for our analysis

Table 2.B.2: Comparison of the orientations based on different methods.

Station ID	Orientation (°; minimization of H_{T1} based on harmonic decomposition & stacking with a 5-degree bin; Table 2.1)	Orientation (°; minimization of a mean of T-RFs; Table 2.1)	Orientation (°; minimization of H_{T1} based on harmonic decomposition & no stack in back azimuth)
BAR	5.5	5.5	4.6
BGD	359.5	359.6	1.1
BOSB	31.5	31.3	33.6
BUS2	9.3	9.4	8.5
CHC2	3.8	3.9	4.3
CHJ2	10.5	10.6	10.5
CHNB	19.4	19.3	18
DACB	268.4	268.5	268.1
DAG2	3.5	3.5	3.1
DGY2	9.6	9.5	8.7
EMSB	338.2	338.2	338.6
EURB	104.4	105.1	102.5
GAHB	128.5	128.6	128.7
GKP1	5.4	5.4	6.2
GOCB	234.5	234.3	234.4
GSU	146.2	146.5	144.5
GWYB	120.5	120	124.9
HALB	355.4	355.1	355.1
HAMB	121	120.8	121.5
HAWB	246.7	247.1	244.4
HKU	8.2	8.3	8.6
HSB	144.7	144.5	149.4
HSB	228.5	228.6	226.2
HWCB	3.3	3.4	3.3
HWSB	60.9	60.7	57.8
HWSB	–	–	198.3
IMWB	196.7	197.1	195.6
INCN^{00}	335.3	327.7	203.8
INCN^{00}	4.6	4	190.5

(continued)

Table 2.B.2: (continued)

Station ID	Orientation (°; minimization of H_{T1} based on harmonic decomposition & stacking with a 5-degree bin; Table 2.1)	Orientation (°; minimization of a mean of T-RFs; Table 2.1)	Orientation (°; minimization of H_{T1} based on harmonic decomposition & no stack in back azimuth)
INCN[10]	359.2	359.2	1.6
INCN[10]	0.1	359.7	359.4
JEO2	2.7	3	2.8
JJB	237.1	236.5	236.5
JJB	233.8	233.3	233.9
JJU	1.9	1.8	4
JRB	194.7	194.7	194.8
JSB	245	245.2	245.6
KOHB	256.3	251.7	187.9
KOHB	–	–	–
KSA	4.4	4.2	4.3
MGB	134.7	134.8	132.7
MGB	10.8	10.8	10.4
MGB	359.2	–	356.6
NAWB	148.6	148.8	147.9
NPR	2.9	3.2	334.8
OKCB	251.1	250.9	250.5
OKEB	35.2	34.8	35.1
SEHB	264.5	264.2	266.2
SEHB	77.2	77.2	78
SEO	358.1	358.1	359.8
SEO2	0.9	1.2	359.3
SES2	7.3	7.2	4.5
SHHB	326.3	326.2	326
SMKB	–	–	–
SMKB	–	–	–
SND	0.9	0.9	0.8
SNU	3.8	3.8	4.7
SNU	–	–	–

(continued)

Table 2.B.2: (continued)

Station ID	Orientation (°; minimization of H_{T1} based on harmonic decomposition & stacking with a 5-degree bin; Table 2.1)	Orientation (°; minimization of a mean of T-RFs; Table 2.1)	Orientation (°; minimization of H_{T1} based on harmonic decomposition & no stack in back azimuth)
SNU	3.5	3.9	4.5
TJN	1.6	1.5	0.6
ULJ2	358	358.1	358.2
ULL	9.7	9.4	11.6
ULLB	10.4	10.2	11.3
YKB	194.9	194.9	194.1
YNCB	309	309.1	309.1
YNCB	21	20.8	22.1
YSB	13.6	13.8	13.8

The orientation angle ranges from 0° to 360° with clockwise direction, and our values indicate the angles that we need to correct from the misaligned north.

Chapter 3

Seismicity and structure of Nazca Plate subduction zone in southern Peru

This chapter is published in

Lim, H., Kim, Y., Clayton, R. W., & Thurber, C. H. (2018). Seismicity and structure of Nazca Plate subduction zone in southern Peru. *Earth and Planetary Science Letters*, **498**, 334–347.

Abstract

We define subducting plate geometries in the Nazca subduction zone by (re)locating intra-slab earthquakes in southern Peru (14–18°S) and using previously published converted phase analysis results to clarify the slab geometry and inferred relationships to the seismicity. We also provide both *P*- and *S*-wave velocity models of the subducting Nazca Plate and mantle layer above the slab using double-difference tomography to understand upper-plate volcanism and subduction zone process. The double-difference constraints for determining the hypocenters and velocity model ensure high accuracy of the relative location of earthquakes with respect to velocity structure. The relocated seismicity shows a smooth contortion in the slab-dip transition zone for ∼400 km between the shallow (30°)-to-flat dipping interface to the northwest and the 30°-dipping interface to the southeast. We find a significant slab-dip difference (up to 10°) between our results and previous slab models along the profile region sampling the horizontal slab at a depth of ∼85–95 km. Robust features in both *P*- and *S*-wave tomography inversions are both arc-normal and along-arc velocity variations. In the arc-normal direction, all profile results show that the slab velocities beneath the forearc (down to a depth of ∼100 km) transition to higher velocities beneath the backarc (at ∼100–140 km depth). In the along-arc direction, velocities of the subducting flat slab are shown to be depressed compared to those of the normal-dip slab. In addition, high shear-wave velocities and low Vp/Vs are detected in the mantle layer above the flat slab, indicating its cold and dry environment. Such differences in the velocity structures for the slab and mantle wedge between the two regions may indicate different hydration states, which greatly affects the upper-plate structure of southern Peru.

3.1 Introduction

Along the South American margin between 2°S and 20°S latitude, the Nazca Plate subducts beneath the South American Plate, causing earthquakes, volcanism and upper-plate deformation. Earthquakes in this region exhibit complex rupture characteristics that are related to subducting asperities on the Nazca Plate (Bilek 2010). In particular, significant subduction-zone complexity in S. Peru has been previously attributed to the moderate-size (∼200 km ×18 km) Nazca Ridge and the Nazca fracture zone (Fig. 3.1). This region includes a transition in slab geometry from flat to normal from north to south (Cahill and Isacks, 1992; Hayes et al., 2012; Phillips et al., 2012; Phillips and Clayton, 2014; Kim and Clayton, 2015; Ma and Clayton, 2015; Bishop et al., 2017), decrease in magmatic activity towards the flat slab subduction (Ramos and Folguera, 2009), and variability in earthquake rupture patterns and coupling state (Chlieh et al., 2011). The flat slab system developed at 11.2 Ma when the buoyant ridge collided with the forearc at ∼11°S, and since that time the ridge has been migrating southward (Hampel, 2002). Its present location coincides with the southern end of the flat subduction segment, where the dense seismic arrays are available. In this study, we exploit array data from the Peru Subduction Experiment (PeruSE, 2013) and the Central Andes Uplift and Geophysics of High Topography (CAUGHT; Beck et al., 2010) experiment to better define the subduction zone geometry and constrain the plate boundary dynamics in the slab-dip transition zone at 14–18°S latitude and at 30–130-km depth (Fig. 3.1).

Earthquake locations typically provide a first-order estimate of the slab geometry, and by exploiting the relatively long South American earthquake catalog, various groups have constructed slab geometry models defined by earthquake locations determined from regional and teleseismic recordings (Figs 3.2, 3.3, 3.A.1, 3.A.2, and 3.A.3). The sparsity of the regional seismic network, however, results in a significant

disagreement among these models, particularly in the iso-depth contour lines of the Nazca slab at 50 and 100 km, which show the least coherence (Figs 3.2, 3.3, 3.A.1, 3.A.2, and 3.A.3). Furthermore, the correlation between the location of the volcanic front and the corresponding slab depth is neither clear nor consistent among the models (Figs 3.2, 3.3, 3.A.1, 3.A.2, and 3.A.3). The location of the plate interface beneath the stations is most directly resolved using methods based on teleseismic P-to-S converted phases (Phillips et al., 2012; Phillips and Clayton, 2014; Kim and Clayton, 2015; Ma and Clayton, 2015; Bishop et al., 2017). However, these types of analyses do not constrain the plate geometry between the two linear arrays (PE and PG; Fig. 3.1) in the region where the horizontally subducting Nazca slab transitions into a normal-dipping slab.

In this study, we focus on the region of flat-slab subduction where the Nazca Ridge subducts; the normal-dip subduction zone south of Nazca Ridge; and most importantly, the region between the two to examine along-strike variations in plate geometry and seismic velocities at depths of 30–130 km. We use regional earthquakes recorded from PeruSE, which consists of three dense seismic array lines surrounding the region between the flat and normal Nazca slab systems and four stations deployed along the coast, and two stations from the CAUGHT network (Fig. 3.1). Using images based on the relocated seismicity and double-difference tomography (Zhang and Thurber, 2003), we clarify the Nazca Plate geometry and inferred relationships to the subduction process, volcanism in the upper plate, and the occurrence of earthquakes.

3.2 Data and methods

3.2.1 Data and initial velocity model

We use the data recorded from the temporary seismic arrays in S. Peru (142 stations from PeruSE and 2 from CAUGHT) from July 2008 to April 2013 (Fig. 3.1).

Interstation spacing of PeruSE is 6–10 km for the PE, PG and PF lines and ∼75 km for the PH line (Fig. 3.1). We detect local earthquakes using *FilterPicker*, an automatic picking program that uses multiple frequency bands (Lomax et al., 2012). The program generates over 34 million picks, of which we select only those in which the difference in trigger times is less than the interstation distances divided by the apparent P-wave velocity of 7.0 km/s. Of the 451 earthquakes selected within the study region (3.B.1), we manually pick the P wave on vertical-component data and the S on the transverse-component data. The S phase effectively reduces a trade-off between origin time and the depth of intermediate-depth (> 100 km) hypocenters.

Initial hypocenters are determined by inverting the arrival times of the P and S phases and using the AK135 velocity model (Kennett et al., 1995) as an initial model. These arrival times are also used to obtain 1-D and 3-D velocity models of the region. Figs 3.A.4a and b and Table 3.B.2 show the optimal 1-D model derived in this study. The hypocenters are then determined based on Markov Chains Monte Carlo method (Myers et al., 2007).

3.2.2 Double-difference tomography

We apply the double-difference tomography method (Zhang and Thurber, 2003), which jointly inverts, for earthquake hypocenters, P-wave velocity (Vp) and S-wave velocity (Vs). The method minimizes residuals between the observed and calculated arrival times, and the differences between pairs of nearby earthquakes, employing an iterative damped-least-squares method. This method builds on the earthquake location procedure of Waldhauser and Ellsworth (2000), which utilizes the differential times of the P and S phases. 6,559 P- and 4,145 S-wave arrival times are used in the inversion, and 24,212 differential times measured using waveform cross-correlation are used to constrain the relative locations of the events. Nodes for the inversion are spaced 20 km apart laterally and placed on both the arc-normal trench-perpendicular

and along-arc trench-parallel directions (Figs 3.A.4c and d). The nodes are placed at 0, 30 and 50 km in depth for sampling the continental crust, and every 20 km in depth from 70 to 410 km for the mantle wedge and slab (Figs 3.A.4c and d). We determine and apply smoothing and damping parameters of 8 to stabilize the inversion process (Fig. 3.A.4e). The variance reduction for the inversion results shows that its rate of the decrease slows after 11 iterations (Fig. 3.A.4f). We then assess the robustness and distribution of the imaged velocity anomalies using checkerboard tests with noise-free data for Vp and Vs in the horizontal and vertical sections (Figs 3.A.5 and 3.A.5, respectively).

Lastly, we apply a 2-D and 3-D Gaussian filter to Vp, Vs and Vp/Vs at each inversion node to suppress small-scale heterogeneities. The standard deviations of the Gaussian function for a filter of 10 km-by-10 km and 0.1°-by-0.1° are used for the vertical and horizontal images, respectively, and 14 km for the 3-D visualization. The inversion results for the Vp, Vs and Vp/Vs models without the Gaussian filtering are shown in Fig. 3.A.7.

3.2.3 Construction of a slab geometry model

Our final slab model for the slab-dip transition zone is based on the double-difference algorithm (Zhang and Thurber, 2003). We incorporate receiver functions to improve the depth resolution of the plate interface in the vicinity of the station arrays because the teleseismic converted phases are sensitive to changes in Vs structure, and hence provide better depth resolution than that of the tomography. Our model shows both horizontal and vertical sections compared to that of previous models (Figs 3.2, 3.3, 3.A.1, 3.A.2, and 3.A.3).

The basis of the model construction is as follows. First we identify seismic and aseismic zones at a depth of 75–115 km (Figs 3.2, 3.3, and 3.A.8). We assume that at this depth range earthquakes occur at and below the slab-mantle interface. To

constrain the slab geometry in the slab-dip transition zone, the hypocenters within ±3 km from the 90-, 110- and 130-km depth are projected onto the horizontal planes at those depths, and the boundary between the seismic and aseismic zones are manually tracked (Figs 3.2d–f). We incorporate the slab-interface depth estimates from the receiver functions along the PF line (Phillips and Clayton, 2014) to constrain the slab depth beyond 130 km in depth. The earthquakes at depths shallower than 90 km are dismissed to avoid ambiguity in distinguishing between intra-slab and crustal earthquakes. For the flat-slab region, we incorporate the estimates from the receiver functions along the PG line (Ma and Clayton, 2015) in addition to our seismicity at 70–85 km to achieve enhanced resolution on the slab depth (with an equal weight on each) (Fig. 3.3). Second, we constrain shallow-depth slab geometries from the trench location (Bird, 2003) and receiver functions for the PH line (Kim and Clayton, 2015). Table 3.B.3 shows our slab depth model.

3.3 Results

We first describe the slab structure derived from the relocated seismicity (Figs 3.2 and 3.3) and then summarize features that are seen in the obtained velocity models using double-difference tomography (Zhang and Thurber, 2003) (Figs 3.5, 3.6, 3.7, 3.8, 3.A.9, and 3.A.10). A series of checkerboard resolution tests using more realistic structures based on our slab model (Figs 3.2, 3.3, and 3.A.11) in addition to the regular checkerboard pattern of opposite polarities (Figs 3.A.5 and 3.A.6) are performed to evaluate the resolution capability of the data set and sensitivity of the models. Fig. 3.4 demonstrates that the inversion fully recovers a thin (10–20 km) velocity structure.

3.3.1 Nazca slab geometry based on the double-difference method

Normal-dip slab region

In the normal-dip Nazca slab region, the relocated seismicity extends down to a depth of ∼240 km. The normal-dipping segment of the slab (along the profile F–F' of Figs 3.5f, 3.6f and 3.8f) subducts at a ∼30° dipping angle, which is consistent with that of previous models (Figs 3.A.1, 3.A.2, and 3.A.3; Cahill and Isacks, 1992; Gudmundsson and Sambridge, 1998; Hayes et al., 2012; Syracuse and Abers, 2006; Dougherty and Clayton, 2014). While the dip of the slab is similar in all the models in the normal-dip segment, depths to the top slab interface vary, with a difference up to 10 km from our result (Fig. 3.A.2f).

Flat slab region

Relocated hypocenters projected to profile D–D' in Figs 3.5d, 3.6d and 3.8d delineate the horizontally dipping slab. The seismicity extends laterally to ∼380 km from the trench and abruptly ceases. The absence of slab seismicity in the region between 71°W and 72.5°W is not an artifact of network coverage because the densely spaced PG-line stations are present near to this region (Fig. 3.1). Kumar et al. (2016) also observed an absence of seismicity along the projected location of the ridge. The seismicity is elevated by 10–20 km within 14.1°S to 14.7°S (a distance of 240–340 km from the trench) along the profile D–D' (Figs 3.5d, 3.6d, 3.8d and 3.A.2d), as also observed by Dougherty and Clayton (2014) and Ma and Clayton (2015), with a slight difference in the location.

We observe scattered seismicity at 70–100 km depth beneath the PG line, and this can be due to the topographical bulge that we observe (Figs 3.5d, 3.6d, 3.8d and 3.A.2d) and the uncertainty in relocated seismicity (e.g., errors in the manual picking of P and S). Our slab model beneath the PG line (profile D–D') does not exactly

follow the seismicity (e.g., Fig. 3.3b) because a subregion of the slab model beneath the PG line is also constrained using the previous receiver functions (Fig. 3.3; Ma and Clayton, 2015). Such difference can be attributed to inconsistent velocity model and/or uncertainty of relocated hypocenter. Furthermore, lateral velocity variation within the continental crust and along the top of the slab can also affect depth estimates of the local earthquakes as well as the top plate interface from the receiver function.

Slab-dip region between the normal-dip slab and flat slab

The relocated seismicity delineates the slab-dip transition geometry between the flat and normal subduction zone. The depth variations between the different models are up to 40 km down to 240 km in depth (Fig. 3.A.2). Based on the synthetic test and considering the realistic station-source geometry, we obtain an earthquake-depth uncertainty of < 10 km in the center of the arrays (Fig. 3.A.3).

Along the PG line (profile D–D'), the top slab interface in the subduction-zone backarc is approximately horizontal at a depth of 85–95 km (Figs 3.5d, 3.6d and 3.8d). The dip of the along-trench slab interface gradually increases towards the SE in the backarc. The transition between the normal and flat slab segments appears smooth based on the seismicity, and we find no sign of a slab tear from the trench to a distance of ∼420 km and down to a depth of 200 km (Figs 3.2, 3.3, and 3.A.2). This is consistent with results based on seismicity (Hasegawa and Sacks, 1981), regression analysis of regional seismicity (Dougherty and Clayton, 2014), and receiver functions (Phillips and Clayton, 2014) along the PF line, sampling the slab-dip transition zone.

3.3.2 3-D seismic velocity structure

Synthetic test results

The checkerboard test results for both *Vp* and *Vs* in the horizontal slices show that the resolution of the *Vp* and *Vs* estimates improves with depth and is stable down to a depth of 130 km (Figs 3.A.5 and 3.A.6). In particular, the resolution of the *Vp* and *Vs* estimates is good down to a depth of 90 km in examining the slab-dip variation along the trench near the coast (Figs 3.A.5 and 3.A.6). The *Vs* estimates show a similar pattern to that of the *Vp* estimates (Figs 3.A.5 and 3.A.6); however, they show reduced spatial resolution primarily because of the lower number of *S*-wave phase picks. However, we note that the resolution for *Vp* and *Vs* is sufficient in the region that covers both the subducting slab and mantle wedge above the slab. The resolution becomes somewhat limited between 130 km and 220–240 km depth, primarily because of the lack of seismicity at deeper depths.

We next explore more realistic input models and observe how well the inversion recovers them (Figs 3.2, 3.3a and 3.A.11). For this test, we use our slab model as an input, assign a 5% increase in *Vp* and *Vs* with respect to the initial 1-D model for the slab and test how sensitive the inversion is to the slab velocity structure. We note that the absence of a high-velocity anomaly along the flat slab region at 90 km (Fig. 3.A.11) represents a case for a topographical bulge on the slab, which is shown by the seismicity (Figs 3.3). The seismicity is elevated by 10–20 km from the horizontal plane (also noted in Section 3.4.1). We observe that an inversion recovers the fast-velocity anomaly reasonably well at a depth range of 50–110 km for both *Vp* and *Vs* (Fig. 3.A.11). The high-velocity anomaly for the flat slab in the backarc at 90 km is not well recovered (Fig. 3.A.11).

We then construct a model based on our slab geometry (Figs 3.2 and 3.3) and examine how sensitive the inversion is to the mantle-wedge velocity structure. Our

slab model (Figs 3.2 and 3.3), as well as receiver functions (Ma and Clayton, 2015; Bishop et al., 2017), indicate that the mantle layer is quite thin (< 20 km) between the overriding plate and the slab in the flat-slab region. We observe that the inversion is sensitive to a thin (10–20 km) structure, and the velocity recovery is moderate with noticeable vertical smearing in all profile images (Fig. 3.4).

P-wave velocity structure

The inversion results of Vp are presented with the top slab interface in Figs 3.5, 3.A.7a and 3.A.9. The estimates of nodes with sufficient ray coverage are enclosed by a green line in the figures. Figs 3.5 and 3.A.9 show the absolute value of Vp from the inversion in the vertical cross-section and horizontal slice views, respectively. Fig. 3.A.7a shows the inversion results in a horizontal slice without Gaussian filtering.

Several structural elements related to the Nazca slab and mantle layer can be identified from the inversion results. The Vp estimates for the slab (the imaged region below the top plate interface) down to a depth of 200 km along all profiles vary significantly in the vertical and lateral (arc-normal) directions, and overall show values between 7.4 to 8.6 km/s (Figs 3.5 and 3.A.9). In the arc-normal direction, all profile results show that the slab velocities beneath the forearc (down to a depth of 100 km) transition to higher velocities beneath the backarc (at a depth of 100–140 km). In the arc-parallel direction, we also observe relatively a low Vp within the slab along the profile D–D' and profile F–F', and a high Vp in between (profile E–E'). In particular, high Vp estimates (8.0–8.6 km/s) are observed along profiles B–B' (distance 180–420 km; Fig. 5b) and C–C' (190–350 km; Fig. 3.5c). Low Vp estimates (7.4–8.0 km/s) are observed along profiles A–A' (40–200 km at 7.4–8.0 km/s; Fig. 3.5a), B–B' (40–180 km at 7.4–8.0 km/s and 440–540 km at 7.8–8.0 km/s; Fig. 3.5b) and C–C' (100–180 km at 7.6–8.0 km/s and 320–480 km at 7.6–8.0 km/s; Fig. 3.5c).

The mantle layer corresponds to the imaged region between the base of the conti-

nental crust (Laske et al., 2013) and the top slab interface defined in our model (Figs 3.2 and 3.3). The *Vp* of the forearc mantle ranges from 7.2 km/s to 8.0 km/s (Fig. 3.5). The *Vp* above the flat slab in the forearc is 7.2–7.6 km/s (distance 170–220 km; Fig. 3.5d), 7.4–8.0 km/s in the slab-dip region (160–230 km; Fig. 3.5e), and 7.6–8.0 km/s in the normal-dip region (160–230 km; Fig. 3.5f). The *Vp* of the backarc mantle ranges from 7.4 to 8.4 km/s (Fig. 3.5). The *Vp* above the flat slab in the backarc is 7.4–7.7 km/s (330–400 km; Fig. 3.5d), 7.8–8.4 km/s in the slab-dip region (260–420 km; Fig. 3.5e), and 7.2–7.8 km/s in the normal-dip region (270–380 km; Fig. 3.5f).

S-wave velocity structure

The inversion results of *Vs* are presented in Figs 3.6, 3.7, and 3.A.7b. Figs 3.6 and 3.7 show the absolute value of *Vs* from the inversion in vertical cross-section and horizontal slice views, respectively, and Fig. 3.A.7b shows a horizontal slice view without Gaussian filtering. The spatial resolution of the recovered *Vs* is slightly less compared to the results of *Vp*, as also observed in the checkerboard test results (Figs 3.A.5 and 3.A.6). Regardless, we observe broadly similar patterns in the *Vp* results.

Similar to the *Vp* estimates, we observe a relatively low *Vs* within the slab beneath the PG (profile D–D') and PE (profile F–F') lines, and high *Vs* in between (profile E–E'). High *Vs* estimates (4.6–5.1 km/s) are obtained along profiles B–B' (distance 180–420 km; Fig. 3.6b) and C–C' (190–350 km; Fig. 3.6c). Low *Vs* estimates (4.2–4.6 km/s) are observed along profiles A–A' (40–200 km at 4.2–4.6 km/s; Fig. 3.6a), B–B' (40–180 km at 4.2–4.6 km/s and 440–540 km at 4.2–4.6 km/s; Fig. 3.6b) and C–C' (100–180 km at 4.4–4.6 km/s and 320–480 km at ∼4.6 km/s; Fig. 3.6c). These velocity anomalies are also observed along three trench-perpendicular profiles (Figs 3.6d–f). In addition, our *Vs* values at the dipping-slab segment at 90 km in depth (profile D–D') agree well with previous estimates (Ma and Clayton, 2014; Ward et al., 2016).

The *Vs* of the forearc mantle ranges from 4.2 km/s to 4.6 km/s (Fig. 3.6). The

Vs above the flat slab in the forearc is 4.2–4.3 km/s (distance 170–220 km; Fig. 6d), 4.5–4.6 km/s in the slab-dip region (160–230 km; Fig. 3.6e), and 4.3–4.5 km/s in the normal-dip region (160–230 km; Fig. 3.6f). The *Vs* of the backarc mantle ranges from 4.0 to 4.7 km/s (Fig. 3.6). The *Vs* above the flat slab in the backarc is 4.5–4.7 km/s (330–400 km; Fig. 3.6), 4.4–4.6 km/s in the slab-dip region (260–420 km; Fig. 3.6e), and 4.0–4.3 km/s in the normal-dip region (270–380 km; Fig. 3.6f).

P-to-*S* wave velocity ratio (*Vp/Vs*) structure

Vp/Vs is obtained by taking the ratio of the *Vp* and Vs estimates retrieved from the inversion. We note that in the inversion the *P*- and *S*-wave travel times are inverted simultaneously with the same damping factor. The resulting ray coverage for *Vp/Vs* is different from that of the *Vp* estimates because the number of *S*-wave arrival times is less than that for the *P*-wave. Because of differing data quality and distribution between the *P* and *S* data, *Vp/Vs* estimated from *Vp* and *Vs* can be difficult to interpret (Zhang and Thurber, 2003). Regardless of such a limitation, *Vp/Vs* provides an important constraint on the physical state of the imaged structure (i.e. the mantle wedge) in terms of temperature and/or composition. Our estimates for *Vp/Vs* are presented in vertical and horizontal slice views in Figs 3.8 and 3.A.10, respectively, and Fig. 3.A.7c shows a horizontal slice view without Gaussian filtering.

The *Vp/Vs* from the inversion shows an approximately similar pattern to values obtained for *Vp* and *Vs* (Fig. 3.8). The *Vp/Vs* of the forearc mantle ranges from 1.65 to 1.80 (Fig. 3.8). The *Vp/Vs* estimates above the flat slab in the forearc are 1.70–1.80 (distance 170–220 km; Fig. 3.8d), 1.65–1.75 in the slab-dip region (160–230 km; Fig. 3.8e), and 1.70–1.80 in the normal-dip region (160–230 km; Fig. 3.8f). The *Vp/Vs* of the backarc mantle ranges from 1.60 to 1.90 (Fig. 3.8). The *Vp/Vs* above the flat slab in the backarc is 1.60–1.70 (330–400 km; Fig. 3.8d), 1.80–1.90 in the slab-dip region (260–420 km; Fig. 3.8e), and 1.80–1.85 in the normal-dip region (270–380 km; Fig.

3.8f).

Crustal low-velocity zones

We identify several localized crustal low-velocity zones along different profiles beneath the PE, PF and PG lines (profiles F–F', C–C' and D–D', respectively; Figs 3.9a and 3.A.12). We confirm this as a low-velocity feature from the filtered seismic phases of the local earthquakes (Figs 3.9 and 3.A.12). The waveform record sections show either attenuated amplitudes of S phases or a complicated body-wave coda for waves passing through those zones (Figs 3.9 and 3.A.12).

The most prominent low-velocity zone is imaged beneath stations PG16–PG27 (Fig. 3.9). The Vs estimates are $<$3.6–3.8 km/s, which are a $<$8–10 % reduction with respect to our 1-D model. Ma and Clayton (2015) also detected this low-velocity zone from teleseismic P-to-S converted phases. Based on our results (considering 3.8 km/s contour values and less), its approximate dimension is $\sim$60 km (arc-normal direction) by $\sim$100 km (along-arc direction). The waveform record of one crustal earthquake at a depth of 30 km near the PG line shows a clear difference in amplitude of the S phase between the waveforms from the stations PG15–PG26 and PG28–PG45 (Fig. 3.9b). The amplitudes from stations PG15–PG26 appear to be substantially attenuated, and their raypaths pass through the low-velocity zone.

In addition, we observe a low-velocity zone (Vs of $\sim$3.8 km/s; 8% reduction beneath volcanoes; Sabancaya and Chachani; Fig. 3.1) along the PE line in a 30 km depth slice (Fig. 3.A.12a and b). The spatial dimension of this zone is $\sim$30 km based on the velocity contour (Fig. 3.7a), and it is coincident with a scatterer location that was discussed in an ambient noise cross-correlation study (Ma et al. 2013). Another low-velocity zone (Vs of $<$3.8 km/s) is observed beneath and near Quimsachata volcano (Fig. 3.1), which is $\sim$160 km from the volcanic front (Fig. 3.A.12c and d). The waveform record section along the PF line from a deep earthquake shows more

complicated S arrivals for stations PF32 and PF33, which pass through this crustal low-velocity zone (Fig. 3.A.12d). Its corresponding lateral dimension is estimated to be ∼5 km or less (Fig. 3.A.12c).

3.4 Discussion

In this study, we define the slab geometry down to a depth of 130 km by relocating the seismicity with the highest resolution and examine the slab-dip velocity transition using the inversion based on the double-difference algorithm. The tomography jointly inverts velocities and hypocenters and thus enables one to compare velocity anomalies directly using seismicity. There is a discrepancy between the velocity and hypocenter unless they are based on the same velocity model. Because the structural feature that we image can be quite thin (i.e. a <20-km-thick mantle layer above the flat slab; Fig. 3.4), a slight error in earthquake locations can lead to erroneous interpretation.

3.4.1 Nazca slab geometry based on seismicity

Flat slab region

In the flat slab region, the Nazca slab subducts at a 30° dipping angle down to 85–95 km depth, and then transition into generally flat geometry for ∼200 km (Fig. 3.3). Although our model domain is limited to a distance of ∼400 km from the trench, the flat slab extends further inland for approximately 100 km based on receiver functions (Phillips and Clayton, 2014; Ma and Clayton, 2015). We observe topographical bulge on the slab, elevated by ∼10–20 km from the slab surface at the localized zone (14.1°–14.7°S) (Figs 3.3, 3.5d, 3.6d, and 3.8d). Given this observation, the slab geometry following the topography of the continental Moho (Ma and Clayton, 2015) probably indicates the presence of an enhanced slab suction force (Tovish et al., 1978).

Although there are many factors contributing to the flat-slab development in Peru (e.g., Manea et al., 2017), the seismological evidence suggests that suction force plays an important role in maintaining the flat plate geometry in the vicinity of the subducting ridge because its buoyancy alone cannot fully explain the slab-flattening process (Kim and Clayton, 2015; Ma and Clayton, 2015). The constriction of the mantle layer between the flat slab and continental crust inhibits typical asthenospheric corner flow, leading to a large negative pressure that further decreases the dip angle of the slab (Ma and Clayton, 2015). The presence of a thick (Ryan et al., 2016; Bishop et al., 2017) and cold continental lithosphere (Currie and Hyndman, 2006) may act as a partial barrier to the mantle-wedge flow, resulting in a decreased pressure in the mantle-wedge corner (O'Driscoll et al., 2012).

The decreasing dip of the slab certainly indicates a decreasing influx of asthenospheric mantle above the slab. As a result, the slab flattening process significantly cools the system, particularly the upper lithosphere (e.g., Ramos et al., 2002), and a decreasing degree of partial mantle melting is expected at the arc location eventually shutting off arc magmatism in the flat slab region. Our seismicity results show that locations of the volcanoes correspond to the 85–105 km iso-depth contour of slab-surface beyond the flat slab region towards the SE (Figs 3.2 and 3.3).

Slab-dip transition zone

The relocated seismicity shows a smooth contortion in the slab-dip transition zone for ∼400 km between the 30°-to-horizontal dipping interface to the NW and 30°-dipping interface to the SE. This slab-dip transition zone is currently under an extensional stress regime based on the N–S and NW–SE extensional mechanisms of the regional earthquakes (Dougherty and Clayton, 2014). Based on our seismicity, we do not observe any sign of slab tear including upwelling of sub-slab asthenosphere (Figs 3.2, 3.3, 3.A.1, and 3.A.2). The slab is estimated to have experienced 10% strain in the

along-strike direction across this transition (Dougherty and Clayton, 2014).

We note that our study has an adequate resolution down to a depth of about 240 km (Figs 3.5, 3.6, and 3.8) for interpreting features associated with the dipping slab and mantle in the vicinity of the subducting slab. The teleseismic tomography study by Scire et al. (2016) covers a larger spatial region with a deeper depth resolution from ∼100 km to 660 km and shows a similar slab-dip transition zone from shallow (flat) subduction in the northern area to more normal dipping subduction to the south. In particular, their results show the transition from horizontally dipping to steeply dipping (∼70°) in the flat slab region. This region of the slab steepening corresponds with the predicted edge of the subducted Nazca Ridge, implying that the geometry of the Nazca slab is at least locally influenced by the presence of the ridge (Scire et al., 2016).

3.4.2 Seismic velocity variation based on tomography

The images of the *Vp*, *Vs* and *Vp/Vs* structures of the dipping slab are interpreted simultaneously with seismicity because these measurements provide different types of constraints and the use of all four structures can reduce ambiguity in interpretation. The velocities, particularly *Vp/Vs*, and earthquake locations are important for discussing variations in temperature and/or composition of the slab and also the mantle layer above the slab.

Nazca slab velocity variation

A relatively higher-velocity slab is imaged along all profiles examined (Fig. 3.1), and the velocity variations are substantial in the arc-normal and along-arc directions (Figs 3.5, 3.6, and 3.10a). The images along the arc-normal profiles show that the velocities of the slab in the backarc are elevated compared to those in the forearc. Such an arc-normal change in velocities can be attributed to a mineral phase change (e.g., eclogi-

tization) within the subducted crust (Peacock, 2004). Typically, teleseismic converted phases at the top of the slab can sharply constrain the basalt-to-eclogite transition and associated slab dehydration along the slab interface. In the normal slab-dip region, such converted signals at the top plate interface disappear at depth of ∼100 km in S. Peru (Phillips et al., 2012l) and 120 km in the central Andes (Yuan et al., 2000). In the flat-slab system, converted signals are well observed down to a depth of ∼80 km and up to ∼500 km from the coast (Phillips and Clayton, 2014; Ma and Clayton, 2015). Although tomography cannot sharply constrain the depth of the eclogitization, the observed arc-normal velocity variation (increasing velocities towards the backarc) can be somewhat constrained by the petrological transition because of changes in pressure (P) and temperature (T) conditions within the slab.

In the along-arc profiles, the flat slab is associated with relatively lower velocities than those of the slab-dip and the normal-dip slab regions (Figs 3.5, 3.6, and 3.10a), which is consistent with the converted phase analysis results (Kim and Clayton, 2015). The flat portion of the upper part of the oceanic crust was shown to be more fluid-rich than the normal-dip region by Kim and Clayton (2015). They observed considerable *Vs* reductions of ∼20–40% near the top plate interface of the flat slab at ∼40–120 km depths (which is ∼10–20% lower than the estimates for the normal slab-dip region). In fact, such velocities are far lower than expected for unaltered mid-ocean ridge basalt (MORB) or gabbro in the appropriate region of P–T conditions at that depth (Hacker et al., 2003), and cannot be fully explained without the presence of fluid (Kim and Clayton, 2015). Considering such a different hydration degree between the flat and normal slabs, the subduction of the ridge could be a critical factor in the supply of the fluid into the system (Kim and Clayton, 2015). Also, it may be that the subduction of the ridge retards the phase transition to a denser mineral (e.g., eclogite), and ultimately contributes to the buoyancy of the flat slab. The retardation of the phase transformation (i.e. the basalt-to-eclogite conversion) in the oceanic crust

is also supported by weakened P-to-S converted signals (Bishop et al., 2017).

The 90 km-depth slice from our inversion (Fig. 3.7d) shows the clearest image of the slab geometry. A faster Vs (4.5–4.6 km/s; Fig. 3.7d) corresponds to (1) a flat-slab segment with intense in-slab seismicity along the PG line (profile D–D') and (2) a dipping-slab segment in both the slab-dip transition and normal-dip zones that extends 250 km from the trench. Such high velocities and the pervasive presence of earthquakes in this high Vs region confirm the presence of the Nazca slab at 90 km depth along the PG line (profile D–D'). A slightly lower Vs (4.3–4.4 km/s) is also obtained in the flat slab region at the same depth (Fig. 3.7d). Earthquakes occur in the vicinity of this low Vs region. It appears that the velocities of the flat slab below the top plate interface laterally vary, and thus this observation points to the heterogeneous nature of the flat slab, which could be closely related to the phase transition and possibly influenced by the subducting ridge. Antonijevic et al. (2015) discussed low-velocity features in the NW region of the ridge (beyond our study region) as a possible slab tear. The relocated seismicity in this study is not consistent with a slab tear (Figs 3.6d and 3.A.8).

Velocities and Vp/Vs of the mantle layer above the Nazca slab

Upon subduction, the fluids are released from the subducting slab in a series of metamorphic reactions, and the flux into the mantle wedge modifies its chemical and physical properties. Such subduction-related hydration plays a significant role in controlling Vs within the upper oceanic crust and overlying mantle wedge, as evidenced in Kim and Clayton, 2015 and Ma and Clayton (2015) for S. Peru, and from the studies in central Mexico (Kim et al., 2013) and central Chile (Porter et al., 2012). The hydration process within the forearc mantle is closely related to serpentinization, which can drastically reduce the seismic velocity and density of the mantle while increasing Poisson's ratio (and Vp/Vs) (Hyndman and Peacock, 2003).

Generally depressed velocities and elevated Vp/Vs in the forearc mantle (Figs 3.5, 3.6, 3.8, and 3.10b) indicate an overall low degree of serpentinization in S. Peru, compared to estimates from other subduction zones (e.g., Alaska-Aleutians (10–20%) and Cascadia (<50–60%) beneath forearc and/or active arc) (Hyndman and Peacock, 2003). The low degree of serpentinization in S. Peru can be attributed to slow dehydration of the slab because of relatively old age of the oceanic plate (Abers et al., 2017). The degree of serpentinization in the flat slab, the slap-dip and the normal-dip regions are 10–30%, 0–20% and 5–15%, respectively (Hyndman and Peacock, 2003). Relatively higher degree of mantle serpentinization in the flat slab region than that in the other regions can be attributed to hydrous compositions in the subducting ridge and metasediments (Kim and Clayton, 2015).

The key features in our velocity models are the relatively high Vs (4.5–4.7 km/s) and low Vp/Vs (1.60–1.70) in the thin mantle layer above the flat slab in the backarc (Figs 3.6, 3.8, and 3.10b). In the flat slab region, Currie and Hyndman (2006) mentioned the presence of a notably cool backarc mantle. Ma and Clayton (2015) also imaged the high-velocity mantle above the initial half of the flat slab and normal velocity values on the remainder of the flat-slab segment. Similar values to ours are observed in central Chile, where the Juan Fernandez Ridge is subducting (Porter et al., 2012), and Wagner et al. (2006) suggested that the high Vs (4.6–4.7 km/s) and low Vp/Vs (1.64–1.74) above the central Chile-Argentina flat slab cannot be modeled using any hydrated composition. In both flat-slab systems where the ridge subduction is involved, the composition of the mantle is probably enhanced by the region's low geotherm, and point to seismic properties of dry Mg-rich peridotite and orthopyroxene enrichment (e.g., Wagner et al., 2006,0; Qian et al., 2018). For orthopyroxene enrichment in the mantle, a large quantity of silica must be added to the mantle (Wagner et al., 2008) and the source for this silica would be the metasediments and subducted crust (Nazca Ridge) in S. Peru (Kim and Clayton, 2015). This process

coincides well with the cessation of arc volcanism at the surface.

We note that our velocity and Vp/Vs estimates can be alternatively explained by the anisotropy of the mantle peridotites (Hacker and Abers, 2012). Our estimates can be biased by anisotropy in mantle rock fabric or by the raypaths through the mantle, leading to relatively high Vs and/or low Vp compared with isotropic averages (Hacker and Abers, 2012). Local S-wave splitting measurements suggest that mantle above the flat slab appears to be anisotropic, with ∼4% anisotropy in a ∼30 km-thick mantle layer (Eakin et al., 2014). This anisotropy estimate is explained by the lattice-preferred orientation of olivine (Eakin et al., 2014), and thus we cannot rule out the possibility for the contribution of seismic anisotropy to our estimates.

The observed low Vs (4.0–4.3 km/s) and high Vp/Vs (1.80–1.85) above the normal-dip slab in the backarc indicate partially molten state of the mantle, which can be attributed to the arc magmatism. The temperature of the subarc mantle is 1100–1300°C at 60–120 km in depth (Currie and Hyndman, 2006).

Presence of crustal low-velocity zones associated with past and present volcanism

Crustal low-velocity zones are identified in the PG, PF and PE lines (profiles D–D', C–C' and F–F', respectively) from both our images and also raw waveform data showing either changes in S-phase amplitudes or complicated body-wave coda primarily because of different path effects (Figs 3.9, 3.10c, and 3.A.12). Such observed seismic anomalies can be closely associated with the presence of partial melt related to past or present volcanism. In particular, the imaged low velocities at the PE and PF lines (Figs 3.10c and 3.A.12) can be associated with present-day volcanism because of their close proximity to active volcanoes present (Sabancaya and Chachani along the PE line; Quimsachata along the PF line). Finally, the most prominent low-velocity zone is observed in the forearc of the flat slab region along the PG line (Figs 3.9 and 3.10c).

Although this region is not coincident with current volcanism, this imaged seismic anomaly represents molten rocks related to volcanism during the steepening of the Oligocene flat slab beneath the Altiplano plateau (Ma and Clayton, 2015).

3.5 Conclusions

We image the Nazca Plate subduction zone system in S. Peru by relocating intra-slab earthquakes and inverting for seismic velocities. For the images, we use data from seismic arrays that were deployed to target geophysical characterization of the subduction system in the slab-dip transition zone between the flat and normally dipping segments of the Nazca Plate. Relocated seismicity from the inversion based on the double-difference method suggests a smooth contortion of the slab along the transition from 30°-to-flat-to-normal subduction. In addition, the slab elevates, following the continental Moho (Ma and Clayton, 2015), in the flat slab region, adding another force for flattening (suction) in addition to the buoyancy of the Nazca Ridge. The slab suction force plays an important role in maintaining the flat plate geometry in the vicinity of the subducting Nazca Ridge because its buoyancy alone cannot fully explain the slab-flattening process. Notable features in the inversions for the flat slab region are the relatively lower velocities for the flat slab and the high Vs and low Vp/Vs in the thin mantle layer in the backarc. The lower slab velocities suggest that the subduction of the Nazca Ridge retards the phase transition to a denser mineral (e.g., ecologite), and contributes to the buoyancy of the flat slab. An observed high Vs and low Vp/Vs in the thin mantle layer above the flat slab at ∼60–85 km in depth may reflect cool conditions and possible chemical alteration via slab-derived fluids, as evidenced in the Chilean flat-slab region. The interaction of slab-derived fluids with the overlying mantle layer influences the overall slab dynamics and the cessation of upper-plate volcanism in the flat slab region.

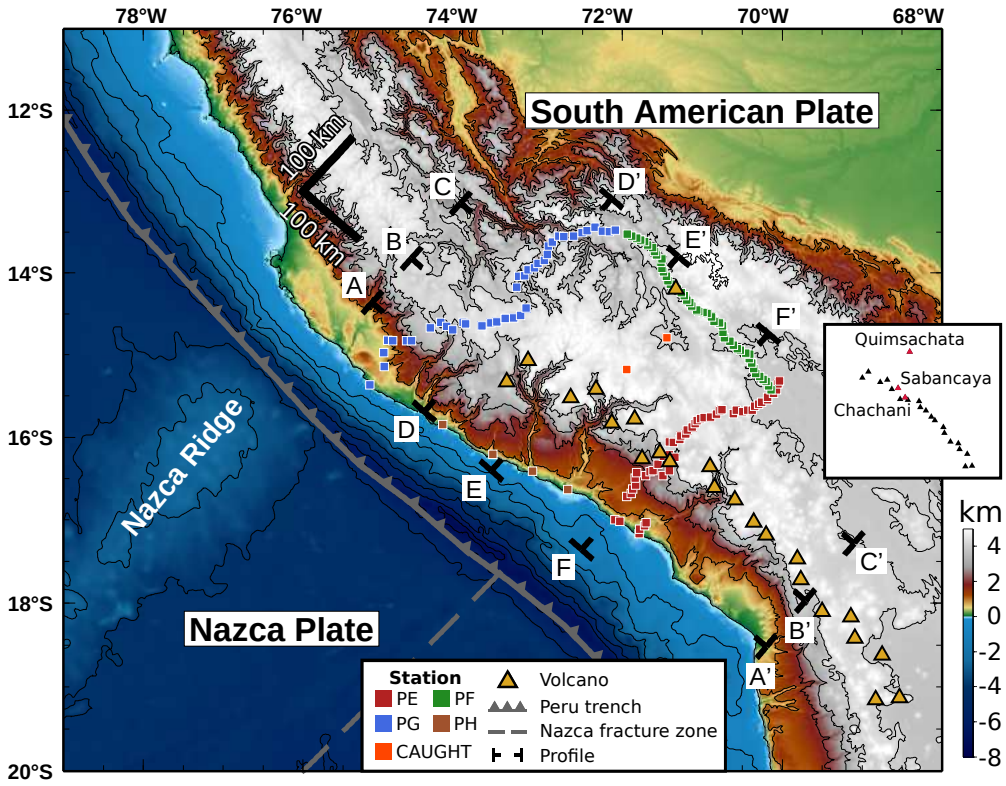

Figure 3.1: Topographic-bathymetric map of the study region. Seismic data used in this study are from Peru Subduction Experiment (PeruSE, 2013) and Central Andes Uplift and Geophysics of High Topography (CAUGHT). The topography and bathymetry are contoured with 1,000 m interval. Inset indicates the locations of volcanos Quimsachata, Sabancaya, and Chachani.

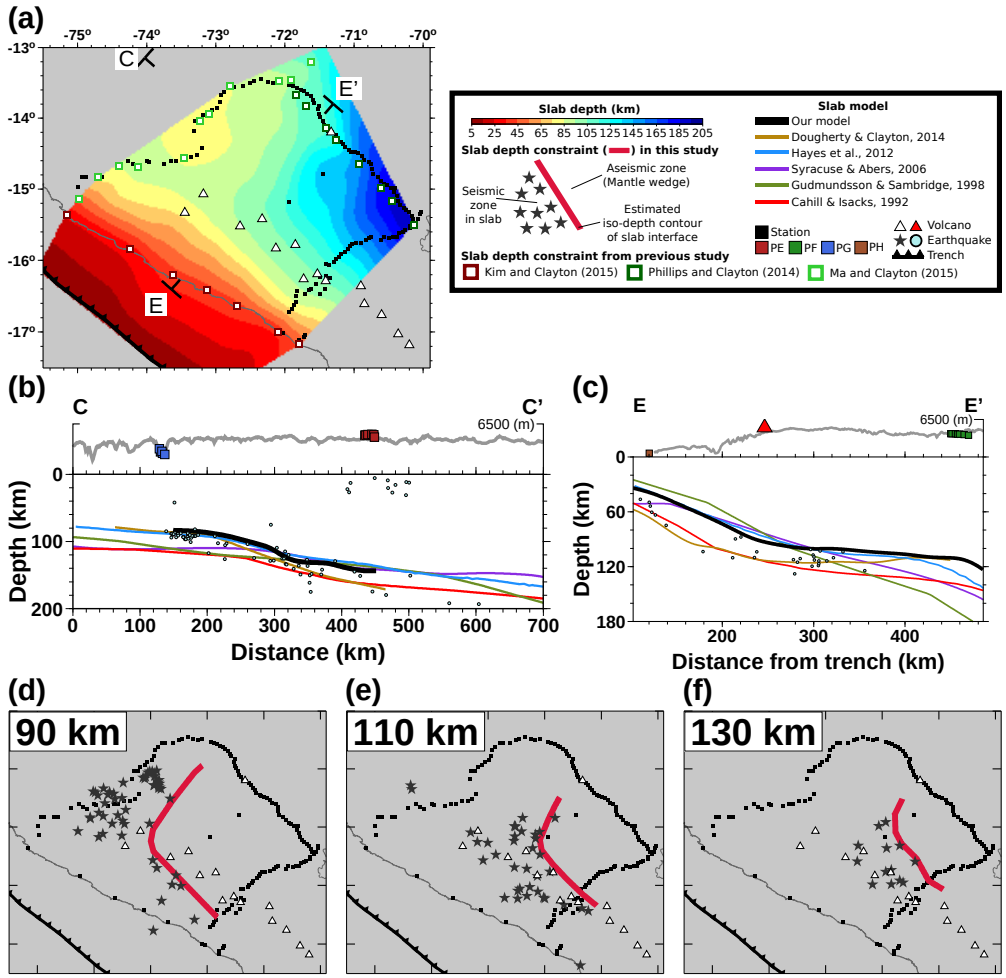

Figure 3.2: The model construction for the top slab interface in the slab-dip transition zone and the normal slab-dip zone. (a) Our final slab model. (b) Comparison with previous slab models (see the legend for references) along the trench-parallel profile (C–C' in Fig. 3.1). (c) Comparison with previous models along the trench-perpendicular profile (E–E' in Fig. 3.1). The model in the slab-dip transition zone is constrained from the iso-depth contour of the slab interface from the relocated earthquakes at the depth of (d) 90 km, (e) 110 km and (f) 130 km. See Fig. 3.A.9 for seismicity plotted on a map view with a depth interval of 5 km.

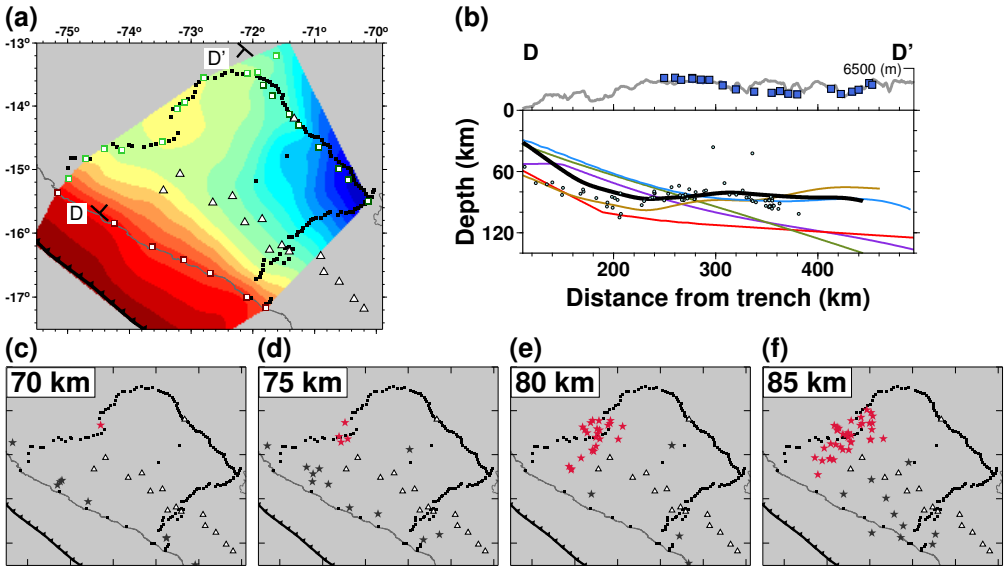

Figure 3.3: The model construction for flat slab region. (a) Our final slab model. (b) Comparison with previous slab models (see the legend in Fig. 3.2 for references) along the trench-perpendicular profile (D–D' in Fig. 3.1). The slab geometry is constrained by incorporating both receiver function result (Ma and Clayton, 2015) and iso-depth contour based on relocated seismicity with an equal weight on each. The iso-depth contour of the slab interface is obtained from the relocated earthquakes at the depth of (c) 70 km, (d) 75 km, (e) 80 km and (f) 85 km. Red stars indicate earthquakes that are used to constrain the slab geometry at the corresponding depth along the D–D'. See Fig. 3.A.9 for seismicity plotted on a map view with a depth interval of 5 km.

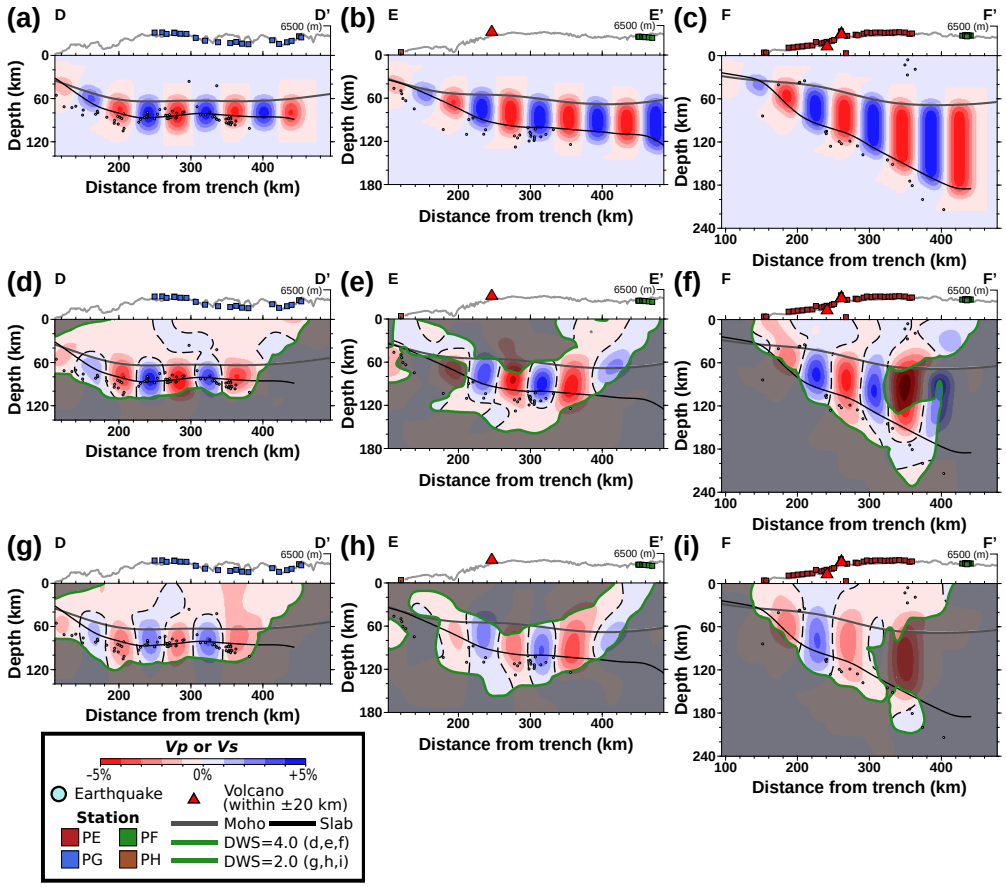

Figure 3.4: The recovery test results for the mantle structure between the continental crust (Crust 1.0 model; Laske et al., 2013) and the subducting Nazca slab using our slab model. (a–c) Input velocity pattern which constitutes alternating flat cuboids parallel to the trench with ±5% relative velocity. (d–i) Recovered *Vp* (d–f) and *Vs* (g–i) models. Images along the profile D–D' (Fig. 3.1) are shown in (a), (d) and (g), profile E–E' (Fig. 3.1) in (b), (e) and (h), and the profile F–F' (Fig. 3.1) in (c), (f) and (i).

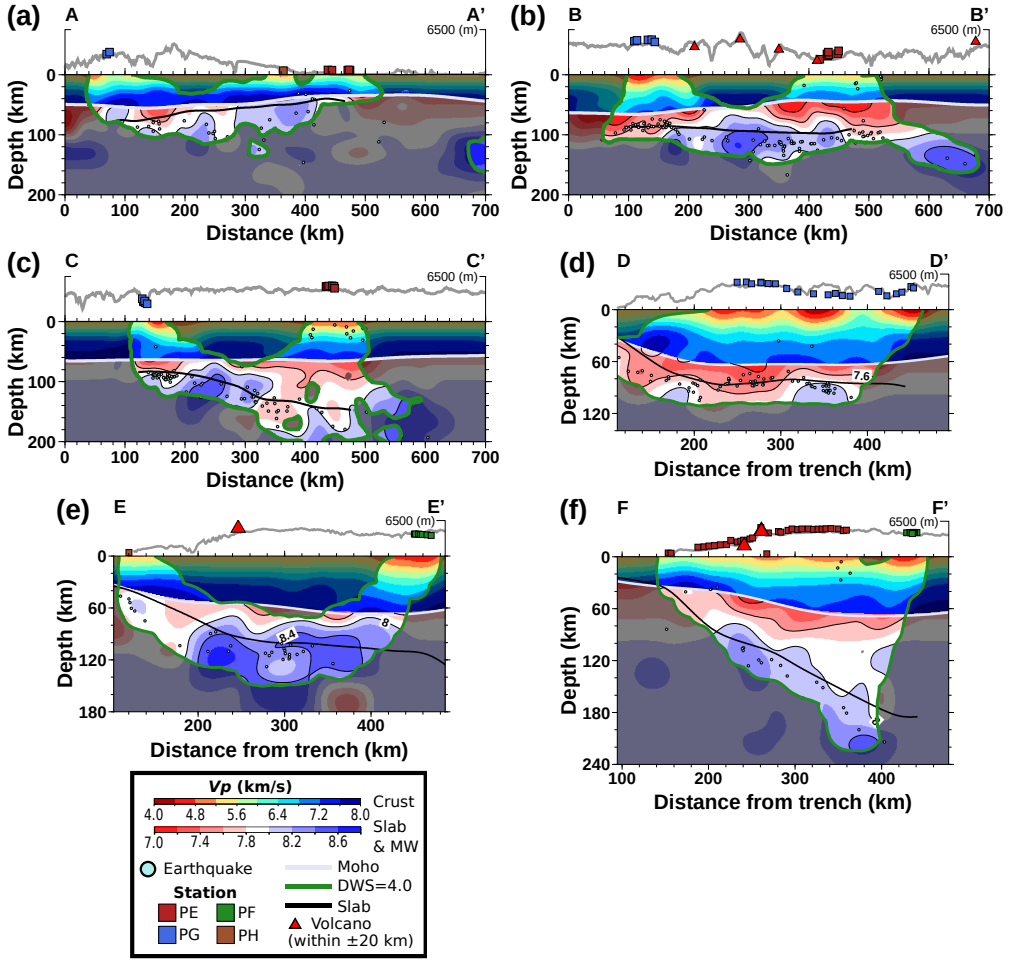

Figure 3.5: *P*-wave velocity in cross-section view along trench-parallel profiles (a) A–A', (b) B–B', and (c) C–C' and arc-normal trench-perpendicular profiles (d) D–D', (e) E–E' and (f) F–F' for which the locations are indicated in Fig. 3.1. The velocity is moving-averaged from the result of the inversion with Gaussian filter of 10 km and 10 km in the horizontal distance and depth. The top plate interface is retrieved from our slab geometry model in Fig. 3.2. Moho from Laske et al. (2013). Note that the ray density is separately computed through the derivative weight sum (DWS), which is a weighted measure of the total ray length close to a node in the inversion grid. The DWS is set as 4 for *P*-wave data.

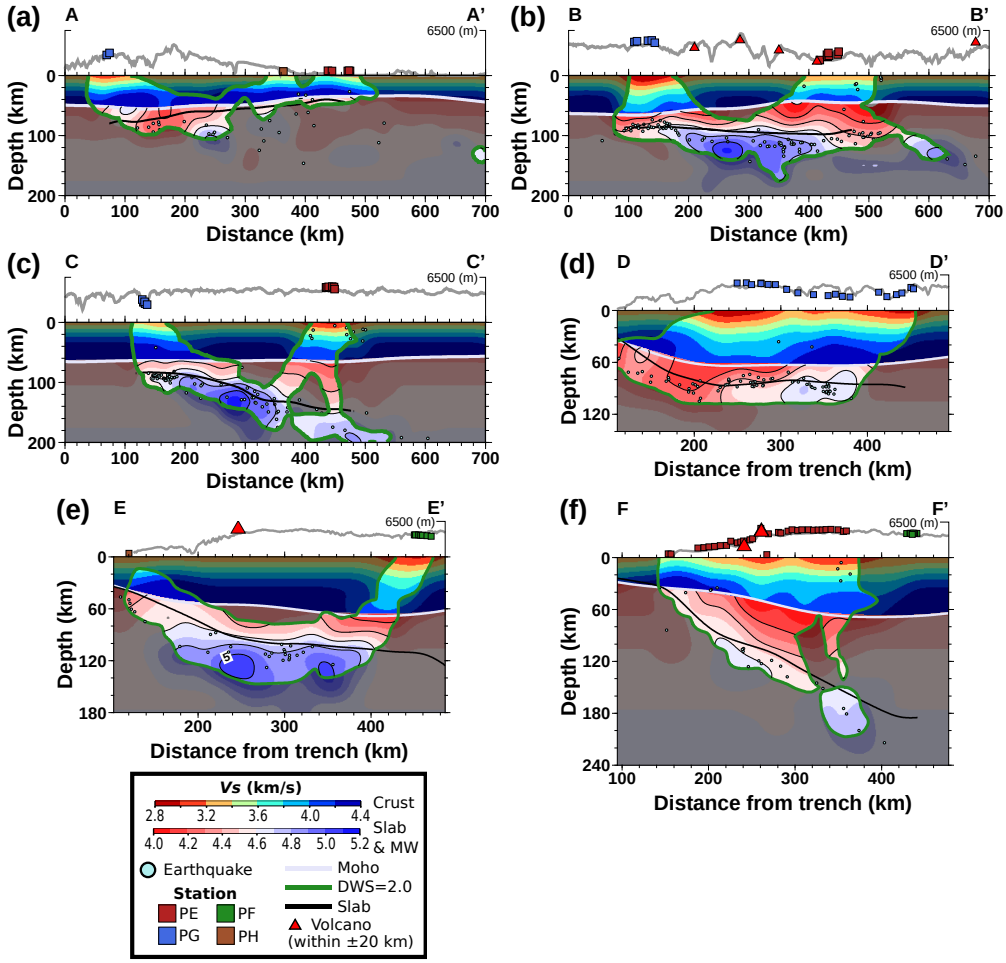

Figure 3.6: S-wave velocity in cross-section view along trench-parallel profiles (a) A–A', (b) B–B', and (c) C–C' and arc-normal trench-perpendicular profiles (d) D–D', (e) E–E' and (f) F–F' for which the locations are indicated in Fig. 3.1. The velocity is moving-averaged from the result of the inversion with Gaussian filter of 10 km and 10 km in the horizontal distance and depth. The top plate interface is retrieved from our slab geometry model in Fig. 3.2. Moho from Laske et al. (2013). Note that the DWS is set as 2 for this S-wave data.

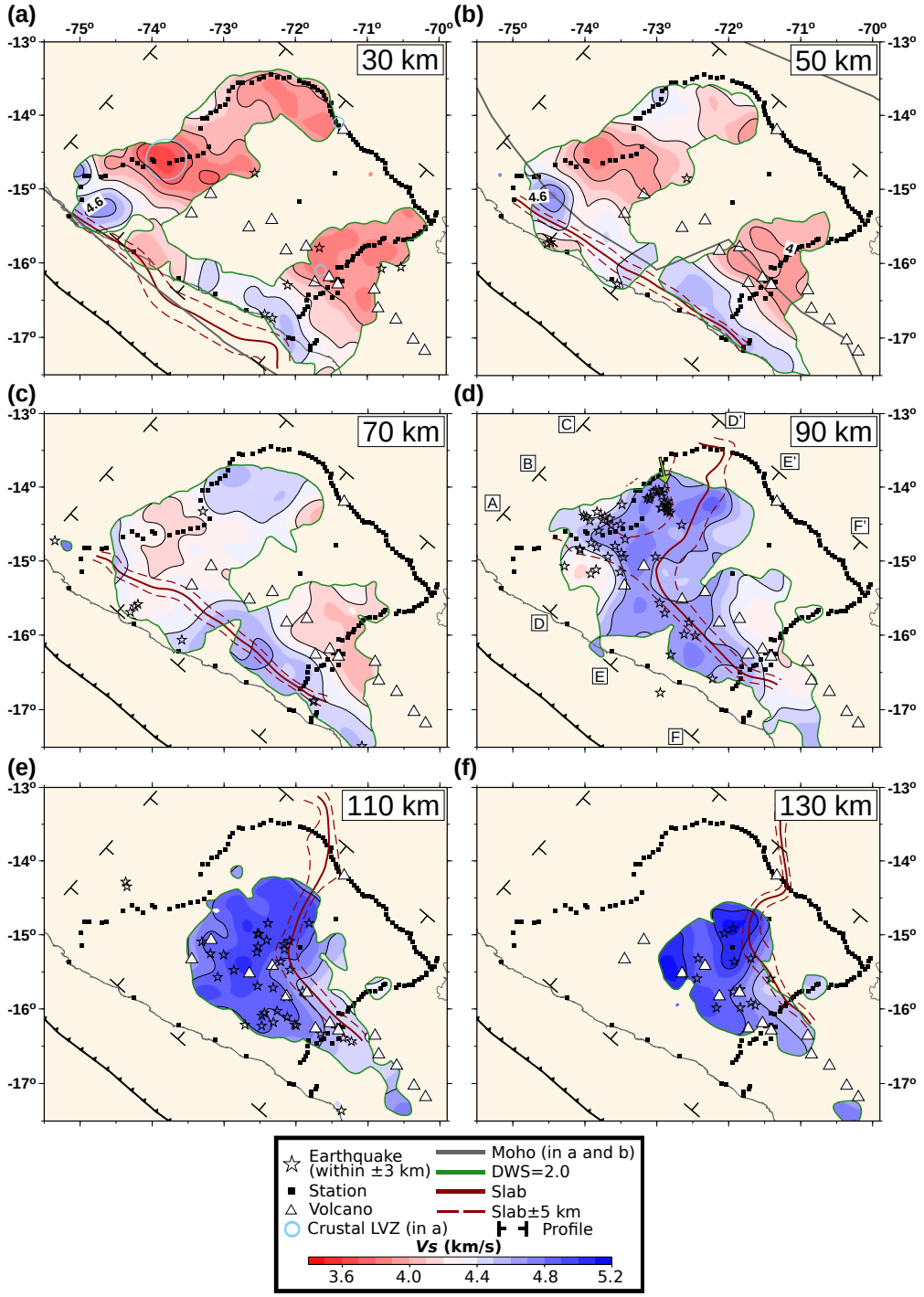

Figure 3.7: Horizontal slices of S-wave velocity at depths (a) 30, (b) 50, (c) 70, (d) 90, (e) 110 and (f) 130 km. (continued)

Figure 3.7: (continued) The Gaussian filter with standard deviation of 0.1°-by-0.1° is applied for simplicity. LVZ—Low velocity zone. An arrow in a panel (d) indicates the region where we observe no slab seismicity at 71°W and 72.5°W longitude.

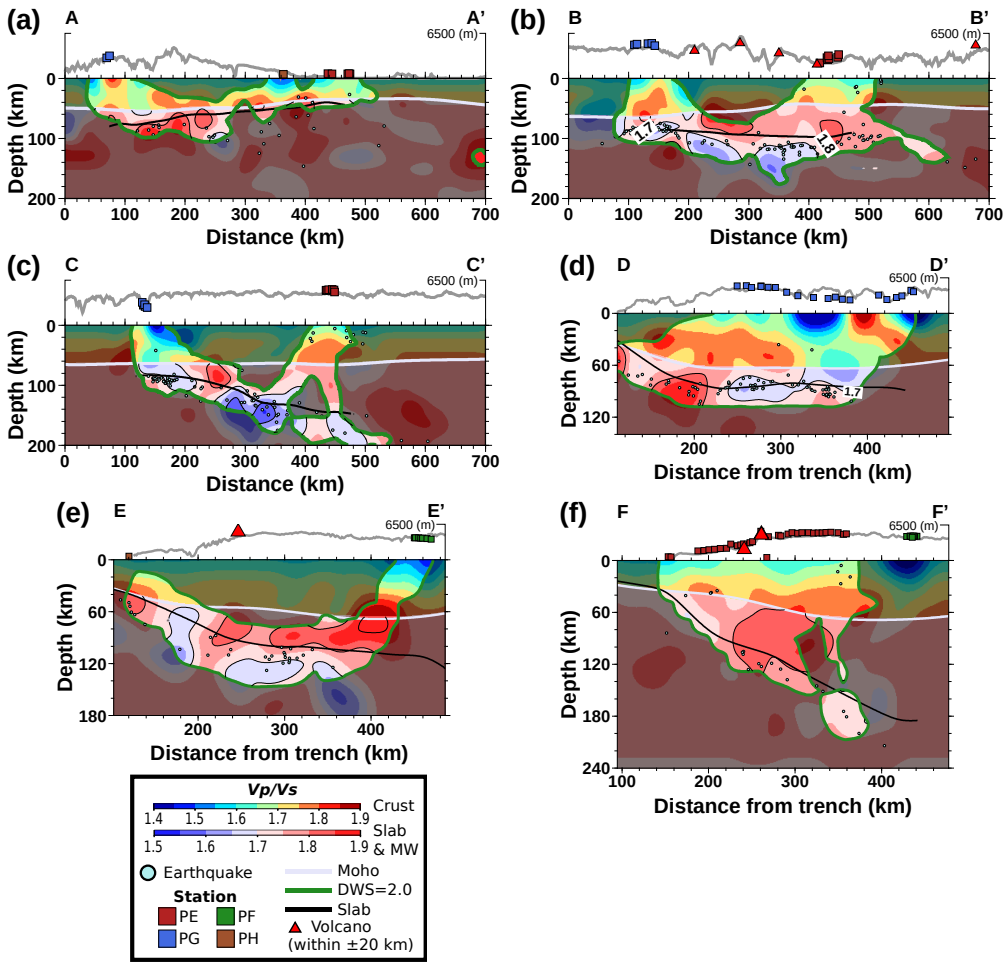

Figure 3.8: *Vp/Vs* in cross-section view along trench-parallel profiles (a) A–A', (b) B–B' and (c) C–C' and arc-normal trench-perpendicular profiles (d) D–D', (e) E–E' and (f) F–F' for which the locations are indicated in Fig. 3.1. The velocity is moving-averaged from the result of the inversion with Gaussian filter of 10 km and 10 km in the distance and depth. The top plate interface is retrieved from our slab geometry model in Fig. 3.2. Moho from Laske et al. (2013). Note that the contour of the DWS is same with that in the *Vs*. See Fig. 3.A.10 for the *Vp/Vs* estimates in a horizontal slice.

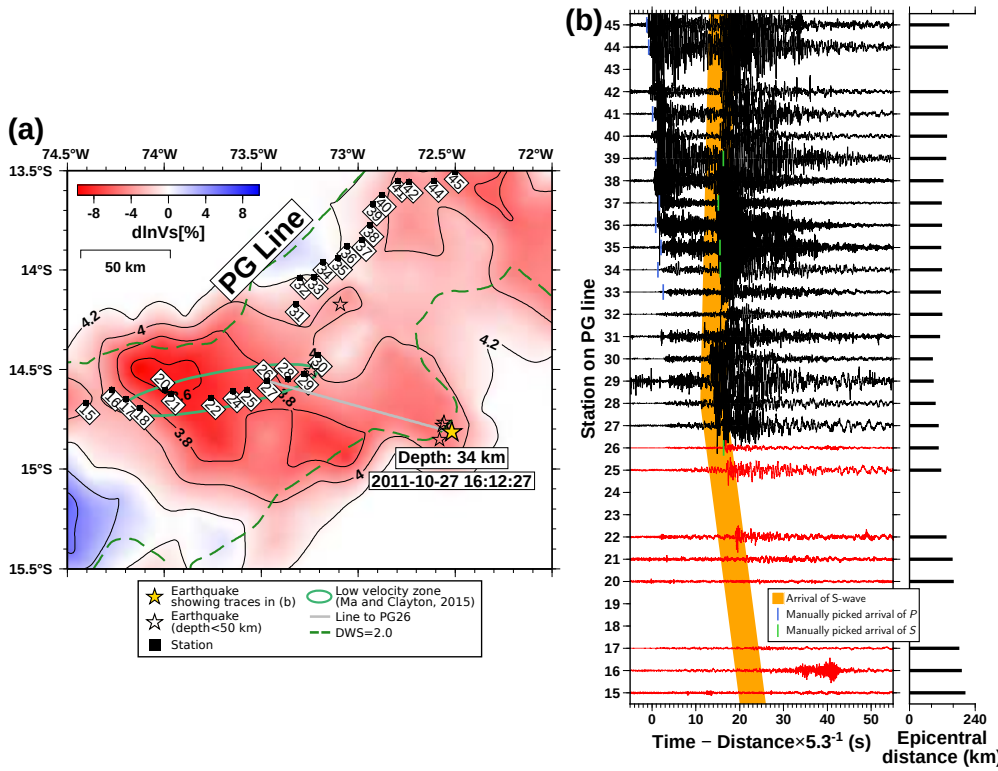

Figure 3.9: Presence of crustal low-velocity zone (LVZ) on the normal-dip subduction zone at a depth of 30 km along the PG line. (a) S-wave velocities without Gaussian filtering at 30 km depth along the PG line. (b) Transverse-component record section of the local earthquake recorded from the PG stations. The highpass filter is applied at 0.25 Hz. A thick orange line in the record section highlights the sudden change in amplitude of S phase, which indicates different path effects due to the LVZ within the continental crust. Traces from stations PG15–PG26 are indicated in red, and their amplitudes are substantially attenuated. See Fig. 3.A.11 for other LVZs along the PE and PF lines.

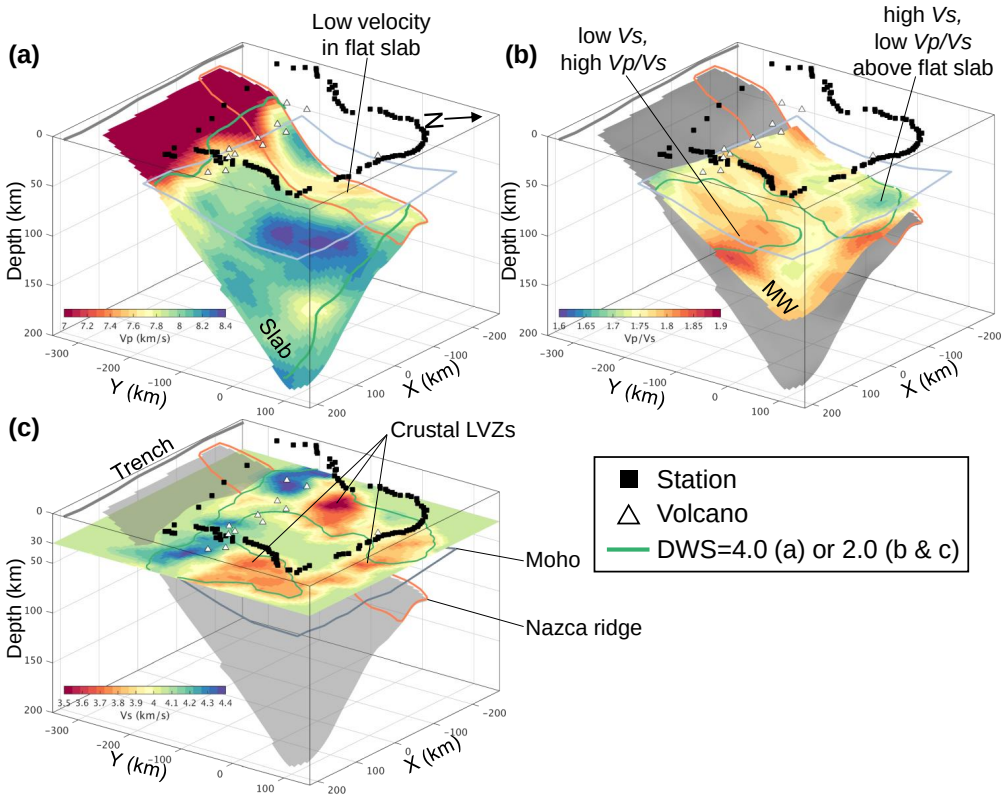

Figure 3.10: 3-D diagram of Nazca Plate subduction system based on our tomographic models. (a) *Vp* structure for Nazca slab which is sliced at 5 km below the top plate interface from our slab model. (b) *Vp/Vs* structure for mantle layer above the subducting slab. (c) *Vs* crustal structure at 30 km depth slice. Note that there is a vertical exaggeration. The approximate shape and location of the Nazca Ridge are taken from Hampel, 2002. 3-D Gaussian filter is applied to (a) and (b) before slicing velocity models. Moho from Laske et al. (2013). LVZ—Low velocity zone. MW—Mantle wedge (layer).

Appendices

3.A Supplementary materials (figure)

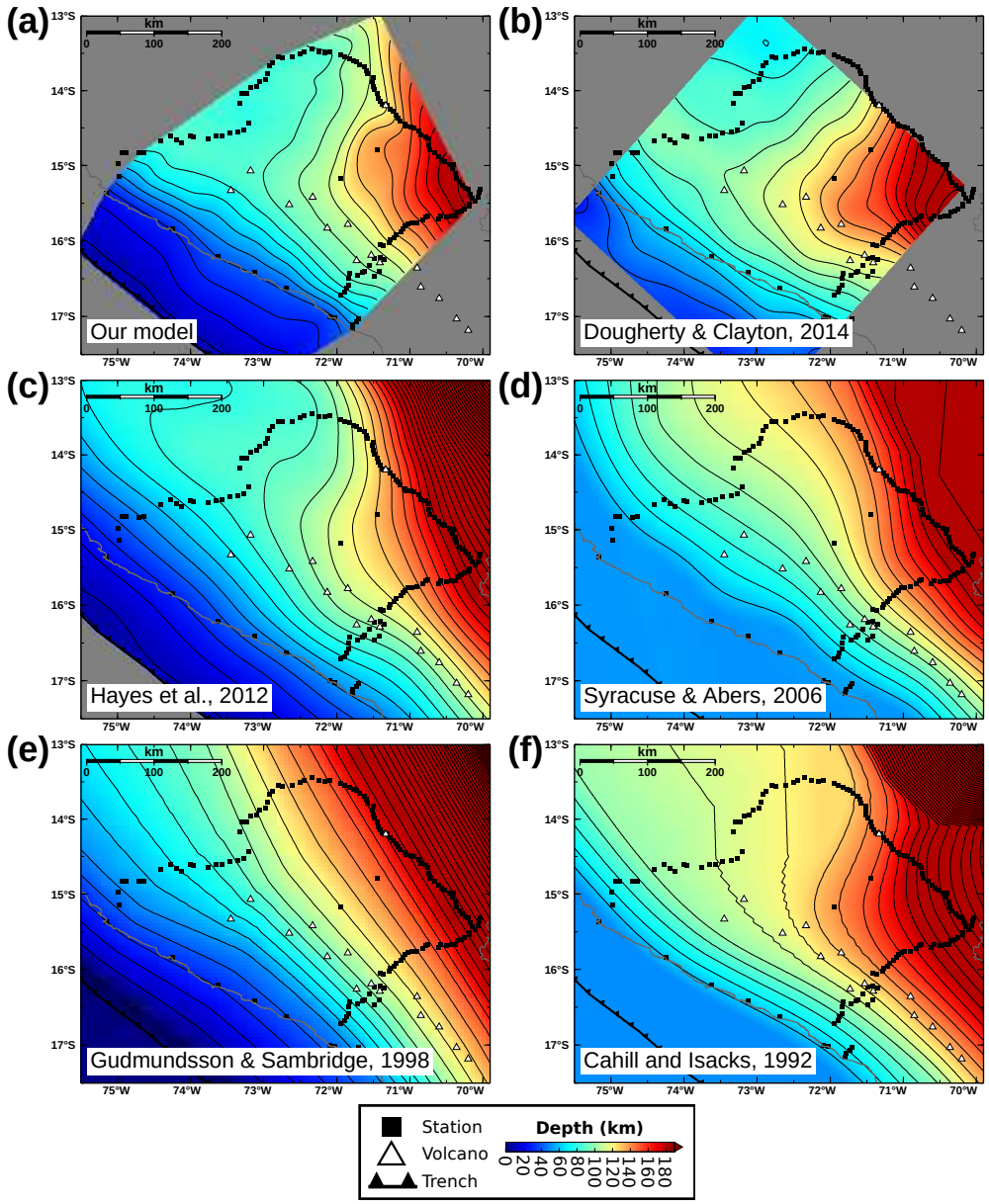

Figure 3.A.1: Comparison of previous slab geometry models with our model based on the relocated seismicity. Interval of contour is 10 km.

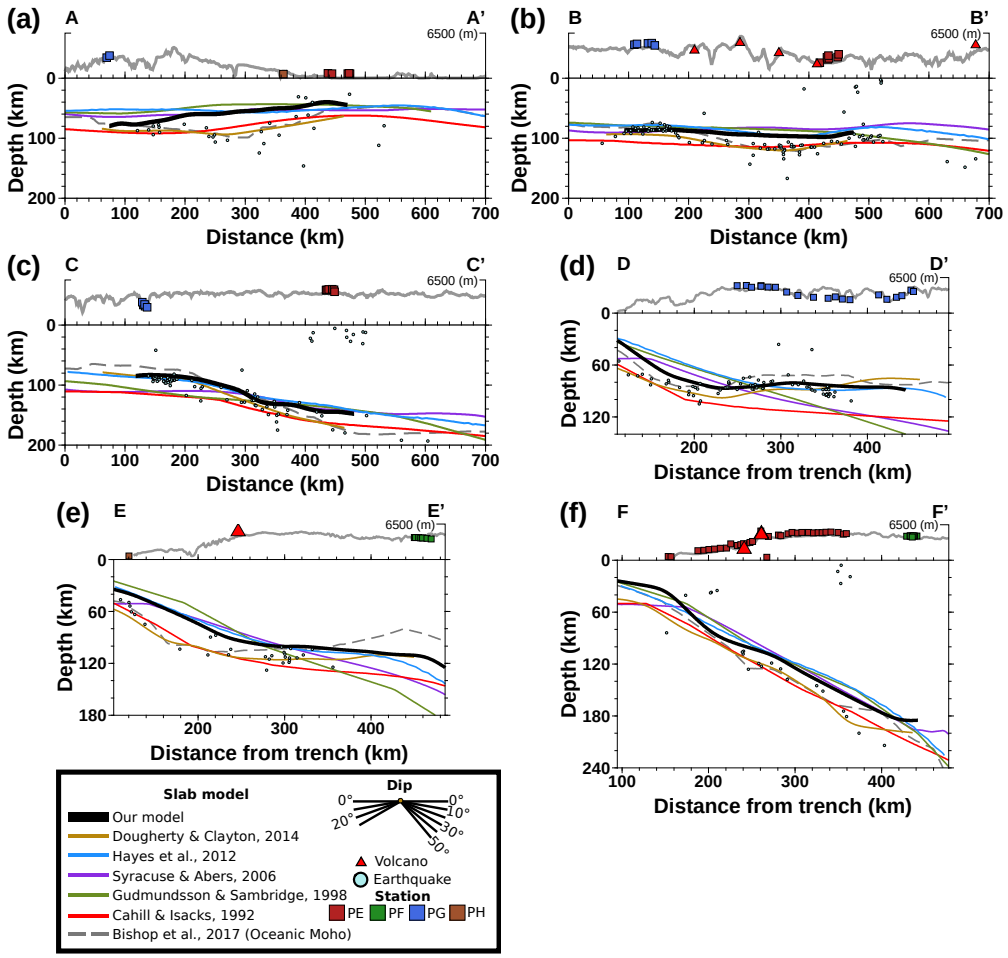

Figure 3.A.2: Comparison of previous slab geometry models with our model in a depth view along trench-parallel profiles (a) A–A', (b) B–B' and (c) C–C' and arc-normal trench-perpendicular profiles (d) D–D', (e) E–E' and (f) F–F' of which locations are indicated in Fig. 3.1.

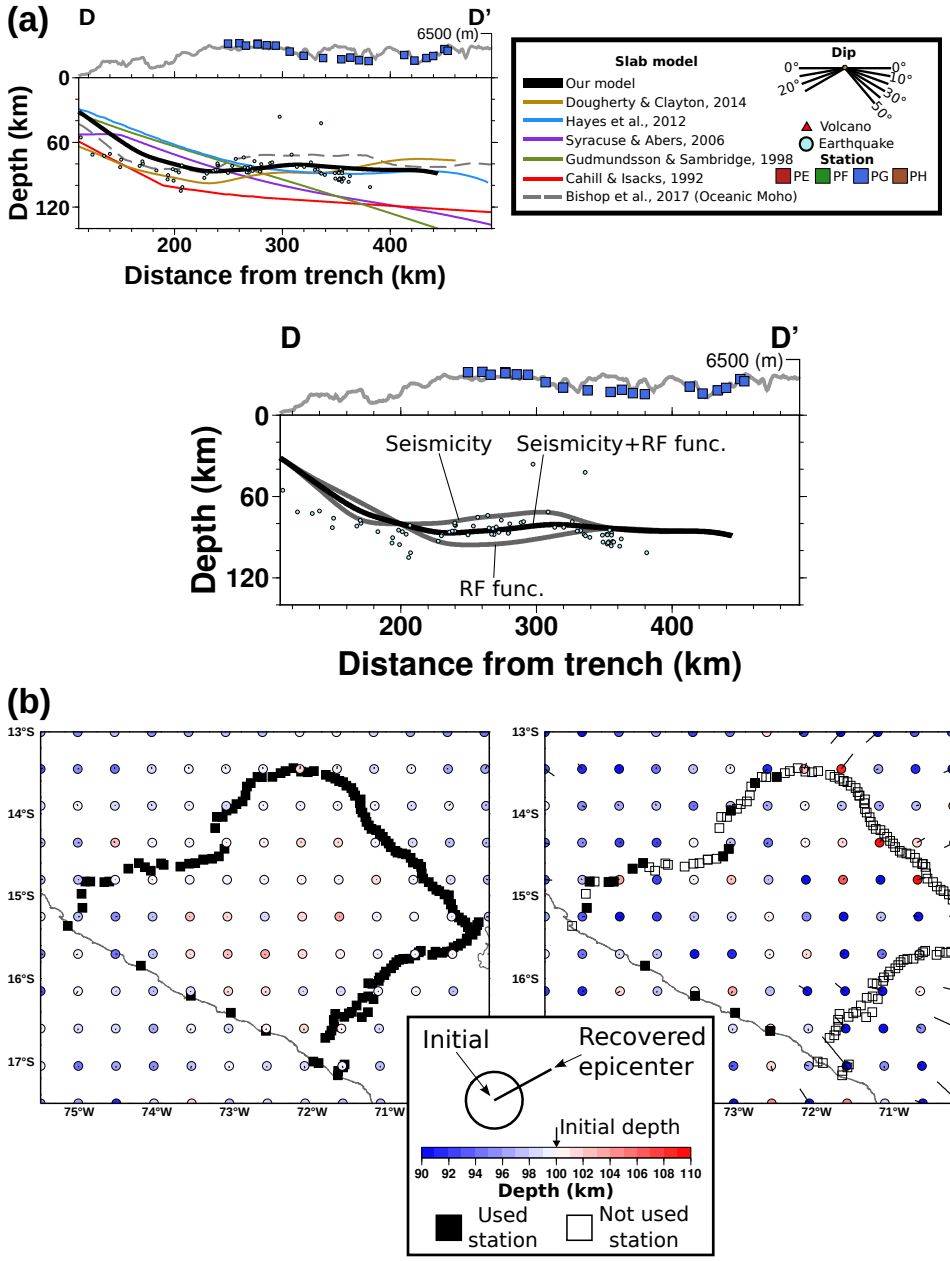

Figure 3.A.3: Slab geometry in the flat slab region (a) and synthetic test results showing the uncertainty in the hypocenter locations (b). (a) The top plate interface constrained by (1) receiver functions (Ma and Clayton, 2015) and (2) both receiver function and relocated seismicity (with an equal weight on each). (continued)

Figure 3.A.3: (continued) (b) Recovery test of the hypocenters with synthetic arrival times to which Gaussian random noise with standard deviation of 0.2 s are added. [Left] Results using synthetic data from all stations. [Right] Results considering a realistic station and earthquake distribution. Note that we took an earthquake located at the center of the arrays.

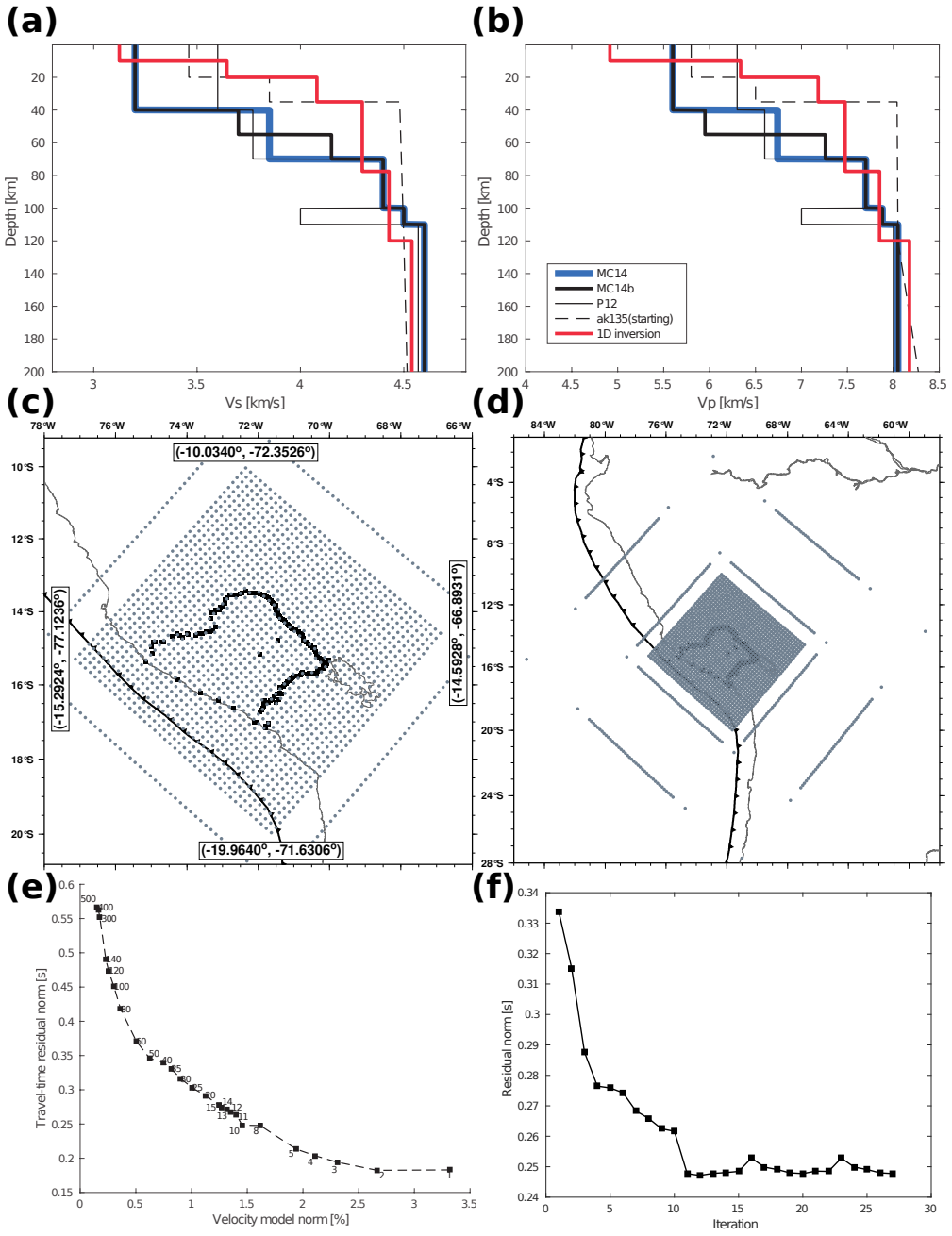

Figure 3.A.4: 1-D velocity models and parameters for inversion. (a) 1-D S wave velocity (Vs) and (b) P wave velocity (Vp) models (see Table 3.B.2 also). (continued)

Figure 3.A.4: (continued) The references for the different models are as follows: MC14 (Ma and Clayton, 2014); MC14b (Dougherty and Clayton, 2014); P12 (Phillips et al., 2012); AK135 (Kennett et al., 1995). Our final 1-D model is shown in red. (c) Nodes in main domain of the inversion. The grid nodes of 40-by-40 are placed every 20 km distance. (d) Enlarged map showing the nodes. The nodes are placed at 0, 30, 50, 70, 90, 110, 130, 150, 170, 190, 210, 230, and 250 km depth. (e) L-curve showing the travel-time residual norm versus the velocity model norm from our final 1-D velocity model. A number next to each square point denotes both smoothing and damping parameters used in the inversion. (f) Trade-off curve for travel-time residual as a function of iteration. After 11 iterations the time variance decreases only slightly. The optimum number of iteration is chosen as 11.

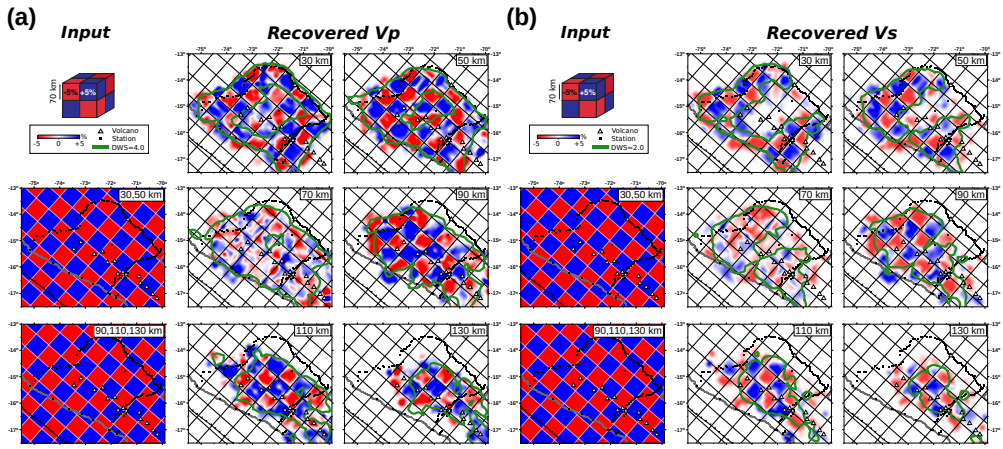

Figure 3.A.5: Horizontal checkerboard resolution test results for (a) P-wave velocity and (b) S-wave velocity at every depth where the inversion nodes are placed. Top panel in column of input shows three-dimensional view of the $70 \times 70 \times 70$ km^3 grid with the maximum and minimum perturbation values. Note that the recovered slice at the depth of 70 km where an upper and lower cells contact are biased because of vertical smearing.

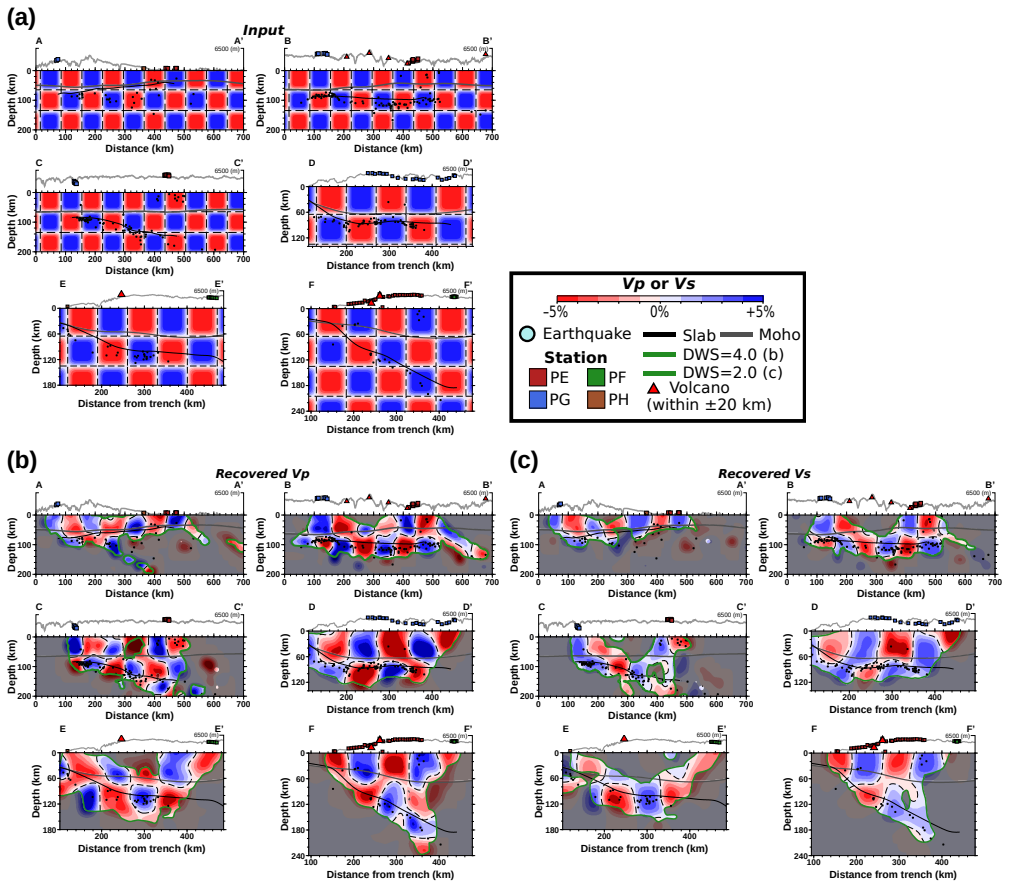

Figure 3.A.6: Checkerboard resolution test results in cross-section view. (a) Input velocity pattern for P and S waves. (b) Recovered P-wave velocities. (c) Recovered S-wave velocities. Locations of profiles A–A', B–B', C–C', D–D', and F–F' are indicated in Fig. 3.1.

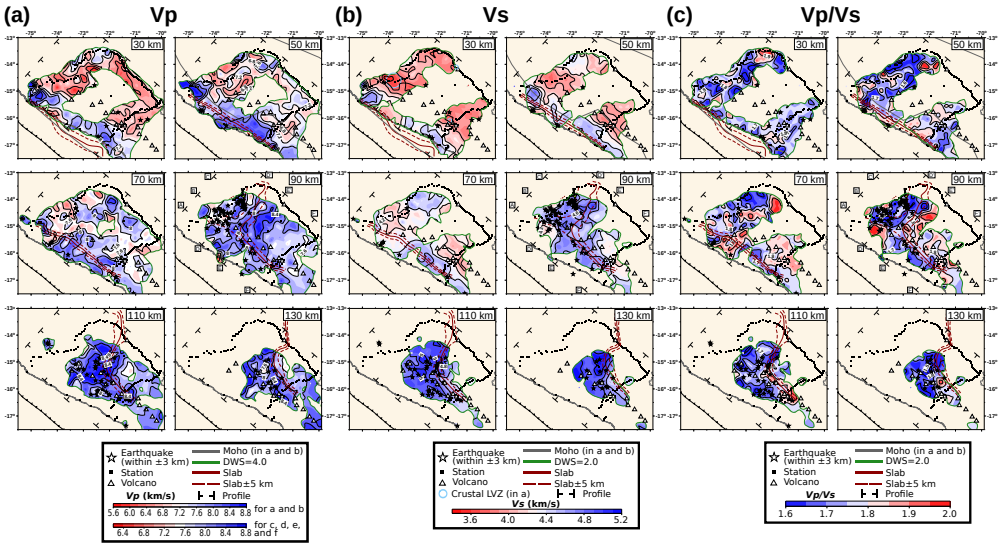

Figure 3.A.7: Horizontal slices of (a) *Vp*, (b) *Vs*, and (c) *Vp/Vs* from the inversion at depths 30, 50, 70, 90, 110, and 130 km without Gaussian filtering. The contour of the DWS for *Vp/Vs* in (c) is same with that in the *Vs* in (b).

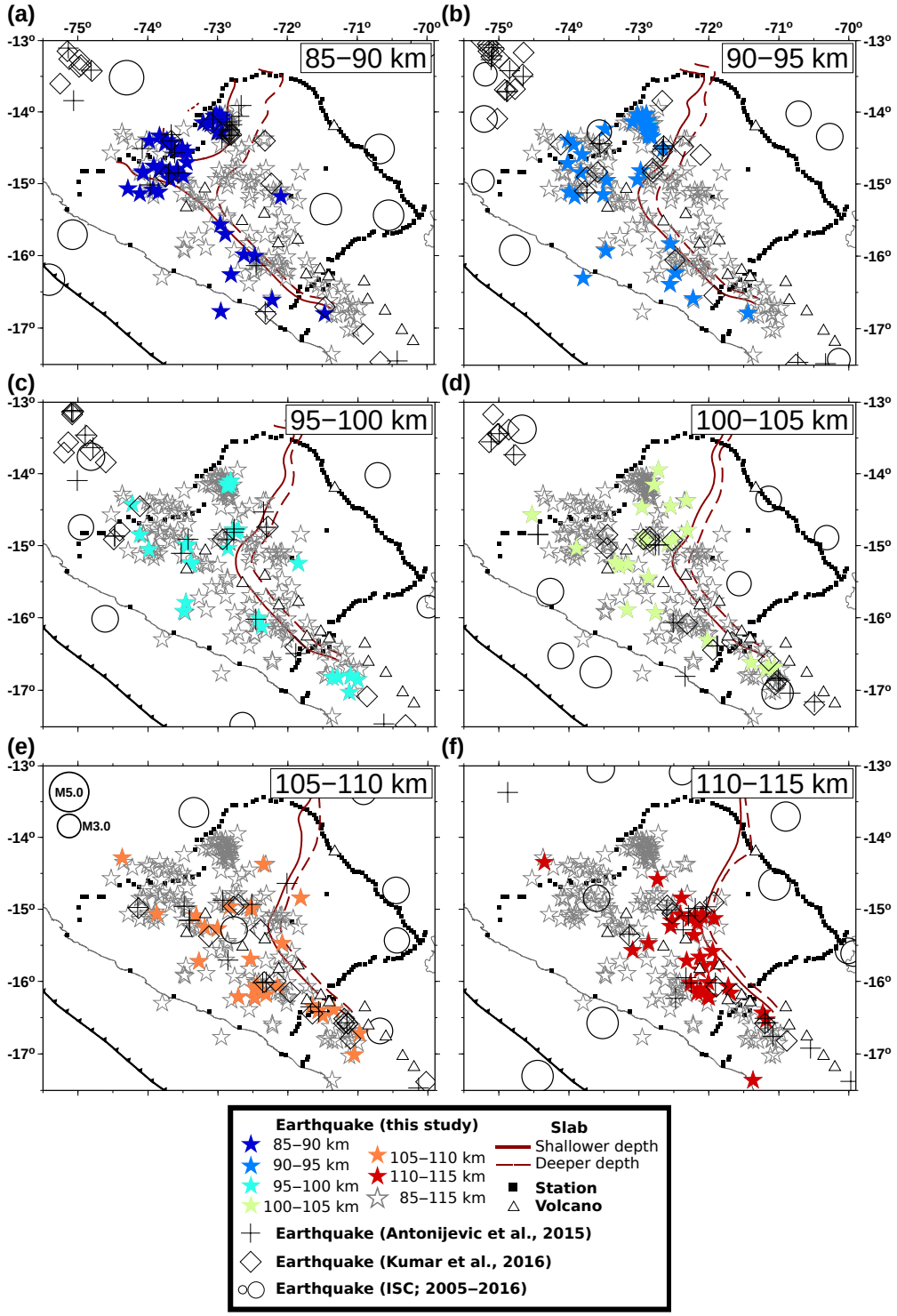

Figure 3.A.8: (Caption in next page)

Figure 3.A.8: Intra-slab earthquakes from 85 km to 115 km depth. ISC—International Seismological Centre.

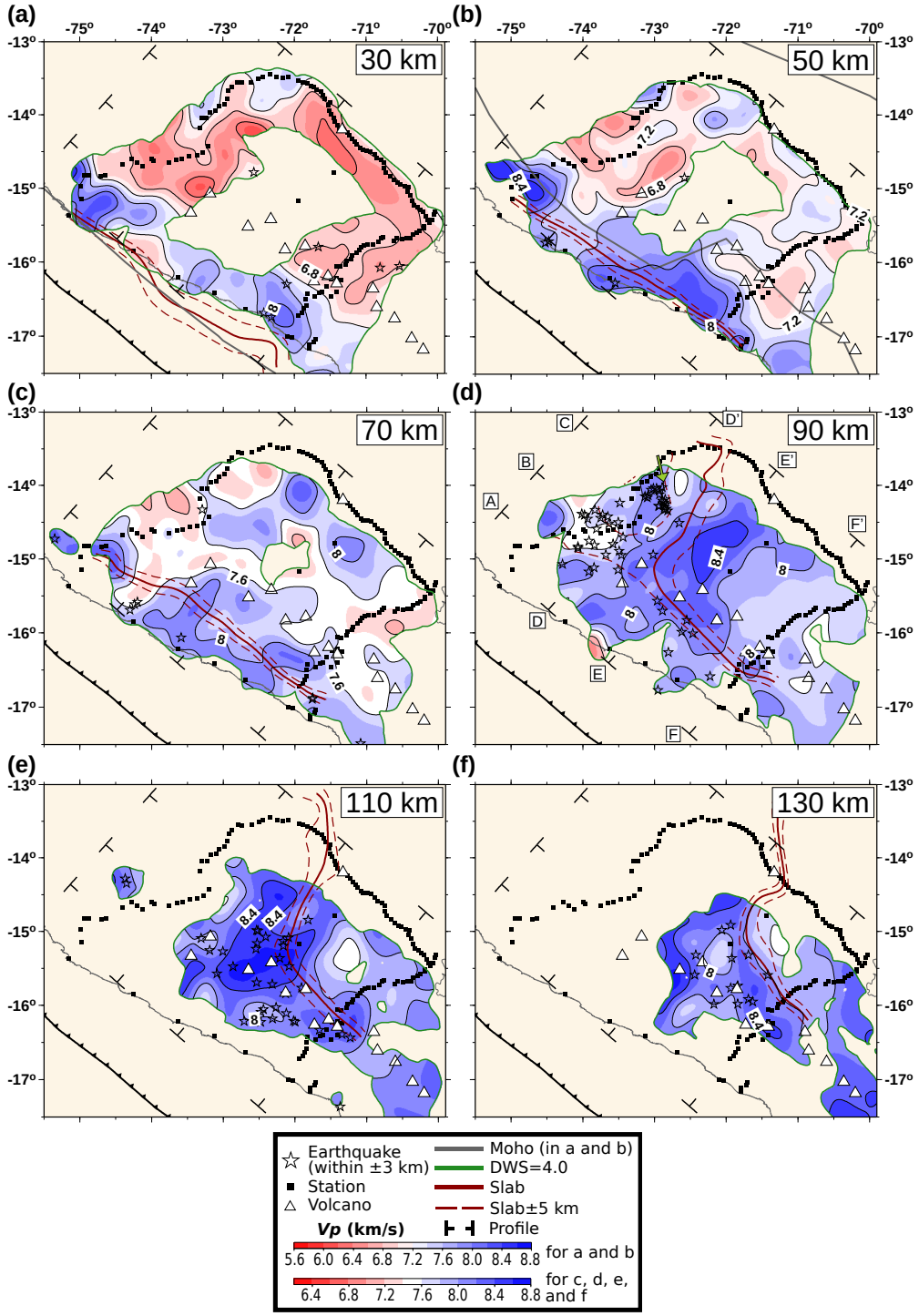

Figure 3.A.9: (Caption in next page)

Figure 3.A.9: Horizontal slices of P-wave velocity at depths (a) 30, (b) 50, (c) 70, (d) 90, (e) 110 and (f) 130 km. The Gaussian filter with standard deviation of 0.1°-by-0.1° is applied for simplicity. An arrow in a panel (d) indicates the region where we observe no slab seismicity at 71°W and 72.5°W longitude.

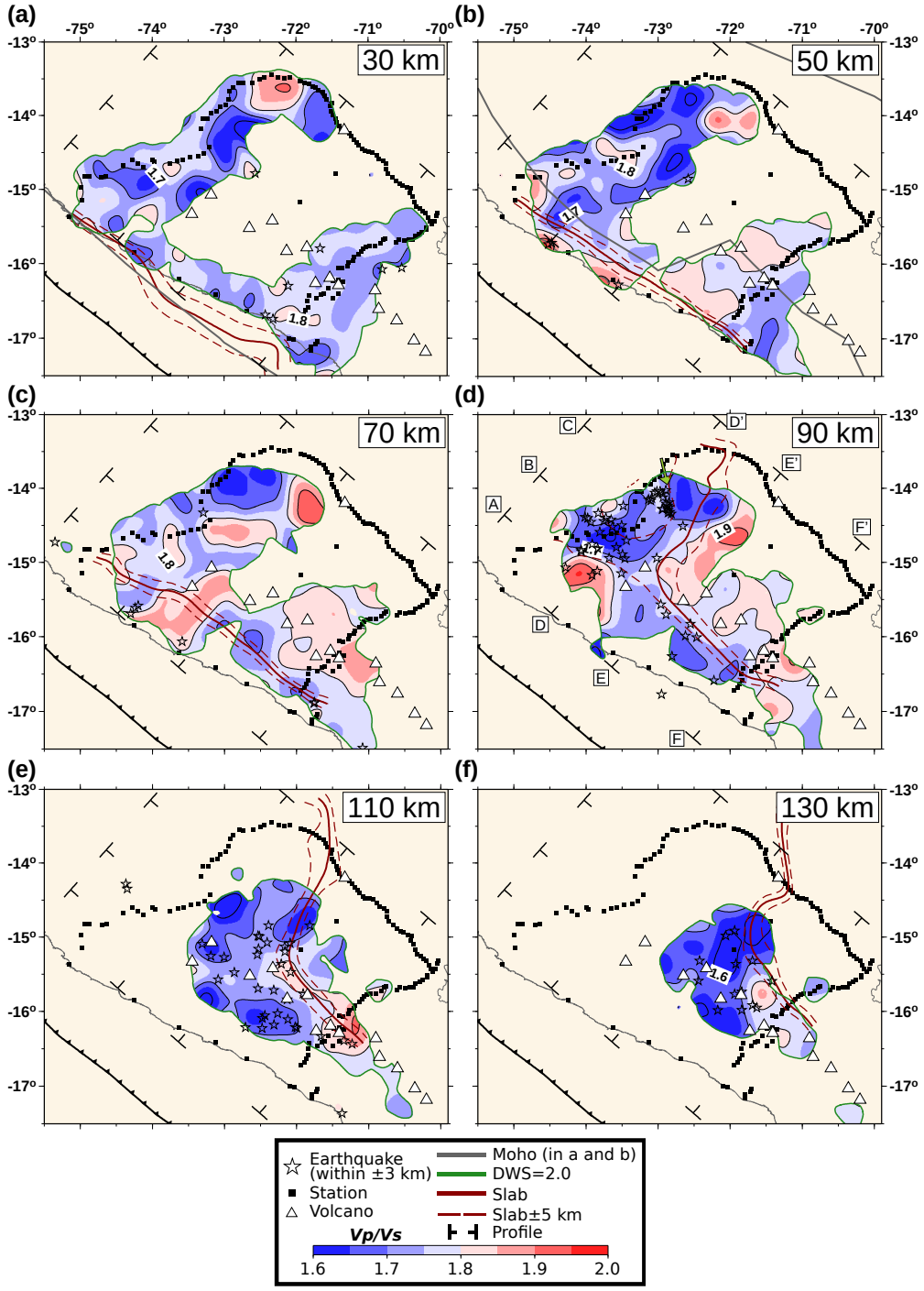

Figure 3.A.10: (Caption in next page)

Figure 3.A.10: Horizontal slices of Vp/Vs at depths 30, 50, 70, 90, 110 and 130 km. The Gaussian filter with standard deviation of 0.1°-by-0.1° is applied for simplicity. The contour of the DWS is same with that in the Vs. An arrow in a panel (d) indicates the region where we observe no slab seismicity at 71°W and 72.5°W longitude.

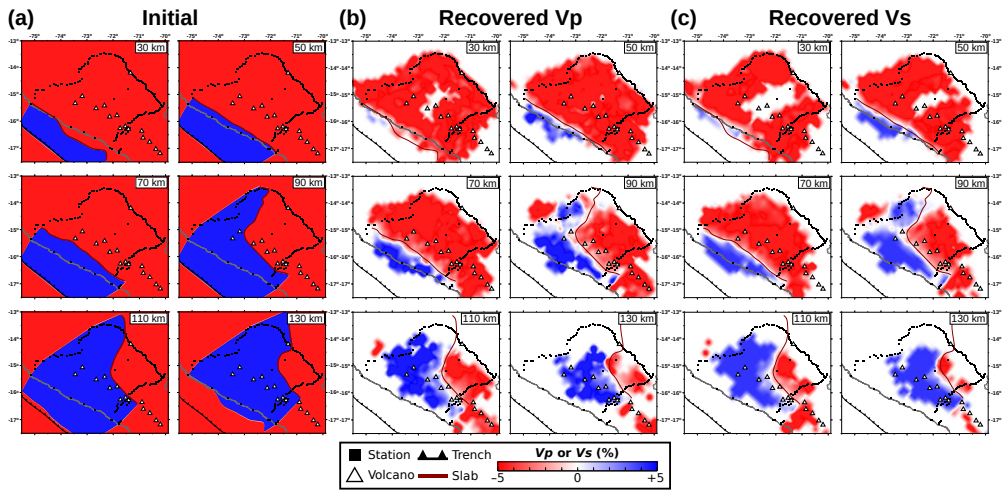

Figure 3.A.11: Resolution test results to test how well the inversion recovers the fast velocity anomaly (i.e., Nazca slab). (a) Input velocity model with different depth slices from 30 to 130 km. (b) Results for P-wave velocity. (c) Results for S-wave velocity.

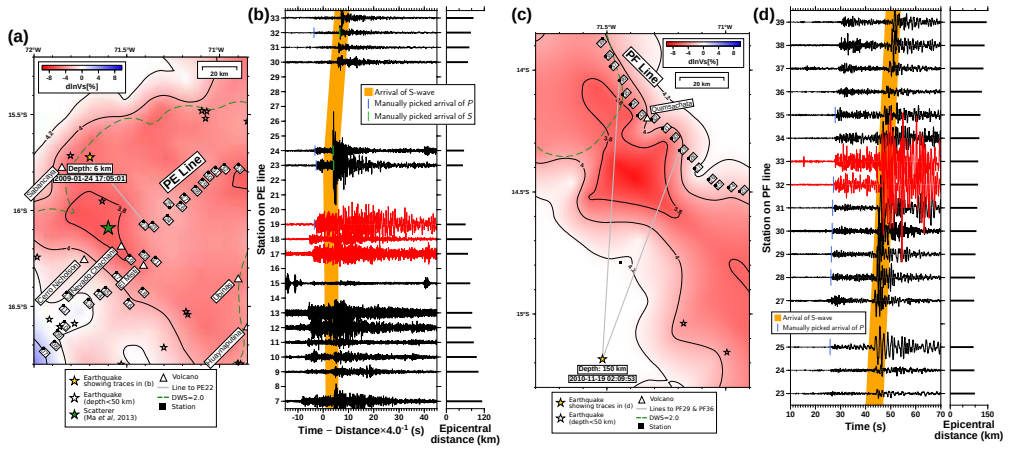

Figure 3.A.12: Crustal low-velocity zones (LVZ). (a) A LVZ in the normal-dip subduction zone at a depth of 30 km along the PE line. The S-wave velocities in the background are not smoothed with Gaussian filtering. (b) Corresponding transverse-component record section of the local event, shown in (a) as a star, recorded from the PE stations. The highpass filter is applied at 0.25 Hz. A thick orange line in the record section highlights the sudden change in amplitude of S phase, which indicates different path effects. Traces from stations PE17–PE19 are indicated in red. (c) A LVZ in the slab-dip transition zone at a depth of 30 km along the PF line. The S wave velocities in the background are not smoothed with Gaussian filtering. (d) Corresponding transverse-component record section of the local event, shown in (c) as a star, recorded from the PE stations. The highpass filter is applied at 0.25 Hz. A thick orange line in the record section highlights the sudden change in amplitude of S phase, which indicates different path effects. Traces from stations PF32–PF33 are indicated in red. Note that Quimsachata volcano sits in the middle of the stations PF32 and PF33.

3.B Supplementary materials (table)

Table 3.B.1: 451 relocated origin time and hypocenter.

Origin time	Latitude (°)	Longitude (°)	Depth (km)
2008-07-08,09:13:03.89	-16.1068	-72.1206	110.859
2008-07-08,19:02:01.86	-16.0649	-72.1509	106.365
2008-07-15,03:19:27.57	-16.0945	-71.3263	125.618
	...		
See an attached file. [click] 			

Table 3.B.2: 1-D velocity models.

This study		
Thickness (km)	*Vs* (km/s)	*Vp* (km/s)
10	3.12	4.91
10	3.64	6.34
15	4.08	7.18
42.5	4.3	7.48
42.5	4.43	7.85
240	4.54	8.18
Phillips et al. (2012)		
40	3.6	6.3
30	3.77	6.6
30	4.4	7.7
10	4	7
140	4.57	8
Ma & Clayton (2014)		
40	3.2	5.6
30	3.85	6.74
30	4.4	7.7
10	4.5	7.88
140	4.6	8.05
Dougherty and Clayton (2015)		
40	3.2	5.6
15	3.7	5.95
15	4.15	7.26
30	4.4	7.7
10	4.5	7.88
140	4.6	8.05

Table 3.B.3: Slab model based on relocated seismicity and receiver functions.

Lat(deg)	Lon(deg)	Dep(km)
-12.975	-71.425	122.208038
-13.000	-71.475	120.658691
-13.000	-71.450	121.366211
	...	
See an attached file. [click] 		

Chapter 4

The 2017 Mw 5.5 Pohang earthquake, South Korea, and poroelastic stress changes associated with fluid injection

This chapter is published in

Lim, H., Deng, K., Kim, Y.H., Ree, J.-H., Song, T.-R. A., Kim, K.-H. (2020). The 2017 Mw 5.5 Pohang earthquake, South Korea, and poroelastic stress changes associated with fluid injection. *Journal of Geophysical Research: Solid Earth.*

Abstract

The 2017 Mw 5.5 Pohang earthquake in South Korea, the first reported and largest-magnitude induced earthquake, occurred near the enhanced geothermal power plant in Pohang on 15 November 2017. We compute the spatiotemporal changes in poroelastic stresses perturbed by injected fluid under various conditions to better understand the occurrences of the Pohang earthquake and the small-magnitude earthquakes preceding it. Space-time variation of the earthquakes that occurred before the Pohang earthquake correlates significantly with fluid injection history between January 2016 and September 2017. We attribute the timing in earthquake occurrence to slow fluid diffusion, making hydraulic diffusivity of bedrock the critical model parameter for representing this slow process. In this context, the delay between the injection and the Pohang earthquake requires diffusivity estimates within a range of 1×10^{-4}–5×10^{-4} m^2/s for damaged granodiorite at 4–5 km, corresponding to the depth range between the well and the focal depth. According to these estimates, the pore pressure, and thus the Coulomb failure stress changes, are further enhanced by each injection with minimum stress dissipation. We find fluid injection can result in a change of the Coulomb stress of up to 0.4–1.1 bar, exceeding those associated with the 2016 Mw 5.5 Gyeongju earthquake by two orders of magnitude.

4.1 Introduction

The first enhanced geothermal system (EGS) project was initiated in late 2010 in Pohang, South Korea (Park et al., 2017), where the highest geothermal gradient and heat flow are observed (Fig. 4.1; Kim and Lee, 2007; Lee et al., 2010). Injection wells (denoted by PX-1 and PX-2) were drilled to depths of 4,362 and 4,341 m, respectively, and the first high-pressure hydraulic stimulation began on 29 January 2016 (Park et al., 2017; Hofmann et al., 2019). Before the last fluid injection on 18 September 2017, an earthquake occurred on 15 April 2017 at or near the EGS site with a moment magnitude, Mw, of 3.2 (Kim et al., 2018; Korean Government Commission, 2019; Woo et al., 2019). Seven months later on 15 November 2017, the Mw 5.5 earthquake occurred in close proximity to the well locations (Grigoli et al., 2018; Kim et al., 2018; Ellsworth et al., 2019; Korean Government Commission, 2019; Woo et al., 2019), and it was the second-largest and the most destructive event on record since seismic instrumental monitoring began in South Korea in 1905 (Lee et al., 2003). Prior to the injection, a mud loss event to the amount of 650 m^3 occurred during drilling in October–November 2015 (Korean Government Commission, 2019). Korean Government Commission (2019) identified two clusters of seismicity associated with fluid injection at PX-1 and PX-2, and further suggested that the Pohang earthquake intiated in an area that was perturbed by the injection at PX-2. Because the focal depth is estimated to be relatively shallow, at about 4–5 km (Grigoli et al., 2018; Kim et al., 2018; Korean Government Commission, 2019; Woo et al., 2019), synthetic aperture radar interferometry (InSAR) constrains the static slip model (Song and Lee, 2019), showing a major slip northeast of the hypocenter.

The space-time variation of seismicity prior to the Mw 5.5 earthquake is well correlated with the history of stimulation activities involving fluid injection and flowback (Kim et al., 2018). The proximity of the focal depth to the well tip and the tempo-

ral correlation between seismicity and hydraulic stimulation support the idea that geothermal plant activities may have caused the Mw 5.5 Pohang earthquake (Grigoli et al., 2018; Kim et al., 2018; Ellsworth et al., 2019; Korean Government Commission, 2019; Woo et al., 2019), making it the largest induced earthquake on record at an EGS site. Herein, the term 'induced' is used to include earthquakes triggered by anthropogenic causes that release tectonic stress, as well as earthquakes that release the stresses created by industrial activities (Doglioni, 2018; Ellsworth, 2013). In regions where the crust is critically stressed (e.g., Hong et al., 2018), small changes in stress can trigger fault slip, causing earthquakes (Reasenberg and Simpson, 1992; Stein, 1999).

It remains unclear how the injected fluid from the Pohang EGS activities affected the stress state at depth and induced the earthquake that occurred about 2 months after the last stimulation activity on 18 September 2017 (Fig. 4.2; Kim et al., 2018). Korean Government Commission (2019) conducted a comprehensive study to investigate the cause of the Pohang earthquake, utilizing datasets from seismology, hydrogeology, geomechanics/structural geology, and geophysical exploration. A condensed version of this work by Korean Government Commission (2019) is presented in Ellsworth et al. (2019). In particular, Korean Government Commission (2019) provided locations for earthquakes that occurred near the EGS site during the period between the start of the EGS activities and the mainshock, which we refer to as 'previous earthquakes'. Korean Government Commission (2019) also provided hydraulic models for limited cases using the hydraulic diffusivities (D) of the fault core and fault damage zone and suggested that an increases in fluid pressure of $\sim$0.7 bar was probably present when the Pohang earthquake occurred on 15 November 2017.

In this study, we perform poroelastic modeling to calculate the injection-related pore pressure and stress perturbations within the framework of linear poroelasticity (e.g., Biot, 1941), but consider a wide range of D in the modeling to assess uncer-

tainties in the medium properties. While both hydraulic and poroelastic analyses predict pore pressure changes, the poroelastic modeling can selfconsistently predict changes in elastic stress due to fluid injection. Under low diffusivity, the elastic stress change could be a dominant triggering mechanism (e.g., Deng et al., 2016). In Pohang, high D is observed only within a localized zone ($<\sim$100 m) near the well during high-pressure stimulation (Yoo, 2018). Furthermore, if the fault associated with the mainshock is located beyond the nearwell fractured zone (e.g., Ellsworth et al., 2019; Korean Government Commission, 2019), the hydraulic diffusivity of bedrock at the basement, likely to be low (e.g., Mizoguchi et al., 2008; Morrow et al., 1994), will play a critical role in affecting the pore pressure change due to the injection.

Considering the history of stimulation activities and geological settings at the Pohang EGS site (Kim et al., 2018; Lee et al., 2015), we investigate the dependence of stress change with respect to D, and compare the relocated seismicity with the spatiotemporal evolution of Coulomb stress change. In this study, we determine the locations of the Mw 5.5 Pohang earthquake and 311 smaller earthquakes at or near the EGS site, including 11 previous earthquakes and 302 aftershocks that occurred between December 2016 and February 2018. We take a probabilistic approach in determining these earthquake locations and tightly link the stress change to the earthquake's location.

4.2 Poroelastic modeling

4.2.1 Poroelastic constitutive equations

Biot's poroelastic equation (1941) describes the equilibrium condition for the solid matrix and pore fluid pressure in a poroelastic medium that shows fluid-matrix coupling. The medium is assumed to be isotropic and fluid-saturated. The governing equations are given as follows (Detournay and Cheng, 1993; Wang and Kümpel, 2003):

$$G\nabla^2 + \frac{2G}{1-2\nu}\nabla\epsilon - \alpha\nabla p = \mathbf{f}\left(\mathbf{x}, t\right) \tag{4.1}$$

and

$$M^{-1}\frac{\partial p}{\partial t} + \alpha\frac{\partial \epsilon}{\partial t} - \nabla\cdot\left(\frac{\kappa}{\eta}\nabla p\right) = Q\left(\mathbf{x}, t\right) \tag{4.2}$$

where $\mathbf{u}$ is the displacement vector, ϵ is the volumetric strain (i.e., $\nabla\cdot\mathbf{u}$), p is the pore pressure, κ is the matrix permeability, η is the dynamic viscosity of the fluid, and $\mathbf{f}$ is the body force per unit volume. $Q\left(\mathbf{x}, t\right)$ is described by $q\left(t\right)\delta\left(\mathbf{x}-\mathbf{x}_{\mathrm{s}}\right)$ for a single point source, where $q\left(t\right)$ is the volume injection rate, $\mathbf{x}_{\mathrm{s}}$ is the location of the injection well, and $\delta\left(\cdot\right)$ is the Dirac delta function. The poroelastic medium is characterized by the independent parameters G, ν, M, α, and D, where G is the shear modulus, ν is Poisson's ratio under drained conditions, M is the Biot modulus (compressibility introduced by Biot (1941)), and α is a dimensionless coefficient of effective stress (Biot, 1941). The permeability κ is related to D by

$$\frac{\kappa}{\eta} = \frac{9}{2}\frac{(1-\nu_{\mathrm{u}})(\nu_{\mathrm{u}}-\nu)D}{(1-\nu)(1+\nu_{\mathrm{u}})^2 GB^2} \tag{4.3}$$

where B is Skempton's coefficient. M^{-1} is expressed as

$$M^{-1} = \frac{9}{2}\frac{(1-2\nu_{\mathrm{u}})(\nu_{\mathrm{u}}-\nu)}{(1-2\nu)(1+\nu_{\mathrm{u}})^2 GB^2} \tag{4.4}$$

where $\nu_{\mathrm{u}} = [3\nu + \alpha B(1-2\nu)]/[3-\alpha B(1-2\nu)]$ is Poisson's ratio under the undrained condition.

For calculating the poroelastic stress and pore pressure changes with given injection rate, we use the poel softwafe (`https://www.gfz-potsdam.de/en/section/physics-of-earthquakes-and-volcanoes/data-products-services/downloads-software` last accessed on 21 June 2017), which is based on an extension of the Thomson–Haskell propagator method (Wang and Kümpel, 2003). We consider the real-time injection

histories at PX-1 and PX-2 (Figs 4.2b and c) and calculate stress and pore pressure changes in cylindrical coordinates system, where the axis of symmetry is defined perpendicular to the fault. We apply no free-surface condition in the calculation as any effect due to a free surface is minimal when the point of interest is close to the wells and away from the free surface (Wang and Kümpel, 2003). The stress tensors from PX-1 and PX-2 are rotated to a specific fault orientation, and the total stress perturbation is obtained by the principle of superposition, taking advantage of the linearity of poroelastic theory.

4.2.2 Poroelastic parameters

All poroelastic parameters used in the modeling except for D (G, B, ν, α, and η) are summarized in Table 4.1. Their ranges represent granite or crustal rock in a confining pressure and temperure at a depth of 4 km (Table 4.1). The values of G, B, ν, α, and η are fixed because their ranges are narrow relatively to D. We also append rationale for selecting the values in Table 4.1.

D represents the ratio between the rock's ability to store and transport fluids in the poroelastic medium. For fixed poroelastic parameters (G, B, ν, α, and η) other than D itself in Table 4.1, D can be converted to κ and vice versa using Equation (4.3). Fig. 4.B.1 shows the linear relationship between D and κ. However, selection of values of D for modeling is not trivial. For example, D of the fractured granite of the Nojima fault zone in Japan (8 m^2/s; $\kappa = 10^{-14}$ m^2) is much higher than that of the fault-wall rocks (8×10^{-6} m^2/s; $\kappa = 10^{-20}$ m^2), while the fault gouge can have very low D (8×10^{-6} m^2/s; $\kappa = 10^{-20}$ m^2) at the effective confining pressure (P_e) of 0.9 kbar (Mizoguchi et al., 2008). For comparison, the measured κ of the intact granodiorite gneiss samples from the Kola well in Russia is 4–7×10^{-21} m^2 (D = 3–6×10^{-6} m^2) at $P_e = 1$ kbar (Morrow et al., 1994).

For the Pohang earthquake, Ellsworth et al. (2019) and Korean Government Com-

mission (2019) used $D = 10^{-2}$ m^2/s for bedrock, 10^{-6} m^2/s for fault core and 10^{-1} m^2/s for the fault damage zone in their pore pressure diffusion modeling. Yoo (2018) calculated the stress-dependent permeability, which reaches 10^{-15} m^2 at a radial distance of 15 m (1 m^2/s) from PX-2, using the densely sampled wellhead pressures and injection rate data during 29–30 January 2016. Also, calculated permeability is 2–5 $\times 10^{-14}$ m^2 at 22.5 m (16–40 m^2/s) from PX-1 for 15–16 December 2016 (Yoo, 2018). This value of D specifically represents the fluid diffusion properties in a spatially localized region near the well ($<\sim$100 m), which must have been transient for 2–3 days. We thus set this value of D as the upper bound in our modeling. Considering previously determined estimates of D for the Pohang EGS and other fault-zones, we explore wide ranges of this variable (10^{-7}–10^{3} m^2/s) for the bedrock (D_{bed}) and fault damage zone (D_{dmz}) in our modeling and compute stress changes with approximately uniform intervals (e.g., $D = 1 \times 10^{-7}$, 2×10^{-7}, 5×10^{-7}, 1×10^{-6} m^2/s, and so on). Although we do not search for a range of D for the fault core (i.e., fault gouge), D_{core}, we discuss the effects of an impermeable fault gouge on the changes in the stresses and pore pressure in Section 4.4.5.

4.2.3 Well geometry and fluid injection history

PX-1 and PX-2 are 6 m apart on the surface, but PX-1 is tilted westward (azimuth of 289°), away from the vertical PX-2; at their bottoms, they are 616 m apart laterally (Hofmann et al., 2019). The openhole sections, along which fluid is injected into or extracted from rock, of PX-1 and PX-2 are at 4,049–4,362 m and 4,208–4,348 m depth, respectively (Hofmann et al., 2019). The locations of vertical PX-2 and the surface-projected location of the openhole section of tilted PX-1 are shown in Fig. 4.3. Geometries of the openhole sections in fault-plane and fault-normal views are presented in Fig. 4.4. Injections are simplified as point sources at the mid-point of the relevant openhole section (Fig. 4.4, white circle). Fluid injection and flowback records

from between 29 January 2016 and 18 September 2017 are presented in Fig. 4.2 (Kim et al., 2018; Korean Government Commission, 2019). The injection phases are grouped into five events dated to January–February 2016 (hereafter, JF16), December 2016 (D16), March–April 2017 (MA17), August 2017 (A17) and September 2017 (S17). The injection events JF16, D16, MA17, A17, and S17 were performed at PX-2, PX-1, PX-2, PX-1, and PX-2, respectively (Fig. 4.2; Kim et al., 2018; Korean Government Commission, 2019).

4.2.4 Coulomb failure stress change

A failure occurs on a fault when the shear stress (τ) exceeds the maximum frictional strength that is determined by a frictional coefficient (μ), normal stress (σ_{n}), and p. τ is resolved on the fault surface geometry, defined by the strike, dip, and rake, from the known stress field, whereas σn is defined only by the strike and dip. p is independent of fault geometry. τ is positive in the rake direction, and σ_{n} is positive for tension. The Coulomb failure stress (CFS) is defined as $CFS = \tau + \mu(\sigma_{\mathrm{n}} + p)$ (e.g., King et al., 1994; Stein, 1999). We consider that failure on a fault is promoted (or inhibited) due to changes in the CFS, or ΔCFS, which is defined as

$$\Delta CFS = \Delta\tau + \mu(\Delta\sigma_{\mathrm{n}} + \Delta p). \tag{4.5}$$

The fault is brought closer to failure when ΔCFS is positive, and vice versa. The increases in $\Delta\tau$, Δp, and $\Delta\sigma_{\mathrm{n}}$ increase the likelihood that the fault will slip toward the assumed slip direction. For most rocks, the frictional coefficient (μ) ranges between 0.6 and 0.85 (Byerlee, 1978) (Table 4.1). In this study, we use μ of 0.6 (Table 4.1), which is close to the coefficient of 0.53 in the granodiorite sample retrieved from the well PX-2 at a depth of 4.2 km (Kwon et al., 2019).

To compute $dCFS$, the stress tensor obtained from Equations (4.1) and (4.2) is projected onto the fault plane to obtain $\Delta\sigma_{\mathrm{n}}$ and $\Delta\tau$ along the slip direction.

The fault defined by the strike, dip and rake is referred to as a 'receiver fault' (e.g., Woessner et al., 2012), which can be of fixed geometry or arbitrarily oriented along the fault plane that is most susceptible to failure (the 'optimal fault orientation') in the modeling domain. We use the fault geometry constrained by the distribution of the Pohang earthquake and previous earthquakes before the mainshock (strike of 214° and dip of 43°; Woo et al., 2019) as our receiver fault. Rake is chosen as 128° from the mainshock focal mechanism (Korean Government Commission, 2019; Woo et al., 2019).

4.3 Earthquake location

The Pohang earthquake was recorded by a permanent seismic network in South Korea, two strong-motion sensors at the EGS site (Grigoli et al., 2018), and a temporary array (Kim et al., 2018), consisting of a total of 68 seismometers near/at the EGS (Figs 4.1 and 4.B.2). In the aftermath of the Pohang earthquake, several temporary seismic arrays were deployed close to the site to monitor aftershocks (Figs 4.1 and 4.B.2). Since earthquake locations are critical for evaluating poroelastic stress changes, we relocate the Pohang earthquake, its aftershocks, and previous earthquakes using available network data. We then assess our estimates by comparing with estimates from previous studies based on different location methods and datasets. See 4.A for details of how to obtain the probability density functions (*pdf*s) of the hypocenters. See Table 4.C.1 for our hypocenter locations and uncertainties.

4.3.1 Pohang earthquake location

Figs 4.3a and b show the epicentral *pdf*s (i.e., marginal pdfs) of the earthquakes. In particular, the median of the epicentral *pdf* for the Pohang earthquake is indicated as a star with an iso-contour line (95% of the *pdf*s). The 95% iso-contour of the

Pohang earthquake has a radius of, at most, 1 km that encompasses the locations of both wells. Furthermore, the iso-contour encompasses the previous estimate of its hypocenter (Ellsworth et al., 2019; Korean Government Commission, 2019; Woo et al., 2019). The observed difference in epicenters between the previous estimate and ours (median of *pdf*) is ∼200–1000 m, which is inevitable considering that different datasets have been utilized in relocation.

The *pdf* of the focal depth for the Pohang earthquake is 5.0 ± 0.8 (2σ) km, ranging from ∼4 to 6 km (Fig. 4.3c). The previous estimates of 4.27 km (Korean Government Commission, 2019) and 6.2 km (Hong et al., 2018) are within our determined range, which corresponds to the depth range of granodiorite basement (Lee and Sheen, 2015).

4.3.2 Relocated hypocenters of previous earthquakes, foreshocks and aftershocks

The median of the epicentral *pdf* for each of the previous earthquakes (Mw 2.1 earthquake on 22 December 2016, Mw 2.3 on 29 December 2016, and Mw 3.2 on 15 April 2017; Fig. 4.2; magnitude information taken from Korean Government Commission, 2019) is indicated by a circle with an iso-contour line (95% of the *pdf*; Fig. 4.3a). Among the detected earthquakes by Kim et al. (2018) and Korean Government Commission (2019; Fig. 4.2a), these three events each have a value of Mw exceeding 2.1. The locations of these previous earthquakes involve large uncertainties and are far from the well positions (Fig. 4.3a) since data from the networks PH, K18, G18 and KG (temp) are unavailable (Fig. 4.1). The depths of the Mw 3.2, Mw 2.2 and Mw 2.3 earthquakes are 5.9 ± 5.5 km, 2.3 ± 2.3 km and 1.5 ± 0.8 km, respectively.

The hypocenters of seven foreshocks with magnitudes less than 2.2 (which occurred from 14 November 2017, 20:04 to 15 November 2017, 05:23) are relatively well determined compared to those of previous earthquakes because of the stations K18 (Fig 4.1 and 4.3a; Table 4.C.1). Most of the foreshocks (six out of seven) are located

near the wells and they are confined to a depth range of 4.0–4.9 km.

As the aftershock monitoring arrays such as KG and PH become available, the aftershock locations involve smaller uncertainties than that of previous earthquakes and the Pohang earthquake by a factor of 7 or better (Fig. 4.3). The epicentral *pdf*s of five large aftershocks (M_L 3.5–4.3) are also located within 1–2 km of both the Pohang earthquake and the wells (Fig. 4.3b). Relocated aftershocks extend farther to the northeast and southwest of the injection well locations (Fig. 4.3b), consistent with the slip distribution imaged by InSAR data (Song and Lee, 2019). The aftershocks are distributed within a depth range of 1.2–6.8 km, and peaked in a depth range between the well tip and the depth of the Pohang earthquake (4.2–4.8 km; Fig. 4.3c). The majority of the aftershocks (86%) are concentrated in the granodiorite basement (Fig. 4.3c; Lee et al., 2015).

4.4 Poroelastic modeling against hydraulic diffusivity

The stress perturbation due to fluid injection highlights how the poroelastic response of the media may potentially cause the Pohang earthquake and previous ones between January 2016 and 15 November 2017. As described in Section 4.2, we explore a wide range (10^{-7} to 10^{3} m^2/s) of values for both D_{bed} and D_{dmz} with fixed poroelastic parameters (ν, ν_u, B, α, G, and η) and μ. We sample stress changes and Δp at the projected location of the mainshock hypocenter (Korean Government Commission, 2019; Woo et al., 2019) onto the fault plane (Fig. 4.4b, yellow star).

4.4.1 Poroelastic stresse changes of four representative models: Example

Fig. 4.5 illustrates the temporal evolution of the stresses and pore pressure changes (ΔCFS, $\Delta\sigma_n$, $\Delta\tau$ and Δp) for various D_{bed} and D_{dmz} during the fluid injection and flowback history (Fig. 4.2). We examine the first-order trends of ΔCFS, $\Delta\sigma_n$, $\Delta\tau$

and Δp by applying a Gaussian lowpass filter with a standard deviation of 2 months (Fig 4.5, colored lines). The filter removes sharp peaks or steps in the stress change curves which can be associated with the injection and flowback practices (Fig. 4.5, grey lines). For the four cases, the filtered stress change curves clearly show different amplitudes and gradients at the time of the Pohang earthquake, highlighting the importance of D_{bed} and D_{dmz} in the earthquake occurrence (Fig. 4.5).

Figs 4.5a and b demonstrate cases in which the amplitude of ΔCFS attains a high value on 15 November 2017. ΔCFS, $\Delta\sigma_{\mathrm{n}}$, $\Delta\tau$ and Δp shown in Fig. 4.5a are computed for a homogeneous model (i.e., $D_{\mathrm{bed}} = D_{\mathrm{dmz}} = 5 \times 10^{-4}$ m^2/s), and those in Fig. 4.5b are for a model involving a fault structure ($D_{\mathrm{bed}} = 5 \times 10^{-4}$ m^2/s; $D_{\mathrm{dmz}} = 1 \times 10^{-2}$ m^2/s). When$D$is homogeneous and low (i.e. $D_{\mathrm{bed}} = D_{\mathrm{dmz}} = 5 \times 10^{-4}$ m^2/s), the overall trend of ΔCFS closely follows the trend of Δp, which increases substantially after injection D16 (Fig. 4.5a). Because of the low D values, the time intervals between subsequent injection events are too short for the stresse changes built up by previous injection events to fully dissipate. The value of ΔCFS is 2.1 bar on 15 November 2017 (Fig. 4.5a).

In the case of a permeable fault damage zone ($D_{\mathrm{dmz}} = 1 \times 10^{-2}$ m^2/s), we obtain a temporal history of the ΔCFS amplitude similar to that obtained for the homogeneous model (Fig. 4.5a), but with slightly reduced magnitude (Fig. 4.5b). The amplitudes of both Δp and $\Delta\sigma_{\mathrm{n}}$ decrease because of fast diffusion within the fault damage zone. As a result, $\Delta\tau$ contributes to ΔCFS to a greater degree. We observe a trend for increasing $\Delta\tau$ close to the time of the mainshock whereas Δp shows a slightly decreasing trend (Fig. 4.5b). The value of ΔCFS is 1.3 bar on 15 November 2017 (Fig. 4.5b).

Notably, in Figs 4.5a and b, we observe that the level of ΔCFS drops and then rises, with a large negative peak in January–February 2017; this feature stems from the practice of alternating injection at PX-1 and PX-2. Fig. 4.6 shows the temporal changes in ΔCFS caused by each well computed using the same values of D as Fig.

4.5b. Fig. 4.6 clearly shows that the drop in ΔCFS in January–February 2017 is closely associated with the injection D16 at PX-1 when the largest volume of fluid is injected (Fig. 4.2).

$\Delta\tau$ shows an increasing trend at injection MA17 (Figs 4.5a and b). Generally, $\Delta\tau$ decreases with injection at PX-1 (i.e., D16 and A17; Fig. 4.2), and increases with injection at PX-2 (JF16, MA17 and S17; Fig. 4.2). These opposite responses to injections at PX-1 and PX-2 are observed more clearly in unfiltered $\Delta\tau$ (Fig. 4.B.5). Fig. 4.B.5 shows unfiltered ΔCFS, $\Delta\sigma_{\mathrm{n}}$, $\Delta\tau$ and Δp for individual well and both wells. Figs 4.B.5b and c show ΔCFS, $\Delta\sigma_{\mathrm{n}}$, $\Delta\tau$ and Δp involving the injection practice at PX-1 or PX-2 with same D_{bed} and D_{dmz} of Fig. 4.5a. Similarly, Figs 4.B.5e and f show ΔCFS, $\Delta\sigma_{\mathrm{n}}$, $\Delta\tau$ and Δp of Fig. 4.5b. In December 2016 and early August 2017, $\Delta\tau$ is decreased sharply by injections at PX-1 (D16 and A17; Figs 4.B.5b and e). In late August 2017, flowback following injection A17 rapidly increases $\Delta\tau$ by a similar amount of the earlier decrease (Figs 4.5b and e). All injections at PX-2 increase $\Delta\tau$ in January–February 2016, March–April 2017 and September 2017 (Figs 4.B.5c and f). Because the distance from the stress sampling point to PX-2 is larger than that to PX-1 (Fig. 4.4), observed changes in $\Delta\tau$ of PX-2 in response to all injections (Figs 4.B.5c and f) are smaller than those of PX-1 (Figs 4.B.5b and e).

Also, we can see that filtered ΔCFS in the period after the negative peak (from May 2017 to February 2018) is larger than in the period January–August 2016 (Figs 4.5a and b). This suggests that, for the mainshock occurrence on 15 November 2017, ΔCFS should be its largest during the period from the beginning of injection (29 January 2016) to that day. This could be a key condition for constraining D and reconciling it with the timing of the mainshock, which is delayed by $\sim$2 years after the first injection in January 2016 and 58 days after the last injection in September 2017. This feature was not captured by previous studies based on hydraulic diffusion modeling (Ellsworth et al., 2019; Korean Government Commission, 2019).

On the other hand, Fig. 4.5c shows a case in which D_{dmz} (= 10 m^2/s) is much higher than D_{bed}, and higher than the value used in Fig. 4.5b by a factor of 3. For this case, the diffusion speed within the fault damage zone is too fast to cause ΔCFS to reach its largest amplitude on 15 November 2017. ΔCFS on 15 November 2017 is 0.24 bar, less than the local peak amplitude in May 2016 (0.25 bar; Fig. 4.5c).

The last example is a case involving extremly low D_{bed} (= 1×10^{-6} m^2/s) with a permeable fault damage zone ($D_{\mathrm{dmz}} = 1 \times 10^{-2}$ m^2/s; Fig. 4.5d). The most prominent feature in this case is that Δp is nearly zero in the entire period considered, because the characteristic time from the wells to the sampling point is very long. Only $\Delta\tau$ changes significantly and thus affects ΔCFS . Although ΔCFS is increasing on 15 November 2017, the amplitude of ΔCFS is still smaller than in the period January–August 2016. In short, ΔCFS does not reach its maximum value at the time of the mainshock if the fault damage zone becomes more permeable ($D_{\mathrm{dmz}} = 1 \times 10^{1}$ m^2/s; Fig. 4.5c), or if the bedrock extremely impermeable ($D_{\mathrm{bed}} = 1 \times 10^{-6}$ m^2/s; Fig. 4.5d).

4.4.2 Search for possible ranges of D for Pohang earthquake occurrence

By examining the temporal evolution of stress changes depending on representative D-values (Fig. 4.5), we can determine possible ranges of D_{bed} and D_{dmz} to reconcile the delay between the timing of the Pohang earthquake and the peak stress change induced by the injection. As described in Section 4.1, we use examples highlighted in Fig. 4.5 as a guide to search for ranges of D_{bed} and D_{dmz} that are critical to induce the Pohang earthquake. Specifically, the range of D_{bed} and D_{dmz} can be defined if the amplitude of ΔCFS on the day of the mainshock (15 November 2017) is the largest from the beginning of the injection (29 January 2016) to that day.

Fig. 4.7 illustrates a classification of the models consisting of the ranges of D_{bed}

and D_{dmz} (10-7–103 m^2/s). Pairs of values lying on the diagonoal line shown represent homogenous model. The zone above that diagonal line represents models with more permeable fault damage zone than the bedrock (i.e., $D_{\mathrm{bed}} < D_{\mathrm{dmz}}$), whereas the zone below represents those with more impermeable fault damage zone than the bedrock (i.e., $D_{\mathrm{bed}} > D_{\mathrm{dmz}}$). The thickness of the fault damage zone is fixed as 85 m, following the value of Ellsworth et al. (2019) and Korean Government Commission (2019) for the purpose of benchmarking (Fig. 4.4b). A tradeoff between the thickness and D_{dmz} does not affect the temporal evolutions of ΔCFS, $\Delta\sigma_{\mathrm{n}}$, $\Delta\tau$ and Δp when the sampling point is within the damage zone (Fig. 4.4b).

The red squares indicate pairs of values of D_{bed} and D_{dmz} that meet our ΔCFS amplitude criterion on 15 November 2017 (Fig. 4.7). D_{bed} ranges 1×10^{-4}–5×10^{-3} m^2/s, and the D_{dmz} has a broad range of 5×10^{-6}–1 m^2/s. If we only consider the case $D_{\mathrm{bed}} \leq D_{\mathrm{dmz}}$, the medians of D_{bed} and D_{dmz} are 5×10^{-4} m^2/s and 5×10^{-3} m^2/s, respectively.

We obtain another values of D_{bed} and D_{dmz} based on the origin time (15 April 2017) and projected location of the hypocenter of the Mw 3.2 earthquake onto the fault (Fig. 4.4) in order to validate the values of D_{bed} and D_{dmz} based on the mainshock (Fig. 4.B.6). For this, the criterion is changed to that the amplitude of ΔCFS on the day of the Mw 3.2 earthquake (15 April 2017) is the largest from the beginning of the injection (29 January 2016) to that day. Similarly, we consider only the values when $D_{\mathrm{bed}} \leq D_{\mathrm{dmz}}$. Fig. 4.B.6 shows estimates of D_{bed} and D_{dmz} for the Mw 3.2 earthquake, and they are quite similar to the values for the Pohang earthquake shown in Fig. 4.7. In particular, the range of D_{bed} in Fig. 4.B.6, which is 2×10^{-4}–5×10^{-3} m^2/s, encloses that for the mainshock (1×10^{-4}–5×10^{-3} m^2/s) in Fig. 4.7.

4.4.3 Stresses and pore pressure changes on the fault plane

Two sets of ΔCFS, $\Delta\sigma_{\mathrm{n}}$, $\Delta\tau$ and Δp caused by the injections at PX-1 and PX-2 are calculated on the fault plane, defined as in Fig. 4.4. The values of D_{bed} and D_{dmz} are chosen as 5×10^{-4} m^2/s and 1×10^{-2} m^2/s, respectively, the same as for those in Fig. 4.5b. ΔCFS, $\Delta\sigma_{\mathrm{n}}$, $\Delta\tau$ and Δp as affected by injection at PX-1 (PX-2) are presented in Figs 4.8a–d (e–h). Fig. 4.9a shows the sum of ΔCFS computed for the two wells (Figs 4.8a and e).

The distributions of Δp and $\Delta\sigma_{\mathrm{n}}$ have spherical symmetry around the injection point on the fault plane (Figs 4.8c, d, g and h). For both wells, the values of Δp are positive (Figs 4.8c and g). $\Delta\sigma_{\mathrm{n}}$ by PX-2 is expected to be compressive (Fig. 4.8h) because the last injection was performed at PX-2 (Fig. 4.2). On the other hand, $\Delta\sigma_{\mathrm{n}}$ by PX-1 is positive with smaller amplitudes than by PX-2 (Fig. 4.8d) because of the flowback following injection that occurred in August 2017 (Fig. 4.2).

The distribution of $\Delta\tau$ shows two lobes with opposite polarities with an axis of symmetry along the rake of the fault (Figs 4.8b and f). $\Delta\tau$ by the injection at PX-2 is negative toward the rake (Fig. 4.8f). On the other hand, the injection at PX-1 generates the reverse pattern, with positive polarity toward the rake, and with much smaller amplitudes than those at PX-2 (Fig. 4.8b). The flowback at PX-1 in August 2017 generates the negative polarity of $\Delta\tau$ toward the rake (Fig. 4.8b).

Δp by PX-1 contributes to ΔCFS the most (Figs 4.8a and c). On the contrary, $\Delta\tau$ and $\Delta\sigma_{\mathrm{n}}$ contiribute most to ΔCFS in the case of the injection at PX-2 (Figs 4.8e–h). The degree of contribution of $\Delta\sigma_{\mathrm{n}}$, $\Delta\tau$ and Δp on the ΔCFS depends on factors such as the injected volume of fluid, hydraulic diffusivity, distance from the well to the fault and time of injection.

4.4.4 Temporal evolution of change in the Coulomb failure stress

Fig. 4.10 shows the variations of ΔCFS amplitude for all 21 cases (grey lines) that satisfy the ΔCFS amplitude criterion (Fig. 4.7, red squares) and have $D_{\mathrm{dmz}} \geq D_{\mathrm{bed}}$. With the determined values of D, all ΔCFS values are maximized on 15 November 2017 for the period from 29 Januaray 2016 to that day. ΔCFS starts with 0.2 bar in January–February 2016 and reaches its maximum, at 0.3–2.2 bar, on 15 November 2017 (Fig. 4.7). The 25th pencentile, median and 75th percentile are 0.4, 0.6 and 1.1 bar, respectively, on 15 November 2017 (Fig. 4.10, red dashed and solid lines). The range of 0.4–1.1 bar is much lower than the coseismic stress drop of ∼20 bar (Song and Lee, 2019), but much greater than the stress perturbations from natural sources (0.001–0.004 bar; Johnson et al., 2017).

4.4.5 Coulomb failure stress change and hypocenters on the fault plane

Fig. 4.9a shows total ΔCFS reflecting the contributions from both PX-1 and PX-2 (computed with the same values of D as Fig. 4.5b), compared with the locations of earthquakes projected onto the fault plane. These earthquakes are associated with injection at PX-2 (Korean Government Commission, 2019; Woo et al., 2019), with the three largest that occurred during injection events at PX-2 (JF16, MA17 and S17) shown as colored and crossed circles (Fig. 4.9a).

ΔCFS is positive in the southwest and deeper on the fault plane, and a boundary between the positive and negative zones occurs roughly at the mid-point of the two wells (Fig. 4.9a). The mainshock hypocenter determined by Korean Government Commission (2019) is located in the positive region, southwest from PX-1 and PX-2 (Fig. 4.9a, blue crossed circle). Hong et al. (2018) also showed that the epicenter of the mainshock is located west of the well positions (Fig. 4.3). Overall, the earthquakes occurred most often in the region with positive $\Delta\tau$ (Figs 4.8f and 4.9).

We also calculate ΔCFS with an impermeable layer at the center of the fault, to reflect the possible existence of a fine-grained fault gouge (Fig. 4.4b). The thickness and D of this core (D_{core}) are 10 m and 10^{-6} m^2/s, respectively, following the values reported by Ellsworth et al. (2019) and Korean Government Commission (2019). Note that the amplitude of ΔCFS is increased for the model with the core (Fig. 4.9b). Nevertheless, the effect of including this impermeable core in our model (Fig. 4.9b) appears minor because the patterns of ΔCFS amplitude are rather similar between the models with and without it (Fig. 4.9). The distributions of $\Delta\sigma_{\mathrm{n}}$, $\Delta\tau$ and Δp for the two models are also similar with slight differences in amplitude (Fig. 4.B.7).

Fig. 4.11 shows ΔCFS on the fault plane at two different times when the Mw 1.6 and 3.2 earthquakes occurred on 7 February 2016 and 15 April 2017, respectively. Because the focal mechanisms of these earthquakes are similar to that of the mainshock, the receiver fault geometry is kept the same in our modeling. The strike, dip and rake of the Mw 1.6 earthquake are 208°, 58° and 156°, respectively, and those of the Mw 3.2 earthquake are 215°, 58° and 128°, respectively (Korean Government Commission, 2019; Woo et al., 2019).

The Mw 1.6 earthquake is located at the boundary between the positive and negative ΔCFS regions (Fig. 4.11a). Also, the locations of the smaller earthquakes are clustered in this boundary, with some in the positive region (Fig. 4.11a). On the other hand, the projected locations of the Mw 3.2 earthquake and smaller earthquakes correlate well with the region of positive ΔCFS (Fig. 4.11b). The Mw 3.2 earthquake is located roughly in the mid-point between the wells, close to a spot where the amplitude of ΔCFS is highest (Fig. 4.11b). The amplitude of ΔCFS at the nearest grid point is 3.2 bar (Fig. 4.11b). Also, at that point location, $\Delta\sigma_{\mathrm{n}}$, $\Delta\tau$ and Δp are -2.5, 2.0 and 4.6 bar, respectively. Therefore, $\Delta\tau$ and Δp play a critical role in inducing the Mw 3.2 earthquake.

4.5 Discussion

4.5.1 Delay in earthquake occurrence

The delayed occurrence of the Pohang earthquake, by 58 days after the last injection S17 or ∼2 years after the first injection JF16, is not explained by a model with high D_{bed} (e.g., $D_{\mathrm{bed}} = 10^{-2}$ m^2/s used in Ellsworth et al., 2019 2019, and Korean Government Commission, 2019). With $D_{\mathrm{bed}} = 10^{-2}$ m^2/s and $D_{\mathrm{dmz}} =$ 10-2 m^2/s, ΔCFS is maximized in January–April 2017 and decreasing on 15 November 2017 (Fig. 4.B.3). To understand the delayed response, we suggest that low D_{bed} values, ranging from 1×10^{-4}–5×10^{-4} m^2/s (if $D_{\mathrm{bed}} \leq D_{\mathrm{dmz}}$) effectively slow the diffusion of Δp (Fig. 4.7). A more elaborate poroelastic modeling scheme showed an increasing trend for ΔCFS at the time of the mainshock (Chang et al., 2020), similar to our study results. Our estimated range of D_{bed} is within the end-member estimates from the numerical simulation, with high permeability range (1×10^{-15}–5×10^{-14} m^2) or a value for D of 1–40 m^2/s in a confined zone around the well position in Pohang (at most 100 m; see Figure 4.7 of Yoo (2018)) and low permeability (4–7×10^{-21} m^2) or a value for D of 3–6×10^{-6} m^2/s for the intact granodiorite gneiss (Morrow et al., 1994).

Although our modeling is based on the classical friction model (i.e., constant static and dynamic coefficients), the rate-and-state friction model can be used to rationalize the observed two-month delay between the last injection and the Pohang earthquake.Dieterich (1994) established a concept of seismicity rate on the rate-and-state friction model. The rate-and-state friction can delay an increase in the seismicity rate compared to an earlier peak of ΔCFS (Dieterich, 1994; Segall and Lu, 2015). In particular, Segall and Lu (2015) observed that the seismicity rate can be delayed by a few days with respect to the peak of the ΔCFS. We note that the delay due to the rate-and-state friction is sensitive to the empirical constitutive frictional parameter

and the background stress state, both of which have a large uncertainty.

4.5.2 Amplitude threshold of change in the Coulomb failure stress

In our analysis, we show that the Pohang earthquake can occur when the amplitude of ΔCFS reaches 0.4–1.1 bar (Fig. 4.10, 25th and 75th percentiles). Given the set-up of our model, the range of 0.4–1.1 bar is likely to be a threshold for the occurrence of this earthquake at the hypocenter where the rupture begins. This range is broadly bounded by the average stress drop of ∼20 bar constrained by static slip inversion using InSAR data (Song and Lee, 2019) and the stress field created by natural processes such as hydraulic surface loading (i.e., rain and snow), thermal expansion, atmospheric pressure, and tide (Johnson et al., 2017). For instance, the three most significant factors in California, USA, are the hydraulic ($\Delta CFS \approx 0.015$ bar), atmospheric (0.004 bar), and thermoelastic sources (0.001 bar; Johnson et al., 2017). Also, our ΔCFS amplitude range is substantially higher than the static ΔCFS caused by the 2016 Mw 5.5 Gyeongju earthquake (South Korea's largest earthquake during the instrumental period; Kim et al., 2017; Grigoli et al., 2018) which occurred on 12 September 2016, 42 km from the epicenter of the Pohang earthquake. The static ΔCFS was only 0.005 bar at the hypocenter of the 2017 Pohang earthquake (Grigoli et al., 2018; Hong et al., 2018). This amplitude range (0.4–1.1 bar) that we have determined is higher than that of other studies, which may imply that the poroelastic stressing due to injection is the most critical mechanism affecting the occurrence of the earthquake. In addition, we demonstrated in Fig. 4.6 that, for either individual well, injection at PX-2 is a larger contributing factor to the occurrence of the Pohang earthquake. This is not surprising because PX-2 has a larger volume of injected fluid (1,695 m^3 at PX-1 and 4,146 m^3 at PX-2; Fig. 4.2).

4.5.3 Amplitude of change in the Coulomb failure stress and magnitude of the Pohang earthquake

The ratio of the induced stress change (or Δp) to the stress drop (e.g. Foulger et al., 2018; Gupta, 2002) can be considered a measure of the anthropogenic contribution to the Pohang earthquake occurrence. In many cases, induced earthquakes are associated with much smaller anthropogenic stress change than pre-existing tectonic stress (Gupta, 2002). Our modeling results show that the ΔCFS in November 2017 peaked at ∼0.6 bar (median), bounded by 0.4 and 1.1 bar (25th and 75th percentiles, respectively; Fig. 4.10). For the Pohang earthquake, the ratio of ΔCFS to the observed stress drop (∼20 bar; Song and Lee, 2019) is 3% for the median or a range of 2–6% for the percentiles.

The Mw 5.5 Pohang earthquake does not follow the empirical relationship between the maximum magnitude and total volume of injected fluid proposed by McGarr (2014). Considering the total fluid volume injected at the Pohang EGS (5,841 m^3), the predicted maximum magnitude (M_{MAX}) is considerably lower (3.5; Grigoli et al., 2018; Kim et al., 2018). Thus, the Mw 5.5 event in Pohang is clearly an outlier in this prediction model (McGarr, 2014). In that model, Δp induced by an injection is assumed to be equal to one half of the stress drop. As the ratio of ΔCFS to the inferred stress drop is low for the Pohang earthquake, M_{MAX} may be underestimated. Furthermore, if the rupture propagates beyond the nucleated zone as a result of Δp, the magnitude may become even greater (Galis et al., 2017). Also, recent studies by Ellsworth et al. (2019), Korean Government Commission (2019) and Woo et al. (2019) support this viewpoint. Foulger et al. (2018) explored datasets from 218 cases, and reported a few outliers from the relationship proposed by McGarr (2014).

We suggest that fluid injection to the basement probably enhanced the release of tectonic stress in Pohang, similar to a case in Oklahoma, USA (Hincks et al., 2018). The focal depth of the Pohang earthquake is close to the tip of the injection

well (Fig. 4.3c), and its depth is well within the range that exhibits slip-weakening behavior (Marone and Scholz, 1988; Scholz, 1998). Most aftershocks (95%) are also distributed through the basement layer (Fig. 4.3c). Injection to the basement may thus be another prerequisite contributing to large-magnitude events such as the Pohang earthquake.

4.5.4 Previous earthquakes in response to poroelastic stresse changes

The low values of D_{bed} (1×10^{-4}–5×10^{-4} m^2/s ; Fig. 4.7, red squares) may be valid if slow fluid diffusion is also applicable to earthquakes before the mainshock. As Fig. 4.B.6 shows, the estimated ranges of D_{bed} and D_{dmz} for the Mw 3.2 earthquake are quite similar to those for the mainshock (Fig. 4.7).

Although the location of the Mw 3.2 earthquake has high uncertainties in depth (at most $\pm$10 km, 2σ) and horizontal distance (at most 5 km, 95%) due to the limited presence or complete absence of nearby stations, the epicenters determined by Korean Government Commission (2019) and Woo et al. (2019) are very close to the median of our epicentral *pdf* (Fig. 4.3a). The projected location of the Mw 3.2 earthquake, and of smaller magnitude ones, onto the fault plane correlates well with the region of positive ΔCFS (Fig. 4.11b). That region around the Mw 3.2 earthquake is a result of $\Delta\tau$ and Δp due to injection at PX-1 and of $\Delta\tau$ due to injection at PX-2 (Figs 4.B.8b, c and f).

We also note that the locations of the Mw 1.6 earthquake and various smaller ones correlate poorly with the positive ΔCFS region (Fig. 4.11a). The observed stress perturbation for this event is small (Fig. 4.11a) and, thus, an ambient tectonic stress or the mud loss to the amount of 650 m^3 at a depth of 3.8 km in PX-2 in October–November 2015 (Korean Government Commission, 2019) may have affected the pattern of ΔCFS to a greater degree.

4.5.5 Heterogeneity of hydraulic property near/at the wells

Previous studies (Yoo, 2018; Korean Government Commission, 2019) suggested that PX-1 and PX-2 have different hydraulic properties. While the critical pressure (attained when the ratio of the injection rate to the injection pressure is changed significantly) of PX-1 is only ∼200 bar (wellhead pressure), the critical pressure of PX-2 is ∼800 bar during its injection events (Park et al., 2017; Korean Government Commission, 2019). Korean Government Commission (2019) interpreted that such a difference might arise from a difference in the fracture network created by high-pressure stimulation. Furthermore, Yoo (2018) observed high permeability that was dependent on pore-pressure, up to 1×10^{-15}–5×10^{-14} m^2 (D = 1–40 m^2/s) in the region closest to the well. Although well-dependent and distance-dependent heterogeneities can change the fields of ΔCFS, $\Delta\sigma_{\mathrm{n}}$, $\Delta\tau$ and Δp, such factors may not be essential to explain the observed delay of the mainshock (58 days after the last injection and about two years after the first injection) if the hypocenter is sufficiently distant from the near-well zone. The mainshock's hypocenter is several hundred meters from the wells (Korean Government Commission, 2019; Woo et al., 2019). The observed high permeability during injection only persists for, at most, 2 days at the wells and recovers to its initial low permeability (Yoo, 2018).

4.6 Summary

The 2017 Mw 5.5 Pohang earthquake in South Korea was the first reported and largest-magnitude induced earthquake associated with the exploitation of deep geothermal energy, and with a relatively small volume of injected fluid. Considering the total fluid volume injected at the Pohang EGS, the predicted maximum magnitude for the Pohang earthquake is considerably low at 3.5. Furthermore, the occurrence of such a large earthquake ∼2 months after the final EGS operation questions how critically

the injected fluid affects the stress state on a fault close to its failure conditions. In this study, we determine the range of the hydraulic diffusivities for the bedrock and the fault damage zone based on the criterion that the Coulomb failure stress should reach its maximum value on the day of the Pohang earthquake. The observed delay between each injection event and the Pohang earthquake on 15 November 2017 can be explained by a low hydraulic diffusivity of the bedrock values in the range 1×10^{-4}–5×10^{-4} m^2/s with the fault damage zone structure (5×10^{-6}–1 m^2/s). In this range, the fluid injection can cause a Coulomb failure stress change of up to 0.4–1.1 bar, although this is still much lower than the average of the stress drop ($\sim$20 bar; Song and Lee, 2019).

Table 4.1: List of poroelastic parameters except for the hydraulic diffusivity.

Name	Range	Used value†	Note
Shear modulus (G)	19–24 GPa (granite at T = 30–150 °C)[a]	22 GPa	Median
Skempton's coefficient (B)	0.5–0.9 (crustal rock)[b,c,d]	0.75	Median
Drained Poisson's ratio (ν)	–	0.25[d]	Granite
Biot coefficient (α)	0.20, 0.25 and 0.32 (granite when P_e = 1 kbar)[e]	0.25	Median
Frictional coefficient (μ)	0.6–0.85[f]	0.6[g]	Measurement of rock from PX-2
Dynamic viscosity (η)	–	0.15×10^{-3} Pa s[i]	T = 170 °C[h]

†Values used in the modeling.

[a]Hughes and Jones (1950).

[b]Detournay and Cheng (1993).

[c]Hart and Wang (1995).

[d]Rice and Cleary (1976).

[e]Coyner (1984).

[f]Byerlee (1978).

[g]Kwon et al. (2019).

[h]Lee et al. (2010).

[i]Wonham (1967).

T—Temperature.

P_e—Effective confining pressure.

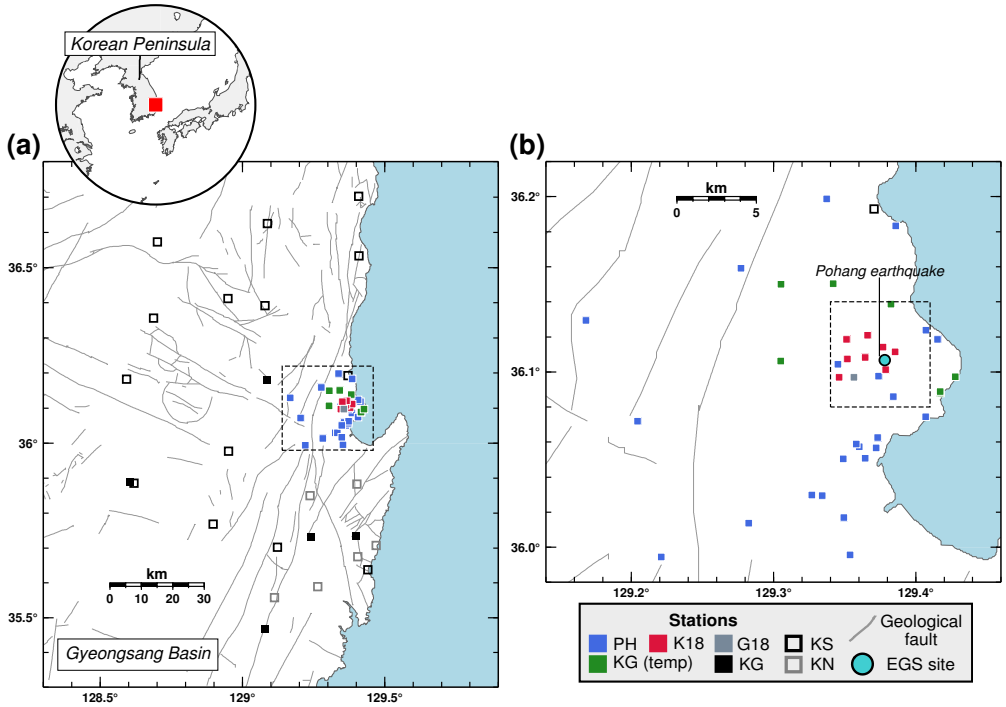

Figure 4.1: Map of the study region. (a) Map including all seismic stations used in the analysis with an inset showing East Asia. Station networks KS, KG, and KN are permanently deployed, while PH, K18, G18, and KG (temp) are temporarily deployed for aftershock monitoring. The area enclosed in the dashed box is shown in (b), and gray lines represent faults. (b) Map showing the temporary stations and one permanent station PHA2 (network KS). The network G18 consists of station POH01. G18—Grigoli et al. (2018). K18—Kim et al. (2018). KG—Korea Institute of Geoscience and Mineral Resources. KS—Korea Meteorological Administration. KN—Korea Hydro & Nuclear Power Co., Ltd. PH—Seoul National University and Pukyong National University. EGS—Enhanced geothermal system. See Fig. 4.B.2 for stations with station ID.

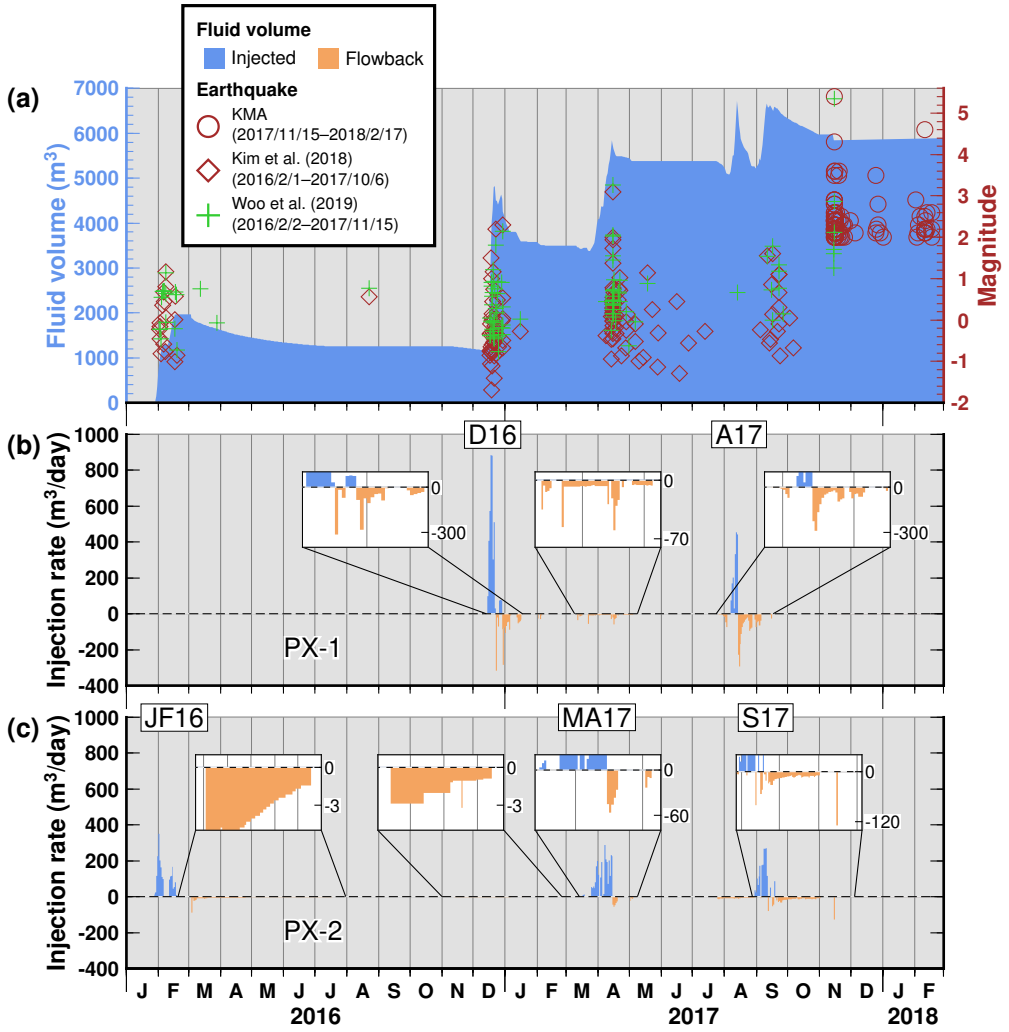

Figure 4.2: Fluid injection and flowback records for the Pohang enhanced geothermal system (EGS) operation (Kim et al., 2018; Korean Government Commission, 2019). The final fluid injection was performed in September 2017 (Kim et al., 2018; Korean Government Commission, 2019). (a) Cumulative net fluid volume and earthquakes. Earthquakes reported by four sources (103 of them by the Korea Meteorological Administration, `http://necis.kma.go.kr/`, last accessed on 26 February 2018; 135 by Kim et al., 2018; and 97 by Korean Government Commission, 2019 and Woo et al., 2019) are shown as circles, diamonds and crosses, respectively. (continued)

Figure 4.2: (continued) The catalogue of Kim et al. (2018) includes unlocatable earthquakes. Note that the magnitude scales are different for the three catalogues. (b) Fluid injection and flowback rate at the well PX-1. (c) Fluid injection and flowback rate at the well PX-2. Insets magnify the smaller rates. Total injected volumes at PX-1 and PX-2 are 1,695 m^3 and 4,146 m^3, respectively.

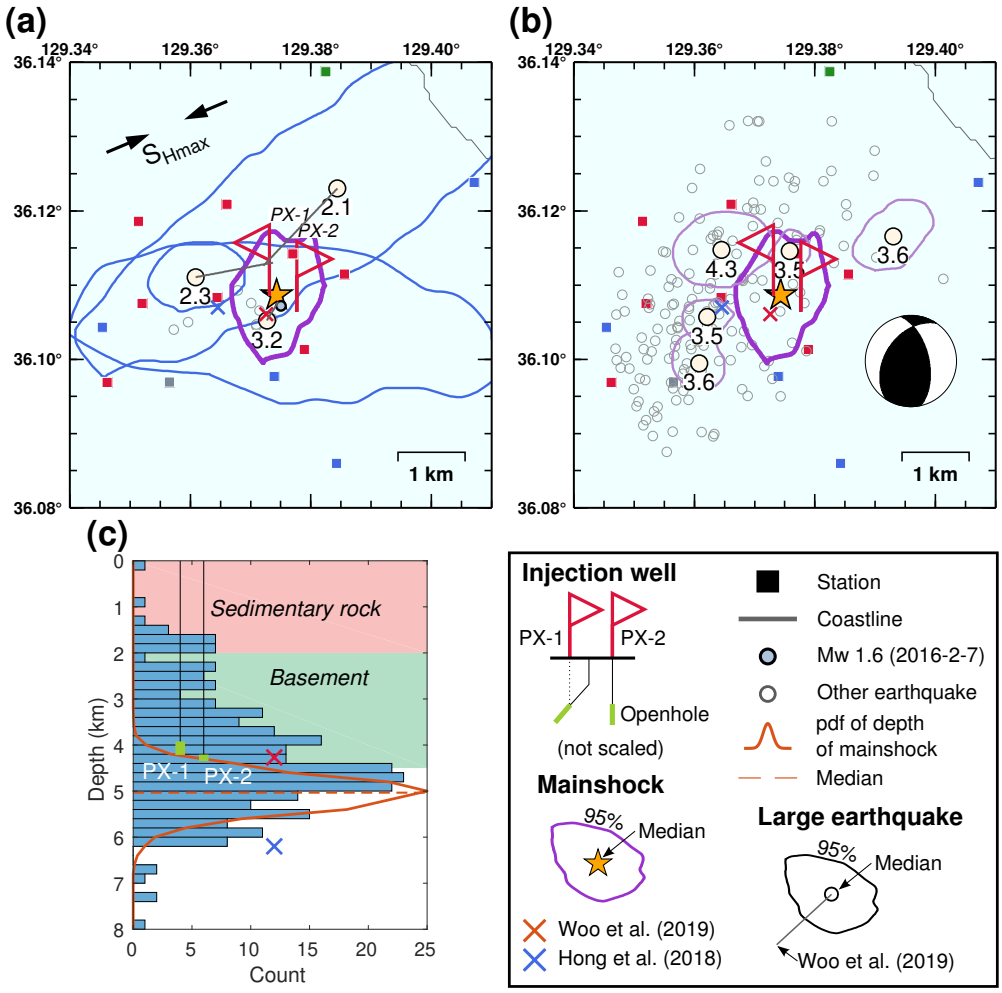

Figure 4.3: Earthquake epicenters in terms of probability density functions (*pdf*s). (a) Epicentral *pdf*s of the Pohang earthquake on 15 November 2017 05:29, Mw 1.6 earthquake on 7 February 2016, 22:04; Mw 2.1 earthquake on 22 December 2016, 20:31; Mw 2.3 earthquake on 29 December 2016, 12:32; and Mw 3.2 earthquake on 15 April 2017, 02:31 (Fig. 4.2a). The direction of the maximum horizontal principal stress (S_{Hmax}) is indicated by black arrows (Soh et al., 2018). The red and blue 'X' symbols indicate the locations of the Pohang earthquake according to Hong et al. (2018) and Woo et al. (2019), respectively. (b) Epicentral *pdf*s of the Pohang earthquake and aftershocks. (continued)

Figure 4.3: (continued) The information on the aftershocks, from top to bottom, is as follows: 16 November 2017, 00:02 for M_L 3.6; 15 November 2017, 07:49 for M_L 4.3; 19 November 2017, 14:45 for M_L 3.5; 25 December 2017, 07:19 for M_L 3.5; and 15 November 2017, 05:32 for M_L 3.6. An inset shows the focal mechanism used to obtain the ΔCFS in the poroelastic model (214°, 43° and 128° for strike, dip and rake, respectively). (c) Focal depth *pdf* of the Pohang earthquake and distribution of the earthquakes. Background colors represent simplified geological strata information at a depth of 0–4.5 km (Lee and Sheen, 2015).

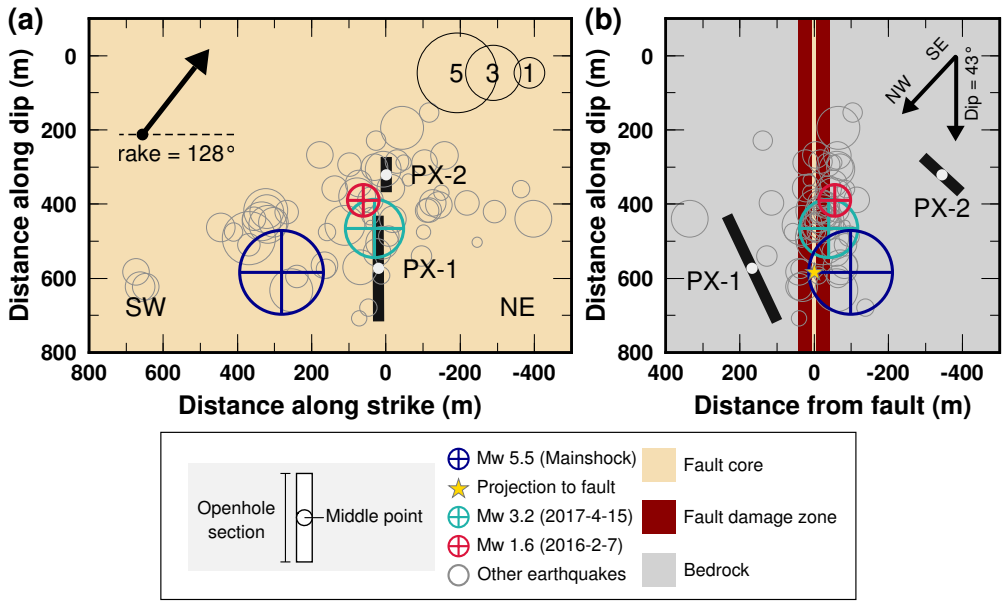

Figure 4.4: Geometry of the poroelastic modeling. (a) Fault-plane view. Openhole sections are represented as thick solid lines. In the model, the injection points for the wells PX-1 and PX-2 are at the mid-points of the openhole sections, marked as white circles. (b) Fault-normal view. The fault-plane in (a) crosses the fault-core perpendicularly. The history of the poroelastic stress is sampled at a projected point, marked as a yellow star, from the mainshock hypocenter. The thicknesses of the fault core and damage zone are 10 m and 85 m, respectively, following the reported values (Ellsworth et al., 2019; Korean Government Commission, 2019). The ranges of hydraulic diffusivity for the damage zone and bedrock (D_{dmz} and D_{bed}, respectively) are searched independently. The strike (214°), dip (43°), and rake (128°) of the fault, and the earthquake locations are from Woo et al. (2019). Only the earthquakes associated with the injection at PX-2 are plotted (Woo et al., 2019). The three largest earthquakes of the injection events JF16 (Mw 1.6), MA17 (Mw 3.2), and S17 (mainshock) are indicated as colored crossed circles. The origin points (0 m, 0 m) in (a) and (b) are in PX-2, which is vertical, at a depth of 3.8 km (Woo et al., 2019).

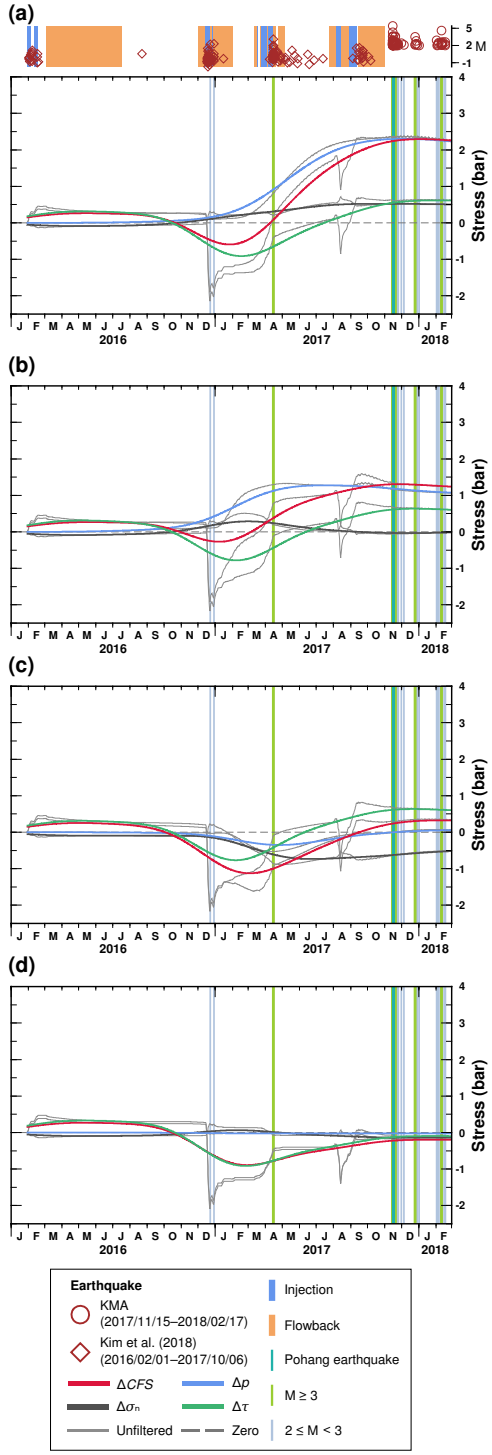

Figure 4.5: (Caption in next page)

Figure 4.5: Temporal changes in poroelastic stress changes between January 2016 and February 2018. The stresses are sampled where the mainshock hypocenter projects onto the fault plane (yellow star in Fig. 4.4b). (a) Homogeneous model. The hydraulic diffusivities for bedrock and fault damage zone are: $D_{\mathrm{bed}} = D_{\mathrm{dmz}} = 5 \times 10^{-4}$ m^2/s. (b) Model including a permeable fault damage zone. $D_{\mathrm{bed}} = 5 \times 10^{-4}$ m^2/s and $D_{\mathrm{dmz}} = 1 \times 10^{-2}$ m^2/s. (c) Model including a highly permeable fault damage zone. $D_{\mathrm{bed}} = 5 \times 10^{-4}$ m^2/s and $D_{\mathrm{dmz}} = 1 \times 10^{1}$ m^2/s. (d) Model with impermeable bedrock and a permeable fault damage zone. $D_{\mathrm{bed}} = 1 \times 10^{-6}$ m^2/s and $D_{\mathrm{dmz}} = 1 \times 10^{-2}$ m^2/s. (Also, see Fig. 4.B.3 for the result from the homogeneous model with $D_{\mathrm{bed}} = D_{\mathrm{dmz}} = 1 \times 10^{-2}$ m^2/s.) Gaussian lowpass filtered stresse changes (with a standard deviation of 2 months) are shown as colored lines. Unfiltered stresse changes in background are shown as grey lines. See Fig. 4.B.4 for a version showing grey and color reversed. The filtered curves show the Coulomb stress change (ΔCFS) tending to increase in (a), slightly increase in (b), decrease in (c), and remain nearly constant in (d) around 15 November 2017. Upper panel shows the history of the injection and flowback (Kim et al., 2018; Korean Government Commission, 2019), and earthquakes (Kim et al., 2018). $\Delta\tau$—Shear stress change. Δp—Pore pressure change. $\Delta\sigma_{\mathrm{n}}$—Normal stress change. M—Magnitude.

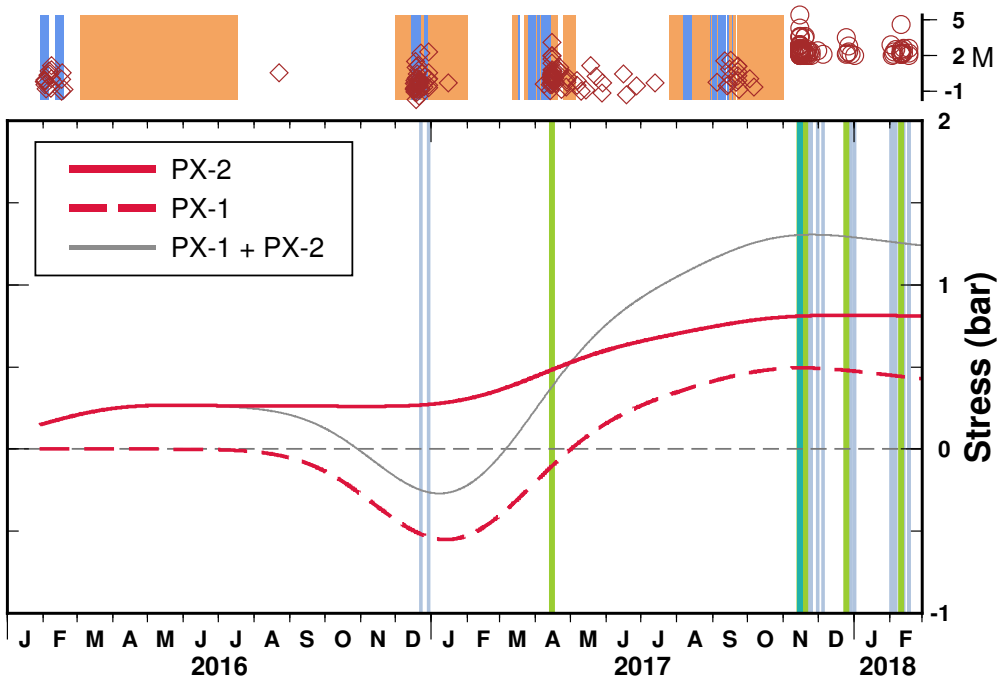

Figure 4.6: Coulomb failures stress change (ΔCFS) due to injection at each well. Hydraulic diffusivities for bedrock and fault damage zone are set as $D_{\text{bed}} = 5 \times 10^{-4}$ m^2/s and $D_{\text{dmz}} = 1 \times 10^{-2}$ m^2/s, respectively, which are the same as those for Fig. 4.5b. The grey line is plotted as a reference and represents ΔCFS considering both wells, also the same as in Fig 4.5b. See the caption of Fig 4.5 for the definitions of the symbols and lines.

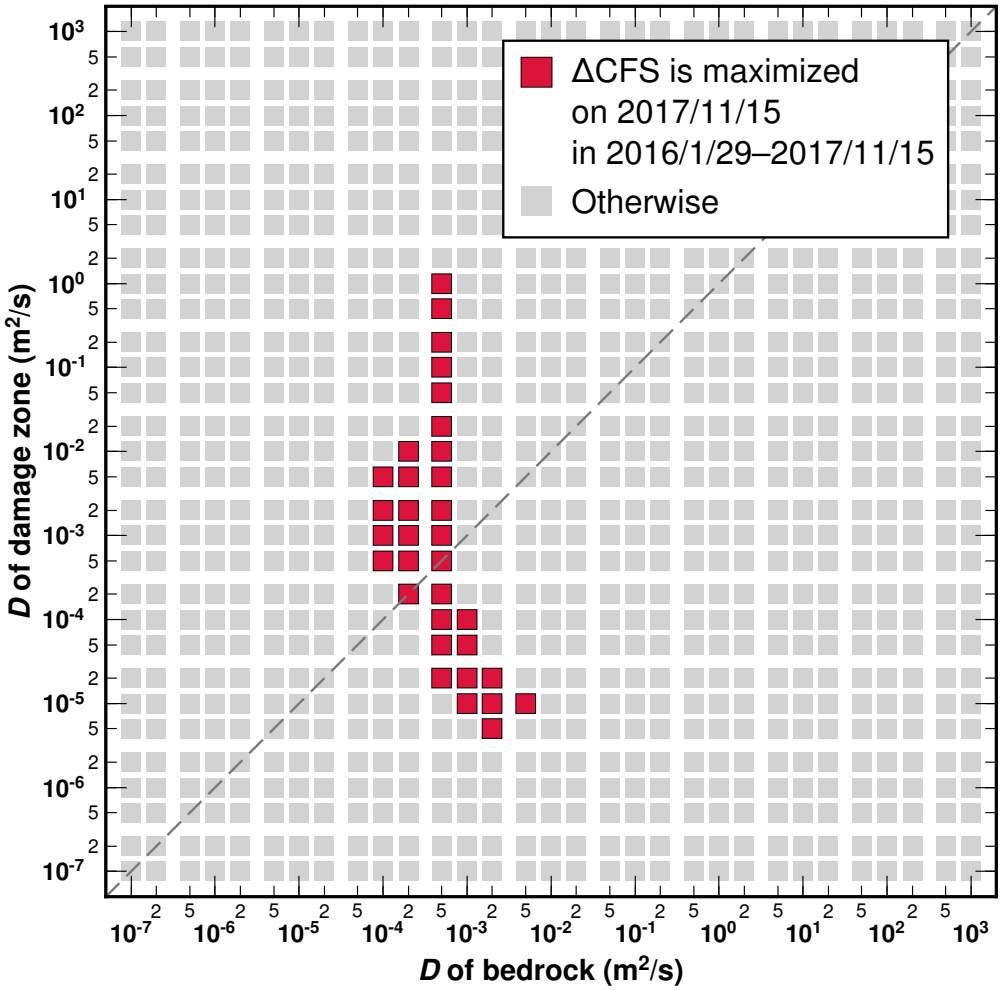

Figure 4.7: The ranges of hydraulic diffusivities for the fault damage zone and bedrock, D_{dmz} and D_{bed} respectively, that satisfy the criteria for the Coulomb stress change (ΔCFS) amplitude at the time of the Pohang earthquake. A red square indicates values that meet the condition that ΔCFS is maximized on 15 November 2017, from within the period from 29 January 2016, until then. Squares lying on the diagonal, dashed line indicate a homogeneous model (i.e., $D_{\mathrm{dmz}} = D_{\mathrm{bed}}$).

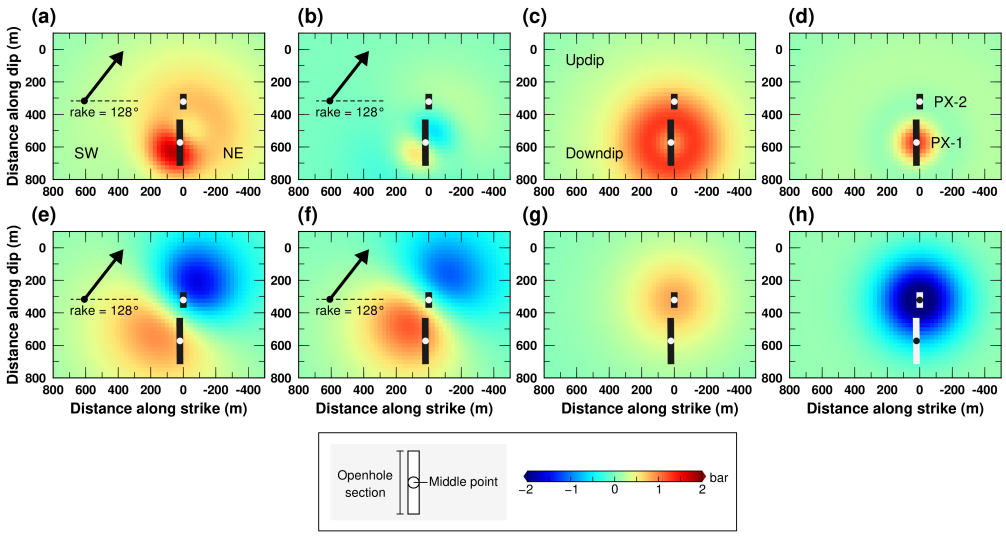

Figure 4.8: Snapshot images on 15 November 2017, for stresses and pore pressure changes due to injection at the wells (a–d) PX-1 and (e–h) PX-2. Hydraulic diffusivities for bedrock and fault damage zone are $D_{\mathrm{bed}} = 5 \times 10^{-4}$ m^2/s and $D_{\mathrm{dmz}} = 1 \times 10^{-2}$ m^2/s, respectively (same as Fig. 4.5b). (a) Coulomb stress change (ΔCFS) by PX-1. (b) Shear stress change ($\Delta\tau$) by PX-1. (c) Pore pressure change (Δp) by PX-1. (d) Normal stress change ($\Delta\sigma_{\mathrm{n}}$) by PX-1. (e) ΔCFS by PX-2. (f) $\Delta\tau$ by PX-2. (g) Δp by PX-2. (h) $\Delta\sigma_{\mathrm{n}}$ by PX-2. ΔCFS is obtained by Equation (5) where $\mu = 0.6$ (Table 4.1). No fault core is included in the model (i.e., $D_{\mathrm{core}} = D_{\mathrm{dmz}}$). No temporal Gaussian filter is applied.

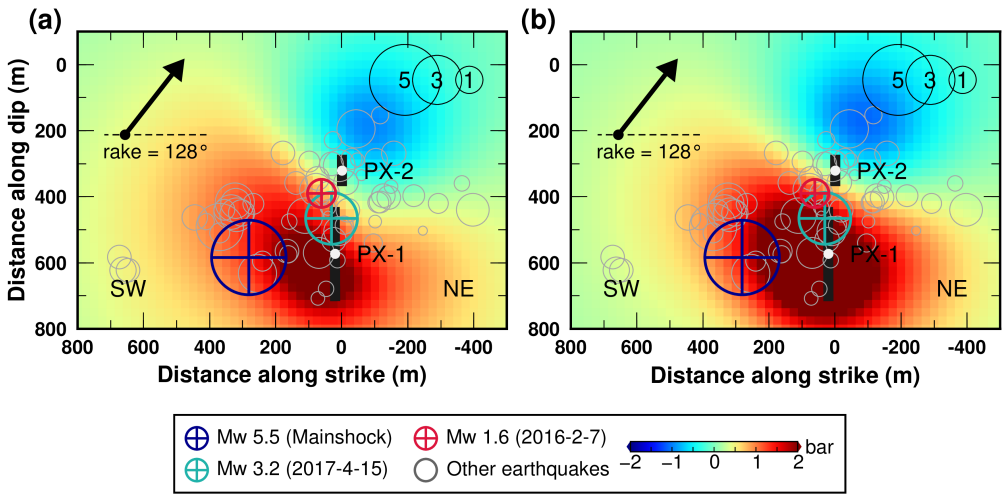

Figure 4.9: Total Coulomb stress (ΔCFS) on the fault plane caused by injection at the wells PX-1 and PX-2. This is the sum of the values of ΔCFS by PX-1 (Fig. 4.8a) and PX-2 (Fig. 4.8e). (a) ΔCFS without an impermeable core. (b) ΔCFS with the impermeable core. Thickness and hydraulic diffusivity, D, of the core are 10 m and 10^{-6} m^2/s, respectively, the same as those of Ellsworth et al. (2019) and Korean Government Commission (2019; Fig. 4.4b). See Fig. 4.B.7 for pore pressure change, shear stress and normal stress changes by PX-1 and PX-2. Only the earthquakes associated with the injection at PX-2 are plotted (Woo et al., 2019). No temporal Gaussian filter is applied. Information of the fault geometry and earthquake locations are taken from Korean Government Commission (2019) and Woo et al. (2019).

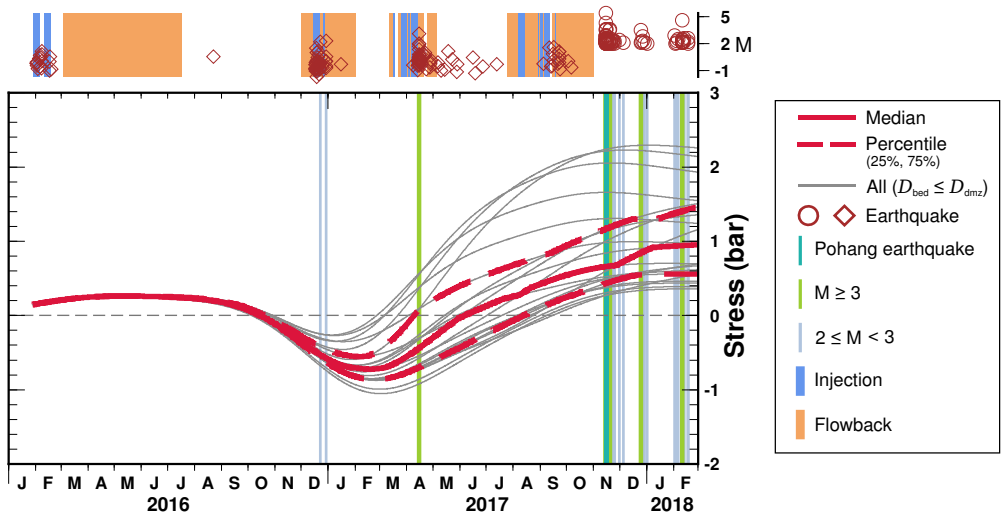

Figure 4.10: Temporal evolution in the Coulomb stress change (ΔCFS) satisfying the criterion for its maximum amplitude on 15 November 2017, and also a condition that the hydraulic diffusivity for the fault damage zone, D_{dmz}, is larger than or equal to that for the bedrock, D_{bed} (the 21 red squares within the upper triangle in Fig. 4.7). The median is indicated as a red solid line and the 25th and 75th percentiles as red dashed lines. Upper panel shows the history of the fluid injection and flowback (Kim et al., 2018; Korean Government Commission, 2019), and earthquakes (Kim et al., 2018). M—Magnitude.

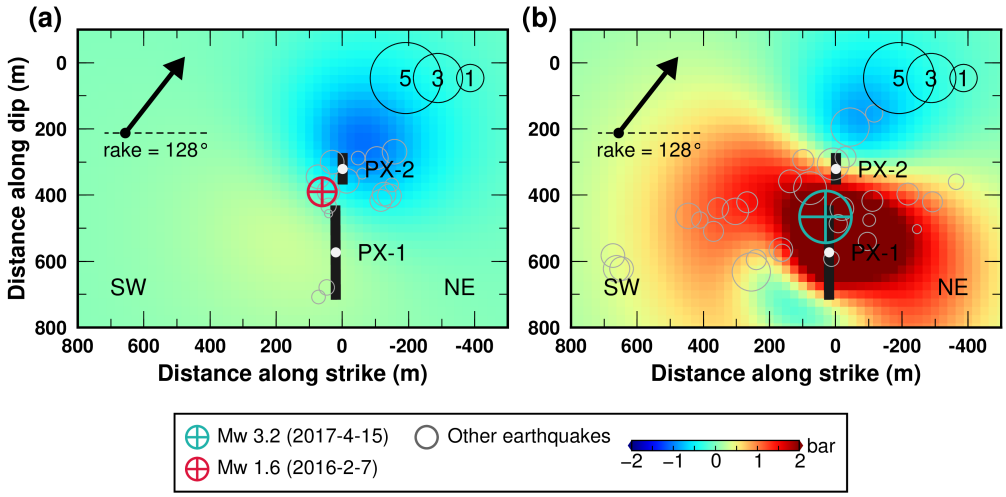

Figure 4.11: Coulomb stress change (ΔCFS) on the fault plane caused by injection at the wells PX-1 and PX-2. The hydraulic diffusivities for bedrock and fault damage zone are $D_{\mathrm{bed}} = 5 \times 10^{-4}$ m^2/s and $D_{\mathrm{dmz}} = 1 \times 10^{-2}$ m^2/s, respectively (same as Fig. 4.5). (a) A snapshot of stress on 7 February 2016, when the Mw 1.6 earthquake, the largest event during the injection event JF16, occurred. The other earthquakes before 22 August 2016 (Korean Government Commission, 2019; Woo et al., 2019) are shown as grey circles. (b) A snapshot of stress on 15 April 2017, when the Mw 3.2 earthquake, the largest event during the injection event MA17, occurred. See Fig. 4.B.8 for pore pressure, shear stress and normal stress changes by PX-1 and PX-2. The other earthquakes from 8 April 2017 to 18 May 2017 are shown as grey circles. No temporal Gaussian filter is applied.

Appendices

4.A Hypocenter determination

We sample the *pdf*s of the hypocenters using the Bayesian hierarchical multiple-event location method (*bayesloc*), applying corrections to the travel-time curve (i.e., one-dimensional velocity model) and different weights to the measurements of the arrival times (Myers et al., 2007). This probabilistic approach permits the resolution of absolute location and is robust against poor network configuration (Myers et al., 2007). In this study, eight Markov chains are used to sample the *pdf* with 10,000 iterations, resulting in 4,000 chains at the final iteration for an individual earthquake. The resulting posterior samples are used to estimate marginal distributions, such as epicenters and probability regions (Myers et al., 2007).

A total of 311 earthquakes that occurred between 22 December 2016 and 17 February 2018 are analyzed for probabilistic earthquake relocation (Fig. 4.3). We use two earthquake catalogues that were available from the Korea Meteorological Administration (KMA) and the study by Kim et al. (2018). Kim et al. (2018) reported six foreshocks and 210 aftershocks in the 3 hours immediately after the Pohang earthquake. Using the bayesloc method for the hypocenters of the aftershocks improves the accuracy of the locations of the mainshock and also the previous earthquakes. Networks KS, KN, KG, K18, and G18 recorded the Pohang earthquake, and networks

PH and KG (temporary stations) only provided waveforms of the aftershocks, since they were deployed a few days after the Pohang earthquake (Fig. 4.1). See Fig. 4.B.9 for a timetable of the seismic data. In this study, we use the one-dimensional velocity model of Korean Government Commission (2019), which is a composite based on an active source survey less than 5 km from the injection wells for constraining the shallow-depth structure and the regional velocity model of Kim et al. (2011) for the deep structure (Fig. 4.B.10). To avoid interference due to diffracted waves from the Moho (i.e., Pn and Sn), P and S wave arrival times from stations within 80 km of the source region are manually measured from the vertical and transverse components of their raw seismic waveforms, respectively.

K18 and G18, located at or near the EGS site (Fig. 4.1), recorded the Pohang earthquake, and they are critical for reducing the uncertainties on its focal depth and epicenter location to less than 1 km. Excluding their data (i.e., using only that from the permanent networks KS, KG, and KN in Fig. 4.1) results in an uncertainty exceeding 1 km for the epicenter location, and of up to 8 km for the focal depth.

The standard deviation of the differences between the measured arrival times and fitted straight lines are 0.02 s for P wave at stations near to the EGS (stations K18 and G18) and 0.18 s for P wave and 0.66 s for S wave at distant stations ($<$80 km; Fig. 4.B.11). The deviations from the straight line indicate a level of three-dimensional heterogeneity in the medium or errors in the measurements, contributing to an epicentral uncertainty of the order of 1 km.

4.B Supplementary materials (figure)

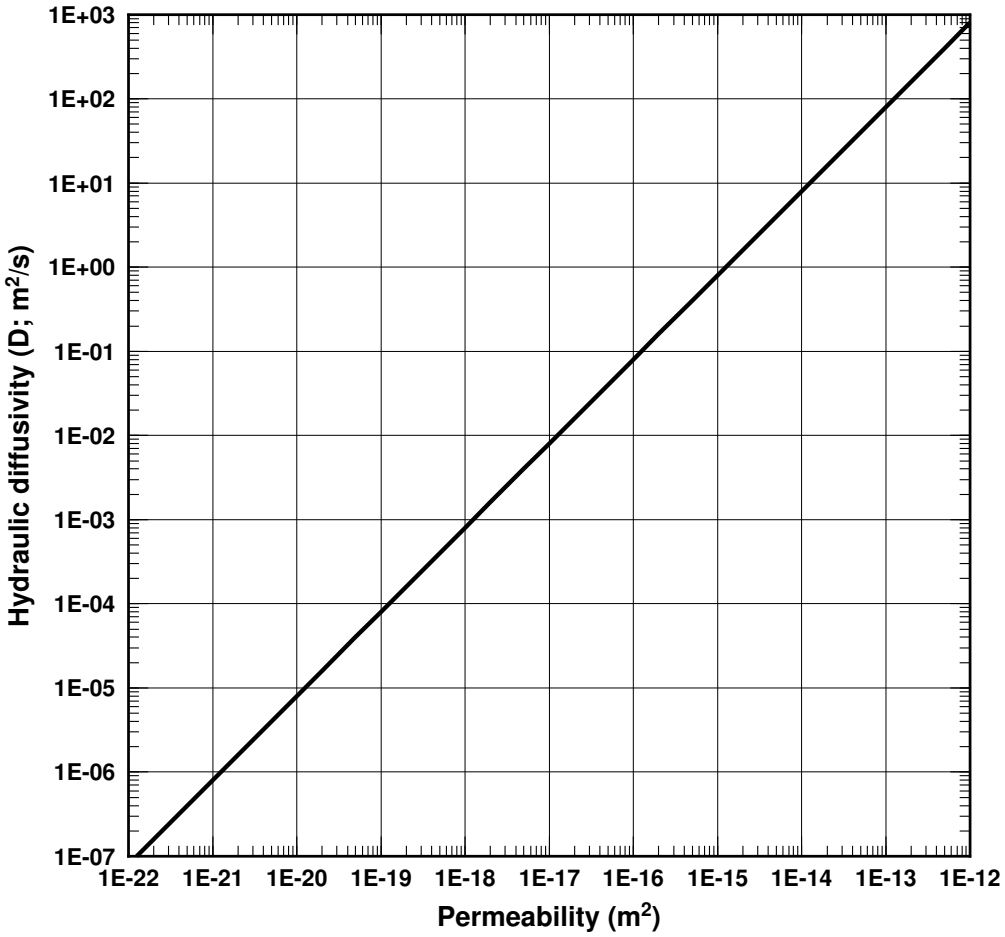

Figure 4.B.1: Relation between the permeability and the hydraulic diffusivity (D) based on Equation (4.3) and poroelastic parameters (Table 4.1).

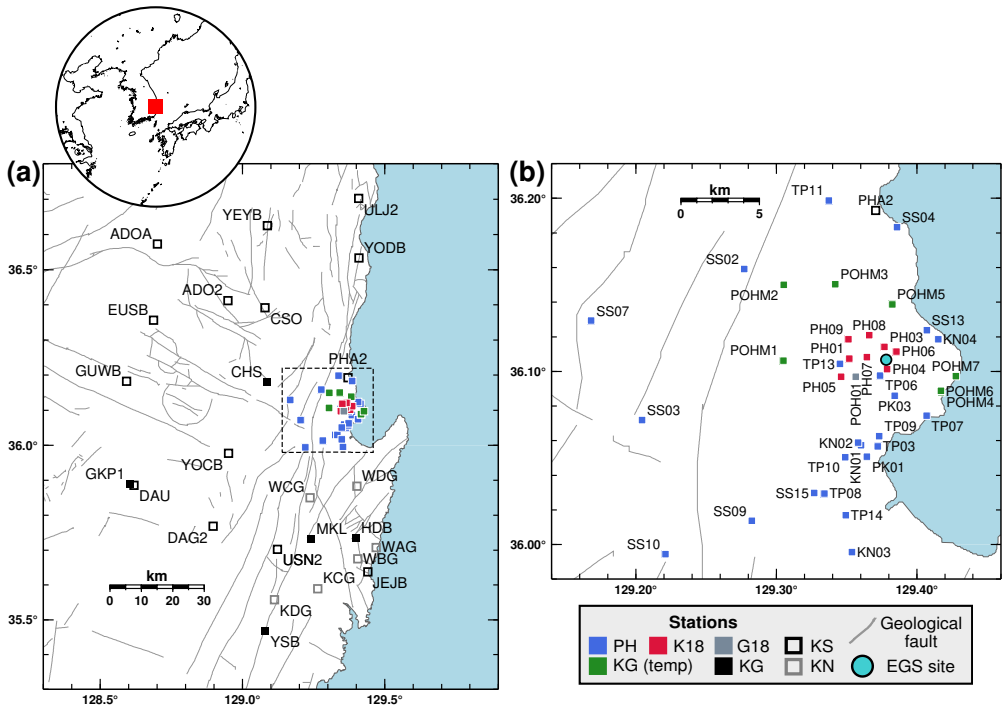

Figure 4.B.2: Map of the study region. (a) Map including all of the seismic stations used in the analysis with an inset showing East Asia. Networks KS, KG, and KN are deployed permanently, and PH, K18, G18, and KG (temp) are deployed temporarily for aftershock monitoring. The area enclosed in a dashed box is shown in (b), and gray lines represent faults. (b) Map showing the temporary stations and one permanent station PHA2. G18—Grigoli et al. (2018). K18—Kim et al. (2018). KG—Korea Institute of Geoscience and Mineral Resources. KS—Korea Meteorological Administration. KN—Korea Hydro & Nuclear Power Co., Ltd. PH—Seoul National University and Pukyong National University. EGS—Enhanced geothermal system.

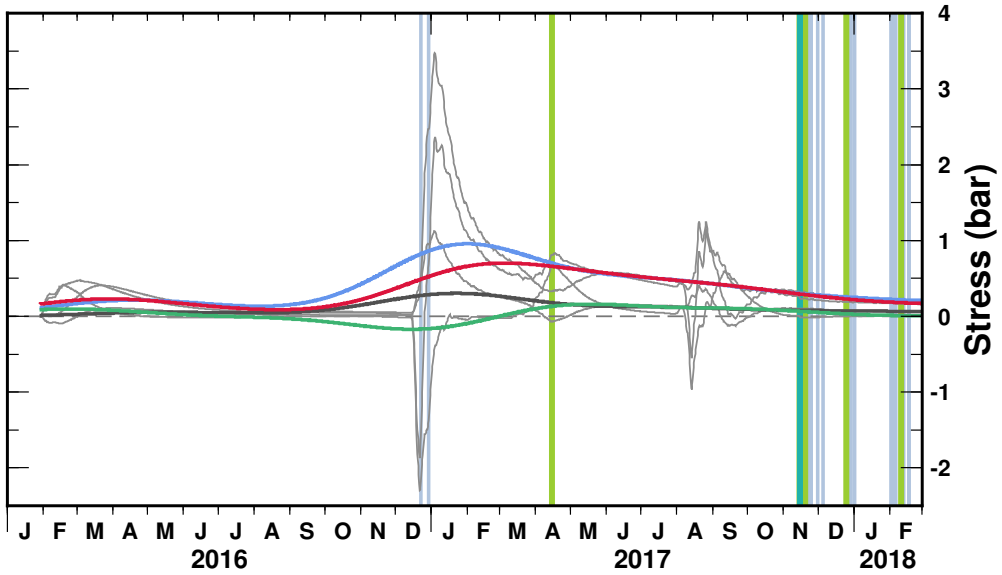

Figure 4.B.3: Similar to Fig. 4.5. $D_{\text{bed}} = D_{\text{dmz}} = 1 \times 10^{-2}$ m^2/s.

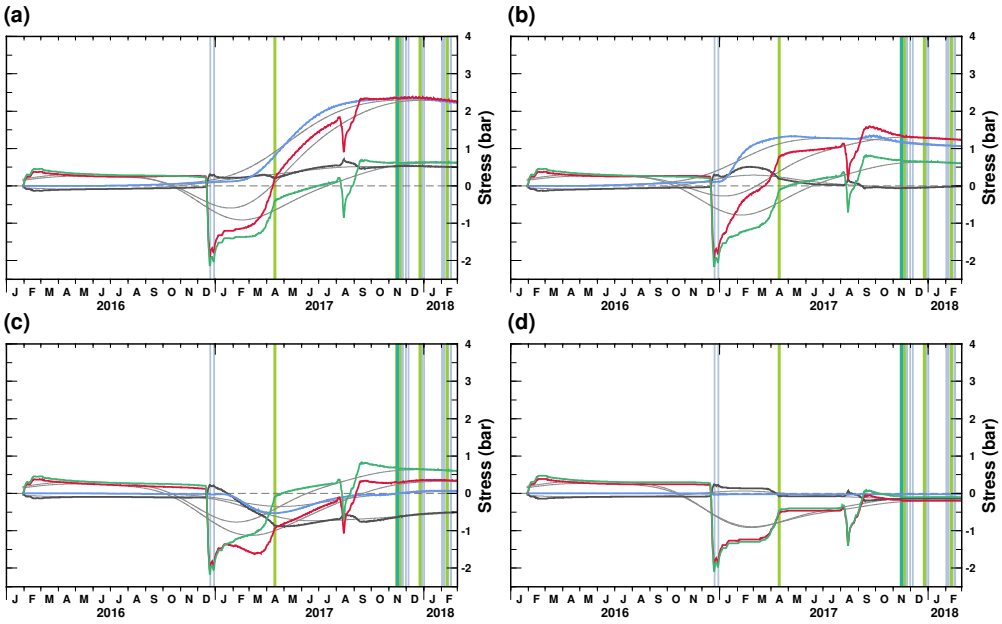

Figure 4.B.4: Same as Fig. 4.5 but with different color scheme. Unfiltered stresses and pore pressure are shown in colors and filtered ones in grey.

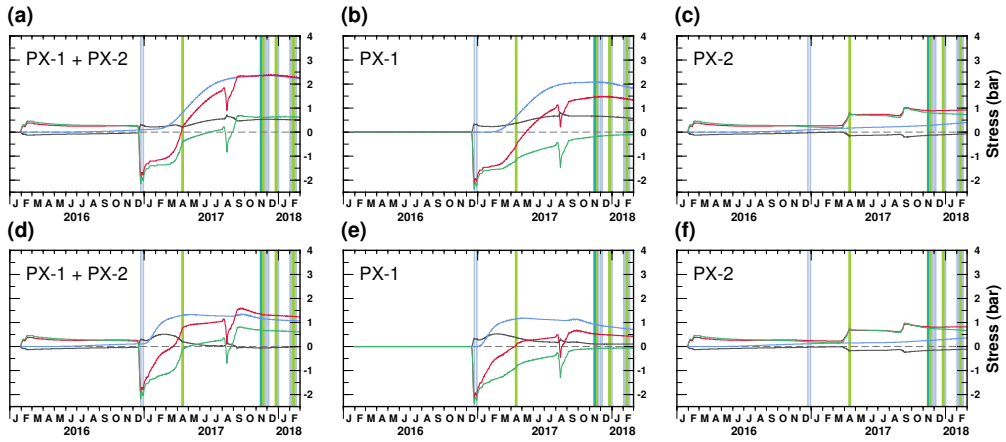

Figure 4.B.5: Changes in stresses and pore pressure by injection at the wells. Gaussian filter is not applied. (a–c) Results from the homogeneous model ($D_{\mathrm{bed}} = D_{\mathrm{dmz}} = 5 \times 10^{-4}$ m^2/s). The stress changes and pore pressure change in (a) are same with those shown in Fig. 4.5a (grey lines) and Fig. 4.B.4a (colored lines). The stress changes and pore pressure change due to the injection at PX-1 and PX-2 are shown in (b) and (c), respectively. (d–f) Results from the model including a permeable fault damage zone. $D_{\mathrm{bed}} = 5 \times 10^{-4}$ m^2/s and $D_{\mathrm{dmz}} = 1 \times 10^{-2}$ m^2/s. The stress changes and pore pressure change in (d) are same with those shown in Fig. 4.5b (grey lines) and Fig. 4.B.4b (colored lines). The stress changes and pore pressure change due to the injection at PX-1 and PX-2 are shown in (e) and (f), respectively. See also a caption of Fig. 4.5.

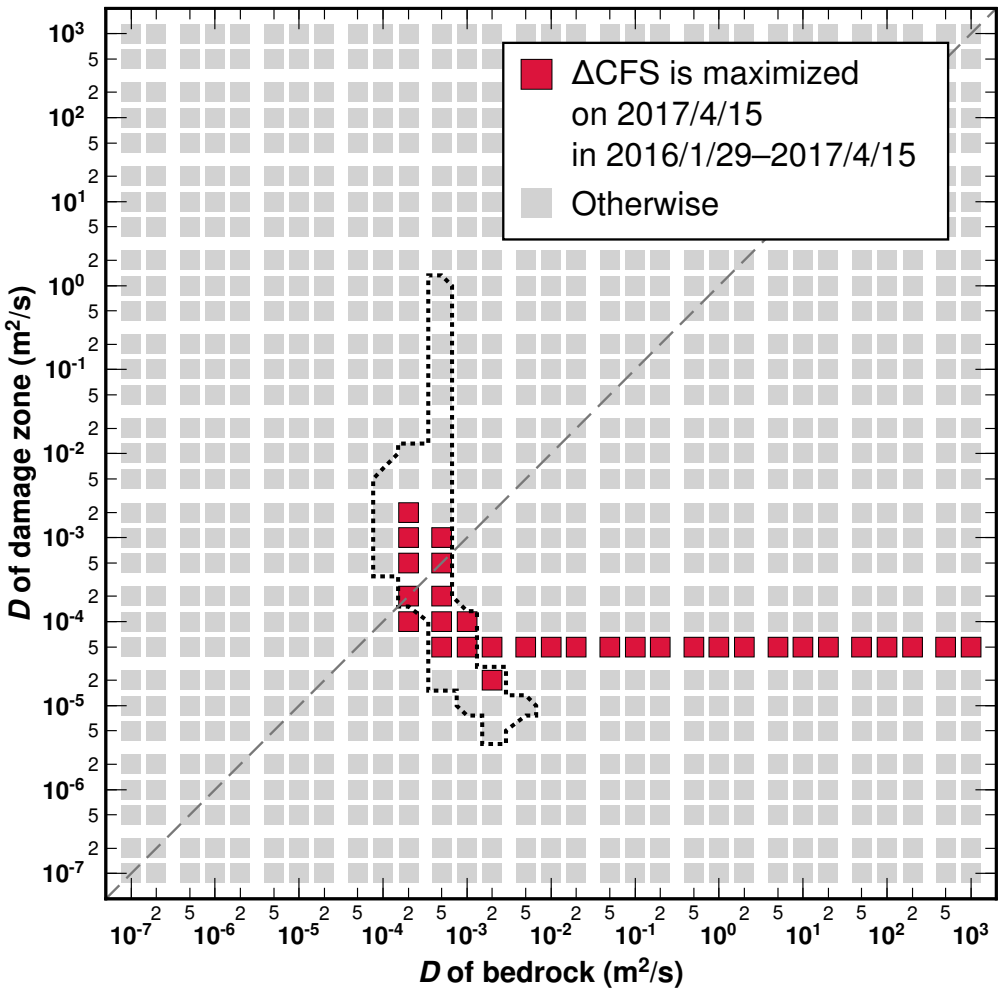

Figure 4.B.6: The ranges of hydraulic diffusivities for the fault damage zone and bedrock, D_{dmz} and D_{bed} respectively, that satisfy the criteria for the Coulomb stress change (ΔCFS) amplitude at the time of the Mw 3.2 earthquake on 15 April 2017. See a caption of Fig. 4.7 for detailed information. Dotted line indicates the red square zone in Fig. 4.7.

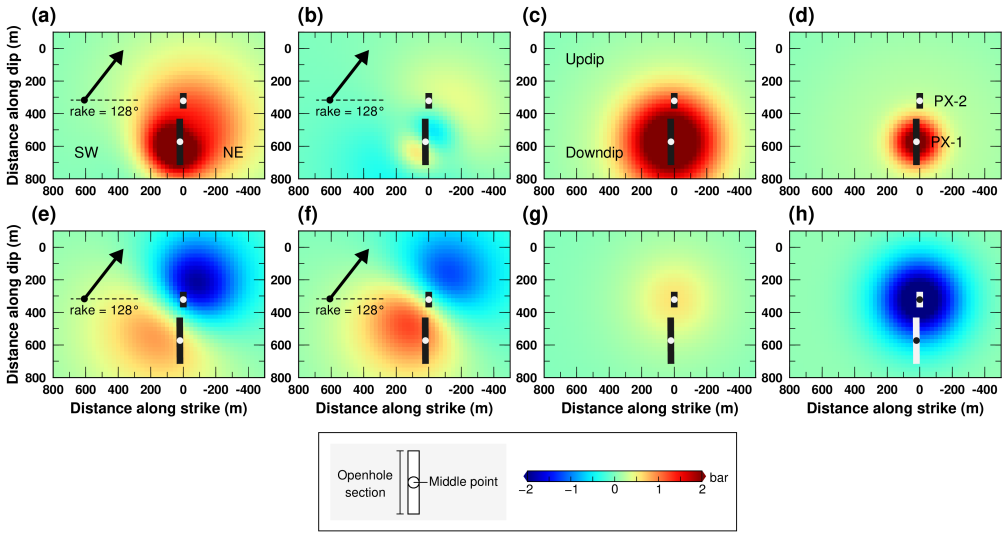

Figure 4.B.7: Stress changes and pore pressure change sampled along the fault plane on 15 November 2017, computed with the impermeable core model (Fig. 4.9b). (a) ΔCFS by the PX-1. (b) $\Delta\tau$ by the PX-1. (c) Δp by the PX-1. (d) $\Delta\sigma_{\mathrm{n}}$ by the PX-1. (e) ΔCFS by the PX-2. (f) $\Delta\tau$ by the PX-2. (g) Δp by the PX-2. (h) $\Delta\sigma_{\mathrm{n}}$ by the PX-2.

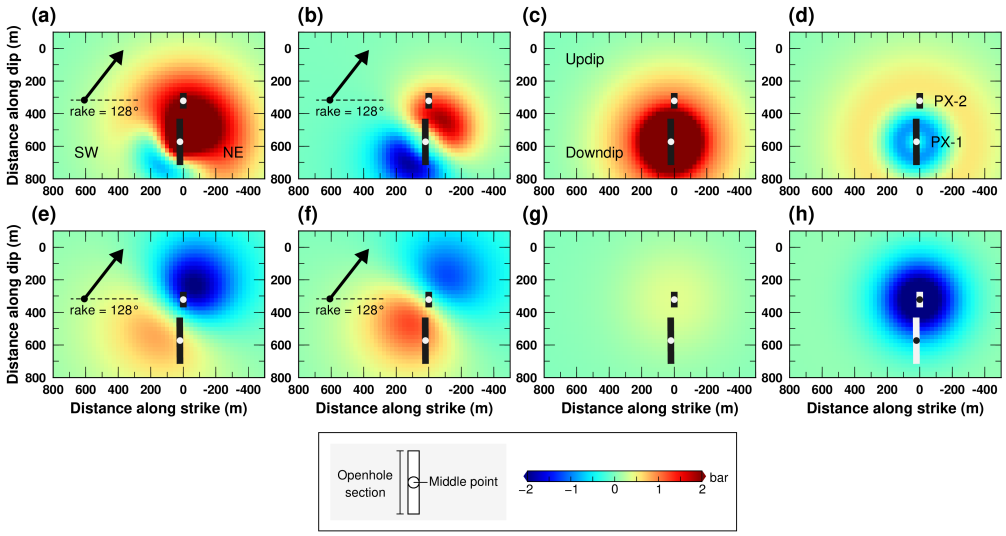

Figure 4.B.8: Stress changes and pore pressure change sampled along the fault plane on 15 April 2017, computed (Fig. 4.11b). (a) ΔCFS by the PX-1. (b) $\Delta\tau$ by the PX-1. (c) Δp by the PX-1. (d) $\Delta\sigma_{\mathrm{n}}$ by the PX-1. (e) ΔCFS by the PX-2. (f) $\Delta\tau$by the PX-2. (g) Δp by the PX-2. (h) $\Delta\sigma_{\mathrm{n}}$ by the PX-2.

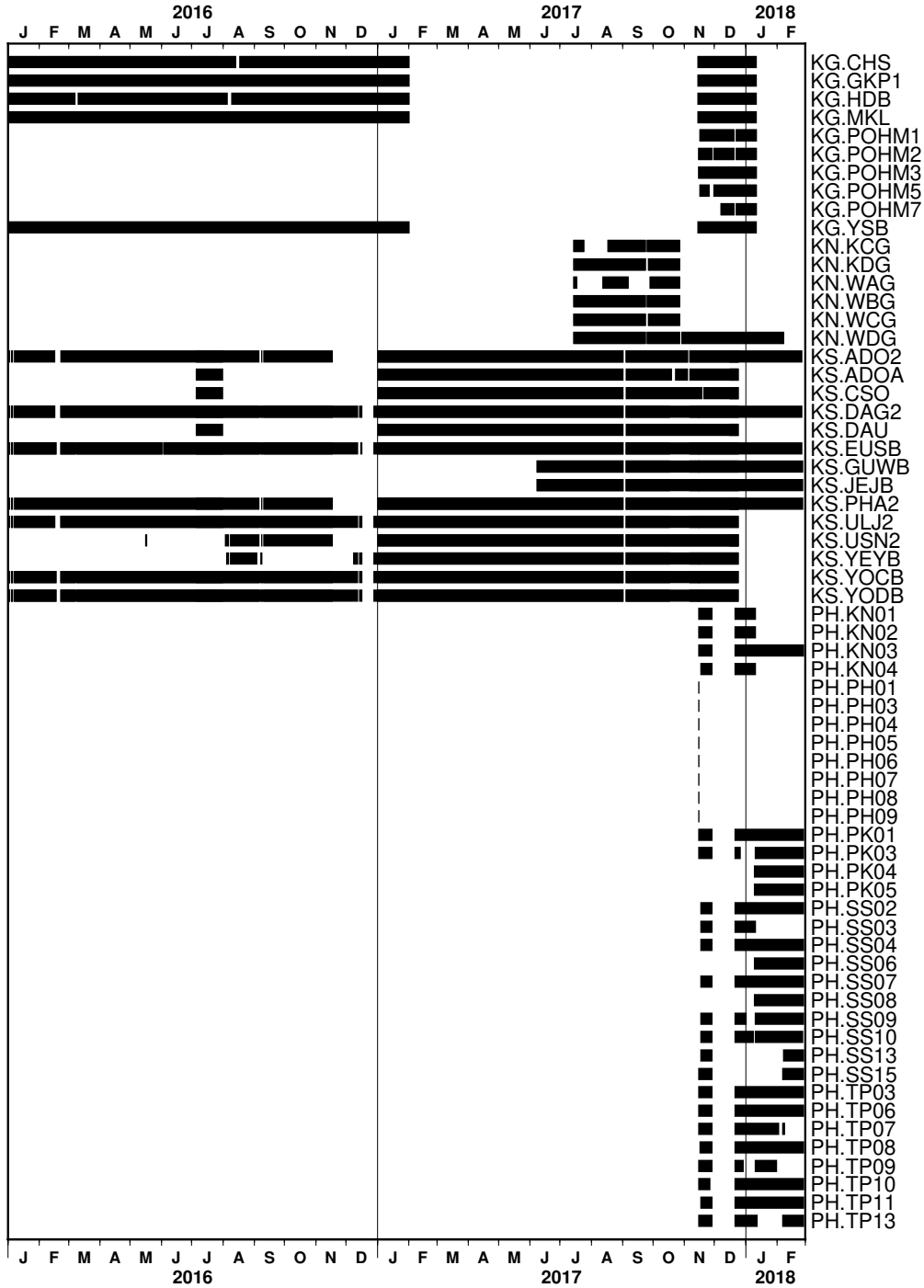

Figure 4.B.9: (Caption in next page)

Figure 4.B.9: Timetable showing used seismic data in this study. The text on the right hand side shows the names of network and station in format of "network.station". See Figs 4.1 and 4.B.2 for the station locations in a map view.

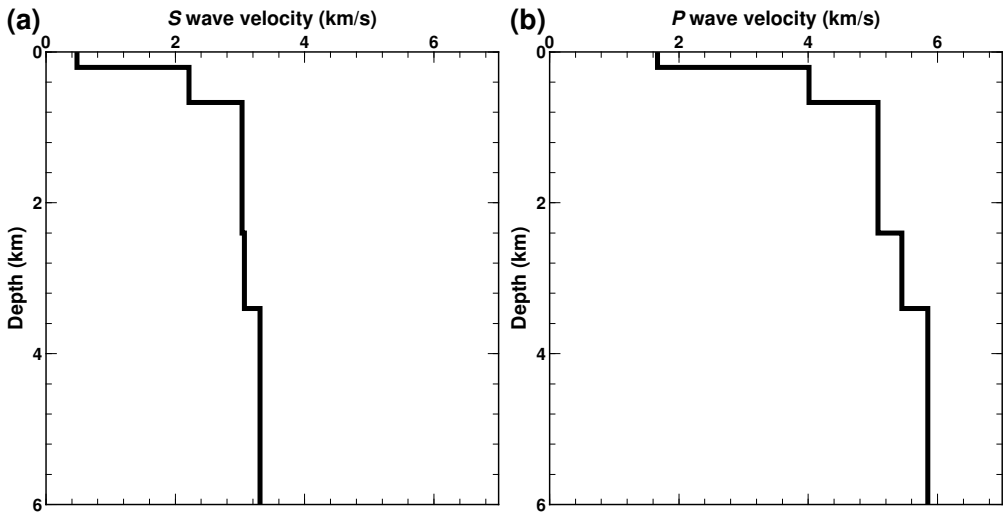

Figure 4.B.10: The one-dimensional velocity model used to locate hypocenters. (a) S wave velocity model. (b) P wave velocity model. The model is taken from Table 5-1 of Korean Government Commission (2019).

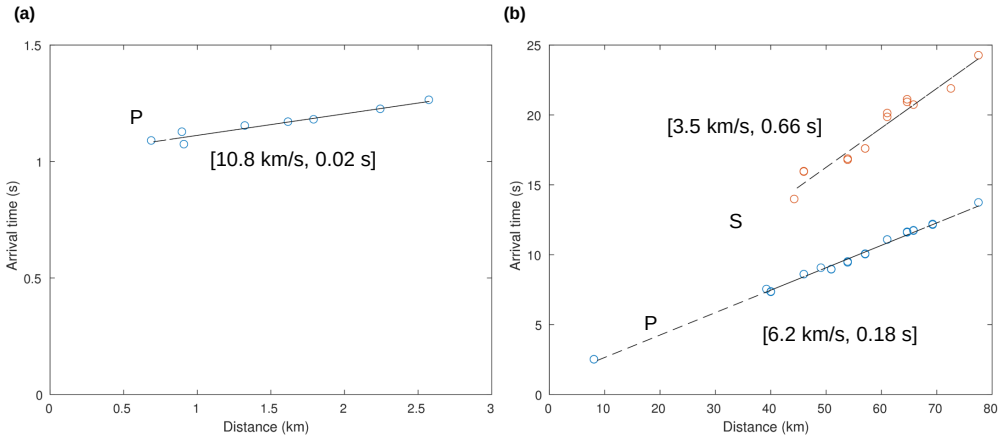

Figure 4.B.11: Measured arrival times as a function of the epicentral distance for the Pohang earthquake. (a) P waves measured at the stations close to the epicenter (K18 and G18; see Figs 4.1 or 4.B.2 for station network location). (b) P and S waves measured at distant stations. Slope of the fitted line and standard deviation of difference between the measured arrival time and the fitted line are shown inside the bracket.

4.C Supplementary materials (table)

Table 4.C.1: Hypocenter and uncertainty determined in this study.

ev_id	lat_median_deg	lon_median_deg	depth_median_km	time_median_s	north_sd_km	east_sd_km	depth_sd_km	time_sd_s	origin_time	ML	source_of_origin_time_ML	Mw	source_of_Mw
20000	36.12302	129.3844075	2.64335	0.6034	1.512898	2.057892	2.7723	0.7638	2016/12/22T20:31:32.000	2.2	KMA	Mw2.1	W19
20001	36.1110595	129.360889	1.63245	0.8396	0.173792	0.288338	1.0691	0.7147	2016/12/29T12:32:25.000	2.3	KMA	Mw2.3	W19
20002	36.1052265	129.3727015	1.79705	0.2523	0.409633	1.573526	6.1026	0.7241	2017/04/15T02:31:13.000	3.1	KMA	Mw3.2	W19
20003	36.1050395	129.359642	3.3288	0.41925	0.576213	5.885508	7.3995	0.9599	2017/04/15T08:16:47.000	2	KMA	-	-
							...						
20308	36.0783405	129.3369415	4.80285	0.9319	0.058923	0.117093	0.1674	0.7055	2018/02/10T20:07:23.000	2.5	KMA	-	-

ev_id—event id.

sd—standard deviation (1σ).

K18—Kim et al. (2018).

W19—Woo et al. (2019).

See an attached file. [click] 

Chapter 5

Fault zone structure imaged by teleseismic receiver function with geophone array in Clark fault, California

Abstract

We probe seismic structure of the fault zone from a linear geophone array across the Clark fault, part of strike-slip San Jacinto Fault Zone, in southern California, U.S. The 129 geophones were deployed across the distance of about 2.5 km, slightly oblique to the strike of the fault, and recorded 42 teleseismic earthquakes with M>5.5 during the deployment period of one month. Of the total 42 events, only one earthquake (2015-11-24 22:45:38, latitude: 10.54°S, longitude: 70.94°W, depth: 606 km, MW 7.6) was able to compute P-wave receiver functions for structural imaging because of low gain of instrument response at low frequencies (less than 1.0 Hz). The width of the fault zone is inferred as about 460 m from the delayed P-wave arrivals (up to 0.6 s) and a bifurcation of a reflection branch. Deconvolution of the vertical-component signal recorded from one station distant ($\sim$1.2 km) from the fault was effective to identify phases that are reverberated in or refracted by the narrow fault zone. We anticipate that the forward waveform modeling will help clarify the fault structure in terms of its geometry and seismic velocity.

5.1 Introduction

A seismic observation of a Clark fault, southern California, is explained in this chapter. The seismic constraint to the fault zone is important because a seismic low velocity within the fault zone is linked to stress, brittle–ductile transition zone, rheological properties, temperature, rupture of an earthquake, and heterogeneity in the source region. Seismic tomography reveals the structure of the fault with a finite width ranging from ten to hundreds of meters. However, the tomography method is not sensitive to velocity contrast. Alternatively, different ways involving high-frequency waves can reveal characteristics that cannot be observed by the tomographic method.

Fault-trapped waves by local earthquakes were used to determine the properties of the faults in various studies (e.g., Li and Leary, 1990; Li et al., 1990; Li et al., 1997; Jahnke et al., 2002; Ellsworth and Malin, 2011; Wu and Hole, 2011). We suggest a slightly different approach that uses a teleseismic earthquake instead of the local earthquake. It can be more advantageous than the approaches using the local earthquake because resolvable domain is not limited to region between seismogenic zone and surface. Also, a single or narrow value of slowness can make waveform stacking or modeling more straightforward.

In this proposal, a way to select a proper teleseismic earthquake for the analysis, first, is introduced. The calculation of the P wave RFs with a conventional deconvolution method using horizontal and vertical components at the same station (Langston, 1979) breaks down because of significant scattered phases in the vertical component by the fault zone. An alternative approach is explained, adopting the vertical component at a remote station that is located away from the fault zone. Lastly, methods for a future research plan to constraint the properties of the fault zone are listed.

5.2 Data and method

125 three-component geophones are deployed along ∼2.5 km profile across the Clark fault that is a segment of San Jacinto fault (Figs 5.1 and 5.2). An averaged interval of stations is ∼20 m. An operational period is from 21 November to 25 December 2015 for about one month. 42 teleseismic earthquakes with a magnitude over than 5.5 occurred in a distance of 30°–90° during this period. *PP* phases that detouring Core-Mantle boundary in a more distant range cannot be used because of low signal-to-noise ratio.

Instrumental response is deconvoluted to compensate low sensitivity of the geophone in low frequency (corner frequency is 5 Hz) and apply a bandpass filter from 0.08 to 15 Hz (Figs 5.3 and 5.4). The fault zone involves high seismic noise because of active crustal seismicity and trapped seismic ambient noise (Fig. 5.1). The noise can lead to a biased interpretation.

5.2.1 Earthquake selection

We not only confirm correlations of the waveforms (EW component) between stations after the arrival of the *P* wave, but also the correlation before the arrival of the *P* wave (signal and noise windows, respectively). Only one of the earthquakes have a low and high correlation in the noise and signal windows, respectively (Fig. 5.3). This earthquake with a magnitude of Mw 7.5 is an earlier one of a doublet that ∼5 minutes and 55 km apart from each other (Ye et al., 2016). An example of unused earthquakes is shown in Fig. 5.4, which show a strong correlation in the noise window although the correlation between the nearby stations is high in the signal window. The later one of the doublet (Ye et al., 2016) with a magnitude of Mw 7.6 is similar to the case in Fig. 5.4 because of coda wave remained after the earlier one.

5.2.2 Receiver function

Receiver function (RF) is obtained from water level deconvolution method to remove the source time function in horizontal components based on an equation 5.1 (Langston, 1979).

$$RF(\omega) = \frac{D(\omega)}{V(\omega)} \tag{5.1}$$

The $D(\omega)$ and $V(\omega)$ are horizontal and vertical components, respectively, in the P wave. The complex division in the equation 5.1 is unstable numerically because of small denominator $V(\omega)$. The equation 5.1 is modified to an equation 5.2 (Langston, 1979).

$$\begin{aligned} RF(\omega) &= \frac{D(\omega)V^*(\omega)}{\Phi(\omega)} \exp\left[-\frac{\omega^2}{2\sigma^2}\right], \\ \Phi(\omega) &= \max\left\{V(\omega)V^*(\omega), c\max\left[V(\omega)V^*(\omega)\right]\right\} \end{aligned} \tag{5.2}$$

In this study, the $D(\omega)$ could be one of radial (R) and tangential (T) components. The σ is a width of the Gaussian filter, the c ranging from 0 to 1 is water level, and the asterisk is a complex conjugate. The smaller value $V(\omega)V^*(\omega)$ than the constant $c\max\left[V(\omega)V^*(\omega)\right]$ in the equation 5.2 is changed to this constant. The padding with this constant loses a high-frequency information in the waveform because of a shape of a source spectrum (Houston and Kanamori, 1986). The high-frequency RF can be obtained by a decrease in c, with a permission of the numerical stability and the sufficiently large σ. The water levels c of 10^{-2} and 10^{-4} are used for low and high-frequency analysis, respectively, in this study.

5.2.3 Conventional P wave receiver functions

In the conventional P wave RFs study, the horizontal and vertical components replace the $D(\omega)$ and $V(\omega)$, respectively, in the equation 5.2 (e.g., Langston, 1979). Assump-

tion of the conventional RFs is that the vertical component approximates a source time function. However, a scattered P wave by a (nearly) vertical fault plane arrives later than the first P wave; the vertical component is no longer good approximation to the source time function.

5.2.4 Receiver functions with a fixed denominator

Source time function in the geophone array is similar because an aperture of the array is short ($\sim$2.5 km) (Fig. 5.2). Therefore, the vertical component at a distant station from the fault can replace that near the fault. A problem with switching is a slight time shift of the source time function. An amount of the time shift is determined from the direction and length of the array, a backazimuth of the earthquake, and a slowness. The expected maximum time shift is $\sim$0.125 s, that is not significant in this study. Although we remain the RFs, a correction to the time shift might not be difficult, using the difference in the arrival time either expected theoretically or measured with cross-correlation.

5.2.5 Z's over a Z of a single station

The interference in the vertical components with the scattered wave by the fault can be effectively visualized by removing the complex source time function (can be called by Z/Z RFs). The $D(\omega)$ is replaced by the vertical components of any stations and the $V(\omega)$ by the vertical component of a reference station that is distant from the fault. Ideally, the trace at the reference station should be the Gaussian function. The incoherent Z/Z RFs with that at the reference station indicate one of them is no longer a proper approximation to the source time function.

5.3 Results

5.3.1 Comparison between conventional and new receiver functions

The radial *RF*s using the conventional data processing (i.e., same station in numerator and denominator) geophone data are shown in Fig. 5.5. The stations 43–49 near the fault line (stations 52–56) in the noise window (before 0 s) involve strong monochromatic oscillation with ∼1.95 Hz (Fig. 5.6).

Using a single denominator, the vertical component of a station distant from the fault line (station 90 in this case), suppresses the monochromatic oscillation in the noise window in the station 43–49 (Fig. 5.7). This approach rules out a possible interference between the oscillation and the *RF*s in the signal window (after 0 s) near the fault line (stations 52–56). The difference in the *RF*s between the Figs 5.5 and 5.7 might come from the distorted vertical components by the scattered wave by the fault. The 'distorted' means that the vertical component is no longer the source time function that is one of the assumptions of the *RF*s method (Langston, 1979). Replacement of the denominator as another vertical component at the station 148, that is located at the northeast end of the array (Fig. 5.2), brings a coherent radial *RF*s with only a slight time shift (∼0.08 s) (Fig. 5.8).

5.3.2 Distortion of the vertical components

We calculate the *Z/Z RF*s with a reference station of 90 that is distant from the fault. The difference in the *Z/Z RF*s with that at the station 90 indicates the difference in the vertical components relative to the station 90. If we assume that the vertical component of the station 90 is a non-distorted source time function, the *Z/Z* at the other stations indicate the distorted vertical components that are no longer the source time function. The distortion relative to the station 90 is large close to the fault (stations 1–85) while the traces of the stations 91–108 have a small difference

with that of the station 90.

Also, the slight time shift of the first arrival phase is observable through all of the stations (earlier in the station 1 and later in the station 108). Although this time shift is minor in Fig. 5.9 and we omit a correction procedure in this study, the correction could not be difficult even in the case that the shift is larger (e.g., in a longer aperture of the array).

5.3.3 Schematics of travel time for a vertical fault model

A schematic figure is introduced to explain raypaths and travel times of a plane (teleseismic) P wave for a vertical fault zone model (Fig. 5.10). The fault zone has low velocity than that of contacting walls that have same arbitrary velocity. Neither conversion to S wave nor diffraction is assumed. Time domain is scaled as the amount of a velocity of a direct wave (Fig. 5.10b). The direct P wave arrives first in the left side of the fault zone (black arrow or line in Fig. 5.10). On the fault zone, the arrival time is delayed proportionally to a length of the ray that penetrates the fault zone (red arrow or line). Outside of the fault zone, the first arrival time is delayed proportionally to a thickness and the velocity of the fault zone (green arrow or line). Reverberation within the fault zone makes repeated branches that looks like '$>$' and '$<$' shapes. Also, one can imagine that introducing the conversion to the slower wave (i.e., S wave) at the boundary of the fault zone makes 'X' shape by interference (not displayed in Fig. 5.10). Bifurcations of the branches are located at the boundary of the fault zone. Duration of the repeated branches by the reverberation depends on attenuation and downward extension of the fault zone. The 'X' shape patterns can also be generated by the complex geometry of the boundary of the fault zones. Also, in the case of a study using local earthquakes instead of the teleseismic earthquakes, the earthquake which occurs inside the fault zone makes the 'X' pattern (e.g., Li et al., 2007).

5.3.4 High frequency *RF*s

The high frequency *RF*s are obtained by decreasing the water level (c) as 10^{-4} and increasing the width of Gaussian filter (σ) as 20 Hz in the equation 5.2. Figs 5.11 and 5.12 show the high frequency radial and tangential *RF*s, respectively, in a time domain of -1–3 s and in a range of the stations 25–80.

The '>', '<', and 'X'-shaped patterns are shown in both radial and tangential *RF*s (Figs 5.11 and 5.12). Southwestern (larger station number) bifurcation of branch begins at the station number of ∼70 and northeastern bifurcation at the station number of ∼32. Then, the length of the fault zone is ∼460 m containing the location where the Clark fault meets the surface. The various slopes of the branches might be because of the interference of the reverberating P and S waves.

5.3.5 Summary

We select the teleseismic earthquake that is proper to investigate the Clark fault, southern California. The high-frequency *RF*s are obtained by using a small water level as (10×10^{-4}). Fixing the denominator of the vertical component to one in the station away from the fault relieves the biased *RF*s. As a preliminary results, the '>', '<', and 'X' shaped phases might stem from the reverberation within the fault zone. The bifurcations of these phases constain the width of the fault zone to ∼460 m. Further calculation such as slowness–time stacking and a waveform modeling might constraint the downward extension, reduction in the seismic velocity, and velocity gradient of the boundary in the fault zone.

Future works

Numerical modeling of the seismic waveform will replace the schematic explanation about the scattered waves to the vertical fault zone (i.e., the section 5.3.3; raypaths and travel times in Fig. 5.10). The waveform modeling can generalize the Fig. 5.10,

involving the complex interference between the scattered P and S waves having different slowness. Also, changes in the RFs with the finite downward extension of the fault zone, a gradient of the velocity of the fault boundary, and the seismic velocity reduction can be dealt with quantitatively (e.g., Li et al., 2007). Also, the RFs stacking in temporal–slowness domain would be effective to decompose the P and S waves and reverberated waves.

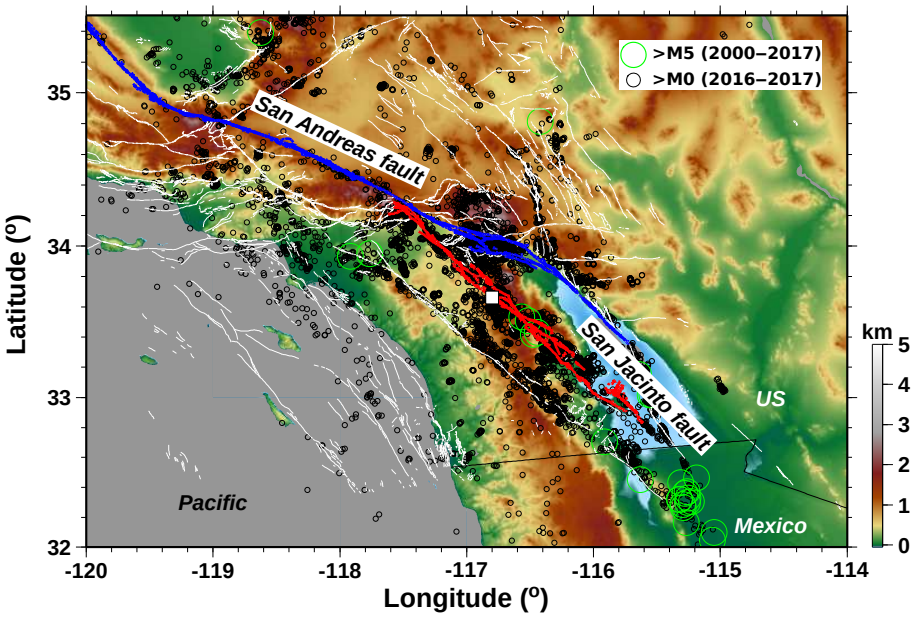

Figure 5.1: Map of San Andreas and San Jacinto faults. White square indicates a location where a geophone array is deployed.

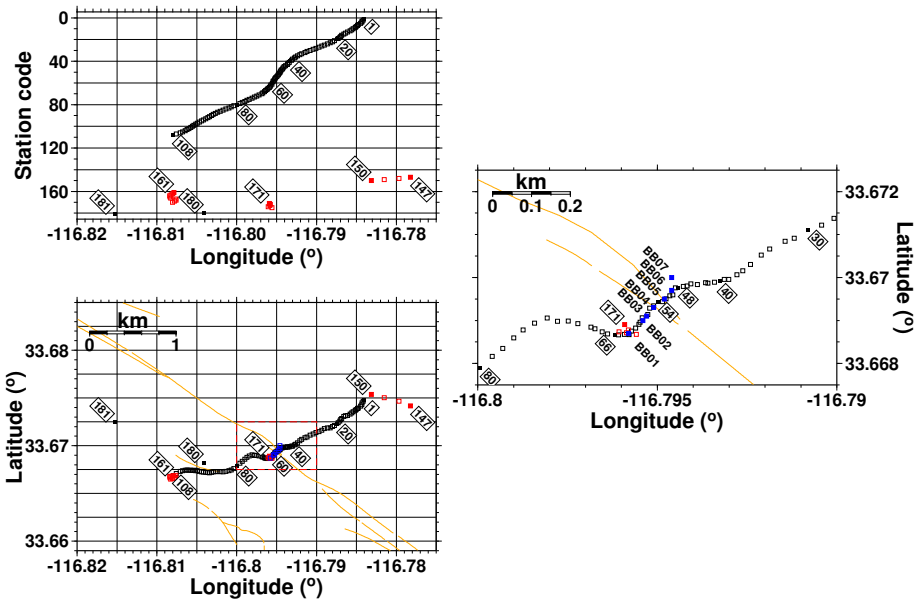

Figure 5.2: Magnified map and station code. (a) Station code according to longitude. (b) Magnified map. (c) Map showing broadband stations. Station code monotonically increases from 1 to 108 along the array southwest. The stations 147–150, 161–170, 171–175, 180, and 181 are located at northeast and southeast ends of the array or near the stations 61–66. The stations 52–56 intersects center of the fault line.

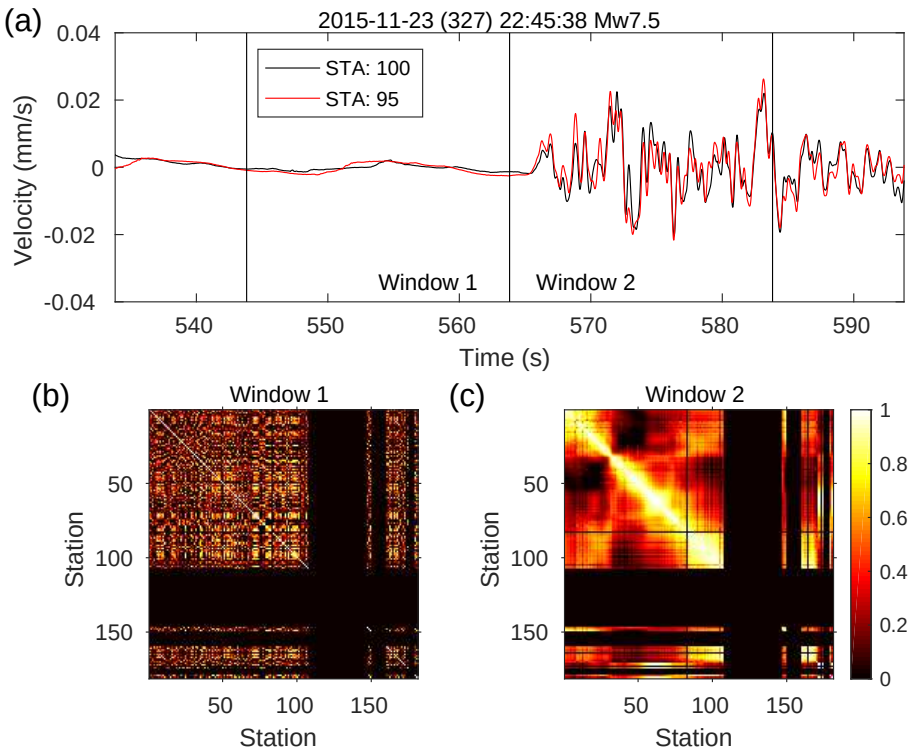

Figure 5.3: Coherency between E–W components of stations of an earthquake 2015-11-23,22:45:38 (Mw 7.5). (a) An example of traces showing high and low similarity in signal and noise windows between the stations 100 and 95. (b) Coherency among the stations in noise window. (c) Coherency among the stations in signal windows. The windows for correlation are indicated vertical solid lines in (a).

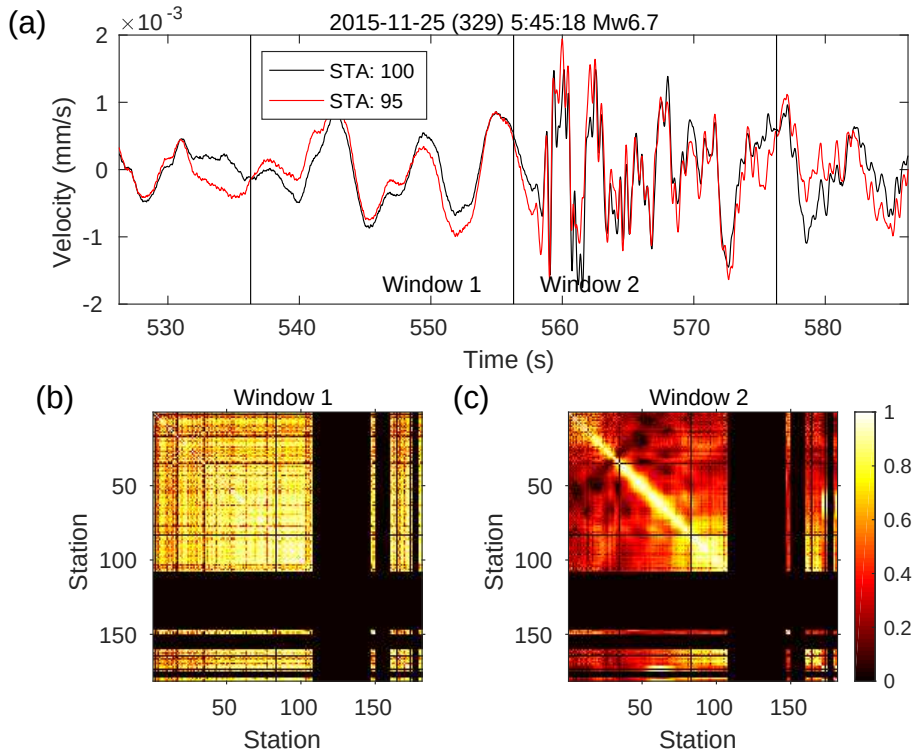

Figure 5.4: Correlation between E–W components of stations of an earthquake 2015-11-25,05:45:18 (Mw 6.7). (a) An example of traces showing high similarity in both signal and noise windows between the stations 100 and 95. (b) Correlation among the stations in noise window. (c) Correlation among the stations in signal windows. The windows for correlation are indicated vertical solid lines in (a).

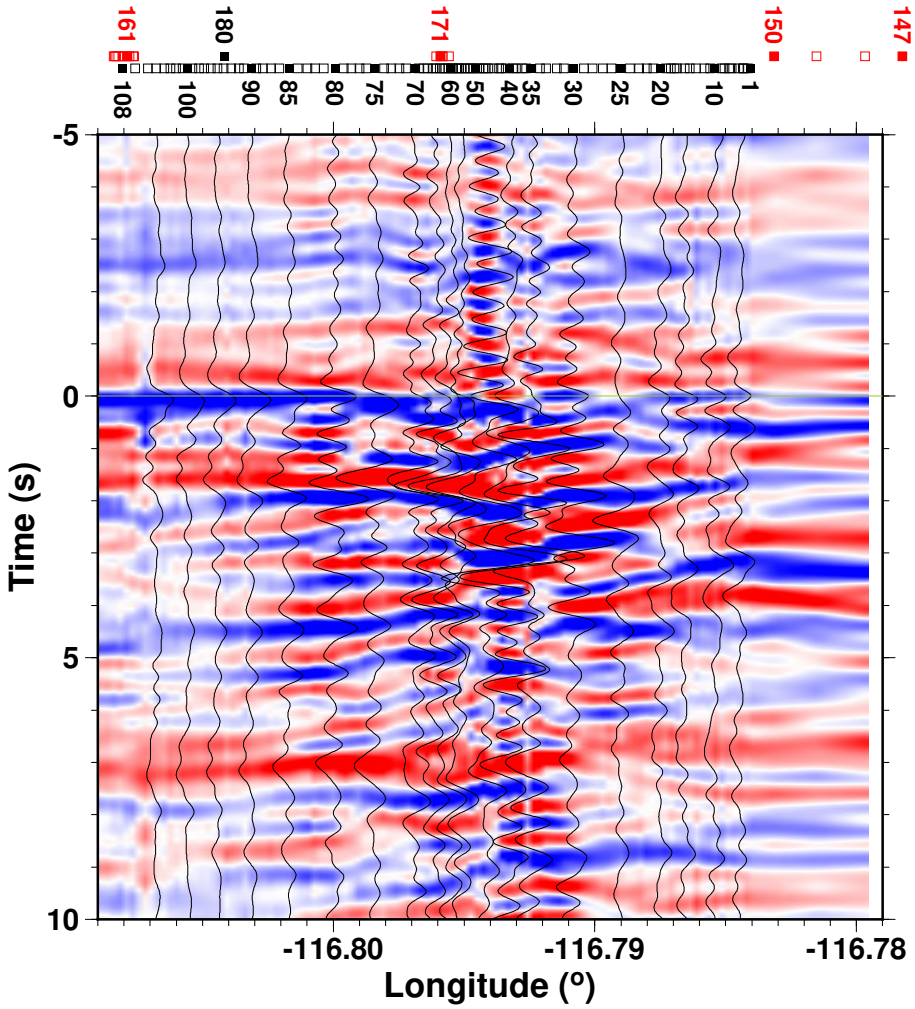

Figure 5.5: Radial receiver function. Positive in blue and negative in red. Station location is indicated in top of the figure. Water level is 10^{-2} and width of Gauss filter (σ) is 2.5 Hz. The stations 52–56 intersects center of the fault line. The stations 43–49 features monochromatic oscillation in a the noise window with ∼1.95 Hz (Fig. 5.6)

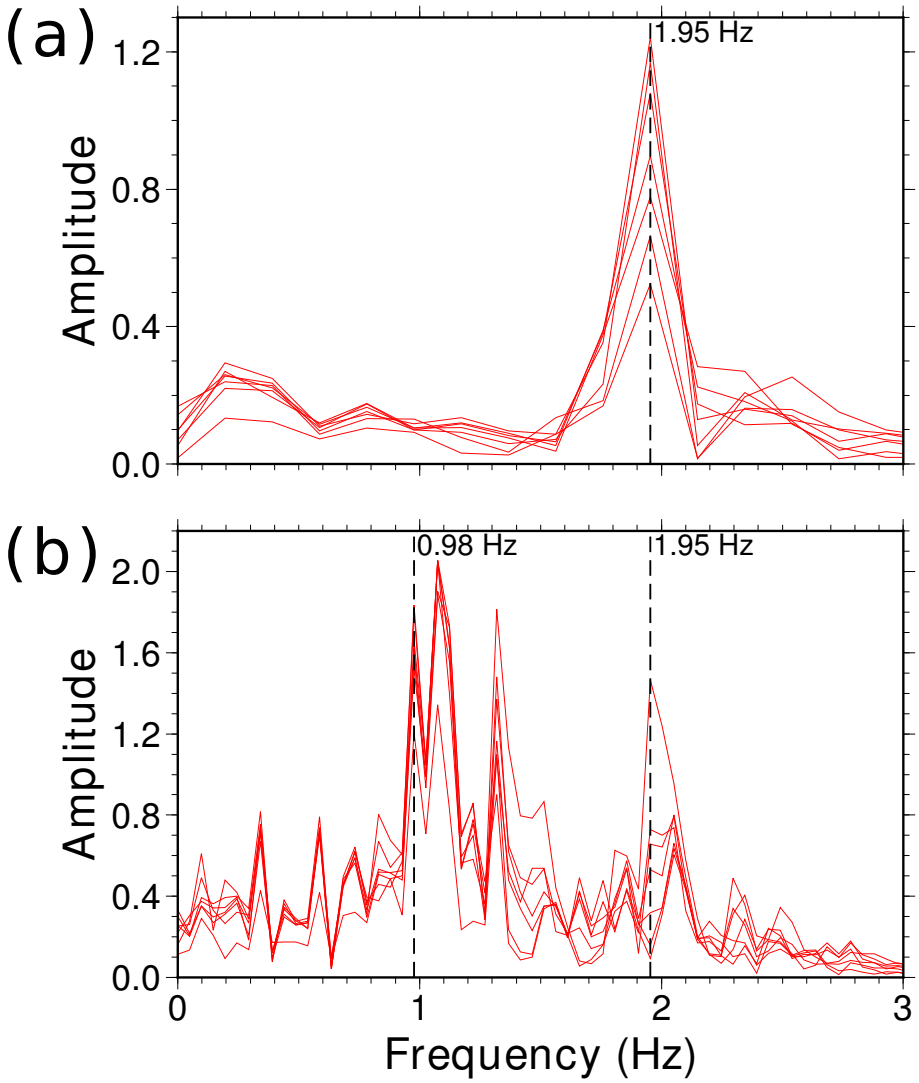

Figure 5.6: Spectrum of the receiver function in Fig. 5.5. (a) Spectrum in a window −5 to 0 s. (b) Spectrum in a window 0 to 20 s. Red line is for the stations 43 to 49 and gray line for the other stations.

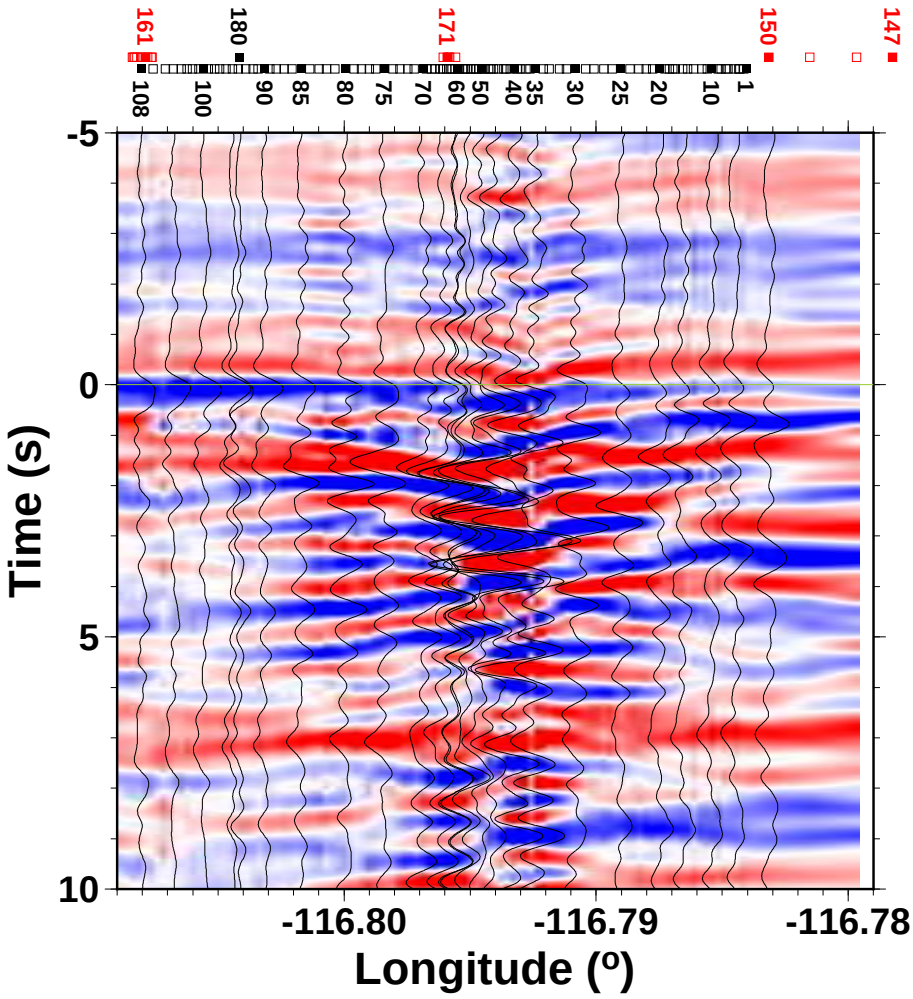

Figure 5.7: Radial receiver function with a fixed denominator, vertical component of stations 90. Station location is indicated in top of the figure. Water level is 10^{-2} and width of Gauss filter (σ) is 2.5 Hz. The stations 52–56 intersects center of the fault line. Note that the oscillation in a noise window is suppressed.

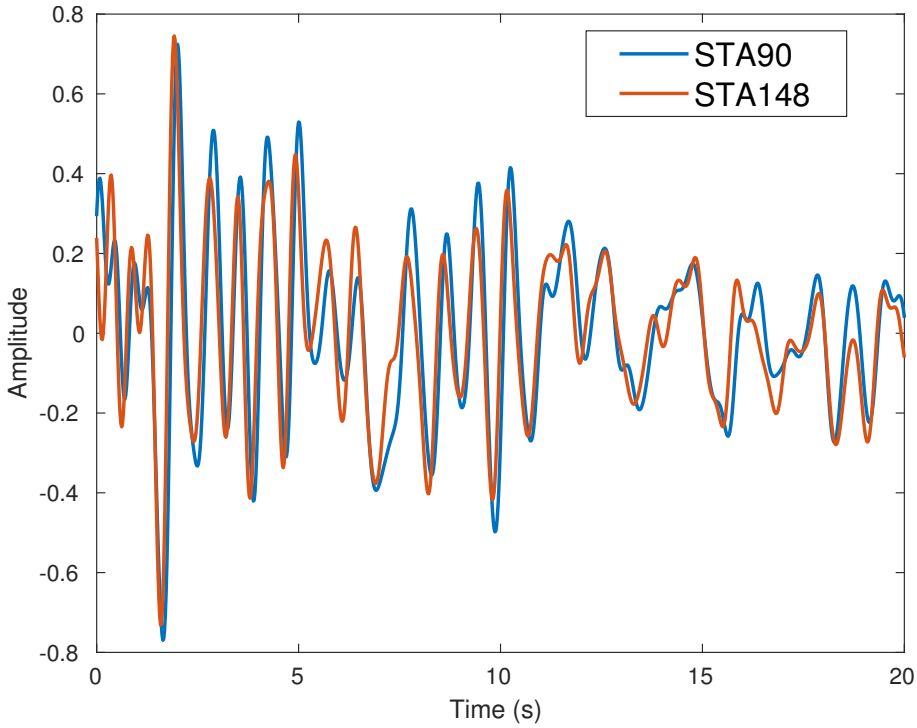

Figure 5.8: Radial receiver functions of the station 70 with different denominators of stations 90 and 148. Note that high correlation between them with a slight time shift of ∼0.08 s.

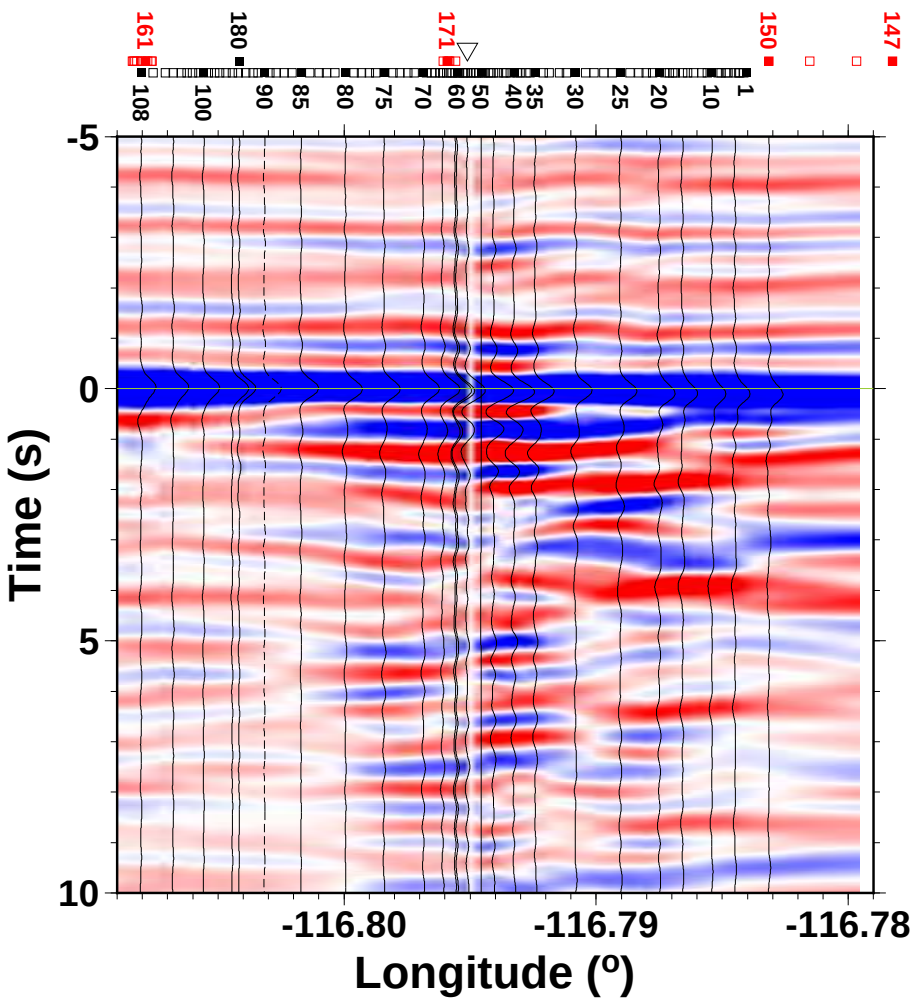

Figure 5.9: Deconvolution of the vertical components by the vertical component at the station 90 (Z/Z RFs). The dashed trace of the station 90 ideally should be Gaussian function. Station location is indicated in top of the figure. Water level is 10^{-2} and width of Gauss filter (σ) is 2.5 Hz. The stations 52–56 intersects center of the fault line (inverted triangle).

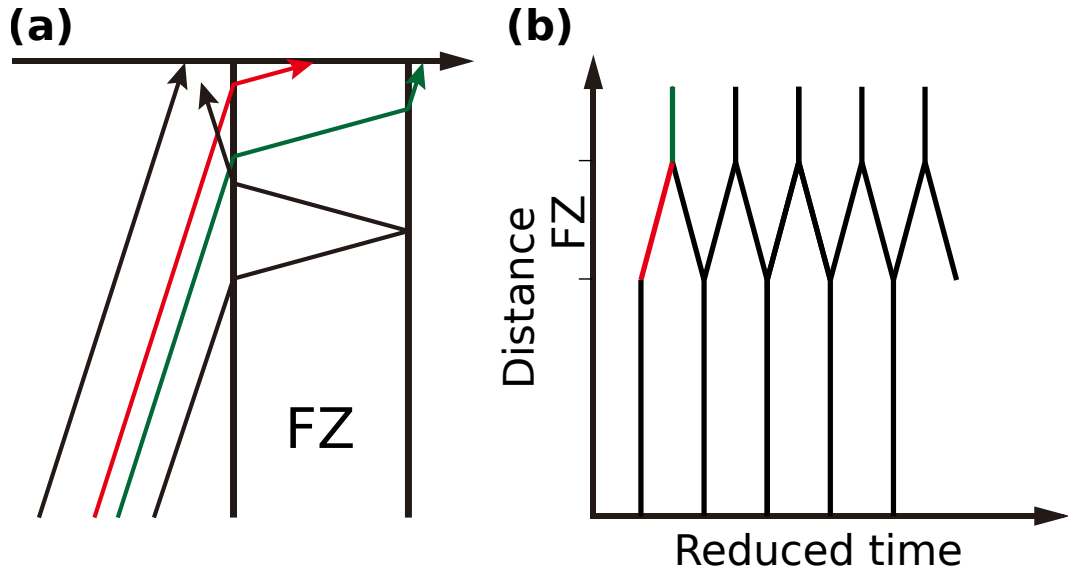

Figure 5.10: Schematics for raypath that interacts with a simple vertical fault zone model with a low velocity and travel time. (a) Raypath for a direct wave (black arrow), refracted wave (red), penetrating wave (green), and revererating wave (black). (b) Travel time for each phase. FZ—fault zone.

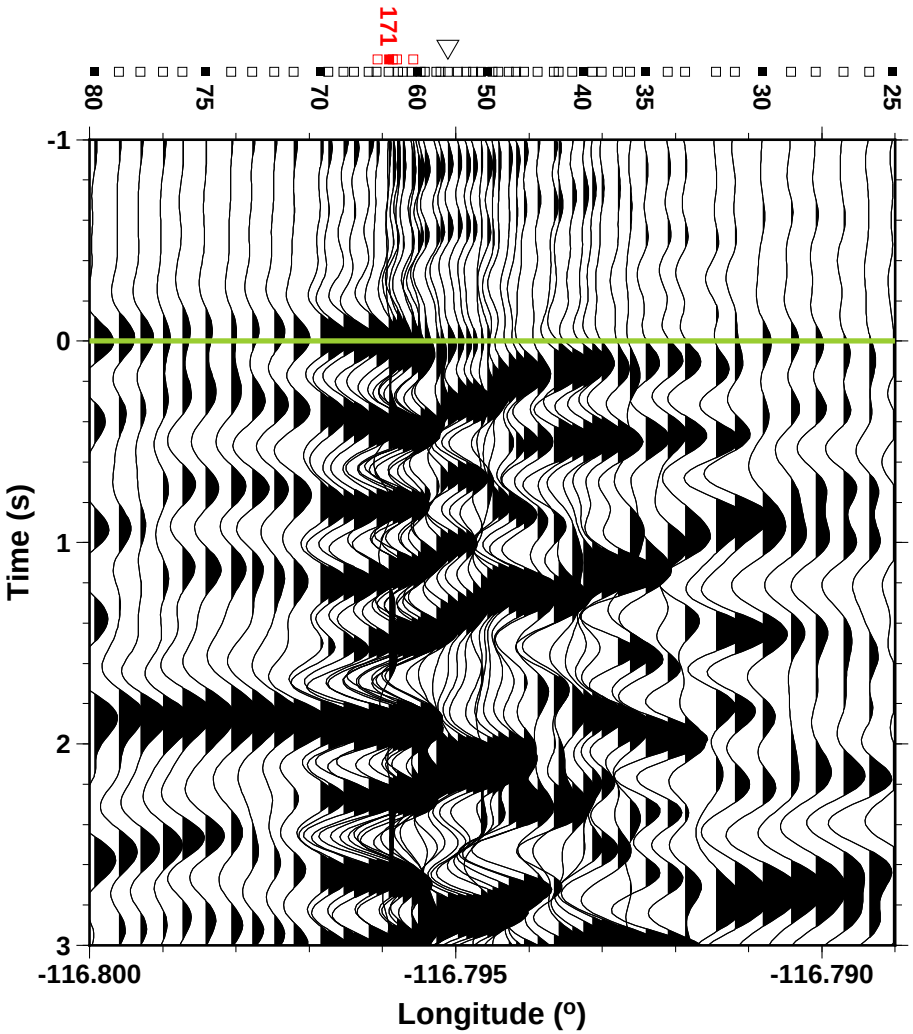

Figure 5.11: High frequency radial receiver function with a fixed denominator, vertical component of station 148. Teleseismic P wave propagates toward the stations 25 from 80. Station location is indicated in top of the figure. Water level is 10^{-4} and width of Gauss filter (σ) is 20 Hz. The stations 52–56 intersect center of the fault line (inverted triangle). Green line marks 0 s.

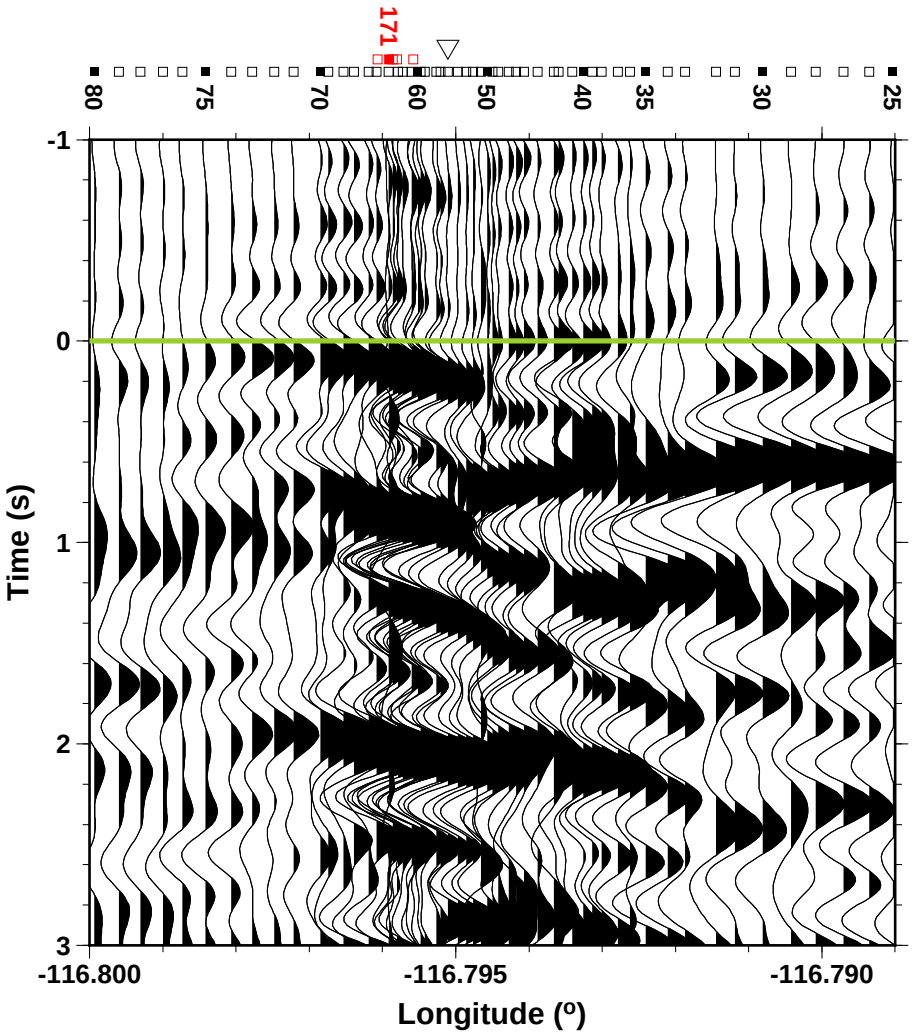

Figure 5.12: High frequency tangential receiver function with a fixed denominator, vertical component of station 148. Teleseismic P wave propagates toward the stations 25 from 80. Station location is indicated in top of the figure. Water level is 10^{-4} and width of Gauss filter (σ) is 20 Hz. The stations 52–56 intersect center of the fault line (inverted triangle). Green line marks 0 s.

Chapter 6

Conclusions

Through the years of Ph.D. student, I have chances to research various topics in seismology. The first topic was to develop a method to determine the orientation of the seismometer (Chapter 2). The motive began with attending an informal meeting about Lithosphere-asthenosphere boundary. An unknown horizontal orientation of the borehole sensors deployed in South Korea was a problem to get an exact calculation of receiver functions. I noticed that previous methods were depending on the assumption that the medium beneath the seismometer is isotropic. I came up with an idea that the assumption can be more general (i.e., being anisotropic) if some conditions are satisfied (e.g., long enough period of available data and good back-azimuthal coverage).

The second topic was to investigate the subduction zone in Peru. The southern Peruvian subduction zone is a snapshot in the evolution from normal-dipping slab to the flat slab by a buoyant Nazca ridge. I could use dense seismic network consisting of 100 stations deployed from 2008 to 2012 (PeruSE, 2013). It was expected that the double-difference tomography (Zhang and Thurber, 2003) is effective to image structures of slab and asthenospheric mantle. The relocated intra-slab seismicity showed that the slab is deformed smoothly. It was observed that timing of phase transition within the oceanic crust to a denser mineral varies along strike. Also, I observed that the heterogeneity of serpentinization in the forearc and hot asthenosphere in the backarc.

The other side of my topics is about an induced earthquake, occurred in a area of Pohang on 15 November 2017. This earthquake was suspected as an induced earthquake by injected fluid at neighboring two wells of enhanced geothermal plant because of strong proximity in space (distance between the wells and epicenter is $\sim$500 m) and time (the earthquake occurred 2 months after the last injection). However, the remained questions were that the magnitude of the earthquake (moment magnitude of 5.5) is very large in terms of a volume of the injected fluid and an inter-period

between the last injection to the earthquake (2 months) was not reconciled with high permeability based on the well test. Chapter 4 is addressing these points.

References

Abers, G. A., van Keken, P. E., and Hacker, B. R. (2017). The cold and relatively dry nature of mantle forearcs in subduction zones. *Nature Geoscience*, 10(5):333–337.

Akuhara, T. and Mochizuki, K. (2015). Hydrous state of the subducting Philippine Sea plate inferred from receiver function image using onshore and offshore data. *Journal of Geophysical Research: Solid Earth*, 120(12):8461–8477.

Antonijevic, S. K., Wagner, L. S., Kumar, A., Beck, S. L., Long, M. D., Zandt, G., Tavera, H., and Condori, C. (2015). The role of ridges in the formation and longevity of flat slabs. *Nature*, 524(7564):212–215.

Audet, P. (2015). Layered crustal anisotropy around the San Andreas fault near Parkfield, California. *Journal of Geophysical Research: Solid Earth*, 120(5):3527–3543.

Audet, P. (2016). Receiver functions using OBS data: Promises and limitations from numerical modelling and examples from the Cascadia Initiative. *Geophysical Journal International*, 205(3):1740–1755.

Beck, S. L., Zandt, G., and Wagner, L. (2010). Central Andean Uplift and the Geodynamics of the High Topography. International Federation of Digital Seismograph Networks. *International Federation of Digital Seismography Networks*.

Ben-Menahem, A. (1995). A concise history of mainstream seismology: Origins, legacy, and perspectives. *Bulletin of the Seismological Society of America*, 85(4):1202–1225.

Bendat, J. S. (2010). *Random data : analysis and measurement procedures*. Wiley series in probability and statistics. Wiley, Hoboken, N.J., 4th ed.. edition.

Bianchi, I., Park, J., Piana Agostinetti, N., and Levin, V. (2010). Mapping seismic anisotropy using harmonic decomposition of receiver functions: An application to Northern Apennines, Italy. *Journal of Geophysical Research*, 115(B12):B12317.

Bilek, S. L. (2010). Invited review paper: Seismicity along the South American subduction zone: Review of large earthquakes, tsunamis, and subduction zone complexity. *Tectonophysics*, 495(1-2):2–14.

Biot, M. A. (1941). General Theory of Three-Dimensional Consolidation. *Journal of Applied Physics*, 12(2):155–164.

Bird, P. (2003). An updated digital model of plate boundaries. *Geochemistry, Geophysics, Geosystems*, 4(3).

Bishop, B. T., Beck, S. L., Zandt, G., Wagner, L., Long, M., Antonijevic, S. K., Kumar, A., and Tavera, H. (2017). Causes and consequences of flat-slab subduction in southern Peru. *Geosphere*, 13(5):1392–1407.

Byerlee, J. (1978). Friction of Rocks. In *Rock Friction and Earthquake Prediction*, pages 615–626. Birkhäuser Basel, Basel.

Cahill, T. and Isacks, B. L. (1992). Seismicity and shape of the subducted Nazca Plate. *Journal of Geophysical Research*, 97(B12):17503.

Cassidy, J. F. (1992). Numerical experiments in broadband receiver function analysis. *Bulletin of the Seismological Society of America*, 82(3):1453–1474.

Chang, K. W., Yoon, H., Kim, Y., and Lee, M. Y. (2020). Operational and geological controls of coupled poroelastic stressing and pore-pressure accumulation along faults: Induced earthquakes in Pohang, South Korea. *Scientific Reports*, 10(1):2073.

Chlieh, M., Perfettini, H., Tavera, H., Avouac, J.-P., Remy, D., Nocquet, J.-M., Rolandone, F., Bondoux, F., Gabalda, G., and Bonvalot, S. (2011). Interseismic coupling and seismic potential along the Central Andes subduction zone. *Journal of Geophysical Research*, 116(B12):B12405.

Coyner, K. B. (1984). *Effects of stress, pore pressure, and pore fluids on bulk strain, velocity, and permeability in rocks*. PhD thesis, Massachusetts Institute of Technology.

Currie, C. A. and Hyndman, R. D. (2006). The thermal structure of subduction zone back arcs. *Journal of Geophysical Research: Solid Earth*, 111(B8).

Deng, K., Liu, Y., and Harrington, R. M. (2016). Poroelastic stress triggering of the December 2013 Crooked Lake, Alberta, induced seismicity sequence. *Geophysical Research Letters*, 43(16):8482–8491.

Detournay, E. and Cheng, A. H.-D. (1993). Fundamentals of Poroelasticity. In *Analysis and Design Methods*, pages 113–171. Elsevier.

Dieterich, J. H. (1994). A Constitutive Law for Rate of Earthquake Production and Its Application to Earthquake Clustering. *J. Geophys. Res.*, 99:2601–2618.

Doglioni, C. (2018). A classification of induced seismicity. *Geoscience Frontiers*, 9(6):1903–1909.

Dougherty, S. L. and Clayton, R. W. (2014). Seismic structure in southern Peru: evidence for a smooth contortion between flat and normal subduction of the Nazca Plate. *Geophysical Journal International*, 200(1):534–555.

Eakin, C. M., Long, M. D., Beck, S. L., Wagner, L. S., Tavera, H., and Condori, C. (2014). Response of the mantle to flat slab evolution: Insights from local S splitting beneath Peru. *Geophysical research letters*, 41(10):3438–3446.

Ekström, G. and Busby, R. W. (2008). Measurements of seismometer orientation at USArray transportable array and backbone stations. *Seismological Research Letters*, 79(4):554–561.

Ellsworth, W. L. (2013). Injection-Induced Earthquakes. *Science*, 341(6142):1225942–1225942.

Ellsworth, W. L., Giardini, D., Townend, J., Ge, S., and Shimamoto, T. (2019). Triggering of the Pohang, Korea, Earthquake (Mw 5.5) by Enhanced Geothermal System Stimulation. *Seismological Research Letters*.

Ellsworth, W. L. and Malin, P. E. (2011). Deep rock damage in the San Andreas Fault revealed by P- and S-type fault-zone-guided waves. *Geological Society, London, Special Publications*, 359(1):39–53.

Farra, V. and Vinnik, L. (2000). Upper mantle stratification by P and S receiver functions. *Geophysical Journal International*, 141(3):699–712.

Foulger, G. R., Wilson, M. P., Gluyas, J. G., Julian, B. R., and Davies, R. J. (2018). Global review of human-induced earthquakes. *Earth-Science Reviews*, 178:438–514.

Frederiksen, A. W. and Bostock, M. G. (2000). Modelling teleseismic waves in dipping anisotropic structures. *Geophysical Journal International*, 141(2):401–412.

Galis, M., Ampuero, J. P., Mai, P. M., and Cappa, F. (2017). Induced seismicity provides insight into why earthquake ruptures stop. *Science Advances*, 3(12).

Girardin, N. and Farra, V. (1998). Azimuthal anisotropy in the upper mantle from observations ofP-to-S converted phases: application to southeast Australia. *Geophysical Journal International*, 133(3):615–629.

Grigoli, F., Cesca, S., Rinaldi, A. P., Manconi, A., López-Comino, J. A., Clinton, J. F., Westaway, R., Cauzzi, C., Dahm, T., and Wiemer, S. (2018). The November 2017 M w 5.5 Pohang earthquake: A possible case of induced seismicity in South Korea. *Science*, 360(6392):1003–1006.

Gudmundsson, Ó. and Sambridge, M. (1998). A regionalized upper mantle (RUM) seismic model. *Journal of Geophysical Research: Solid Earth*, 103(B4):7121–7136.

Gupta, H. K. (2002). A review of recent studies of triggered earthquakes by artificial water reservoirs with special emphasis on earthquakes in Koyna, India. *Earth-Science Reviews*, 58(3-4):279–310.

Hacker, B. R. and Abers, G. A. (2012). Subduction Factory 5: Unusually low Poisson's ratios in subduction zones from elastic anisotropy of peridotite. *Journal of Geophysical Research: Solid Earth*, 117(B6).

Hacker, B. R., Abers, G. A., and Peacock, S. M. (2003). Subduction factory 1. Theoretical mineralogy, densities, seismic wave speeds, and H 2 O contents. *Journal of Geophysical Research: Solid Earth*, 108(B1).

Hampel, A. (2002). The migration history of the Nazca Ridge along the Peruvian active margin: a re-evaluation. *Earth and Planetary Science Letters*, 203(2):665–679.

Hart, D. J. and Wang, H. F. (1995). Laboratory measurements of a complete set of poroelastic moduli for Berea sandstone and Indiana limestone. *Journal of Geophysical Research: Solid Earth*, 100(B9):17741–17751.

Hasegawa, A. and Sacks, I. S. (1981). Subduction of the Nazca Plate beneath Peru as determined from seismic observations. *Journal of Geophysical Research: Solid Earth*, 86(B6):4971–4980.

Hayes, G. P., Wald, D. J., and Johnson, R. L. (2012). Slab1.0: A three-dimensional model of global subduction zone geometries. *Journal of Geophysical Research: Solid Earth*, 117(B1):B01302.

Hincks, T., Aspinall, W., Cooke, R., and Gernon, T. (2018). Oklahoma's induced seismicity strongly linked to wastewater injection depth. *Science*, 359(6381):1251–1255.

Hofmann, H., Zimmermann, G., Farkas, M., Huenges, E., Zang, A., Leonhardt, M., Kwiatek, G., Martinez-Garzon, P., Bohnhoff, M., Min, K.-B., Fokker, P., Westaway, R., Bethmann, F., Meier, P., Yoon, K. S., Choi, J. W., Lee, T. J., and Kim, K. Y. (2019). First field application of cyclic soft stimulation at the Pohang Enhanced Geothermal System site in Korea. *Geophysical Journal International*, 217(2):926–949.

Hong, T.-K., Lee, J., Park, S., and Kim, W. (2018). (Supp)Time-advanced occurrence of moderate-size earthquakes in a stable intraplate region after a megathrust earthquake and their seismic properties. *Scientific Reports*, 8(1):13331.

Houston, H. and Kanamori, H. (1986). Source spectra of great earthquakes: teleseismic constraints on rupture process and strong motion. *Bulletin of the Seismological Society of America*, 76(1):19–42.

Hughes, D. S. and Jones, H. J. (1950). Variation of elastic moduli of igneous rocks with pressure and temperature. *Bulletin of the Geological Society of America*, 61(8):843–856.

Hyndman, R. D. and Peacock, S. M. (2003). Serpentinization of the forearc mantle. *Earth and Planetary Science Letters*, 212(3-4):417–432.

Jahnke, G., Igel, H., and Ben-Zion, Y. (2002). Three-dimensional calculations of fault-zone-guided waves in various irregular structures. *Geophysical Journal International*, 151(2):416–426.

Janiszewski, H. A. and Abers, G. A. (2015). Imaging the plate interface in the Cascadia seismogenic zone: New constraints from offshore receiver functions. *Seismological Research Letters*, 86(5):1261–1269.

Johnson, C. W., Fu, Y., and Bürgmann, R. (2017). Stress Models of the Annual Hydrospheric, Atmospheric, Thermal, and Tidal Loading Cycles on California Faults: Perturbation of Background Stress and Changes in Seismicity. *Journal of Geophysical Research: Solid Earth*, 122(12):10,605–10,625.

Kawakatsu, H. and Abe, Y. (2016). Comment on "Nature of the Seismic Lithosphere-Asthenosphere Boundary within Normal Oceanic Mantle from High-Resolution Receiver Function" by Olugboji et al. *Geochemistry, Geophysics, Geosystems*, 17(8):3488–3492.

Kennett, B. L. N., Engdahl, E. R., and Buland, R. (1995). Constraints on seismic velocities in the Earth from traveltimes. *Geophysical Journal International*, 122(1):108–124.

Kim, H. C. and Lee, Y. (2007). Heat flow in the Republic of Korea. *Journal of Geophysical Research*, 112(B5):B05413.

Kim, K.-H., Ree, J.-H., Kim, Y., Kim, S., Kang, S. Y., and Seo, W. (2018). Assessing whether the 2017 M w 5.4 Pohang earthquake in South Korea was an induced event. *Science*, 360(6392):1007–1009.

Kim, S., Rhie, J., and Kim, G. (2011). Forward waveform modelling procedure for 1-D crustal velocity structure and its application to the southern Korean Peninsula. *Geophysical Journal International*, 185(1):453–468.

Kim, Y. and Clayton, R. W. (2015). Seismic properties of the Nazca oceanic crust in southern Peruvian subduction system. *Earth and Planetary Science Letters*, 429:110–121.

Kim, Y., Clayton, R. W., Asimow, P. D., and Jackson, J. M. (2013). Generation of talc in the mantle wedge and its role in subduction dynamics in central Mexico. *Earth and Planetary Science Letters*, 384:81–87.

Kim, Y., He, X., Ni, S., Lim, H., and Park, S. (2017). Earthquake Source Mechanism and Rupture Directivity of the 12 September 2016 Mw 5.5 Gyeongju, South Korea, Earthquake. *Bulletin of the Seismological Society of America*, 107(5):2525–2531.

King, G. C. P., Stein, R. S., and Lin, J. (1994). Static stress changes and the triggering of earthquakes. *Bulletin of the Seismological Society of America*, 84(3):935–953.

Korean Government Commission (2019). Final report of the Korean Government Commission on relations between the 2017 Pohang earthquake and EGS Project. Technical report, The Geological Society of Korea, Seoul.

Kumar, A., Wagner, L. S., Beck, S. L., Long, M. D., Zandt, G., Young, B., Tavera, H., and Minaya, E. (2016). Seismicity and state of stress in the central and southern Peruvian flat slab. *Earth and Planetary Science Letters*, 441:71–80.

Kwon, S., Xie, L., Park, S., Kim, K.-I., Min, K.-B., Kim, K. Y., Zhuang, L., Choi, J., Kim, H., and Lee, T. J. (2019). Characterization of 4.2-km-Deep Fractured Granodiorite Cores from Pohang Geothermal Reservoir, Korea. *Rock Mechanics and Rock Engineering*, 52(3):771–782.

Langston, C. A. (1979). Structure under Mount Rainier, Washington, inferred from teleseismic body waves. *Journal of Geophysical Research: Solid Earth*, 84(B9):4749–4762.

Larson, E. W. F. (2000). *Measuring refraction and modeling velocities of surface waves*.

Larson, E. W. F. and Ekström, G. (2002). Determining surface wave arrival angle anomalies. *Journal of Geophysical Research: Solid Earth*, 107(B6):ESE 7–1–ESE 7–15.

Laske, G. (1995). Global observation of off-great-circle propagation of long-period surface waves. *Geophysical Journal International*, 123(1):245–259.

Laske, G. and Masters, G. (1996). Constraints on global phase velocity maps from long-period polarization data. *Journal of Geophysical Research: Solid Earth*, 101(B7):16059–16075.

Laske, G., Masters, G., Ma, Z., and Pasyanos, M. (2013). Update on CRUST1.0 - A 1-degree Global Model of Earth's Crust. In *Geophysical Research Abstracts*. EGU General Assembly.

Lee, H. and Sheen, D. (2015). A study on determination of orientation of borehole seismometer. *Journal of the Geological Society of Korea*, 51(1):93–103.

Lee, K., Chung, N. S., and Chung, T. W. (2003). Earthquakes in Korea from 1905 to 1945. *Bulletin of the Seismological Society of America*, 93(5):2131–2145.

Lee, S.-J. and Rhie, J. (2015). Determining the orientations of broadband stations in South Korea using ambient noise cross-correlation. *Geophysics and Geophysical Exploration*, 18(2):85–90.

Lee, T. J., Song, Y., Park, D.-W., Jeon, J., and Yoon, W. S. (2015). Three Dimensional Geological Model of Pohang EGS Pilot Site, Korea. *World Geothermal Congress 2015*, (April):6.

Lee, Y., Park, S., Kim, J., Kim, H. C., and Koo, M.-H. (2010). Geothermal Resource Assessment for EGS in Korea. In *Proceedings World Geothermal Congress*, Bali.

Levin, V. and Park, J. (1997). P-SH conversions in a flat-layered medium with anisotropy of arbitrary orientation. *Geophysical Journal International*, 131(2):253–266.

Levin, V. and Park, J. (1998). P-SH Conversions in Layered Media with Hexagonally Symmetric Anisotropy: A CookBook. In *Geodynamics of Lithosphere Earth's Mantle*, pages 669–697. Birkhäuser Basel, Basel.

Li, H., Zhu, L., and Yang, H. (2007). High-resolution structures of the Landers fault zone inferred from aftershock waveform data. *Geophysical Journal International*, 171(3):1295–1307.

Li, Y.-G., Ellsworth, W. L., Thurber, C. H., Malin, P. E., and Aki, K. (1997). Fault-zone guided waves from explosions in the San Andreas fault at Parkfield and Cienega Valley, California. *Bulletin of the Seismological Society of America*, 87(1):210–221.

Li, Y.-G., Leary, P., Aki, K., and Malin, P. (1990). Seismic Trapped Modes in the Oroville and San Andreas Fault Zones. *Science*, 249(4970):763–766.

Li, Y.-G. and Leary, P. C. (1990). Fault zone trapped seismic waves. *Bulletin of the Seismological Society of America*, 80(5):1245–1271.

Lin, C.-R., Kuo, B.-Y., Liang, W.-T., Chi, W.-C., Huang, Y.-C., Collins, J., and Wang, C.-Y. (2010). Ambient noise and teleseismic signals recorded by ocean-

bottom seismometers offshore eastern Taiwan. *Terrestrial, Atmospheric and Oceanic Sciences*, 21(5):743–755.

Lodewyk, J. and Sumy, D. (2014). Cascadia Amphibious Array Ocean Bottom Seismograph Horizontal Component Orientations, 2013-2014 OBS Deployments.

Lomax, A., Satriano, C., and Vassallo, M. (2012). Automatic Picker Developments and Optimization: FilterPicker–a Robust, Broadband Picker for Real-Time Seismic Monitoring and Earthquake Early Warning. *Seismological Research Letters*, 83(3):531–540.

Long, M. D. and Becker, T. W. (2010). Mantle dynamics and seismic anisotropy. *Earth and Planetary Science Letters*, 297(3-4):341–354.

Long, M. D. and Silver, P. G. (2009). Shear wave splitting and mantle anisotropy: measurements, interpretations, and new directions. *Surveys in Geophysics*, 30(4-5):407–461.

Ma, Y. and Clayton, R. W. (2014). The crust and uppermost mantle structure of Southern Peru from ambient noise and earthquake surface wave analysis. *Earth and Planetary Science Letters*, 395:61–70.

Ma, Y. and Clayton, R. W. (2015). Flat slab deformation caused by interplate suction force. *Geophysical Research Letters*, 42(17):7064–7072.

Ma, Y., Clayton, R. W., Tsai, V. C., and Zhan, Z. (2013). Locating a scatterer in the active volcanic area of Southern Peru from ambient noise cross-correlation. *Geophysical Journal International*, 192(3):1332–1341.

Manea, V. C., Manea, M., Ferrari, L., Orozco-Esquivel, T., Valenzuela, R. W., Husker, A., and Kostoglodov, V. (2017). A review of the geodynamic evolution of flat slab subduction in Mexico, Peru, and Chile. *Tectonophysics*, 695:27–52.

Marone, C. and Scholz, C. H. (1988). The depth of seismic faulting and the upper transition from stable to unstable slip regimes. *Geophysical Research Letters*, 15(6):621–624.

McGarr, a. (2014). Maximum magnitude earthquakes induced by fluid injection. *Journal of Geophysical Research: Solid Earth*, 119(2):1008–1019.

Mizoguchi, K., Hirose, T., Shimamoto, T., and Fukuyama, E. (2008). Internal structure and permeability of the Nojima fault, southwest Japan. *Journal of Structural Geology*, 30(4):513–524.

Morrow, C., Lockner, D., Hickman, S., Rusanov, M., and Röckel, T. (1994). Effects of lithology and depth on the permeability of core samples from the Kola and KTB drill holes. *Journal of Geophysical Research*, 99(B4):7263.

Myers, S. C., Johannesson, G., and Hanley, W. (2007). A Bayesian hierarchical method for multiple-event seismic location. *Geophysical Journal International*, 171(3):1049–1063.

O'Driscoll, L. J., Richards, M. A., and Humphreys, E. D. (2012). Nazca-South America interactions and the late Eocene-late Oligocene flat-slab episode in the central Andes. *Tectonics*, 31(2).

Park, J. and Levin, V. (2016). Anisotropic shear zones revealed by backazimuthal harmonics of teleseismic receiver functions. *Geophysical Journal International*, 207(2):1216–1243.

Park, S., Xie, L., Kim, K. I., Kwon, S., Min, K. B., Choi, J., Yoon, W. S., and Song, Y. (2017). First Hydraulic Stimulation in Fractured Geothermal Reservoir in Pohang PX-2 Well. *Procedia Engineering*, 191:829–837.

Peacock, S. M. (2004). Thermal structure and metamorphic evolution of subducting slabs. pages 7–22.

PeruSE (2013). Peru subduction experiment. *Caltech. Dataset.*

Phillips, K. and Clayton, R. W. (2014). Structure of the subduction transition region from seismic array data in southern Peru. *Geophysical Journal International*.

Phillips, K., Clayton, R. W., Davis, P., Tavera, H., Guy, R., Skinner, S., Stubailo, I., Audin, L., and Aguilar, V. (2012). Structure of the subduction system in southern Peru from seismic array data. *Journal of Geophysical Research: Solid Earth*, 117(B11):B11306.

Porter, R., Gilbert, H., Zandt, G., Beck, S., Warren, L., Calkins, J., Alvarado, P., and Anderson, M. (2012). Shear wave velocities in the Pampean flat-slab region from Rayleigh wave tomography: Implications for slab and upper mantle hydration. *Journal of Geophysical Research: Solid Earth*, 117(B11):B11301.

Qian, W., Wang, W., Zou, F., and Wu, Z. (2018). Elasticity of orthoenstatite at high pressure and temperature: Implications for the origin of low VP/VS zones in the mantle wedge. *Geophysical research letters*, 45(2):665–673.

Ramos, V. A., Cristallini, E., and Pérez, D. J. (2002). The Pampean flat-slab of the Central Andes. *Journal of South American Earth Sciences*, 15(1):59–78.

Ramos, V. A. and Folguera, A. (2009). Andean flat-slab subduction through time. *Geological Society, London, Special Publications*, 327(1):31–54.

Reasenberg, P. A. and Simpson, R. W. (1992). Response of Regional Seismicity to the Static Stress Change Produced by the Loma Prieta Earthquake. *Science*, 255(5052):1687–1690.

Rice, J. R. and Cleary, M. P. (1976). Some basic stress diffusion solutions for fluid-saturated elastic porous media with compressible constituents. *Reviews of Geophysics*, 14(2):227.

Ryan, J., Beck, S., Zandt, G., Wagner, L., Minaya, E., and Tavera, H. (2016). Central Andean crustal structure from receiver function analysis. *Tectonophysics*, 682:120–133.

Scholz, C. H. (1998). Earthquakes and friction laws. *Nature*, 391(6662):37–42.

Schulte-Pelkum, V. and Mahan, K. H. (2014). A method for mapping crustal deformation and anisotropy with receiver functions and first results from USArray. *Earth and Planetary Science Letters*, 402:221–233.

Schulte-Pelkum, V., Masters, G., and Shearer, P. M. (2001). Upper mantle anisotropy from long-period P polarization. *Journal of Geophysical Research: Solid Earth*, 106(B10):21917–21934.

Scire, A., Zandt, G., Beck, S., Long, M., Wagner, L., Minaya, E., and Tavera, H. (2016). Imaging the transition from flat to normal subduction: variations in the structure of the Nazca slab and upper mantle under southern Peru and northwestern Bolivia. *Geophysical Journal International*, 204(1):457–479.

Segall, P. and Lu, S. (2015). Injection-induced seismicity: Poroelastic and earthquake nucleation effects. *Journal of Geophysical Research: Solid Earth*, 120(7):5082–5103.

Shin, J. S., Sheen, D.-H., and Shin, I. C. (2009). Orientation correction for borehole seismic stations in South Korea. *Journal of the Geological Society of Korea*, 45(1):47–54.

Soh, I., Chang, C., Lee, J., Hong, T.-K., and Park, E.-S. (2018). Tectonic stress orientations and magnitudes, and friction of faults, deduced from earthquake focal

mechanism inversions over the Korean Peninsula. *Geophysical Journal International*, 213(2):1360–1373.

Song, S. G. and Lee, H. (2019). Static Slip Model of the 2017 Mw 5.4 Pohang, South Korea, Earthquake Constrained by the InSAR Data. *Seismological Research Letters*, 90(1):140–148.

Stachnik, J. C., Sheehan, A. F., Zietlow, D. W., Yang, Z., Collins, J., and Ferris, A. (2012). Determination of New Zealand Ocean Bottom Seismometer Orientation via Rayleigh-Wave Polarization. *Seismological Research Letters*, 83(4):704–713.

Stein, R. S. (1999). The role of stress transfer in earthquake occurrence. *Nature*, 402(6762):605–609.

Syracuse, E. M. and Abers, G. A. (2006). Global compilation of variations in slab depth beneath arc volcanoes and implications. *Geochemistry, Geophysics, Geosystems*, 7(5):n/a–n/a.

Toomey, D., Allen, R., Barclay, A., Bell, S., Bromirski, P., Carlson, R., Chen, X., Collins, J., Dziak, R., Evers, B., Forsyth, D., Gerstoft, P., Hooft, E., Livelybrooks, D., Lodewyk, J., Luther, D., McGuire, J., Schwartz, S., Tolstoy, M., Trehu, A., Weirathmueller, M., and Wilcock, W. (2014). The Cascadia Initiative: A Sea Change In Seismological Studies of Subduction Zones. *Oceanography*, 27(2):138–150.

Tovish, A., Schubert, G., and Luyendyk, B. P. (1978). Mantle flow pressure and the angle of subduction: Non-Newtonian corner flows. *Journal of Geophysical Research: Solid Earth*, 83(B12):5892–5898.

Vinnik, L. (1977). Detection of waves converted from P to SV in the mantle. *Physics of the Earth and Planetary Interiors*, 15(1):39–45.

Vinnik, L., Kiselev, S., Weber, M., Oreshin, S., and Makeyeva, L. (2012). Frozen and active seismic anisotropy beneath southern Africa. *Geophysical Research Letters*, 39(8).

Wagner, L., Beck, S., Zandt, G., and Ducea, M. (2006). Depleted lithosphere, cold, trapped asthenosphere, and frozen melt puddles above the flat slab in central Chile and Argentina. *Earth and Planetary Science Letters*, 245(1-2):289–301.

Wagner, L. S., Anderson, M. L., Jackson, J. M., Beck, S. L., and Zandt, G. (2008). Seismic evidence for orthopyroxene enrichment in the continental lithosphere. *Geology*, 36(12):935.

Waldhauser, F. and Ellsworth, W. L. (2000). A Double-Difference Earthquake Location Algorithm: Method and Application to the Northern Hayward Fault, California. *Bulletin of the Seismological Society of America*, 90(6):1353–1368.

Wang, R. and Kümpel, H. (2003). Poroelasticity: Efficient modeling of strongly coupled, slow deformation processes in a multilayered half-space. *Geophysics*, 68(2):705–717.

Wang, X., Chen, Q., Li, J., and Wei, S. (2016). Seismic Sensor Misorientation Measurement Using P -Wave Particle Motion: An Application to the NECsaids Array. *Seismological Research Letters*, 87(4):901–911.

Ward, K. M., Zandt, G., Beck, S. L., Wagner, L. S., and Tavera, H. (2016). Lithospheric structure beneath the northern Central Andean Plateau from the joint inversion of ambient noise and earthquake-generated surface waves. *Journal of Geophysical Research: Solid Earth*, 121(11):8217–8238.

Webb, S. C. (1998). Broadband seismology and noise under the ocean. *Reviews of Geophysics*, 36(1):105–142.

Woessner, J., Jónsson, S., Sudhaus, H., and Baumann, C. (2012). Reliability of Coulomb stress changes inferred from correlated uncertainties of finite-fault source models. *Journal of Geophysical Research: Solid Earth*, 117(7):1–14.

Wonham, J. (1967). Effect of Pressure on the Viscosity of Water. *Nature*, 215(5105):1053–1054.

Woo, J., Kim, M., Sheen, D., Kang, T., Rhie, J., Grigoli, F., Ellsworth, W. L., and Giardini, D. (2019). An In-Depth Seismological Analysis Revealing a Causal Link Between the 2017 M W 5.5 Pohang Earthquake and EGS Project. *Journal of Geophysical Research: Solid Earth*, pages 13060–13078.

Wu, J. and Hole, J. A. (2011). Refraction of Fault-Zone Guided Seismic Waves. *Bulletin of the Seismological Society of America*, 101(4):1674–1682.

Ye, L., Lay, T., Kanamori, H., Zhan, Z., and Duputel, Z. (2016). Diverse rupture processes in the 2015 Peru deep earthquake doublet. *Science Advances*, 2(6):e1600581—-e1600581.

Yoo, H. (2018). *Numerical modeling of hydraulic stimulation at a fractured geothermal reservoir*. PhD thesis, Seoul National University.

Yoshizawa, K., Yomogida, K., and Tsuboi, S. (1999). Resolving power of surface wave polarization data for higher-order heterogeneities. *Geophysical Journal International*, 138(1):205–220.

Yuan, X., Sobolev, S. V., Kind, R., Oncken, O., Bock, G., Asch, G., Schurr, B., Graeber, F., Rudloff, A., Hanka, W., Wylegalla, K., Tibi, R., Haberland, C., Rietbrock, A., Giese, P., Wigger, P., Röwer, P., Zandt, G., Beck, S., Wallace, T., Pardo, M., and Comte, D. (2000). Subduction and collision processes in the Central Andes constrained by converted seismic phases. *Nature*, 408(6815):958–961.

Zha, Y., Webb, S. C., and Menke, W. (2013). Determining the orientations of ocean bottom seismometers using ambient noise correlation. *Geophysical Research Letters*, 40(14):3585–3590.

Zhang, H. and Thurber, C. H. (2003). Double-difference tomography: The method and its application to the Hayward Fault, California. *Bulletin of the Seismological Society of America*, 93(5):1875–1889.

초록

페루 남부 섭입대와 모멘트 규모 5.5의 2017년 포항에서 발생한 지진을 연구하였다. 페루 남부 섭입대는 섭입한 판이 점차 편평해지는 지역이다. 섭입판 안에서 발생한 지진과 원거리 변환 위상(후자는 이전 연구 결과)을 활용해서 섭입판의 기하적 구조가 급격한 변화 없이 점진적이라는 것을 보였다. 이중 차분 토모그래피 방법을 적용하여 3차원 P파와 S파의 속도 구조를 얻었으며, 이것의 변화가 지표의 화산활동과 섭입 메커니즘에 어떤 의미를 지니는지 해석하였다. 전호분지와 배호분지 아래의 섭입판과 맨틀쐐기(또는 얇은 맨틀 층)의 수화 정도에 불균질성으로 해석하였다. 포항 지진은 심부 지열 발전소 근처에서 2017년 11월 15일에 발생했다. 공극탄성이론을 바탕으로 포항 지진이 발생한 물리적 이유를 밝혀내기 위한 연구를 하였다. 포항 지진이 발생한 시간은 느린 유체 확산으로 설명할 수 있음을 보였다.

대한민국에 설치된 영구 지진 관측 데이터의 가용성을 늘리는데 기여하였다. 광대역 지진계 대부분(2016년 기준 52개 중 30개)은 시추공에 삽입하는 형태의 지진계이다. 시추공 지진계는 인위적 잡음이 낮지만, 방위각을 알 수 없다는 단점이 있다. 비등방적 매질을 가정하면서도 방위각을 결정할 수 있는 새로운 방법을 개발하였다. 이 방법은 지진 효과를 제거하면서 지진계의 방위각을 결정한다. 2005년부터 2016년까지 대한민국에 설치된 지진계 데이터에 적용하여 방위각을 결정하였다. 또한, 이 방법이 잡음이 더 심한 환경(e.g., 해양저)에 설치된 지진계에도 일부 적용할 수 있음을 부분적으로 확인하였다.

진행 중인 연구 주제는 조밀한 지오폰(geophone) 임시 관측망을 활용한 캘리포니아 남부 클라크 단층(Clark fault)에 대한 연구이다. 129개의 지오폰이 2.5 km에 걸쳐 단층에 약간 비스듬히 설치되었다. 42개의 원거리 지진 중에서 1개가 P파 수신함수를 계산하기 적합한 것을 확인하였다. 지진파의 지연(0.6초 이내), 분기와 반사를 관찰해서 단층의 넓이가 약 460 m 임을 알아내었다. 디컨볼루션(deconvolution)하는 수직 성분을 단층에서 약 1.2 km 떨어진 하나의 지오폰으로 고정하는 것이 단층에 의해 다중 반사되는

위상을 분별하는데 도움이 되는 것을 알아내었다.

주요어: 섭입대, 2017년 포항 지진, 공극탄성, 비등방성, 방위각, 클라크 단층
학번: 2014-21308

Acknowledgements

It is a great pleasure to express my appreciation to all of the people who supported me and encouraged me to finish my Ph.D. First, I thank my advisor YoungHee Kim for supporting me. She gave me much advice and shared her intuition, experience, and knowledge. It is difficult to reward her patience. Her research philosophy helped me to grow.

I also thank Junkee Rhie and Tae-Kyung Hong (Yonsei University). Especially, I sincerely thank T.-K. Hong for permission to attend his class as a guest student for four semesters. The classes at Yonsei University were invaluable for widening my knowledge and establishing a theoretical background. Junkee Rhie, Seongryong Kim, Sang-Hyun Lee, and Tae-Gyu Yee first allowed me to experience research in an undergraduate internship program.

I thank my colleagues. I gained important insights from discussions with Junhyung Lee (Yonsei University) and Jeong-Ung Woo about two large earthquakes that occurred during my Ph.D. I thank Eunyoung Kim, who was a senior student and helped me considerably when I joined Dr. Kim's laboratory. I also thank Hyunsun Kang, HyeJeong Kim, Sang-Jun Lee, HyeJeong Cho, and Hyoihn Jang, fellow graduate students, and I would like to encourage Jun Yong Park, Jae Woo Kim, Jeena Yun, Min Seong Seo, and Young Oh Son on their successful journey to graduate studies.

I thank my thesis committee, Haemyeong Jung, Tae-Seob Kang, Junkee Rhie, and Seongryong Kim for their encouragement and numerous comments on my research and dissertation.

Jeong-Woong Park first introduced me to geophysics and gave me the opportunity to attend an academic symposium in memory of Jeon. Thank you. I also thank the members of the department office, Hyunhee Ryu, Sung-mi Shin, Jongwon Kim, Kangjun Lee, and Jungran Jang, and the laboratory secretaries Songhee Park and Sujeong Noh. They all provided assistance that was essential for enabling me to graduate from Seoul National University. I have also been fortunate to have a professional programmer as a friend for 15 years; Hasang Jeong guided me with suggestions many times when I encountered a problem, including the first time I used Linux in 2012.

Finally, I would like to express my deepest appreciation to my parents. It would have been impossible to complete the Ph.D. course without their long support, belief, and sacrifice.